Finite-beta simulations of HIT-SI and HIT-SI3 using the NIMROD code

Kyle Morgan

A dissertation
submitted in partial fulfillment of the
requirements for the degree of

Doctor of Philosophy

University of Washington

2018

Reading Committee:

Thomas R. Jarboe, Chair

Brian Nelson

Boris Spivak

Program Authorized to Offer Degree:
Department of Physics

Abstract

Finite-beta simulations of HIT-SI and HIT-3 using the NIMROD code

Kyle Douglas Morgan

Chair of the Supervisory Committee:

Professor Thomas R. Jarboe

Department of Physics

The Helicity Injected Torus with Steady Inductive helicity injection (HIT-SI) and HIT-SI3 experiments are a pair of devices that form and sustain spheromak plasmas through the use of Steady Inductive Helicity Injection (SIHI). SIHI is accomplished through a set of semi-toroidal injectors that inductively drive oscillating non-axisymmetric helical magnetic fields on the surface of the equilibrium plasma. As magnetic helicity is injected the central plasma will relax towards a minimum energy state while conserving helicity, which is the spheromak state. This non-axisymmetric helicity injection additionally enables the usage of Imposed Dynamo Current Drive (IDCD) to sustain the equilibrium that forms.

Numerical studies have been performed based on the extended MagnetoHydroDynamics (eMHD) fluid model using the NIMROD code to study the 3-D dynamics present in the devices. The goal of these simulations is two-fold: increased understanding of the dynamic processes at play and validation of the models for use as a predictive tool. A number of simulations have been performed spanning both the experimental operation space of both devices and predictive studies of similar devices.

Studies of the HIT-SI device focused on matching the experimental results that were obtained during a parameter scan of the oscillating frequency of the injectors. It was found that zero-β models, which neglected the role of pressure gradients in the system, were ill-equipped to capture experimental results that were observed at higher frequencies. To improve agreement between the models and the experimental results, a finite-β model was implemented that while showing improvement in qualitative agreement with experimental observations,

still fails to exactly capture the observed effects. Further improvements to the fluid model have been explored, though currently the computational limits make them untractable.

Studies of the HIT-SI3 device focused on comparisons between different injector drive structures. The three-injector setup allows for a variety of modal spectra of the imposed perturbation, allowing control over the equilibrium plasma profile that is eventually achieved. Simulations were able to capture the appropriate modal spectra of a set of HIT-SI3 discharges and similarly demonstrate that the formation of the spheromak is agnostic to the applied perturbation spectrum.

Finally, predictive simulations were performed to examine the possibilities for future devices based on SIHI and IDCD. A high-gain version of HIT-SI showed the spontaneous formation of closed-flux surfaces, beneficial in increasing energy confinement, which has not been seen before in other simulated models of helicity injected plasmas. Additionally, a more generalized set of injectors has been created which provides more flexibility in the perturbation spectrum that is applied, to begin quantifying the key differences observed. Finally, expanding beyond spheromak physics, initial simulations of the HIT-SI3 device with an externally produced toroidal magnetic field show promising results for the use of SIHI in forming a tokamak equilibrium.

TABLE OF CONTENTS

LIST OF FIGURES

LIST OF TABLES

ACKNOWLEDGEMENTS

I would like to thank a variety of people for assisting with this work. Tom Jarboe provided me the chance to begin this research and was instrumental every step up the way, helping me keep an open eye as we had a wide variety of conversations attempting to understand HIT-SI. Brian Nelson provided support through the entire process, and was always looking out for me. The results in this work would not be possible without the support from the entire (former and present) HIT-SI team and the PSI-Center: in particular Aaron Hossack, Derek Sutherland, Cihan Akcay, Chris Hansen, Richard Milroy, John Rogers, Rian Chandra, Chris Everson, Brian Victor, Tom Benedett, James Penna, David Ennis and Alan Kaptanoglu. Finally, my family and friends provided support I needed to keep going forward: My parents Doug and Carolyn, my brother Ryan, and Jenny Chu all kept encouraging me to finish this work.

GLOSSARY

HIT-SI: The Helicity Injected Torus with Steady Inductive helicity injection, an experiment at the University of Washington.

MAGNETIC AXIS: The center of the poloidal magnetic field in a toroidal plasma.

MAGNETIC HELICITY: $K = \int \vec{A} \cdot \vec{B} \mathrm{d}^3x$ where $\vec{A}$ is the magnetic vector potential and $\vec{B}$ is the magnetic field.

MAGNETOHYDRODYNAMICS (MHD): A collisionless single-fluid model for describing a magnetized plasma. Different flavors of MHD are primarily described by the generalized Ohm's law used, with extensions to MHD to include collisional and electron influences.

SAFETY FACTOR: A useful metric for ideal-MHD stability of a plasma. In a toroidal plasma, the safety factor $q = \frac{\text{Number of Rotations Toroidally}}{\text{Number of Rotations Poloidally}}$ on a given poloidal flux surface.

SPHEROMAK: A simply-connected magnetized plasma topology that is characterized by the minimization of externally applied magnetic fields. Instead large plasma currents are used to generate the magnetic fields.

TORUS: A doubly-connected topology that often describes the shape of magnetically confined plasmas. Can be visualized as a cylinder that is curved to make its ends periodic. The two circular degrees of periodicity are called the toroidal (long-path) and poloidal (short-path) directions.

Chapter 1
INTRODUCTION

1.1 Magnetic Confinement Fusion

A current problem facing the world is the requirement of a clean, long lasting energy source. Currently the majority of energy production in the world relies on fossil fuels which release pollutants into the air when burned. Nuclear fusion is among the candidates for a future energy source.

Fusion occurs when two atomic nuclei become close enough together for the strong nuclear force to overpower the Coulomb repulsion. In the most likely case for a fusion reactor, the two nuclei are a deuterium (^2H) and tritium (^3H). The reaction:

$$^2H +^3 H \rightarrow^4 He + n + 17.59 \text{ MeV}$$

produces a ^4He and neutron, imparting a significant amount of kinetic energy to the particles. This energy can be collected in the form of heat by capturing the emitted neutrons, which allows the generation of electrical energy.

The primary barrier to the fusion reaction occurring is the Coulomb repulsion of the particles. In the case of a Hydrogen nucleus at rest being approached by another nucleus, a powerful $\frac{1}{r}$ potential is seen. As the particles get closer, an attractive potential from the strong nuclear force takes over and initiates the reaction. This leads to the requirement of the fusing particles having large enough kinetic energies to overcome this potential. To impart large enough kinetic energies onto the particles they generally must be confined.

The methods of initiating the fusion reaction can be described in three categories of confinement. The first, gravitational, is the process through which the sun confines a plasma. A plasma can be confined by gravity when the gravitational pressure overcomes the thermal

and electrostatic pressures. Gravitational confinement results in low reaction rates and high confinement time, but is only possible in bodies with high mass ($M \sim M_{sun}$), making it impossible on earth. The second technique is inertial, where the particles are given a short burst of large energy. This is accomplished through high electric fields, an intense laser pulse, or a similar high power discharge of energy. By providing the particles with high amounts of kinetic energy, they are able to fuse for a short period of time before the energy is dissipated. Inertial confinement leads to high output powers but short confinement times.

The final method of confinement, and the main focus of this research, is through the use of magnetic fields. Because fusion requires temperatures such that a plasma is formed, magnetic forces can dominate the physics. A charged particle will undergo a magnetic force of the form:

$$\vec{F} = q(\vec{V} \times \vec{B})$$

which will result in the particle orbiting the magnetic field lines while the center of motion is along $\vec{B}$. If a magnetic field configuration is created where the $\vec{B}$ field connects back with itself in a circular fashion, a confinement region is created. This is referred to as a toroidal magnetic confinement device.

The most active area of magnetic confinement research is on the tokamak configuration. Invented in the Soviet Union in the 1960's, the tokamak relies on a solenoid wrapped in a donut shape to create the toroidal magnetic field, and then forms the equilibrium by driving a current along that magnetic field. This current then contributes to the heating of the plasma through Ohmic heating and allows the device to reach fusion conditions. Previously operated tokamaks have achieved energy gains ($\frac{power-out}{power-in}$) approaching 1, and a device currently being constructed in France (ITER)[1] is expected to achieve a gain of 10. A picture of the ITER design is seen in Fig. 1.1.

While the tokamak is a successful device at confining a plasma and initiating a fusion reaction, it has limited application due to cost. A successful power plant requires that the device be cost-competitive with existing technology. While the ITER device is expected to

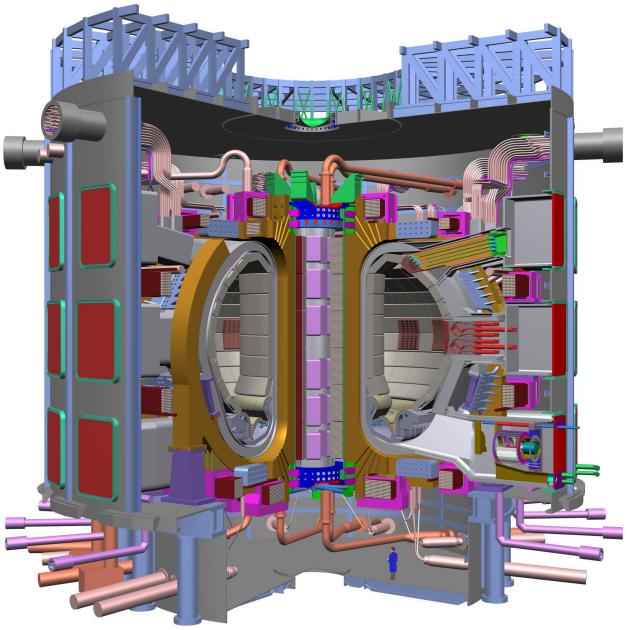

Figure 1.1: The ITER tokamak, currently under construction in Cadarache, France. The device is expected to get a power gain of 10.

be capable of outputting $P_{th} = 500$ MW, it comes with a price tag of $25 \sim 50$ billion USD, an order of magnitude larger than a typical coal-fired plant, justifying research into cheaper methods of creating confined plasmas.

1.2 Magnetic Helicity and the Spheromak

In order to reduce the price of a fusion reactor, the complexity of the magnetic confinement device needs to be reduced. The spheromak is an example of such a device [2], with a graphical view of the magnetic structure seen in Fig. 1.2. Treating the magnetized plasma as a single fluid via the MagnetoHydroDynamics (MHD) model (described in detail later), the momentum equation gives us that a time-independent equilibrium of a fusion plasma must obey:

$$\vec{J} \times \vec{B} = \nabla p$$

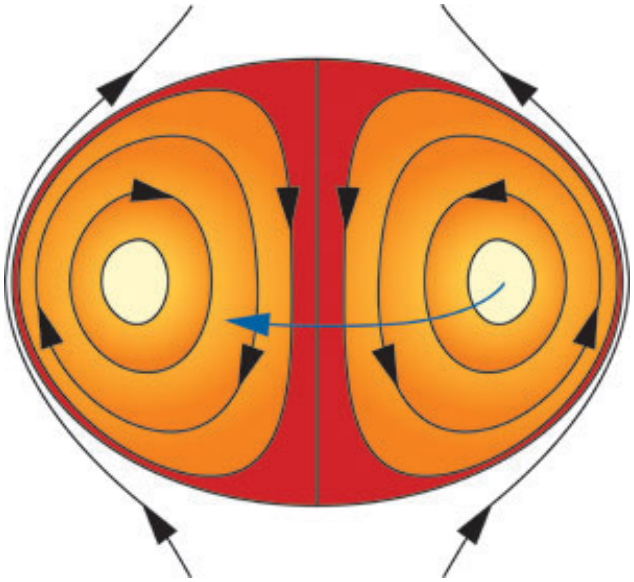

Figure 1.2: The magnetic field structure of a spheromak equilibrium. [3] The closed flux region consists of helically shaped magnetic fields with the toroidal component of the fields going to zero at the edge of the plasma. The *magnetic axis* exists at the null in the poloidal field and represents the core of the plasma.

Where $\vec{J}$ is the current density, $\vec{B}$ is the magnetic field, and p is the thermal pressure. If we examine the force-free case $\vec{J} \times \vec{B} = 0$, we obtain an equilibrium that requires $\vec{J} \parallel \vec{B}$. This allows us to reconstruct Ampère's law as an eigenvalue equation of $\vec{B}$:

$$\nabla \times \vec{B} = \mu_0 \vec{J} = \lambda \vec{B}$$

Where $\lambda = \frac{\mu_0 \vec{J}}{\vec{B}}$. Solutions to this equation are referred to as Taylor states of the plasma. Examination of this equilibrium in a short cylinder shows that it is stable, and more importantly that the toroidal magnetic fields are produced through currents internal to the plasma. This allows the removal of the toroidal field coils from the configuration and provides a more compact design, drastically reducing the cost.

The formation of a spheromak equilibrium is accomplished through the injection of mag-

netic helicity. Magnetic helicity, a global quantity of the plasma, is defined by:

$$K = \int \vec{A} \cdot \vec{B}\, \mathrm{d}^3x$$

Where $\vec{B} = \nabla \times \vec{A}$ is the magnetic field and $\vec{A}$ is the magnetic vector potential. This can be expressed visually as a linkage of magnetic flux tubes. Assuming that the plasma exists in a Taylor state with constant λ everywhere, we can evaluate $\vec{A} = \frac{\vec{B}}{\lambda}$ and find:

$$K = \int \frac{B^2}{\lambda} \mathrm{d}^3x = \frac{2\mu_0}{\lambda} \int \frac{B^2}{2\mu_0} \mathrm{d}^3x = \frac{2\mu_0}{\lambda} W_B$$

where W_B is the magnetic energy of the system. We see that this describes $\lambda = \frac{2\mu_0 W_B}{K}$ as the ratio of magnetic energy to helicity.

Looking at the temporal derivative of K yields the following:

$$\dot{K} = \int \frac{\partial \vec{A}}{\partial t} \cdot \vec{B} \mathrm{d}^3\mathrm{x} + \int \vec{A} \cdot \frac{\partial \vec{B}}{\partial t} \mathrm{d}^3x \tag{1.1}$$

Assuming that the scalar potential $\Phi = 0$, we can easily evaluate the first term using $\vec{E} = -\frac{\partial \vec{A}}{\partial t}$. The second term requires using Faraday's law ($\frac{\partial \vec{B}}{\partial t} = -\nabla \times \vec{E}$) and the vector identity $\vec{A} \cdot \nabla \times \vec{E} = \nabla \cdot (\vec{E} \times \vec{A}) + \vec{E} \cdot \nabla \times \vec{A}$. This gives us (assuming $\vec{E} \times \vec{A} = 0$):

$$\dot{K} = \int -2\vec{E} \cdot \vec{B} \mathrm{d}^3\mathrm{x}$$

We note that inside of a flux conserving boundary ($\vec{B}_\perp = \vec{0}$, $\vec{E}_\parallel = \vec{0}$) with no external forces, only the resistive losses contribute to the evolution of K. Using $\dot{K}_{loss} = -2 \int \eta \vec{J} \cdot \vec{B} \mathrm{d}^3x$ and assuming the plasma is in a Taylor state ($\vec{J} = \frac{\lambda}{\mu_0} \vec{B}$), we can write:

$$\dot{K}_{loss} = -4\eta\lambda \int \frac{B^2}{2\mu_0} \mathrm{d}^3x = -4\eta\lambda W_B = \frac{-2\eta\lambda^2}{\mu_0} K$$

seeing that the resistive losses exponential in nature, with a loss rate comparable to the resistive-diffusion time of the system ($\tau_{L/R}$). We conclude from this that magnetic helicity is conserved on timescales much faster than $\tau_{L/R}$. Taylor relaxation [4] refers to any process

through which the plasma spontaneously reorganizes into its minimum energy state on a time-scale fast enough to conserve helicity, typically described as some turbulent reconnection process. We can further identify this state as being the lowest eigenvalue λ solution to $\nabla \times \vec{B} = \lambda \vec{B}$. Thus the basic description for spheromak creation is to inject helicity into a volume and let it undergo Taylor relaxation.

Helicity injection can be described by looking at the boundary conditions of Eq. 1.1. We simplify this by thinking in the context of an injector that drives an electric current parallel to a magnetic flux. The volume integral can be separated into a line integral of the electric field and an area integral of the magnetic field. This gives:

$$\dot{K}_{inj} = -2 \int \vec{E} \cdot \mathrm{d}\vec{l} \int \vec{B} \cdot \mathrm{d}\vec{a} = -2 V_{inj} \psi_{inj}$$

Historically spheromaks have been formed through the use of coaxial helicity injector (CHI) gun [5]. CHI uses an electrode to create the injected voltage and drive an axial current along with a coil to generate an axial magnetic field. This helically shaped field then propagates into the central volume. After a short period of time, the plasma then undergoes a relaxation event, where the plasma reorganizes to form a minimum energy state [6] & [4]. During this relaxation, the amount of magnetic helicity in the volume is conserved, which sets the magnitude of the magnetic fields in the state the plasma reaches. This process is illustrated in Fig. 1.3 and described in detail in [7] & [8].

In a similar process, tokamaks and Reversed Field Pinch (RFP) devices have been exploring non-inductive startup using helicity injection. The Helicity Injected Torus - II (HIT-II) [9] and National Spherical Tokamak Experiment (NSTX) [10] tokamaks have successfully used CHI while the Pegasus tokamak has used Localized-Helicity Injection (LHI) [11]. Additionally the Madison Symmetric Torus (MST) RFP device has used oscillating-field current drive (OFCD) [12] & [13]. The planned procedure for operation in a non-inductive mode is the helicity injection forms the initial equilibrium and heats the plasma to $T \sim 500$ eV then passes the current drive/heating responsibility to neutral beam/RF wave methods to sustain the equilibrium. This removes the need for a central solenoid in the tokamak configuration.

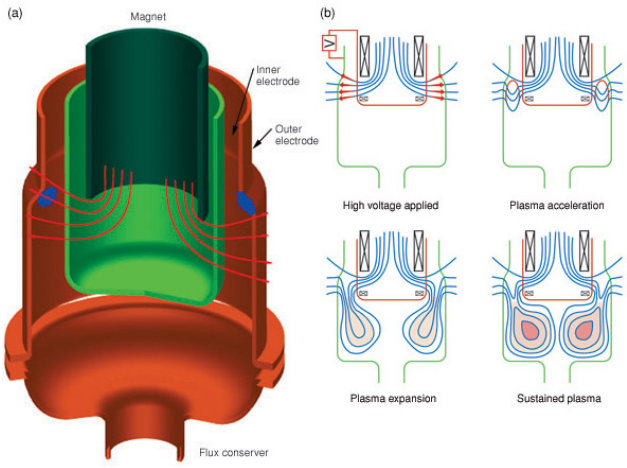

Figure 1.3: The formation of a spheromak equilibrium via CHI [3]. An electrostatic potential is applied between the red and green regions to drive a current, with an axial field generated by external coils. The helically shaped magnetic fields bubble into the confinement region, eventually undergoing a relaxation event and forming the spheromak.

Unfortunately, while these methods (CHI, LHI, OFCD) have been successful in the injection of magnetic helicity, sustainment of these equilibria using only helicity injection has historically led to states with poor confinement. As an example, the Sustained Spheromak Plasma Experiment (SSPX) found that when $\lambda_{inj} < \lambda_{sph}$, a period when magnetic helicity is not being injected into the spheromak, stable spheromaks with both high temperatures ($T > 400$ eV) and low non-equilibrium activity are observed [7], though without helicity injection the state decays resistively. However, when helicity is injected into the spheromak ($\lambda_{inj} > \lambda_{sph}$), the state loses both its confining ($T_e < 100$ eV) and stability properties. Other devices (NSTX, Pegasus, MST) have similarly found that their helicity injection scheme is incompatible with confinement, and as such energy confinement is severely limited.

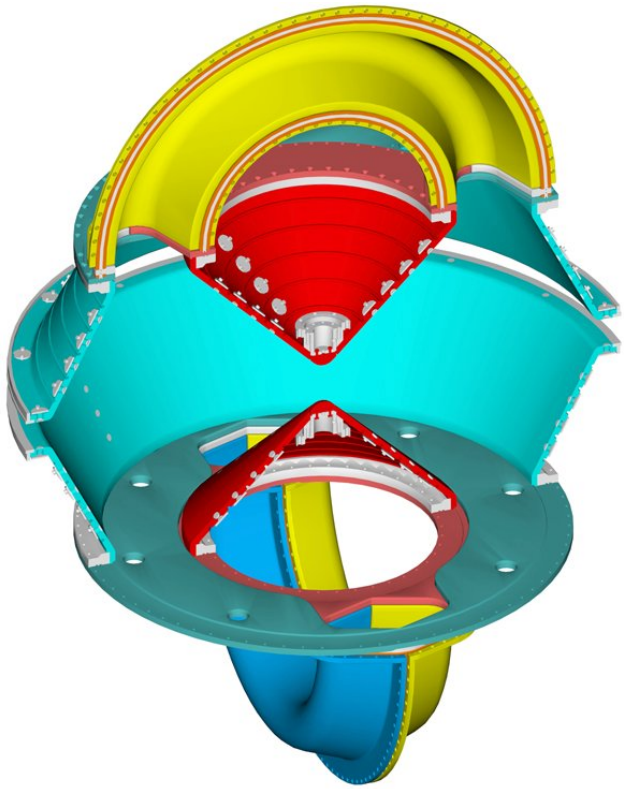

Figure 1.4: A cutaway of the HIT-SI vessel. A bow-tie shaped central confinement region contains steady-inductive helicity injectors on the top and bottom. These injectors have a current and flux driven inductively in AC to drive a spheromak in the central volume.

1.3 The Helicity Injected Torus with Steady Induction (HIT-SI) Experiments

The focus of this research is on spheromaks formed and sustained on the HIT-SI and HIT-SI3 devices [14]. These two devices share a common confinement vessel and diagnostic suite, differing only in the configuration of the helicity injectors, with HIT-SI seen in Fig. 1.4. Whereas previous spheromak devices used an electrode-based gun to form the equilibrium, HIT-SI uses a purely inductive set of injectors, referred to as Steady Inductive Helicity Injection (SIHI).

These injectors are half-toroids connected to the plasma and have two sets of coils driving

magnetic fields inside. The first set of coils resembles a solenoid coil and drives magnetic flux through the injector. The second coil acts as the first leg of a transformer and drives a current through the plasma, which acts as the second leg of a transformer. Since inductive drive of current cannot be sustained in a steady-state fashion, these injectors have to be operated in an alternating current drive. Because $\dot{K}$ is the product of voltage and flux, this allows the same sign helicity to be injected into the volume throughout the cycle.

In order to maintain a constant helicity injection through a discharge, multiple injectors are operated with a phase difference. In HIT-SI this is two injectors phased 90° in time, in HIT-3 this is three injectors phased either 60° or 120° in time. In the case of HIT-SI, when both injectors are operated with similar powers, this leads to:

$$\dot{K} = -2\left(V_0\psi_0 \sin(\omega t) + V_0\psi_0 \cos(\omega t)\right) = -2V_0\psi_0$$

A typical discharge of the experiment exhibits four main stages. The first stage is the growth of an injector-dominated mode in which field lines connect between the mouths of the injectors. These modes are dependent on the operational conditions of the injectors, but share the dominant trait of being non-axisymmetric. In HIT-SI the injectors exhibit a toroidal Fourier n=1 symmetry and as such this injector mode has that toroidal structure inside the central volume. The second stage is a very rapid relaxation event where this toroidally asymmetric structure converts into a toroidally axisymmetric spheromak state. This axisymmetric state is the minimum energy state, and in the process the magnetic helicity is conserved. The third stage of the discharge is the sustainment phase, where the current in the spheromak is driven to sustain the equilibrium from resistive losses. The magnetic field structure of these states can be seen in Fig. 1.5. Finally, at the end of the discharge, the injectors are turned off and the spheromak is allowed to resistively decay and vanish.

A major difference between the HIT-SI device and CHI driven spheromaks (SSPX, CTX) is the sustainment of a confined-pressure equilibrium during the driven phase of the discharge. CHI-driven spheromaks have previously been unable to confine a plasma while the helicity

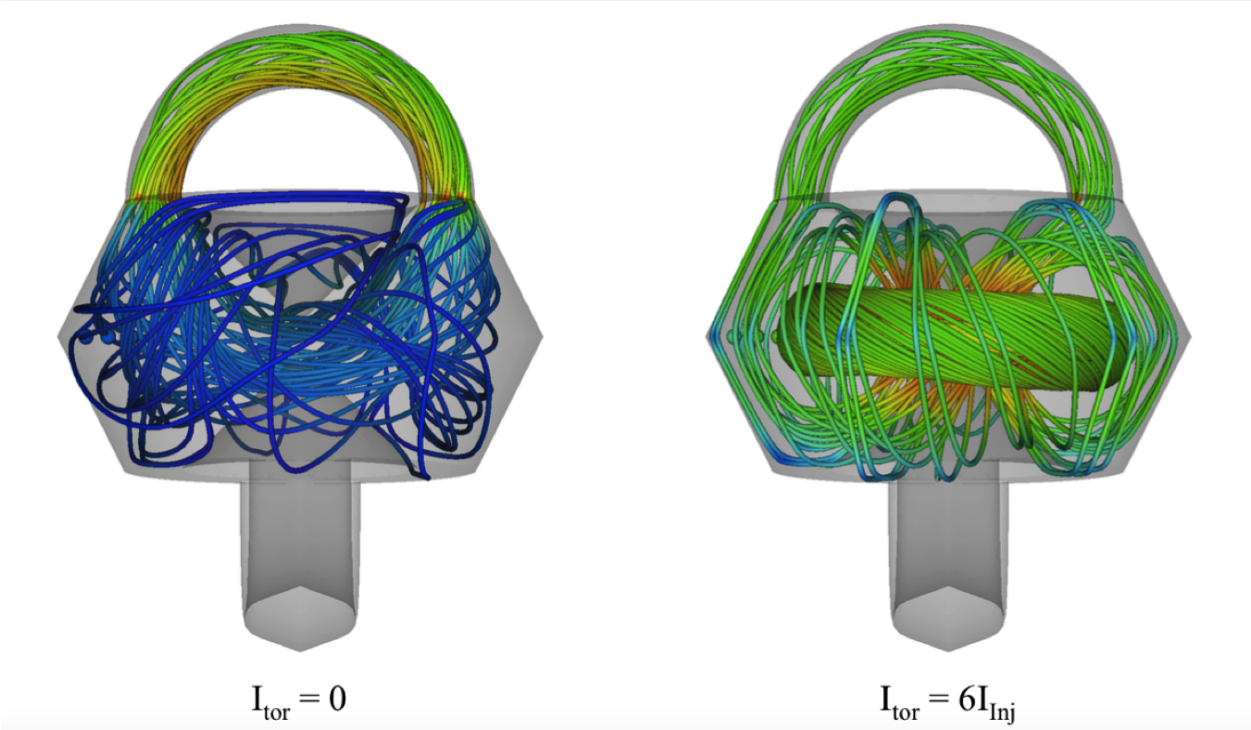

Figure 1.5: Magnetic streamlines for the composite Taylor states for HIT-SI for a current gain of 0 and 6 [16]. The left image shows the initial state before relaxation while the right shows the state after relaxation during sustainment.

injection is on, only obtaining confinement during the decaying portion of discharges. A primary point of study in this work is the attempt to replicate experimental results shown in [15] using simulation. Additionally, evidence of the spontaneous formation of closed-flux surfaces at current amplifications ~ 6 are likely to improve energy confinement.

1.3.1 Diagnostics on HIT-SI

Detailed descriptions of the diagnostics of HIT-SI can be found in various papers and Ph.D. theses [17, 18, 19, 20, 21] but a brief overview will be provided here.

Two main sets of magnetic probes exist for the measurements of $\vec{B}$, a trident-shaped internal magnetic probe and an array of surface magnetic probes. These are the primary

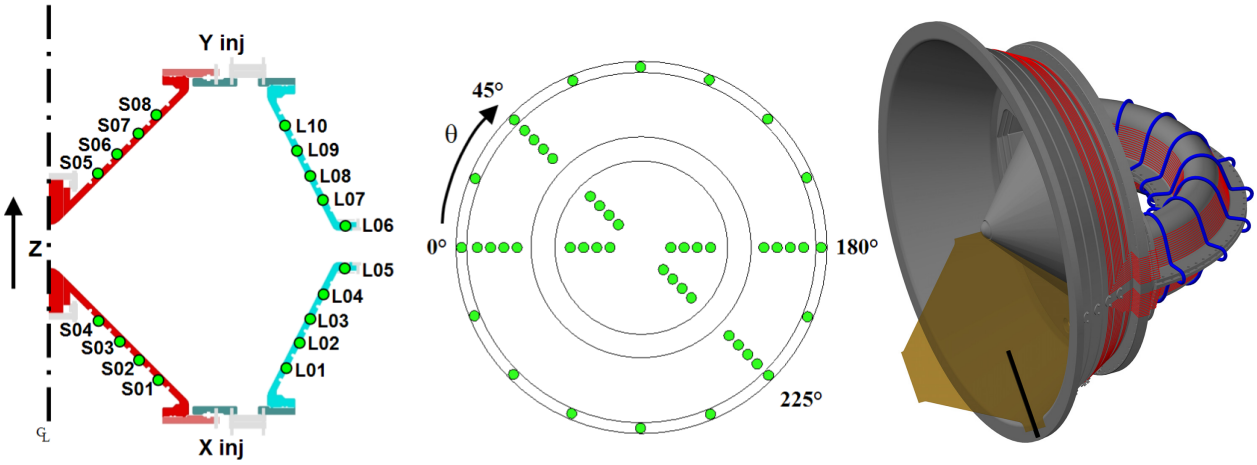

Figure 1.6: The locations of the magnetic probes in HIT-SI are illustrated. The surface probes are spaced both toroidally and poloidally while the internal probe penetrates radially to near the magnetic axis at one toroidal location, shown as a black line on the rightmost drawing.

point of comparison for validation of magnetic signals between simulation and experiment. Figure 1.6 shows the location of these probes. The internal probe is the primary driver of equilibrium reconstructions of the experiment, fitting to solutions of the Grad-Shafranov equation [15, 16, 22]. The surface probes allow for a calculation of the total toroidal plasma current and the toroidal Fourier mode structure.

The fluid parameters are measured through a variety of diagnostics. Ion velocity and temperature ($\vec{V}_i$, T_i) are chord-averaged measurements through Ion Doppler Spectroscopy (IDS). Chord-averaged electron density (n_e) is measured through far-fnfrared interferometry. Electron temperature (T_e) on HIT-SI was measured with a Langmuir probe, while HIT-SI3 is in the process of commissioning a Thomson-scattering diagnostic made of components previously used on the HIT-II and TCSU experiments. [20, 21].

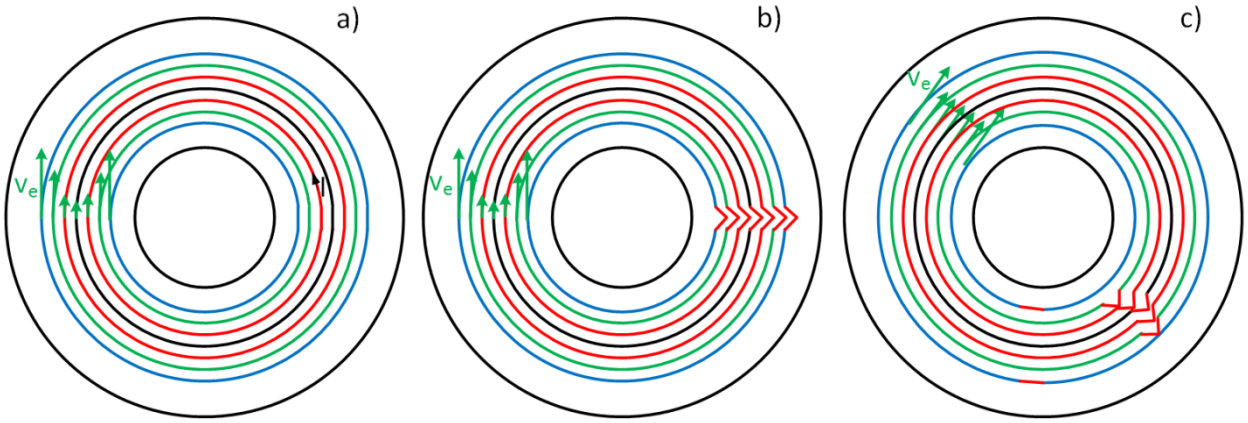

Figure 1.7: The nested flux model for IDCD: (a) begins with a gradient in $\vec{V}_e$. An external force creates a perturbation in the flux surfaces (b) which the rigid nature of these surfaces causes a locking (c). This locking flattens the current profile transferring external drive to the inner flux surfaces.

1.4 Imposed Dynamo Current Drive

The mechanism by which SIHI is able to sustain a spheromak equilibrium is one of the primary research focuses of HIT-SI. The 0-D analytic model that agrees best with experimental results is called Imposed Dynamo Current Drive (IDCD) [23, 24, 25, 26].

A qualitative way to understand IDCD is the nested flux model shown in Fig. 1.7. We begin with a stable closed flux equilibrium which is rigid to cross-field perturbations and has a gradient in the electron flow velocity. By directly driving a perturbed $\delta\vec{b}$ and $\delta\vec{j}$ along the edge, the flux surfaces interfere with each other. This interference leads to a locking of the flux surfaces which flattens out the electron flow gradient, driving the current within the inner flux surfaces.

To quantitatively examine the mechanism, IDCD is derived from looking at perturbed electric fields from the Hall term in the two-fluid generalized Ohm's law:

$$\vec{E} = -\vec{V} \times \vec{B} + \eta\vec{J} + \frac{1}{ne}\vec{J} \times \vec{B} = -\vec{V}_e \times \vec{B} + \eta\vec{J}$$

If we assume a magnetic equilibrium such that $\vec{J}_0 \parallel \vec{B}_0 \parallel \vec{V}_0$, then we can look at the effects of a perturbed field on this equilibrium. Taking the dynamo term and dotting into $\hat{J}$ in the frame with $\delta\vec{v}_e = 0$:

$$\begin{aligned} -\left(\vec{V}_e \times \vec{B}\right) \cdot \hat{J} &= -\left(\vec{V}_0 \times \left(\vec{B}_0 + \delta\vec{b}\right)\right) \cdot \frac{\left(\vec{J}_0 + \delta\vec{j}\right)}{\left|\vec{J}_0 + \delta\vec{j}\right|} \\ &= \left(\delta\vec{b} \times \vec{V}_0\right) \cdot \frac{\delta\vec{j}}{\left|\vec{J}_0 + \delta\vec{j}\right|} \end{aligned}$$

With a specified $\delta\vec{b}$ and $\delta\vec{j}$, an electric field can drive current parallel to this perturbed current. The drive must cancel the $\eta\vec{J}$ component of $\vec{E}$ in order to sustain the plasma by bringing $\int \vec{E} \cdot \vec{J}dl = 0$ along each path of current. Figure 1.8 shows an example of a configuration, where the current is driven in the small perturbed regions to cancel the resistive losses along the current path. This example is described in detail in reference [25].

Currently, IDCD provides the best analytical model for explanation of magnetic results on HIT-SI. The model accurately predicts the injector impedance (Z_{inj}), the toroidal current gain ($\frac{I_{tor}}{I_{inj}} \propto \frac{j}{n}$), and the $\lambda = \frac{\mu_0 \vec{J} \cdot \vec{B}}{B^2}$ profile. These are detailed in reference [23].

1.5 Outline of this Dissertation

This dissertation consists of four primary chapters, followed by a conclusion and appendices. The next chapter discusses the simulation code (NIMROD) and a physical model that is used for the entirety of the results discussed throughout the document. Chapters 3 through 5 discuss the results of simulations of HIT-SI, HIT-SI3, and predictions of future devices, respectively. Following the conclusion, a set of appendices describe the details involved in setting up, running, and post-processing the simulations that are analyzed in this document.

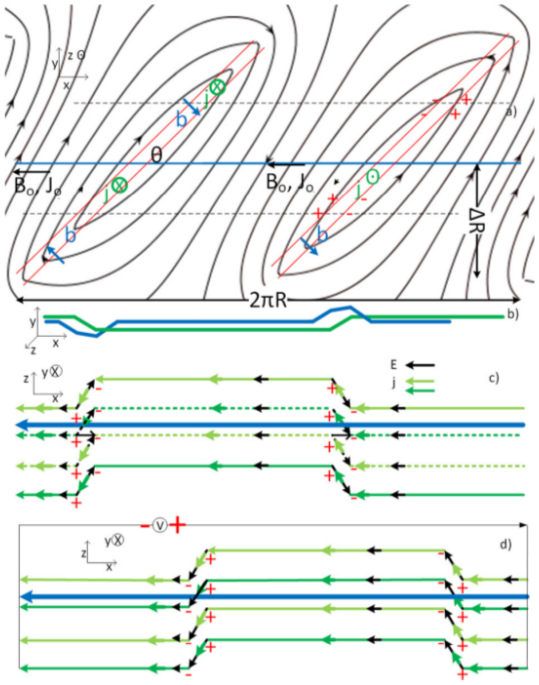

Figure 1.8: An example of a perturbation that leads to imposed-dynamo current drive from [25]. (a) shows the perturbation that becomes distorted by the differential flow. (b) is a 3-D sketch showing the orientation of these perturbations. (c) and (d) show the current path and the direction of $\vec{E}$ along that path that sums to zero in the sustainment case.

Chapter 2

THE MODEL USED

2.1 The NIMROD Code

The code used to simulate the HIT-SI device is the Non-Ideal Magnetohydrodynamics with Rotation - Open Discussion (NIMROD) code [27]. This code solves the equations of MHD in 3 spatial dimensions:

$$\frac{\partial n_e}{\partial t} = -\nabla \cdot n_e \vec{V} + D\nabla^2 n_e + \nabla^2 D_h \nabla^2 n_e \tag{2.1}$$

$$\frac{\partial \vec{V}}{\partial t} + \left(\vec{V} \cdot \nabla\right)\vec{V} = \frac{1}{\rho}\left(\vec{J} \times \vec{B} - \nabla p + \nabla \cdot \Pi\right) \tag{2.2}$$

$$\frac{n_e}{\gamma - 1}\left(\frac{\partial}{\partial t} + \vec{V} \cdot \nabla\right) T = -p\nabla \cdot \vec{V} - \Pi : \nabla\vec{V} - \nabla \cdot \vec{q} + \eta J^2 \tag{2.3}$$

$$\frac{\partial \vec{B}}{\partial t} = -\nabla \times \left(-\vec{V} \times \vec{B} + \eta\vec{J} + \frac{\vec{J} \times \vec{B} - \nabla p_e}{n_e e} + \frac{m_e}{n_e e^2}\frac{\partial \vec{J}}{\partial t}\right) \tag{2.4}$$

Where:

$Zn_i = n_e$

$\rho = m_i n_i + m_e n_e$

$\vec{J} = \frac{1}{\mu_0}\nabla \times \vec{B}$

$\Pi = \rho\nu\nabla\vec{V}$

$p = n_e k_B T$

$\vec{q} = \left(k_\parallel \hat{b}\hat{b} + k_\perp\left(I - \hat{b}\hat{b}\right)\right) \cdot \nabla T$

Extended-MHD (eMHD) models have seen success at modeling the formation of plasma equilibria via helicity injection, with examples of this including CHI on the SSPX [8], HIT-II [28], and NSTX [29, 30] devices and LHI on the Pegasus Toroidal Experiment [31]. In

the past, numerical models implemented by Izzo [32], Akcay [33], and Hansen [34, 35] have focused on the low-f_{inj}, low-β parameter space in HIT-SI.

The code is designed around modeling toroidal magnetically confined plasmas and so solves the equations in cylindrical coordinates. Because toroidal plasmas generally exhibit Fourier symmetry in the toroidal direction, the azimuthal dimension of the code is represented as a finite Fourier series. The modal coefficients of these Fourier series are indexed by the toroidal Fourier number, n. The R and Z dimensions are expressed as finite elements with HIT-SI typically being modeled as polynomials of degree 4 or 5. Due to the Fourier symmetry toroidal plasmas often take, NIMROD is typically able to run with a coarse resolution in the azimuthal axis with a fine resolution in the R-Z plane.

There are two main types of simulations run in NIMROD for modeling HIT-SI. The first is the zero-β model, which assumes n_e and T are both uniform in space and constant in time, resulting in $\nabla p = 0$. All previous work on simulating HIT-SI used this zero-β model. The second type is a finite-β model, which allows these two terms to evolve in time and space.

Two formulations of the energy conservation equation are used, the one presented above is the *single temperature* form which assumes $T_i = T_e$. In the case of $T_i \neq T_e$, two equations are instead solved with the same form, using the relevant species velocity and thermal conductivity. The viscous-heating is used as the heat source for the ion-temperature while the ohmic heating is used for the electron temperature. This looks like:

$$\frac{n_e}{\gamma - 1}\left(\frac{\partial}{\partial t} + \vec{V_i}\cdot\nabla\right)T_i = -p_i\nabla\cdot\vec{V_i} - \Pi : \nabla\vec{V_i} - \nabla\cdot\vec{q_i} \tag{2.5}$$

$$\frac{n_e}{\gamma - 1}\left(\frac{\partial}{\partial t} + \vec{V_e}\cdot\nabla\right)T_e = -p_e\nabla\cdot\vec{V_e} - \nabla\cdot\vec{q} + \eta J^2 \tag{2.6}$$

Where the species velocities are expressed as:

$$\vec{V_i} = \vec{V} + \frac{\vec{J}}{n_e e} \frac{\frac{Zm_e}{m_i}}{\frac{Zm_e}{m_i} + 1}$$
$$\vec{V_e} = \vec{V} - \frac{J}{n_e e \frac{Zm_e}{m_i}}$$

with Z being the charge state of the ions.

2.1.1 The Hall term

The Ohm's law used to model HIT-SI relies on the usage of the Hall term ($\frac{\vec{J}\times\vec{B}}{ne}$) to capture two-fluid effects that standard MHD neglects. This Hall term leads to complications of numerical convergence, requiring high iteration counts when added on its own, and as such the electron inertia term ($\frac{m_e}{ne^2}\frac{\partial J}{\partial t}$) is added to improve convergence properties. For modeling of HIT-SI, an increase in the electron mass is required to fully stabilize the advance of the magnetic field, which in most cases a ratio of $\frac{m_i}{m_e} = 36$ is used. This enhanced electron mass relates to an increased electron skin depth ($d_e = c\sqrt{\frac{m_e \epsilon_0}{ne^2}} = c/\omega_e$), and as such the resolution of the model is limited to the length scale of d_e.

2.1.2 Transport coefficients

The viscosity (ν) and thermal conduction ($k_\parallel$, $k_\perp$) coefficients arise from collisions between particles. Two formulations of the coefficients are used in the modeling of HIT-SI, one by Braginskii [36] and one by Ji [37]. In previous modeling the Braginskii formulation is commonly used [31] with the following heat conduction:

$$k_{\parallel,s} = \frac{T_s \tau_s}{m_s} \frac{\gamma_{0,s}}{\delta_{0,s}} \tag{2.7}$$
$$k_{\perp,s} = \frac{T_s \tau_s}{m_s} \frac{(\gamma_{1,s} x_s^2 + \gamma_{0,s})}{\Delta_s} \tag{2.8}$$

Where:

$x_s = \Omega_s \tau_s$

coefficient	ion	electron
γ_1	2.000	4.6640
γ_0	2.645	11.920
δ_1	2.700	14.790
δ_0	0.677	3.7703

Table 2.1: The coefficients for the Braginskii formulation of thermal conductivities

$\Delta_s = x_s^4 + \delta_{1,s} x_s^2 + \delta_{0,s}$

The s indicates which species (either electron or ion). Ω_s represents the cyclotron frequency and τ_s is the collision time. For the plasmas we are attempting to describe ($Z = 1$) we have the δ and γ coefficients described in Tab. 2.1. In the single temperature model, the extremes of thermal conduction are taken to maximize the heat conducted, $k_\perp = k_{\perp,i}$ and $k_\parallel = k_{\parallel,e}$.

The formulation by Braginskii neglects the effects of ion-electron collisions by assuming them to be negligible. In the formulation by Ji, these terms are included and are expected to be important in the condition of $T_i > T_e$. HIT-SI experimental results indicate that typically $T_i \approx 2T_e$ so this is expected to matter in the two-temperature model. In this formulation the coefficients have the form:

$$k_{\parallel,s} = \frac{T_s \tau_s}{m_s} f1(x_s, \zeta) \tag{2.9}$$

$$k_{\perp,s} = \frac{T_s \tau_s}{m_s} f2(x_s, \zeta) \tag{2.10}$$

Where $\zeta = \frac{\sqrt{\frac{m_e T_i}{m_i T_e}}}{Z}$, and $f1$ and $f2$ are fitting functions obtained detailed in reference [37].

2.2 The Boundary Conditions

2.2.1 SIHI as Boundary Condition in NIMROD

Due to the representation of fields in NIMROD by a finite-Fourier series in the azimuthal dimension, the code requires axial symmetry to the simulation grid. Because the HIT-SI injectors are axially asymmetric, care has to be taken to implement them into the code. This is accomplished by specifying the injector fields as boundary conditions onto the toroidally symmetric confinement volume. This allows us to model the interaction between the inductively driven injectors and the confined plasma. A graphical view of this is illustrated in Fig. 2.1.

The magnetic field boundary condition is described by a $\vec{B}_{norm}$ and an $\vec{E}_{tan}$ which are detailed in [32, 33, 38] to mimic the injector fields that enter the central volume. The fields are applied via solving the Grad-Shafranov equation on the injector geometry.

$$\Delta^* \psi \equiv R^2 \nabla \cdot \left(\frac{1}{R^2} \nabla \psi \right) = -\mu_0 R^2 \frac{\mathrm{d}p}{\mathrm{d}\psi} - \frac{1}{2} \frac{\mathrm{d} \left(RB_T \right)^2}{\mathrm{d}\psi}$$

$\vec{B}_{inj}$ at the entrance to the confinement volume can be evaluated as an equilibrium to this equation. It is assumed that the fields on the injector mouth match this equilibrium shape but oscillate sinusoidally in time. The magnitude of the injector current and flux are controlled to match similar magnitudes of the experiment.

The fields normal to the wall are implemented directly as a reevaluation of the fields at the end of each timestep. The fields tangential to the wall are implemented as a surface integral term during the $\vec{B}$ advance. Previous modeling applied a constant amplitude I_{inj} and ψ_{inj} which led to large-scale discrepancies when compared with experimental discharges, as seen in Fig. 2.2.

While the NIMROD code has been successful at modeling the HIT-SI device with this approximation of the injector fields, we can directly compare with simulations from the PSI-Tet code. The PSI-Tet code uses a tetrahedral array of finite elements to solve the same eMHD model as NIMROD, allowing the direct simulation of the injector regions. We can

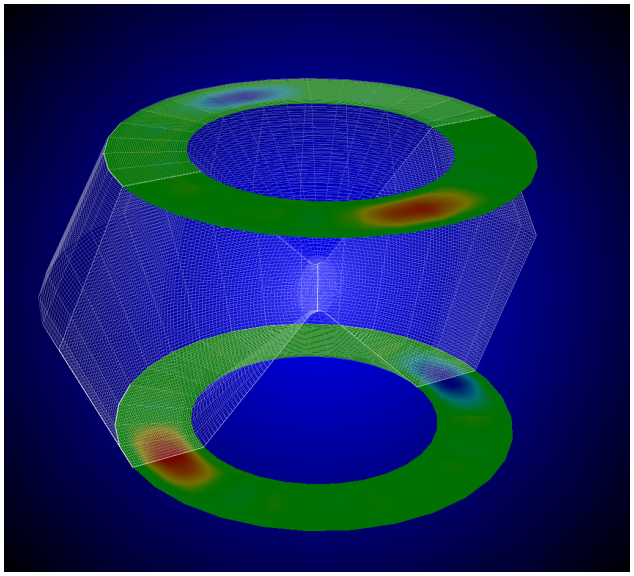

Figure 2.1: The mesh used for NIMROD simulations of HIT-SI. NIMROD requires a toroidally symmetric grid, so the injectors must be represented as boundary conditions. The pseudocolor represents the $\vec{B}_{normal}$ used for the flux injection boundary condition. An $\vec{E}_{tan}$ condition is similarly used to create an analogous $\vec{J}_{normal}$. A thin layer of high resistivity $\frac{\eta_{wall}}{\eta_{plasma}} \sim 10^5$ is used to simulate the insulating wall of the experimental device.

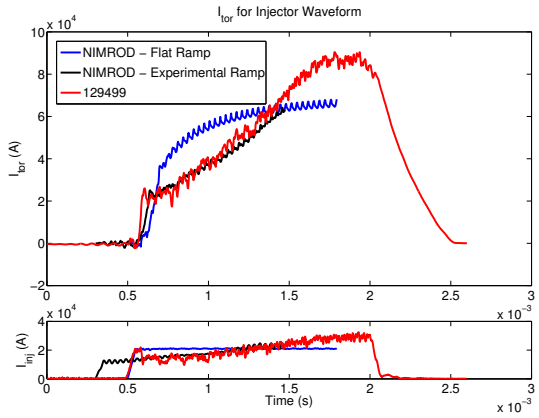

Figure 2.2: Toroidal current for 2 simulations and an experimental discharge. In one simulation a flat-amplitude injector waveform was used, leading to a discrepancy in the shape of I_{tor} compared to the more closely matched case.

compare the typical magnetic profile on the surface, and see that the PSI-Tet profile of the magnetic field in the region of the injector mouths does not match the Grad-Shafranov solution assumed in NIMROD simulations. Figure 2.3 shows us that instead of $B_z(R)$ being parabolic like our Grad-Shafranov solution, the profile instead has a linear dependence. As seen from experimental comparisons [35], this seems to be a relatively minor correction to the simulation agreement.

2.2.2 The Temperature and Density Conditions

A Dirichlet condition is used for both the T and n boundary conditions, that is

$$\frac{\partial n_{e,wall}}{\partial t} = \frac{\partial T_{wall}}{\partial t} = 0$$

.

The condition on n_e leads to the wall alternating between being a source and a sink of particles in the volume as the shot goes on. The total particle inventory of a typical simulation is shown in Fig. 2.4 that illustrates this. Early in the calculation, when the fields are dominated by the injector state, the particle inventory increases. After the relaxation, the mean density then drops below the wall density, indicating loss of particles in the system. The pressure in the core remains higher than the edge however, due to a temperature gradient which forms. While not used in any of the simulations performed thus far, the density on the wall can be modified in time, instead changing the boundary condition to $\frac{\partial n_{wall}}{\partial t} = f(t)$, with $f(t)$ being a defined function. This would likely improve the agreement with experimental measurements of density.

The condition on T requires attention near the injector mouths. Because the injector mouths are a connection to a region of plasma, it is expected that they will be warmer than the wall due to reduced thermal losses and increased current. As a result, an additional temperature profile matching $|B_z|$ is added to the wall temperature to model the injector temperature. This can be seen in Fig. 2.5.

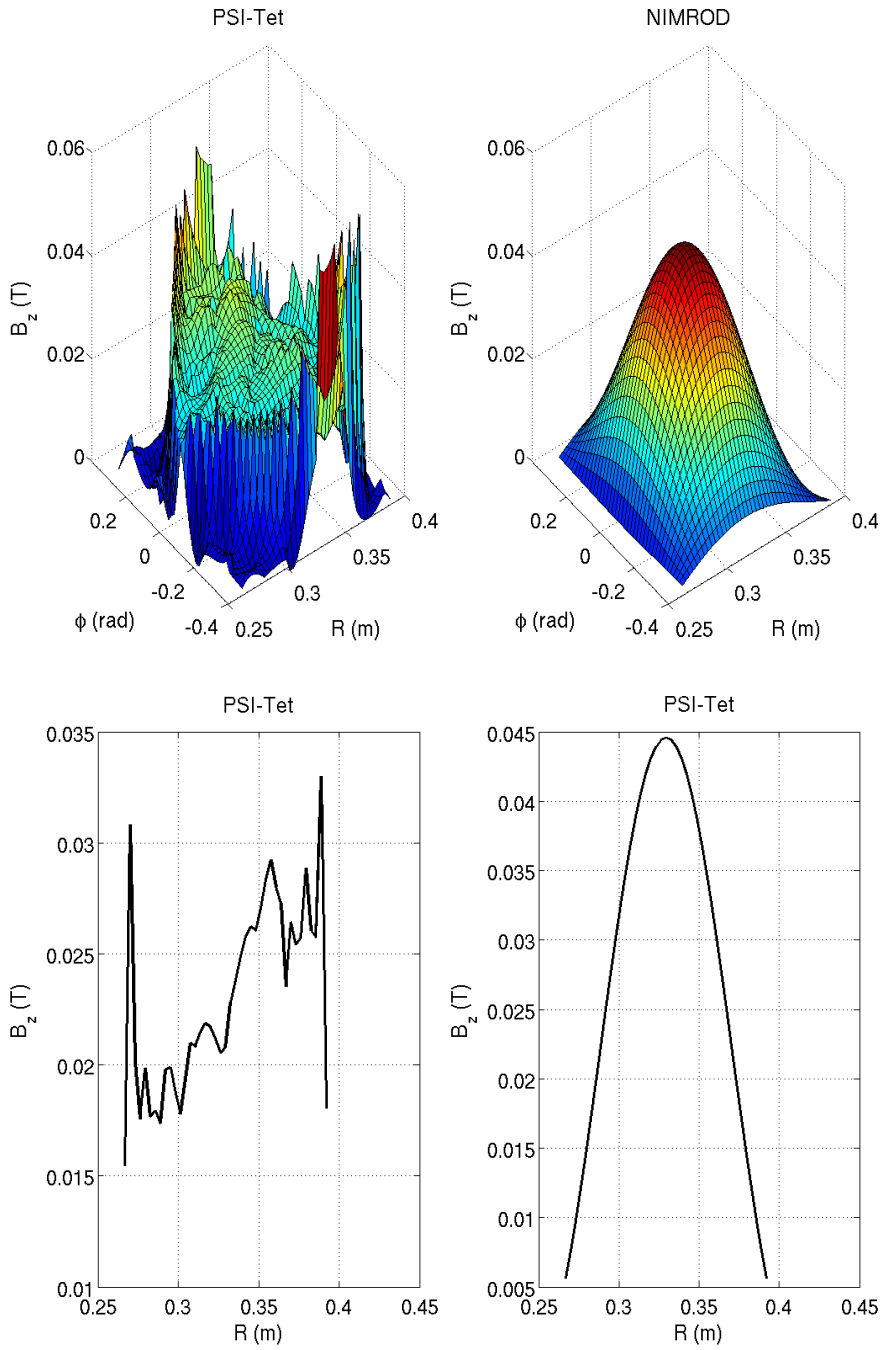

Figure 2.3: $\vec{B_z}$ on the X-injector mouth in the simulated geometry in both the PSI-Tet (left) and NIMROD (right) codes. In NIMROD this is applied as a boundary condition, while in PSI-Tet the fields are free to evolve according to the MHD model. The top plots show the 2-D profile while the bottom is the radial profile through the midplane of the injector at $\phi = 0$.

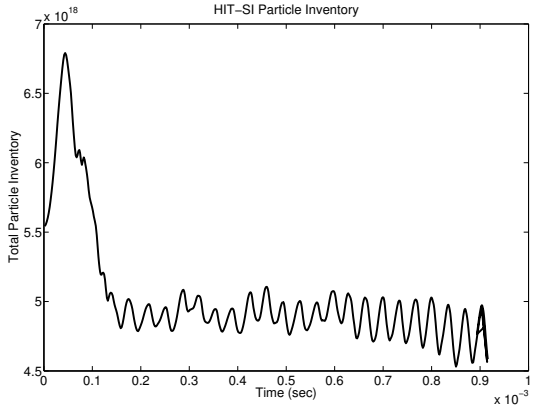

Figure 2.4: $\int n \mathrm{d}^3 x$ for a $f_{inj} = 14.5$ kHz simulation. Early in time during the injector-dominated phase particles flow into the confinement region, while later in time the mean density has dropped below the wall level. The oscillations are at f_{inj}.

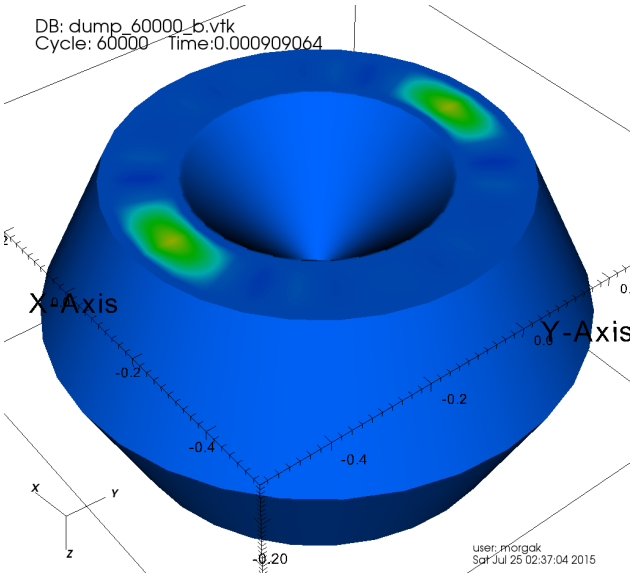

Figure 2.5: The boundary condition on T for simulating HIT-SI with temperature evolution. The profile on the injector mouths matches the $|B_z|$ condition that is applied for ψ_{inj}. This makes the boundary condition primarily $n = 2, 4, 6, 8...$

2.2.3 The High-Resistivity Edge Layer

One unique feature of the HIT-SI device is the use of a thin insulating layer covering the copper flux conserver. This insulating layer serves to modify the boundary condition of $\vec{B}$ to make $\vec{B}_{norm} = \vec{0}$ and $\vec{J}_{norm} = \vec{0}$. The NIMROD code does not natively support this boundary condition on current, so to accomplish this a thin edge layer with large resistivity ($\frac{\eta_{edge}}{\eta_{plasma}} \sim 10^5$) is added into the geometry. This has the effect of imposing this boundary condition onto the simulation. A layer thickness of 1 mm was selected to match the electron skin depth of the HIT-SI plasma. Since this layer covers the injector mouths a large voltage has to be applied to drive the specified current through the layer, on the order of 10 kV. To stop the non-physical heating that would occur from this, both Ohmic and viscous heating are set to 0 in this layer.

2.3 Biorthogonal Decomposition as a Validation Metric

2.3.1 Biorthogonal Decomposition

As complex simulations of an experiment are performed, it is important to check the level of agreement between the model being solved and reality. Because these systems have many degrees of freedom it becomes important to relate the dataset of both experiment and simulation to a common style that facilitates comparisons. Biorthogonal Decomposition (BD) [39] serves as a tool to reduce the dataset into the dominant modes and examine the largest coherent structures.

BD is accomplished by constructing a data matrix with rows and columns corresponding to two independent variables. An example of these would be a signal B which is a set of M spatial signals sampled at N time-points:

$$B = \begin{bmatrix} b(x_1,t_1) & \cdots & b(x_1,t_N) \\ \vdots & \ddots & \vdots \\ b(x_M,t_1) & \cdots & b(x_M,t_n) \end{bmatrix}$$

The decomposition seeks to rewrite this in the following form (where K is the minimum of N and M):

$$B_{mn} = \sum_{k=1}^{K} A_k \phi_k(x_m) \psi_k(t_i)$$

where $\sum_{i=1}^{N} \psi_k(t_i)\psi_l(t_i) = \sum_{j=1}^{M} \phi_k(x_j)\phi_l(x_j) = \delta_{kl}$ so that the data are decomposed into a set of K orthonormal eigenfunctions with weights given by A_k. These weights allow us to sort the modes in order of magnitude and identify the dominant modes of the system.

The decomposition is obtained by solving a pair of eigenvalue problems. We can write this decomposition in a matrix form:

$$B = \Phi A \Psi^T$$

And using the orthonormality of the system ($\Phi^T\Phi = \Psi^T\Psi = 1$) can express

$$B^T B\Psi = \Psi A \Phi^T \Phi A \Psi^T \Psi \qquad BB^T\Phi = \Phi A \Psi^T \Psi A \Phi^T \Phi$$

$$B^T B\Psi = A^2 \Psi \qquad BB^T\Phi = A^2 \Phi$$

to obtain the decomposed eigenfunctions. Typically for signals one dimension will be spatial and one will be temporal. To identify the names of these eigenfunctions we call the spatial functions Ψ topos and the temporal functions Φ chronos.

This decomposition is useful for examining the dominant structures of a signal without knowing the shape of those structures beforehand. As an example, we will look at a set of synthetic signals and compare the results from Fourier decompositions with the BD.

Shown in Fig. 2.6 we see that BD is able to pick out the dominant modes for a pair of synthetic datasets. In both cases, the data from a set of 64 spatial locations (uniformly spaced in θ around a unit circle) at 64 time points is examined. In the first case the synthetic signal is formed by a linear combination of two Fourier signals:

$$B(\theta) = B_1 \cos(\theta + t) + B_3 \cos(3\theta)$$

Due to the input signal matching the character of a Fourier transform, Fourier analysis is easily able to pick out the dominant modes. Similarly, BD does a comparable job and is able to identify the dominant modes as well. Of note is that BD picks out three modes from here, and we see that two of the modes have a degenerate weight. Looking at the topo and chrono of these degenerate modes, we see that they form the rotating $n = 1$ component of the signal. So we see that signals that oscillate show up as a pair of signals in BD.

The second synthetic signal shown is a step function:

$$B(\theta) = \begin{cases} 0 & \theta < 1 \\ 1 & : 1 < \theta < 2 \\ 0 & \theta > 2 \end{cases}$$

As we can see in the results, BD is able to pick out the single mode that composes the signal. This is a significant improvement over Fourier, which we can see has a significant contribution from every mode. This helps showcase the advantage of BD, it allows the data to show the dominant structures present without prior assumptions of their shape.

2.3.2 Usage as a Validation Metric

BD can be used to construct a comparison metric between different datasets, in this case between simulations and experimental results. The primary way this is accomplished is through projections of the BD modes from one dataset to another. This is enabled because BD produces a set of orthonormal modes that fully describes the space of the dataset. Say two datasets exist, one called the *reference* set and the other our comparison set. It becomes possible to express the modes from our comparison set as a linear combination of modes from the *reference* set:

$$\left(\phi_k^{ref}\right)^T \cdot B = \left(\phi_k^{ref}\right)^T \cdot \tilde{\phi}_k \tilde{A}_k \tilde{\psi}_k^T = \tilde{A}_k \tilde{\psi}_k^T = \Sigma_j B_{ij} \phi_k^{ref}(x_j) \tag{2.11}$$

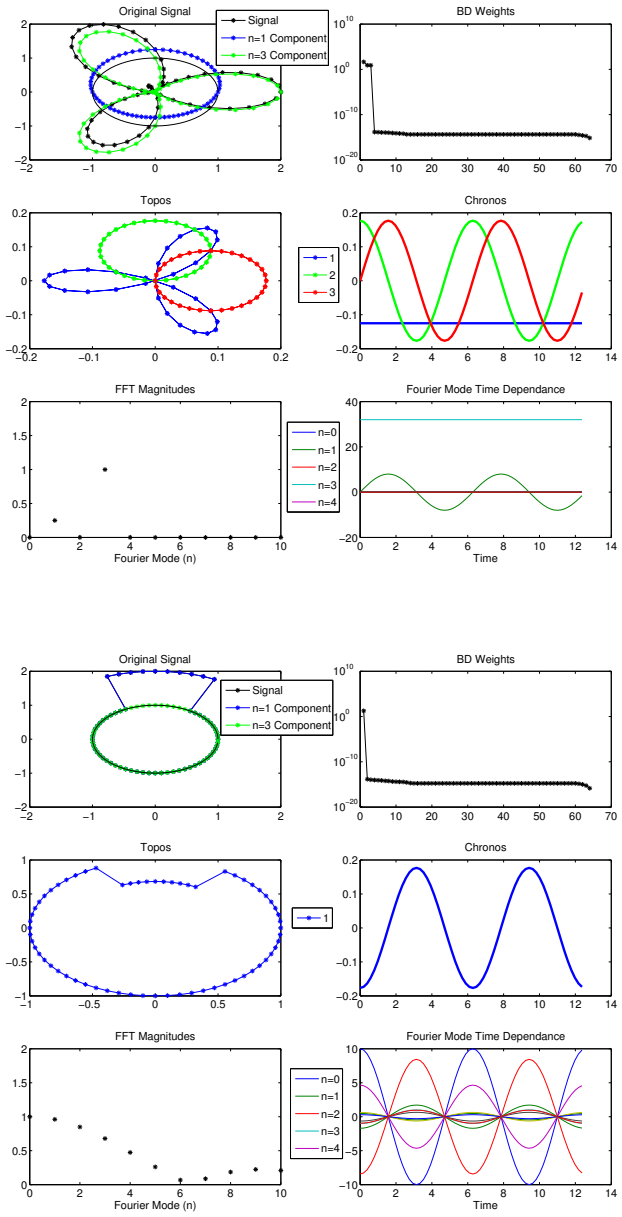

Figure 2.6: Results of Biorthogonal and Fourier decomposition for two different cases. In the top case, the synthetic signal is made up of the sum of two Fourier modes, locked $n = 3$ and rotating $n = 1$. The bottom case the signal is a step function oscillating in time. As can be seen, BD is able to identify the dominant modes in both cases, while the FFT fails to pick out the step function.

with the new projection represented by tildas.

We can calculate the individual coefficients of this expansion by looking at the *correlations* between the two datasets:

$$C_k(\phi_n) = \left(\phi_k^{ref}\right)^T \cdot \phi_n \tag{2.12}$$

We note that these correlations can range in value from $-1 < C_k(\phi_n) < 1$ and that the correlations form the coefficients of the projection:

$$\tilde{A}_k\tilde{\psi}_k = \left(\phi_k^{ref}\right)^T \cdot \sum_{n=1}^{K} \phi_n A_n \psi_n = \sum_{n=1}^{K} C_k(\phi_n) A_n \psi_n \tag{2.13}$$

In addition to these, the individual correlations can provide insight into the structure of the disagreement. The product of the topo and chrono correlations for a set of modes give a combined correlation:

$$T_{kj} = C_k(\phi_j) C_k(\psi_j) \tag{2.14}$$

These combined correlations allow us to control for relative sign errors in the individual correlations between topos and chronos. In the decomposition there is an ambiguity in the sign of the decomposed modes, a minus sign applied to both the topos and chronos will reproduce the same dataset. An example of this is seen on the step function BD example in Fig. 2.6. This ambiguity can result in well-correlated modes having individual correlation values of -1. Similar to the individual correlations, these range from $-1 < T_{kj} < 1$, however negative values indicate an anti-alignment in either the topo or chrono, but not both.

A set of metrics has been devised to evaluate the level of agreement between two datasets [40]. These three metrics compare the signal magnitude, the total agreement in shape, and the individual modal shapes.

1. $\langle B^2 \rangle$ gives a measure of the agreement in signal strength.

$$\langle B^2 \rangle = \frac{\Sigma_{k=1}^{K} A_k^2}{MN} \tag{2.15}$$

2. Total correlations give a measure of the agreement in total shape.

$$Y = \frac{\Sigma_k A_{k,ref}^2 T_{kk}}{\Sigma_k A_{k,ref}^2} \tag{2.16}$$

3. Can look at individual mode correlations to see the points of disagreement

$$\frac{A_{k,p}^2}{A_{k,ref}^2} = C_k(\tilde{\psi}_k) \tag{2.17}$$

To understand these metrics for comparison and how they are influenced by noise in measurements, we can apply them to sets of synthetic signals. We start by looking at the dependence on random noise, so we take our earlier example of the combination of a locked $n = 3$ and a rotating $n = 1$ Fourier mode. We then create a second signal that is the original signal plus some noise, either through the addition of another coherent mode or random noise. We can compare how the validation metrics respond to these types of noise and how effective they are able to capture agreement.

Random noise is found to have little impact on the decomposition until the noise is significantly greater in magnitude than the original signal, as seen in Fig. 2.7.

Coherent noise is similarly found to have an effect based on the magnitude of the added signal. Adding another signal on top of our synthetic comparison signal lets us see how that changes the total correlation. As this additional signal becomes larger than the original signals, large disagreements start being seen in the total correlation Y. This is expected, as the addition of another signal would indicate differences in the physics at play between the two datasets.

2.4 Results of Previous Modeling of HIT-SI

Previous modeling of the HIT-SI device using the NIMROD code [32, 33, 38] and the PSI-Tet code [16, 34, 35] assumed that the density and temperature (n and T) were uniform in space and constant in time, which removes pressure gradients from the system. Experimental results from a parameter scan of the device indicate regimes where pressure gradients play a significant role in the dynamics [15].

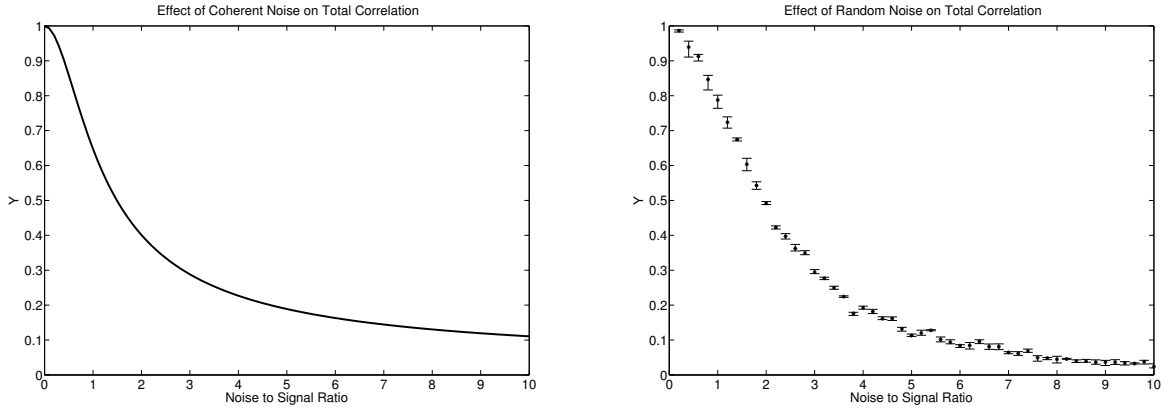

Figure 2.7: Total correlation Y when one of the signals has a spatial mode added. On the left is coherent noise and on the right is random noise. As can be seen, when the mode is not a dominant component of the dataset it has little effect on the total correlation. As the additional mode is made larger, the value of Y falls off as expected.

The results from Akcay's work [33, 38], in particular, indicate a thorough understanding of the operation and simulation of HIT-SI in the low-injector frequency regime ($f_{inj} < 40$ kHz), and the strength of two-fluid terms in the generalized Ohm's law. The Hall term was found to play a significant role in the relaxation and sustainment in the experiment, and agreement was found for operations at $f_{inj} = 14.5$ kHz. As the device was operated in the high-frequency regime, the pressureless Hall-MHD model used showed a decrease in the quality of agreement. [40]

We can use the BD validation metrics described above to get an understanding of the level of agreement on the magnetic topology between the simulation and the experiment. This is accomplished by looking at the decomposition of a set of surface magnetic probes. The experiment contains 4 poloidal arrays that consist of 16 3-axis probes to measure the magnetic fields on the outer surface of the wall. These are pictured in Fig. 1.6.

Performing the BD on the array of surface probes produces the set of eigenmodes of HIT-SI. The structure of the first 3 modes can be seen in Fig. 2.8. The first mode can

be characterized as the *spheromak* mode with its large strictly-poloidal spatial profile and a temporal profile matching I_{tor}. The 2^{nd} and 3^{rd} modes are the *injector* modes with oscillating structures at f_{inj}. Most ($> 95\%$) of the energy is contained within these 3 modes.

The three metrics described in the previous section can be used to evaluate the agreement of the simulations. A series of zero-β simulations were performed that attempted to match high-performance shots at each f_{inj} that was operated experimentally. These simulations used flat-amplitude injector waveforms and two values of η were run, corresponding to $T_e =$ 6 and 12 eV. To assess the meaning of the BD validation metrics, a set of experimental discharges were additionally compared to the reference shot. This allows us to determine whether the simulation is within the range of experimental repeatability. The results of this scan are described in detail in [40] and the results are seen in Fig. 2.9.

A second set of simulations at $f_{inj} = 14.5$ kHz was run with both the NIMROD and PSI-Tet codes matching the waveform of the experimental shot, described in [35]. This set found improved agreement over the flat-waveform case. Additionally, agreement in modes 4 and 5 was found to be improved in PSI-Tet over NIMROD, thought to be a consequence of the simplified injector boundary condition NIMROD uses.

A set of injector waveforms were generated for each f_{inj} and simulations were run at $f_{inj} = 14.5$, 53.5, and 68.5 kHz. For these cases, it is useful to look at the cross-mode correlations (T_{kj}). While total shape correlation is still good (from most of the energy being in the first mode), the 2^{nd} and 3^{rd} modes become swapped at high f_{inj}. While these modes are similar in amplitude and shape, the asymmetry of the probes breaks their degeneracy so they are distinct modes.

The primary result of these scans with the zero-β model is that the agreement is better at low-f_{inj} than high-f_{inj}. The next chapter attempts to improve on these results and provide an explanation for the incorrect assumptions of the model.

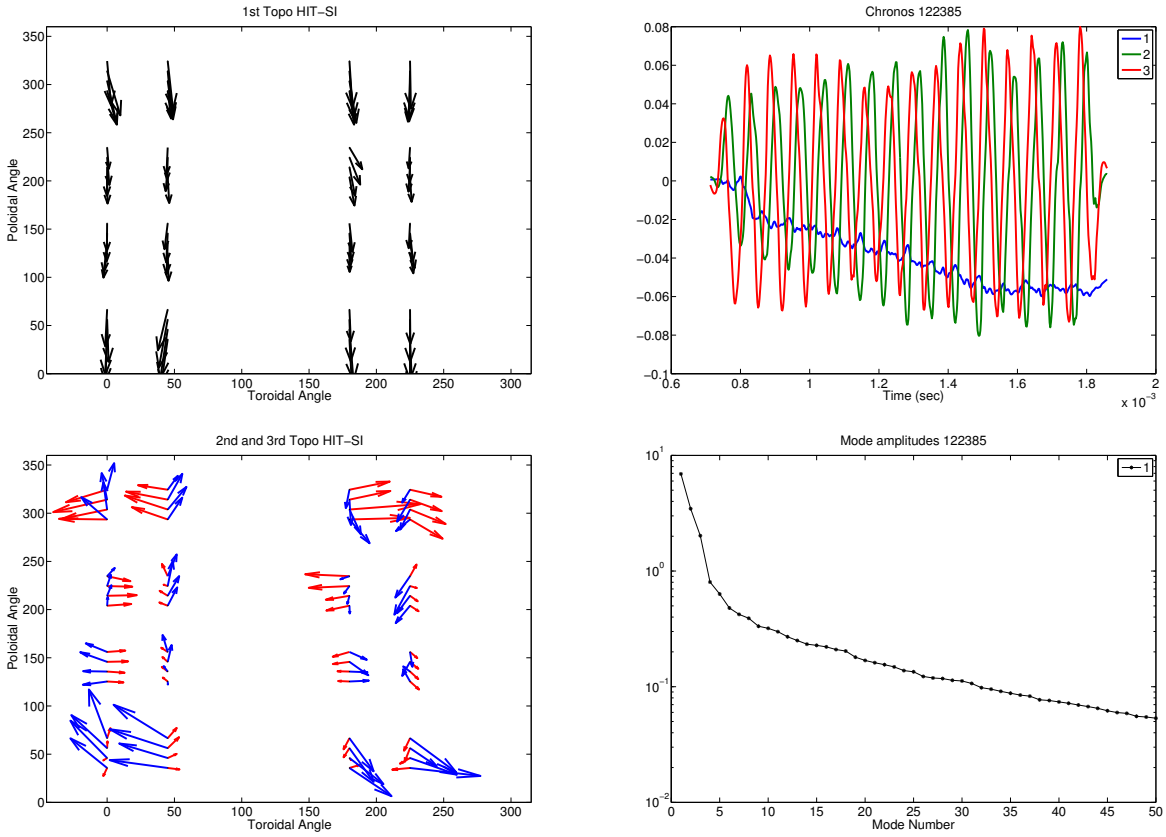

(a) Topos

(b) Chronos and Energy spectrum

Figure 2.8: Mode spectrum of the Biorthogonal Decomposition of the HIT-SI surface probe data. The majority of the energy is contained in the first 3 modes. The first mode represents the spheromak mode while the 2^{nd} and 3^{rd} are the injector fields.

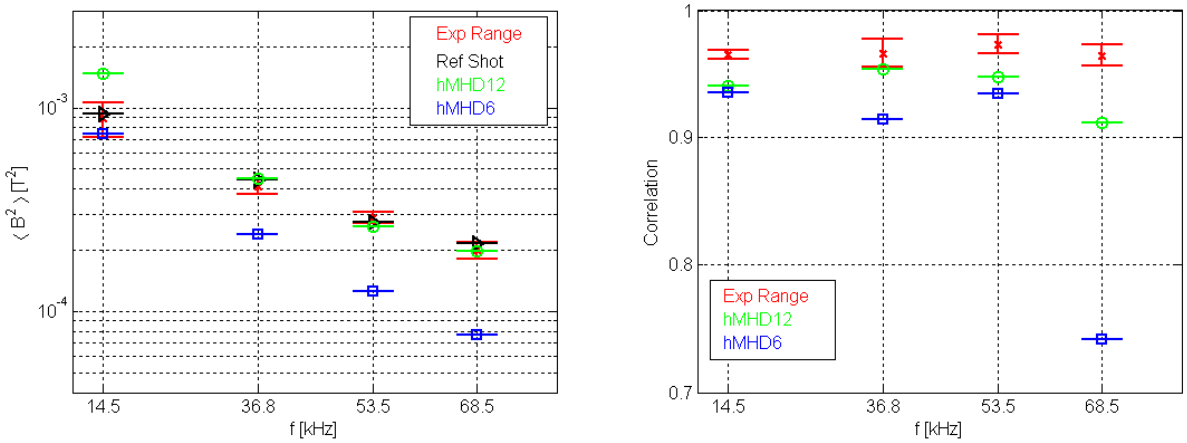

(a) Energy metric

(b) Total correlation of shape

Figure 2.9: Metrics 1 and 2 applied to a set of NIMROD simulations [40] scanning f_{inj}.

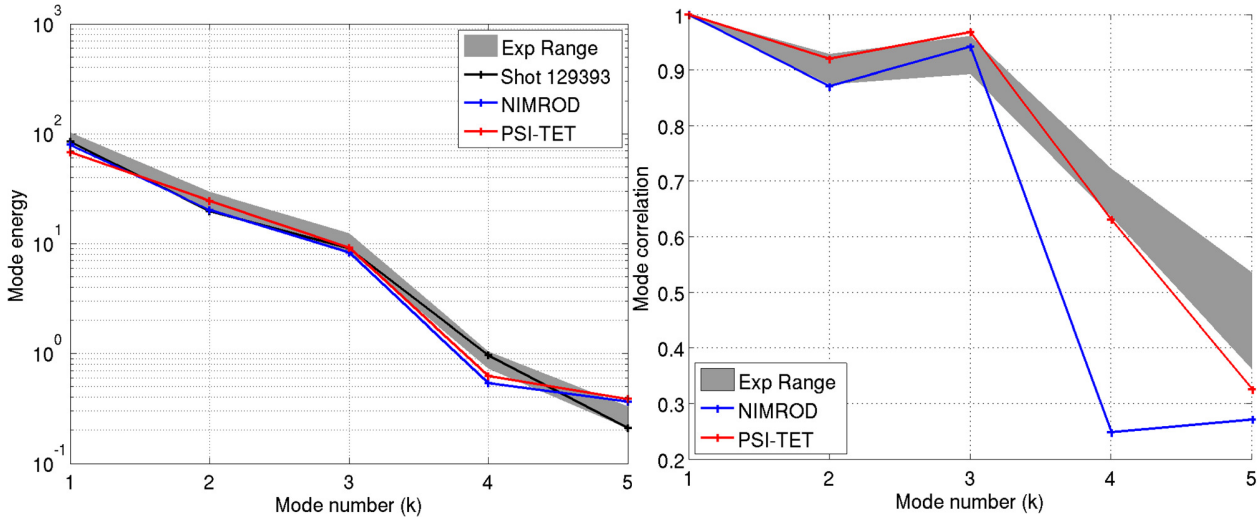

(a) Energy metric

(b) Correlation of individual modes

Figure 2.10: Metrics 1 and 2 applied to a set of NIMROD simulations [35] at $f_{inj} = 14.5$ kHz.

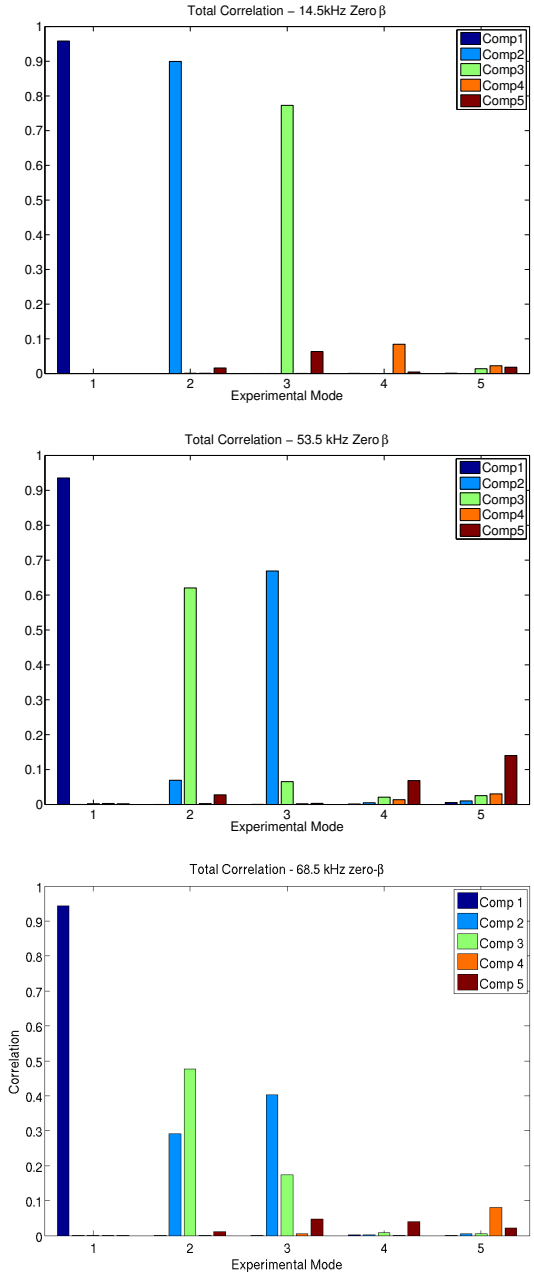

Figure 2.11: Cross mode correlations of three simulations with their experimental reference shot. As can be seen, high-f_{inj} tends to swap modes 2 and 3.

2.5 Grad-Shafranov fits of experimental data

Due to the experiment lacking diagnostics for measuring plasma pressure, equilibrium fitting has been relied on as a tool. The Grad-Shafranov equation [22]:

$$R^2\nabla\cdot\left(\frac{1}{R^2}\nabla\psi\right) = -\mu_0 R^2\frac{\mathrm{d}p}{\mathrm{d}\psi} - \frac{1}{2}\frac{\mathrm{d}F^2}{\mathrm{d}\psi}$$

describes toroidally symmetric plasma equilibria, ψ is the stream function and both p and $F \equiv RB_T$ are functions of ψ. For equilibrium fitting of HIT-SI performed in [15] and [16], p was assumed to be linear in ψ and F was assumed to follow the IDCD profile. The IDCD profile is a two-step profile in F', or λ, where the edge of the equilibrium is at the injector λ value and the core is lower, below the Taylor value of the flux conserver. The relative sizes of the two regions are determined by the ratio of injector to spheromak current.

The equilibrium fitting is performed using the PSI-Tri code, developed by Chris Hansen [16]. This code use a triangular finite-element mesh to solve the Grad-Shafranov equation, then fits the coefficients that describe the pressure and flux functions to match an input set of experimental data. Typically, the signals used for fitting are injector λ, toroidal current, current gain, surface magnetic fields, and internal magnetic probe data. Fits from experimental and simulation data will be shown in future chapters.

Chapter 3

FINITE-β SIMULATIONS OF HIT-SI

Experimental results in the final run campaign of HIT-SI prompted a series of simulations with the full anisotropic extended MHD model in NIMROD [15], referred to as the finite β simulations, with $\beta = p/\frac{B^2}{2\mu_0}$ being the ratio of thermal to magnetic pressure in the plasma. This final run campaign featured a scan over the injector operational frequency from $f_{inj} = 14.5$ to 68.5 kHz. An increase in β with f_{inj} was seen experimentally, indicating the assumptions of the zero-β model may be incorrect. This scan features an injector period passing over several timescales of interest, notably the toroidal Alfvèn transit time and the radial sound transit time.

This chapter will begin by discussing the experimental observations which prompted this study. Next, the simulations that were performed will be described in detail. Finally, discussion at the end will focus on two aspects: the physics involved in the dependance of dynamics on injector frequency and the physical models required to capture these results.

3.1 Experimental Observations

HIT-SI observed significant differences in the magnetic profile and structure of the spheromak as f_{inj} was varied, as detailed in a paper by Victor [15]. An experimental scan was performed which operated the experiment at five frequencies: 5.8, 14.5, 36.8, 53.5, and 68.5 kHz. Three main results were seen from this scan: an increase in current gain ($\frac{I_{tor}}{I_{inj}}$) with f_{inj}, an outward shift of the magnetic profile indicating higher $\langle\beta\rangle$, and evidence of stability to $n = 1$ kink modes. The increase in current gain is seen in Fig. 3.1

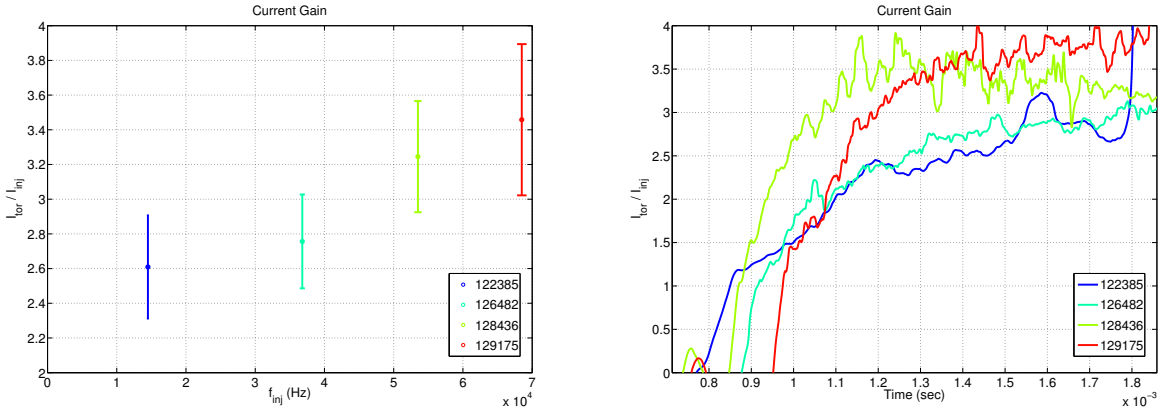

Figure 3.1: $\frac{I_{tor}}{I_{inj}}$ for experimental discharges at different f_{inj}. We see the current gain increases with f_{inj}.

3.1.1 Magnetic profile

As f_{inj} was increased, the magnetic structure of the spheromak changed. This is easily seen in Fig. 3.2, where the magnetic axis is shifted outward. Typically, there are three ways for this outward shift to be present in a spheromak. The first is a bulk toroidal flow, though a flow velocity $v_{tor} = 100$ km/s would be required and measurements indicate $v_{tor} \sim 5 - 10$ km/s so can be dismissed as the sole reason.

The second and third relate to the pressure and current profiles of the equilibrium. Equilibrium fits have been performed on the experimental data with a variety of $\lambda = \frac{\mu_0 \vec{J}}{\vec{B}}$ and p profiles. These are shown in Fig. 3.2, and it can be seen that the outward shift strongly correlates with an increase in the plasma pressure. It is seen that the high f_{inj} discharges seen $\beta \sim 25\%$.

The surface probes also provide insight into the toroidal structure of the equilibrium. Using the four ampèrian arrays, one can construct a measurement of the *current centroid* of the plasma, defined as the expectation value of the mean poloidal magnetic field:

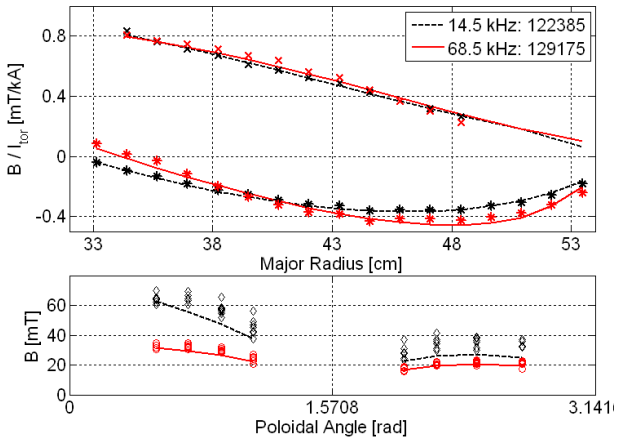

Figure 3.2: The magnetic profile observed (markers) and from an equilibrium reconstruction (lines) for experimental shots at $f_{inj} = 14.5$ and 68.5 kHz (details in [15])

$$\langle B \rangle = \frac{\Sigma B_{pol,i} r_i}{\Sigma B_{pol,i}} \tag{3.1}$$

Shown in Fig. 3.3, we see an outward shift of this centroid at high f_{inj}, similar to the internal probe measurements. In addition, we also see an increase in the toroidal symmetry of the centroid location.

Details of the magnetic profile are looked at with equilibrium fits to experimental data. Fig. 3.4 and 3.5 show the time evolution of equilibrium reconstructions of two experimental discharges, which are typical at their respective frequencies.

3.1.2 Mode activity and stability

The midplane surface probes provide a measurement of the toroidal Fourier mode structure of the magnetic field, up to $n = 7$. This measurement can be used to identify activity in the plasma, such as instability growth. The mode activity in two regions of time is of interest, the spheromak formation and the sustainment.

The toroidal mode structure of the spheromak formation changes as f_{inj} is increased. At low f_{inj}, the injectors directly drive an $n = 1$ helical state that connects the two injector

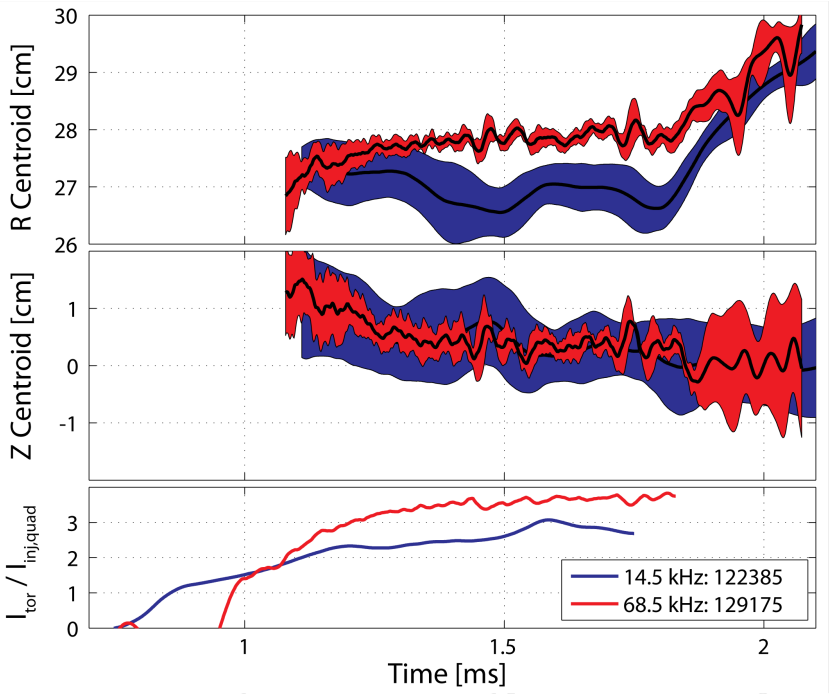

Figure 3.3: The current centroid and gain for two experimental shots [15]. The solid line is the mean of the 4 toroidal locations with the filled region representing the range. The high f_{inj} shot sees both an outward shift of the centroid as well as an increased toroidal symmetry.

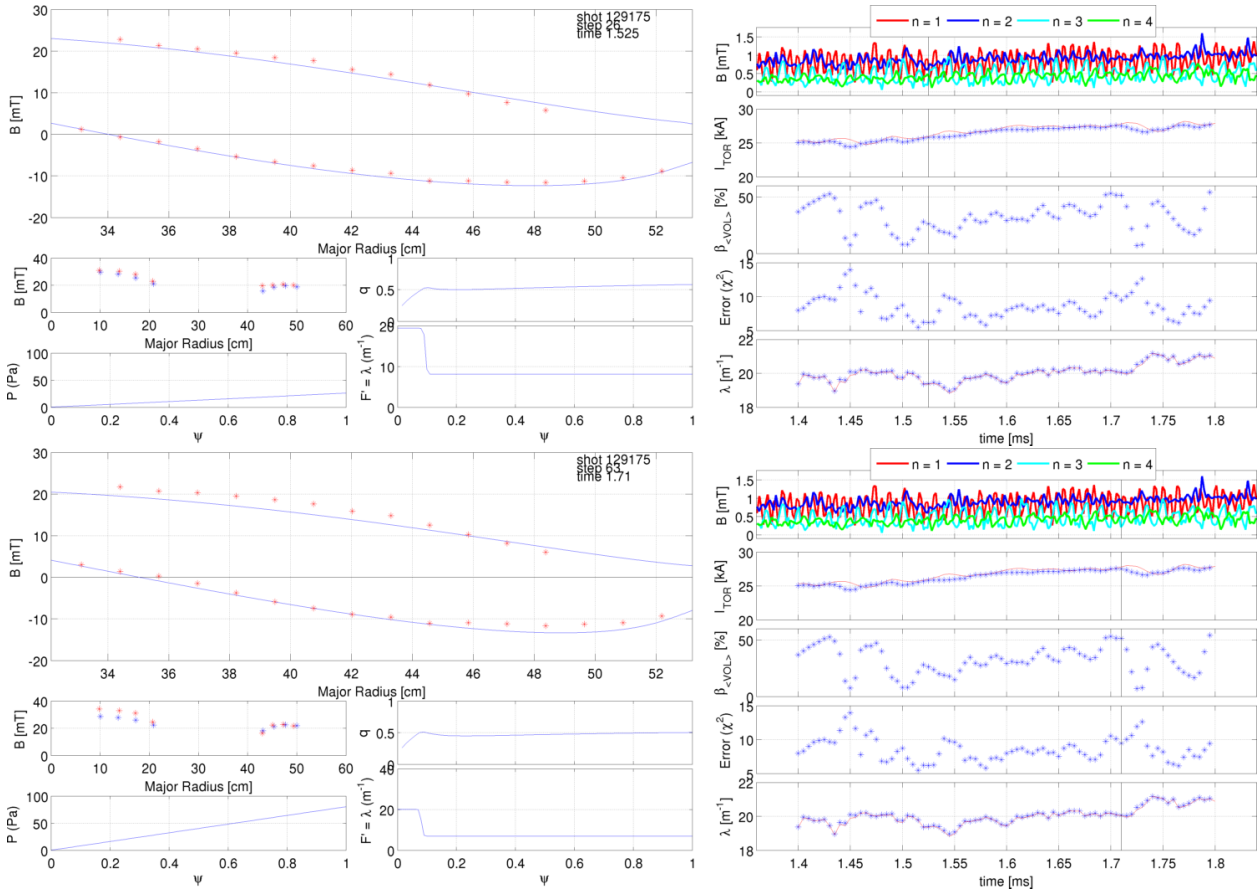

Figure 3.4: The time evolution of parameters in equilibrium fits of shot 129175, a typical high-f_{inj} discharge, is shown. On the left are spatial profiles of the equilibrium at the time marked with the black line on the right plots, which are identical otherwise. The internal probe signals from a typical fit are also shown at two points in time. The top plot is a typical stable equilibrium, while the bottom is one with an $n = 2$ kink unstable q profile ($q < 1/2$ everywhere).

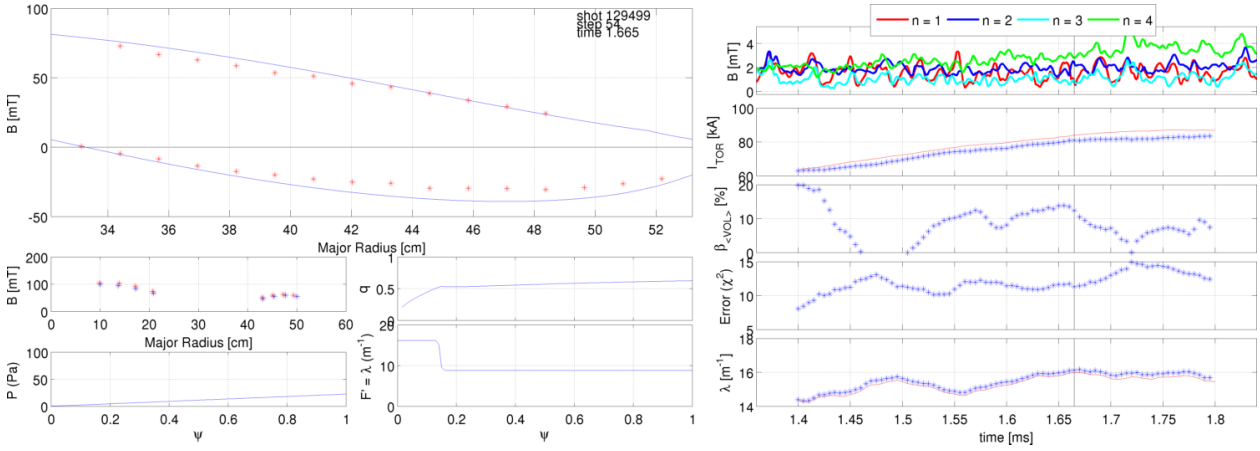

Figure 3.5: The time evolution of parameters in equilibrium fits of shot 129499, a typical low-f_{inj} discharge. The internal probe signals from a typical fit are also shown.

mouths, and after a period of time a relaxation event occurs converting the energy into the $n = 0$ state. This $n = 1$ state is believed to be a Taylor state ($\nabla \times \vec{B} = \lambda \vec{B}$) at a higher λ value than the minimum energy state. At high f_{inj}, a large $n = 2$ with similar magnitude and appears to play a role in the relaxation. Due to the shape of the injectors, an $n = 2$ mode would likely connect between the injectors, while $n = 1$ modes likely are isolated to a single injector. In both cases after relaxation the $n = 2$ activity is minimal, and the plasma is dominated by a large $n = 0$ object (the spheromak) and the lower amplitude $n = 1$ injector mode.

During the sustainment phase, the question arises of is our observed $n = 1$ magnetic energy entirely the driven injector mode. To answer that question, we can perform a biorthogonal decomposition on the surface probe array, with the addition of the two injector currents to the data matrix. By applying an appropriate coefficient to the injector current signals, we can force the 2^{nd} and 3^{rd} eigenmodes to correlate directly with those signals, identifying the component of the surface probe signal that is the injector mode. By then subtracting off those modes and reconstructing our data without the injector mode, we can now look for other activity. In addition, confirmation of this is done by of comparing the temporal shape

of I_{inj} to B_1 allows us to see a close match. The result of this is seen in Fig. 3.6.

The main result seen is that the observed $n = 1$ magnetic energy is almost entirely the injector state, indicating there are no large-scale $n = 1$ instabilities in the plasma. Because an $n = 1$ kink instability would be expected if there was a $q = 1$ resonant surface, this agrees with the q profile obtained from equilibrium fits that show $q < 1$ everywhere. The $n = 2$ activity that is observed is indicative of two different possibilities. Shortly before spikes in $n = 2$ activity, the equilibrium fits show a $q = 1/2$ resonant surface form, which is indicative of a $n = 2$ current-driven kink instability. Alternatively, the $\langle\beta\rangle_{vol}$ obtained in equilibrium fits is likely unstable to an $n = 2$ pressure-driven instability, which have growth rates linear to $\langle\beta\rangle_{vol}$ [41].

In summary, the experimental parameter scan showed 3 important results that we would like to replicate with the simulations: The increase in $\frac{I_{tor}}{I_{inj}}$ with f_{inj}, the outward shift and increased symmetry of the magnetic profile, and the toroidal modal activity.

3.2 Simulation Parameters

Simulations using the extended MHD model described in Chapter 2 were performed to try and model these experimental results. The simulations can be divided into two primary types which will be referred to as 'formation' and 'sustainment'. Formation simulations attempt to model the entire discharge of an experimental shot, beginning with plasma breakdown, proceeding through the spheromak relaxation event, and ending with the spheromak sustainment. Sustainment simulations being with a large equilibrium, and are useful for examining the sustainment phase of the discharge without dealing with the stiff numerical properties during the relaxation event.

3.2.1 Formation simulations

The mesh resolution used for all of the simulations shown is the same as the $f_{inj} = 14.5$ kHz zero-β validation simulations: 24x24 poloidal mesh with polynomial degree 4 and 11 Fourier modes toroidally. Limited convergence scans have indicated little need to increase grid

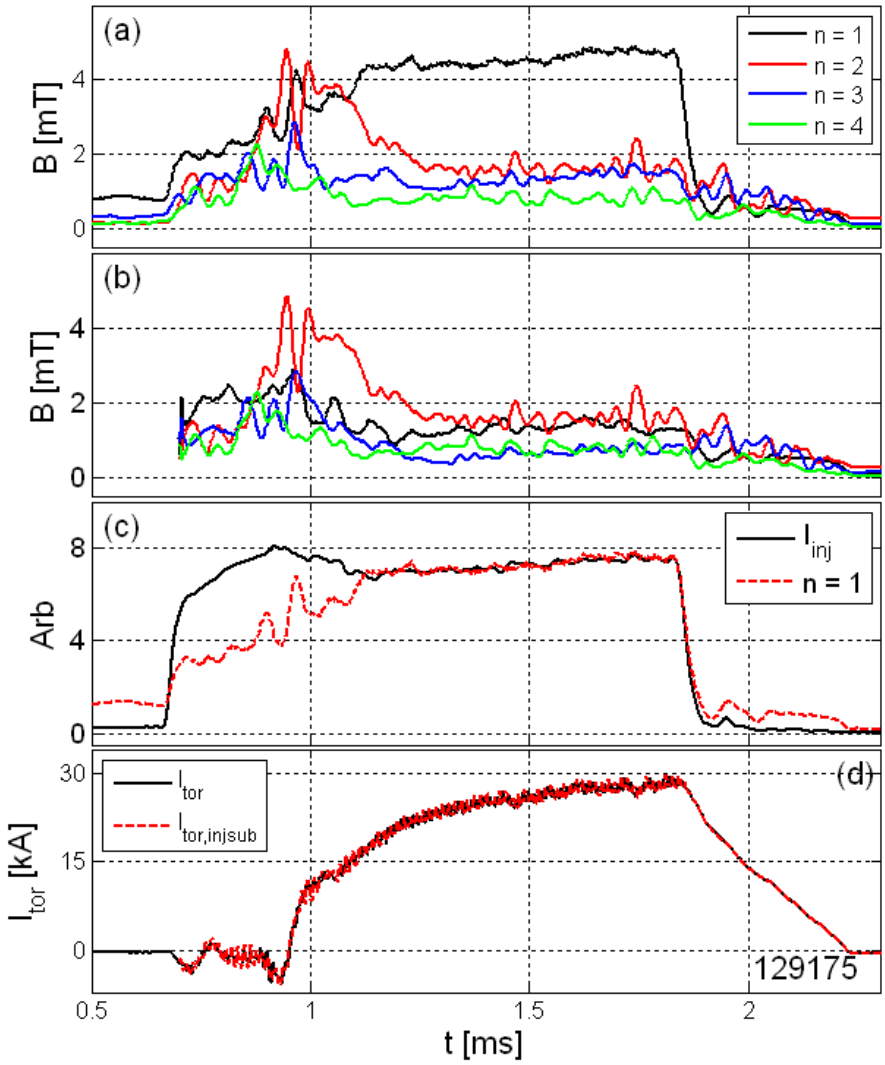

Figure 3.6: The magnetic energy spectrum of the plasma [15]: (a) includes the full data, (b) has subtracted the injector components. We see a significant $n = 2$ mode prior to relaxation as well as the $n = 1$ mode being largely associated with the injector modes.

resolution. Two types of formation simulations have been performed, ones attempting to match an experimental discharge and ones that focused on scanning a specific parameter. All of these simulations used $T_{wall} = T_{inj} = 1$ eV. Effects of hot injectors was explored on the simulations of HIT-SI3.

Simulations attempting to match a specific discharge used experimental measurements for the initial and boundary conditions. FIR measurements provided $\langle n_e \rangle$ to use as n_{wall} and a similar injector waveform was used. It is important to note that due to experimental power supply constraints, $\frac{P_{14.5}}{P_{68.5}} \sim 5$, so a significant disparity in injector power was seen. In addition, $\frac{\langle n_{e,14.5} \rangle}{\langle n_{e,68.5} \rangle} \sim 5 - 10$, which plays a large role in the finite-β effects. A particle diffusivity of $D = 1000$ m^2/s was used to numerically stabilize the continuity equation.

To help us remove the consequences of the difference in injector power and focus on f_{inj}, another set of simulations was run with the boundary conditions of experimental shot 129175, an $f_{inj} = 68.5$ kHz discharge. This included $n_{wall} = 10^{19}$ m^{-3}, $I_{inj} \approx 6$ kA, and $\lambda_{inj} \approx 25$ m^{-1}.

One important consideration for the simulation scan in f_{inj} is the electron inertia term in the generalized Ohm's law: $\frac{m_e}{ne^2}\frac{\partial \vec{J}}{\partial t}$. This term is used as a numerical tool to improve the numerical stability of the Hall term and is assumed to have no real physical influence. Early in time, when the magnetic energy of the system is entirely in the oscillating injector modes, we expect this term to be proportional to f_{inj}:

$$\frac{m_e}{ne^2}\frac{\partial \vec{J}}{\partial t} \approx \frac{\omega_{inj} m_e}{ne^2}\vec{J}.$$

In order to keep this term from influencing results between simulations of different f_{inj}, it makes sense to vary our electron mass. The quantity $\frac{\omega_{inj}}{\Omega_e^2}$ is kept constant, with Ω_e being the electron plasma frequency. In practice, this leads to $\frac{m_i}{m_e} = 36$ at $f_{inj} = 14.5$ kHz and 175 at $f_{inj} = 68.5$ kHz.

Additionally, split electron and ion temperature simulations were attempted in these formation simulations, as experimental results have implied that $T_i \sim 2T_e$. The full two-temperature model was attempted on the injector waveforms of shot 129175, though the

simulation did not proceed significantly far past the relaxation event due to numerical stiffness of the electron temperature equation.

A modified two-temperature model was also used, where the electron temperature is held fixed at $T_e = 12$ eV, analogous to the temperature assumed in zero-β simulations. Two simulations will be looked at using this model, at injector frequencies $f_{inj} = 14.5$ and 68.5 kHz. It is important to note that this model no longer strictly conserves energy, it is instead assumed that all Ohmic heating from currents and the plasma exactly cancel out the electron thermal losses.

3.2.2 Sustainment simulations

The set of simulations discussed in the previous subsection all required high particle diffusivity D, which while necessary for numerical stability had the downside of significantly damping oscillations and dynamics occurring in n. The primary issue causing the need for this diffusivity was density leaving the volume, a density hole would eventually appear at the magnetic axis crashing the simulation. To resolve this a normal boundary condition on $\vec{V}$ can be applied, which refuels the plasma as the density leaves the system. The boundary conditions used ($V_\perp = V_0 g(R, \phi)$) was directed into the volume with spatial shape equivalent to the $B_\perp$ boundary condition and a peak magnitude of $V_0 = 15$ km/s, the same order of magnitude of experimental measurements of the injector flow velocity [18]. Using this a set of simulations were performed $D = 250$ m^2/s, a factor of 4 reduction from the prior section.

Unfortunately, due to grid-scale noise in n introduced during the highly chaotic relaxation event, these simulations needed to be started from an already-formed equilibrium and allowed to decay into their final state. Eight values of f_{inj} were used for this scan, with each simulation having identical parameters otherwise. The simulation parameters are seen in table 3.1.

Additionally, in order to more closely match the current amplification, two different models of thermal conduction were used for the single-temperature model. The first set of simulations is performed using the Braginskii thermal conduction model, while the second

Parameter	Simulation	Experiment
m_e (kg)	9.1×10^{-29}	9.1×10^{-31}
n_e (m^{-3})	0.75×10^{19}	$4–10 \times 10^{18}$
T_{wall} (eV)	2	13 ± 7
η/μ_0 (Spitzer) (m^2/s)	8.8	25–9
Viscosity (ν) (m^2/s)	300	100–500
f_{inj} (kHz)	5–100	14.5–68.5

Table 3.1: The parameters for sustainment simulations of HIT-SI are shown.

reduces the parallel heat flux $q_\parallel$ by a factor of 10. This reduction was chosen based on results of the HIT-SI3 simulations seen in chapter 4. While we know from the previous section that this model does not perfectly capture the results seen experimentally, we can use these results to gain more insight into how the thermal conduction and particle diffusivity influence the profile. Finally, an equivalent zero-β simulation was done at each setting to compare with the 'pressureless' case.

3.3 Simulation Results and Diagnostics

A variety of diagnostics can be used to examine the dynamics involved in the simulation, both for physics understanding and comparison with experimental results. These diagnostics take the form of both equivalent signals from experimental measurements, such as magnetic probes, and values extracted from the simulations that the experiments are unable to measure.

3.3.1 Relaxation Dynamics

As mentioned when discussing the experimental results, high f_{inj} discharges saw an increase in $n = 2$ activity during the relaxation event. This is also seen in the simulations, as shown

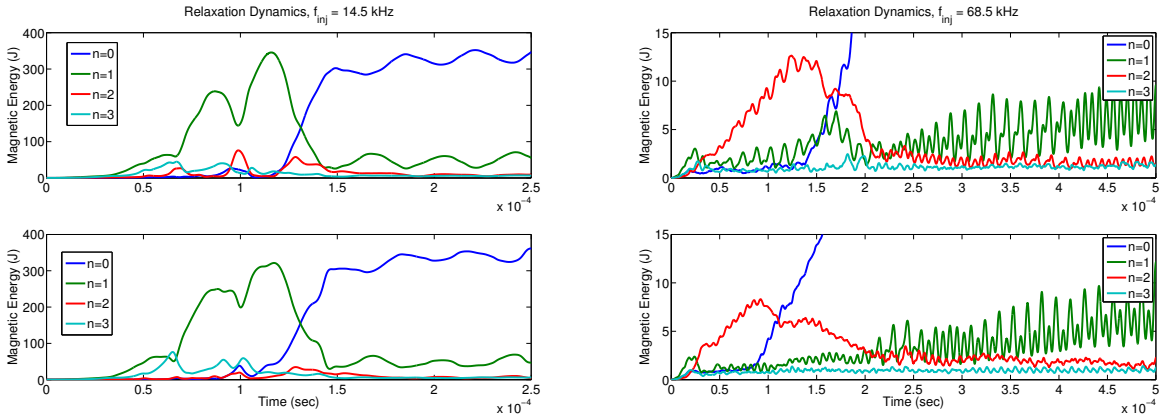

Figure 3.7: The magnetic energy spectrum $\left(\int B_n^2/2\mu_0 \mathrm{d}^3x\right)$ during relaxation for low and high f_{inj} simulations for both the zero (top) and finite (bottom) β cases. The low f_{inj} case sees a large $n = 1$ mode form then relax into the large $n = 0$ spheromak mode, while high f_{inj} sees a large $n = 2$ state precede relaxation.

in Fig. 3.7. At low f_{inj} there is little change in the relaxation dynamics between zero and finite-β, in both cases the $n = 1$ mode dominates then relaxes into the $n = 0$ mode.

At high f_{inj} some changes are seen. In both the zero and finite-β cases at $f_{inj} = 68.5$ kHz the $n = 2$ mode dominates pre-relaxation and transitions to an $n = 1$ perturbation after relaxation. The main difference between the zero and finite-β cases is seen in the dynamics of the relaxation event, where the zero-β model sees a spike in $n = 1$ activity during relaxation. This contrasts with the finite-β model where little $n = 1$ activity is seen until after the spheromak is finished forming.

This volume-integrated energy spectrum looks different than the experimentally-observed spectrum seen from surface magnetic probes. In the experimental measurements the $n = 1$ and $n = 2$ mode amplitudes are at similar magnitudes. Synthetic surface magnetic probes in the simulation, as seen in Fig. 3.8, show a spectrum closer to the experiment. The reason the probes see such a difference from the total energy spectrum has to do with the poloidal distribution of the mode. The $n = 2$ mode tends to have most of its energy near the core

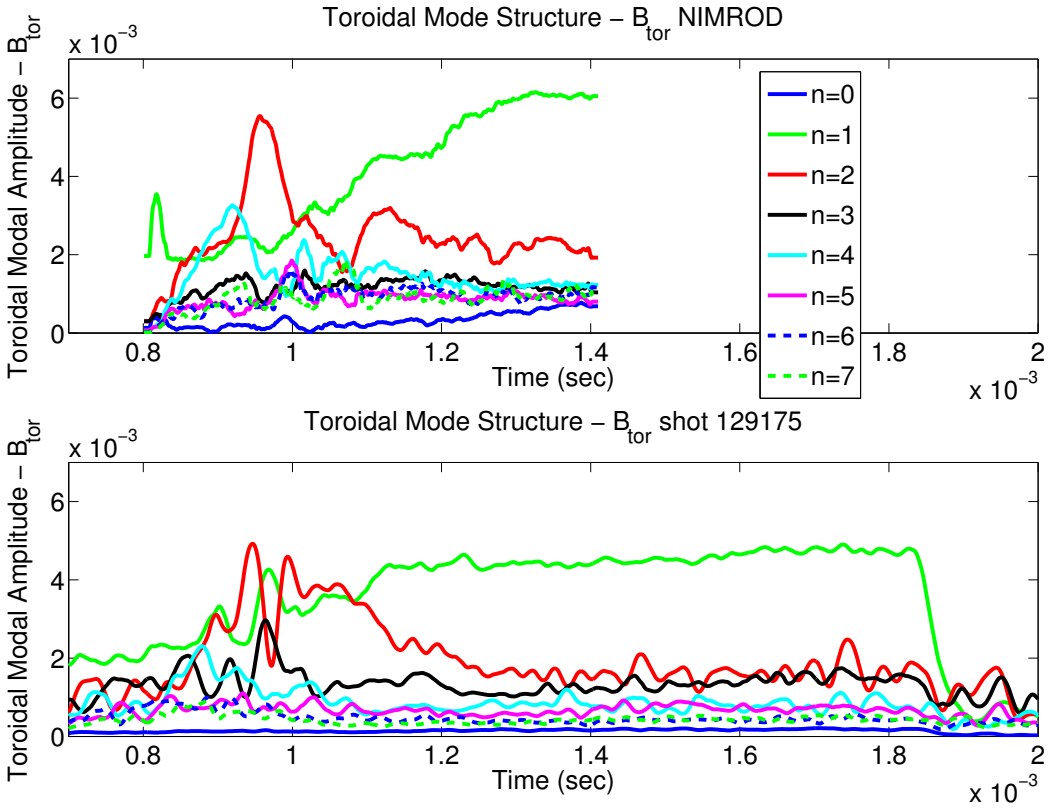

Figure 3.8: The magnetic Fourier spectrum for a NIMROD calculation and an experimental discharge at high frequency using the surface probe measurements. We see similar behavior pre-relaxation of n=2 activity, though larger amplitude activity on all signals. This is likely due to the large differences between the experimental and simulation geometry near the location of these midplane probes.

of the plasma, away from the wall where the surface probes are located. This is opposed to the $n = 1$ mode which connects the injectors and exists predominantly near the wall.

We can look at the structure of this $n = 2$ state in Fig. 3.9 and 3.10. This state features long field lines that wrap into 4 distinct helical tubes, centered near the injector mouths. Each $\vec{B}$ fieldline travels between all 4 tubes which appears to connect the injector mouths together. This is different than the $n = 1$ dominated state at low f_{inj} where the injector fields are disconnected from each other. It is important to note that while the typical $n = 1$ state rotates at f_{inj} throughout the machine, this $n = 2$ state stays fixed in shape through multiple injector cycles and simply grows in magnitude until the relaxation event occurs.

The details of the relaxation event in both cases are seen in Fig. 3.11. In the $n = 2$ relaxation case, two of the helical flux tubes attract and merge together at the geometric axis, forming the toroidal O-point of the spheromak. The $n = 1$ relaxation case sees the $n = 1$ structure driven by the plasmas rotating around the volume at the injector frequency until it flips into position.

In both cases, 3-D asymmetries driven by the injectors are what determine the vertical orientation of the spheromak that forms. Because no external magnetic fields are generated directly inside the flux conserver, the minimum energy state of the system has a degeneracy in which direction the magnetic dipole of the spheromak points. Ennis [42] showed experimentally that each of the HIT-SI injectors preferred a different orientation of spheromak. In performing simulations of HIT-SI, it was additionally found that the vertical orientation of the spheromak was strongly dependent on which injector was at its peak amplitude when the relaxation event begins.

In the $n = 1$ relaxation case, we see a tilted spheromak mode that rotates toroidally at the injector frequency. The current paths in this case often pass only through a single injector, and the state features currents traveling into each injector, depending on their relative amplitude each point in time. When the relaxation event begins, the state appears to flip into position and thus operates in the way that an individual injector would prefer. Because there is a vertical asymmetry to the two injectors, that determines why the spheromak

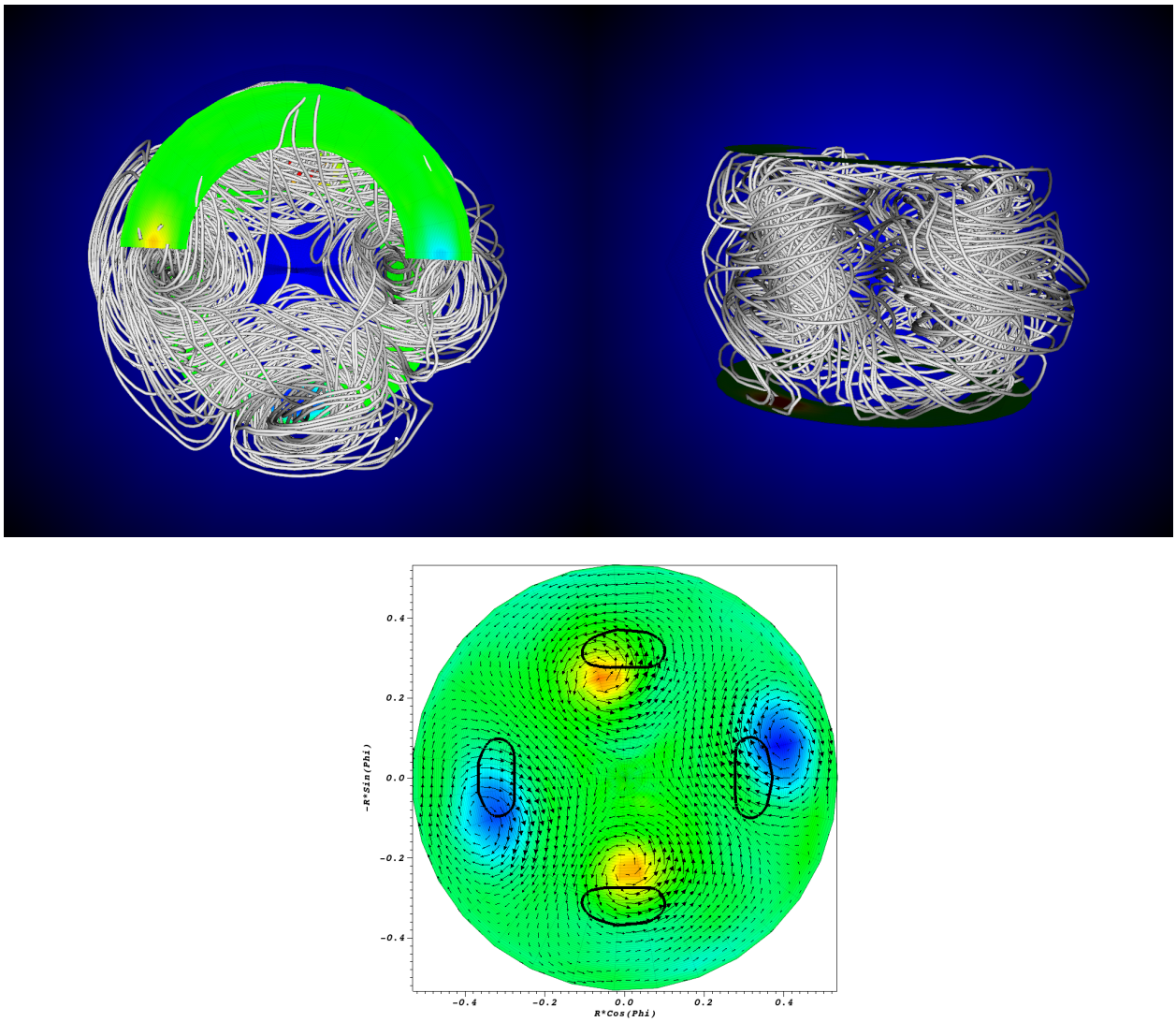

Figure 3.9: On top are streamlines of the magnetic field during the $n = 2$ dominated portion of the relaxation event. The lower image is a midplane slice of $\vec{B}$, with arrows representing in-plane fields and pseudocolor representing out of plane fields. The black lines represent the location of the injector mouths.

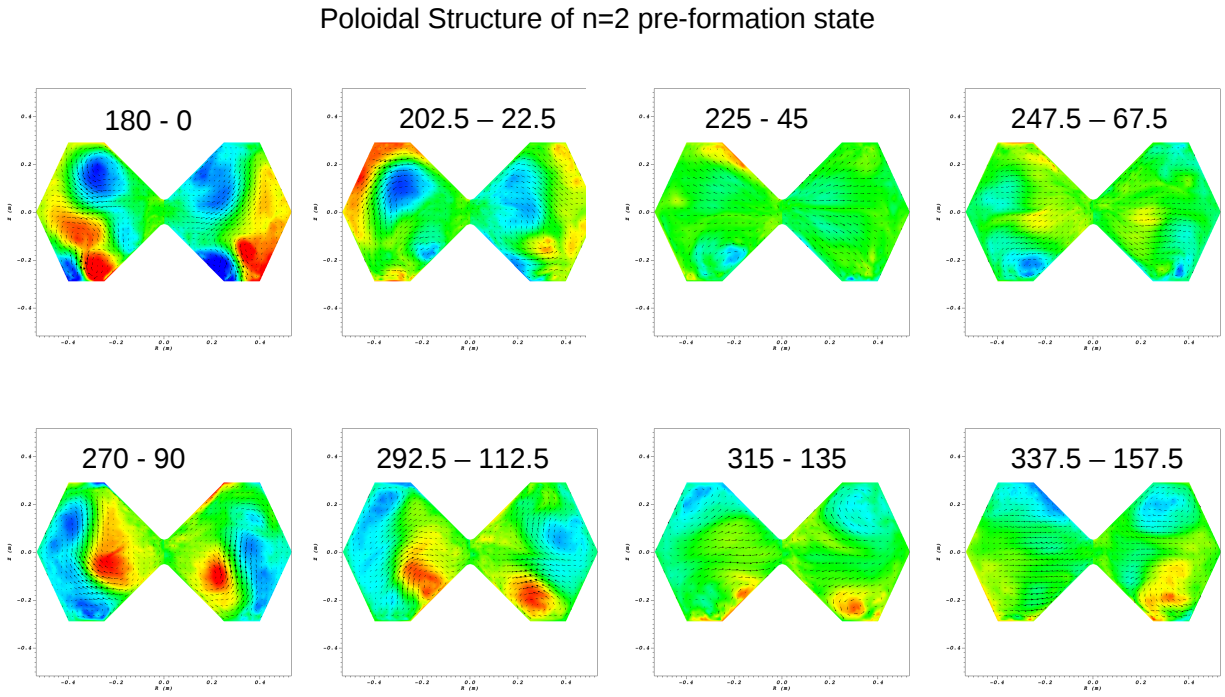

Figure 3.10: The magnetic field structure at different toroidal cross sections during the $n = 2$ dominated state is shown. The pseudocolor represents the toroidal component of B while the arrows represent the in-plane fields. The numbers above each plot show the toroidal angle of each half of the image.

orientation is seemingly random.

In the $n = 2$ relaxation case, the two flux tubes that eventually attract and form the spheromak have the same vertical orientation as the formed equilibrium. Additionally, the asymmetry away from the $n = 2$ structure this mode sees prior to relaxation determines which two tubes will be closest together, and thus be the ones dominating the attraction. Thus the orientation of the spheromak seen is dependent on when in time relative to the injector oscillation waveforms the relaxation event occurs. We also note that this $n = 2$ state differs from the $n = 1$ driven state in that the injector current paths are more likely to pass through both injectors instead of just one. Experimentally, it was seen that the 'preferred' orientation of the two injectors broke apart at higher frequencies, it is for this reason that the relaxation process fundamentally depends on how this $n = 2$ state evolves, less which injector is dominating.

To understand this difference, we can look at the Alfvèn time of the system, and assume that a plasma current can only remain coherent between the two mouths of a single injector when the injector frequency is slower than the Alfvèn time of the length of the current path. Using a current path length $l = \pi R + a$, with R and a being the major and minor radii of the torus, we can evaluate $\tau_A = l/v_A = (\pi R + a)\sqrt{\mu_0 m_i n}/B$. Using typical values during the formation period of $B = 10$ mT and $n = 10^{19}$ m^{-3}, we obtain a threshold value of about $f_{inj} < 30$ kHz to observe the $n = 1$ state pre-formation. At higher frequencies ($f_{inj} > \tau_A$), the injector fields are switching faster than the Alfvèn time of the state, instead releasing the flux tubes into the volume which instead quickly relax to form the observed $n = 2$ state, before eventually forming the spheromak.

3.3.2 Bulk Parameters

The time evolution and final steady state values of bulk plasma properties are useful for seeing large scale variations in the different simulations and experiment. A dimensionless figure of merit for quality of the plasma discharges used is the current gain, I_{tor}/I_{inj}. Figure 3.12 shows the current obtained experimentally in the sustainment simulations and the experimental

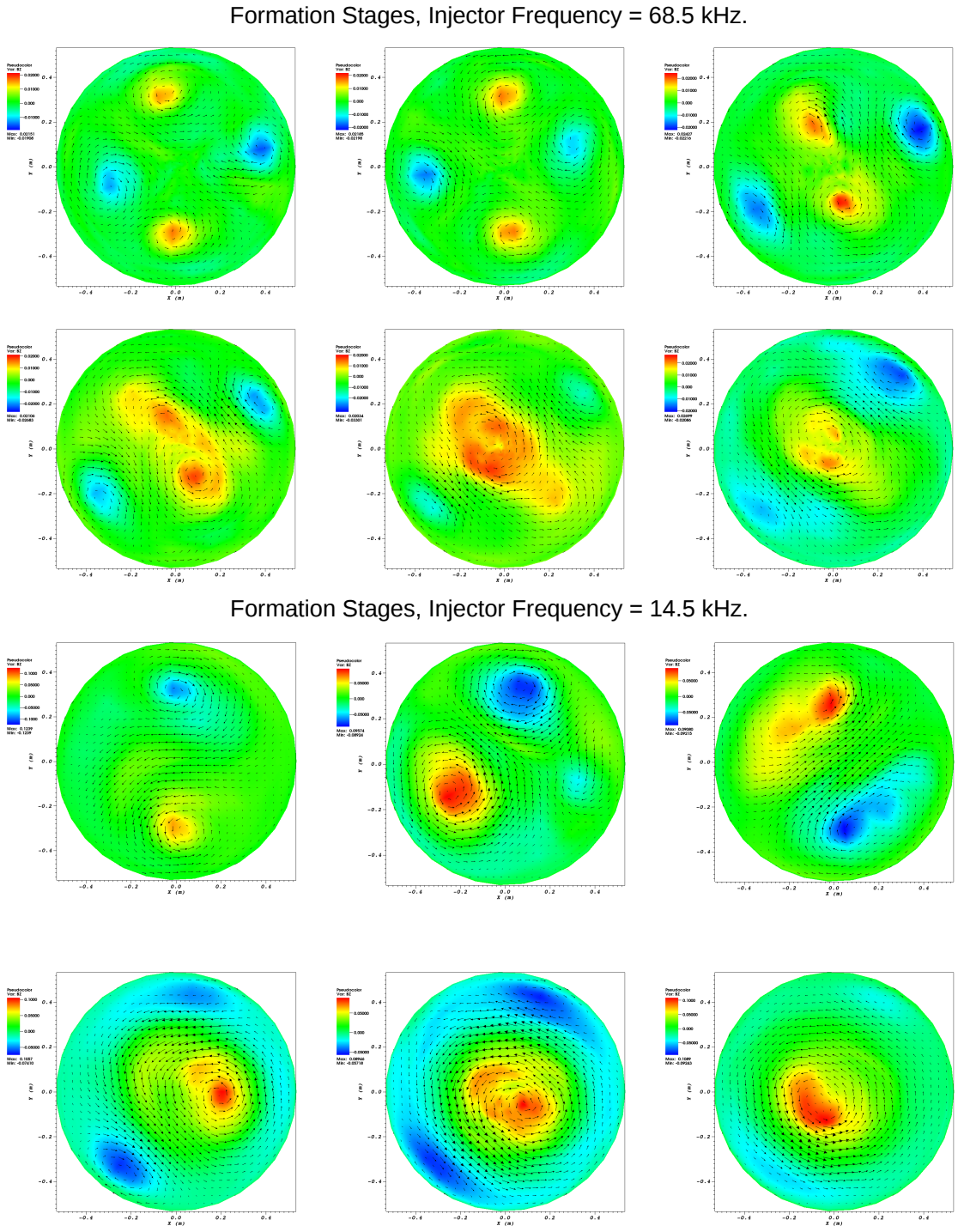

Figure 3.11: The magnetic field in the midplane, with arrows representing B_{tor} and B_R while the pseudocolor represents B_Z. From left to right then top to bottom, each image represents a point in time during the spheromak formation event. The top shows the $n = 2$ formation typical of high-f_{inj} discharges while the bottom shows the $n = 1$ formation seen in low-f_{inj} discharges.

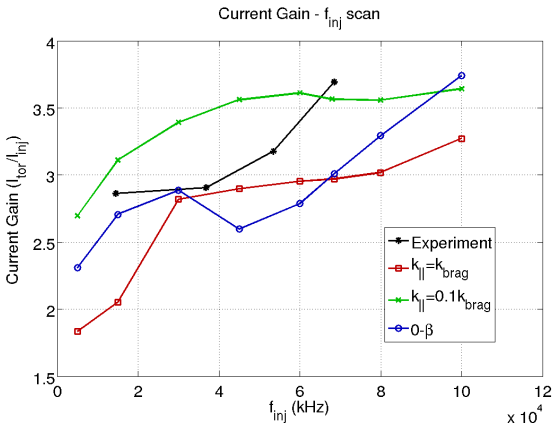

Figure 3.12: Current gain I_{tor}/I_{inj} as a function of f_{inj}.

results, while Fig. 3.13 and 3.14 show the time evolution of the current gain through the formation simulations.

Additionally, the volume averaged $\langle\beta\rangle_{vol} = \int p\,\mathrm{d}V / \int B^2/2\mu_0\,\mathrm{d}V$ is a useful measure of the pressure confinement in the equilibrium. Figure 3.15 shows $\langle\beta\rangle_{vol}$ for the sustainment scans and the experimental equilibrium reconstructions, while Fig. 3.16 shows the time evolution of the parameter. We see that while the low and high f_{inj} cases see the same value of $\langle\beta\rangle_{vol}$ in the single-temperature model, the two-temperature models show different results between the two frequencies.

The temporal evolution of the entire system can be seen in plots of the magnetic energy spectrum. While the typical formation spectra were shown in Fig. 3.7, the sustainment period energy spectra are seen in Fig. 3.17 through 3.18.

3.3.3 Magnetic Profile

The magnetic profile of the equilibrium that forms serves as an important tool to compare with experimental observations and understand equilibrium stability. Experimental diagnostics consist of the surface probes described in Chapters 1 and 2 as well as an internal magnetic probe.

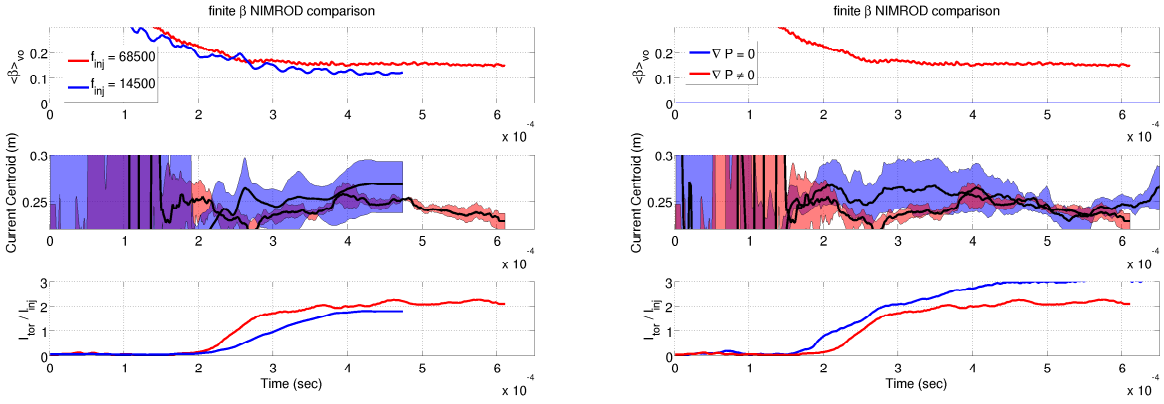

Figure 3.13: On the left is the current centroid for two finite-β simulations at $f_{inj} = 14.5$ and 68.5 kHz where we see the toroidal symmetry is captured but not the outward shift. On the right is two $f_{inj} = 68.5$ kHz simulations, zero and finite-β. Similarly, the finite-β captures the symmetry but not the outward shift.

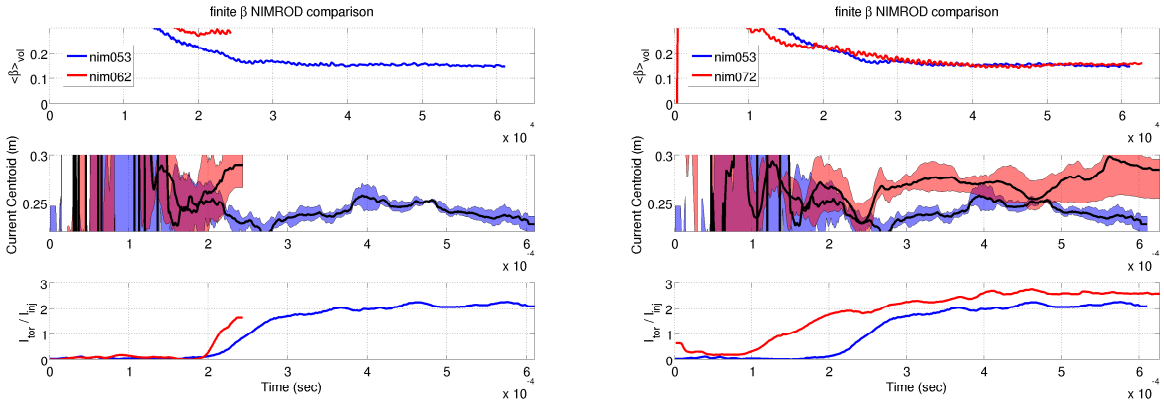

(a) T_e free to evolve

(b) $T_e = 13$ eV

Figure 3.14: Split and single T simulations for two models of T_e at $f_{inj} = 68.5$ kHz. In both cases the outward shift of the centroid is seen. In the right case the symmetry is not seen.

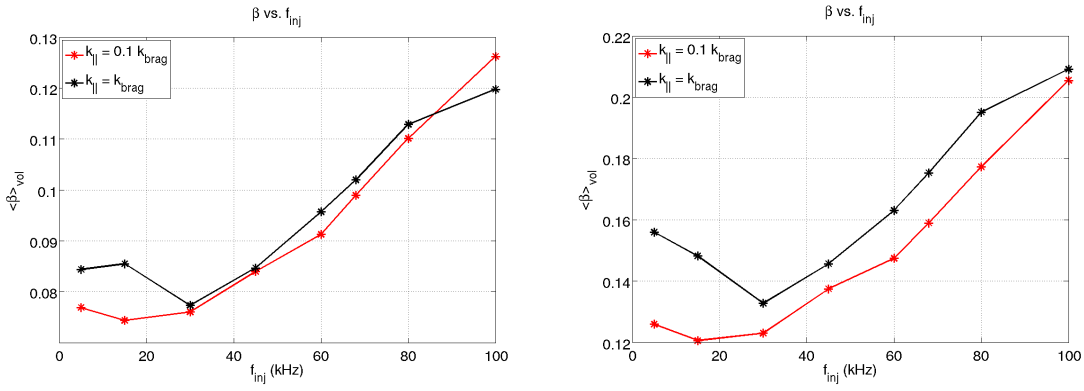

Figure 3.15: The result of two methods of calculating volume averaged β are plotted. On the left is $\langle\beta\rangle_{vol} = \frac{\int p\mathrm{d}V}{\int B^2/2\mu_0 \mathrm{d}V}$ as a function of f_{inj}, while on the right is $\langle\beta\rangle_{vol} = \int \frac{p}{B^2/2\mu_0}\mathrm{d}V$ / V.

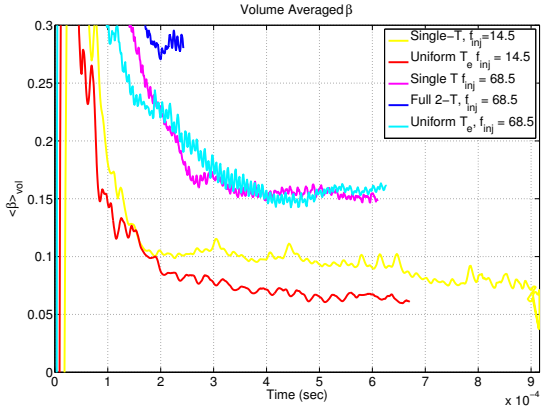

Figure 3.16: $\langle\beta\rangle_{vol}$ for a series of simulations at high and low f_{inj}. As can be seen splitting the temperatures lowers β for low f_{inj} and raises for high f_{inj}, with results closer to experimental observations.

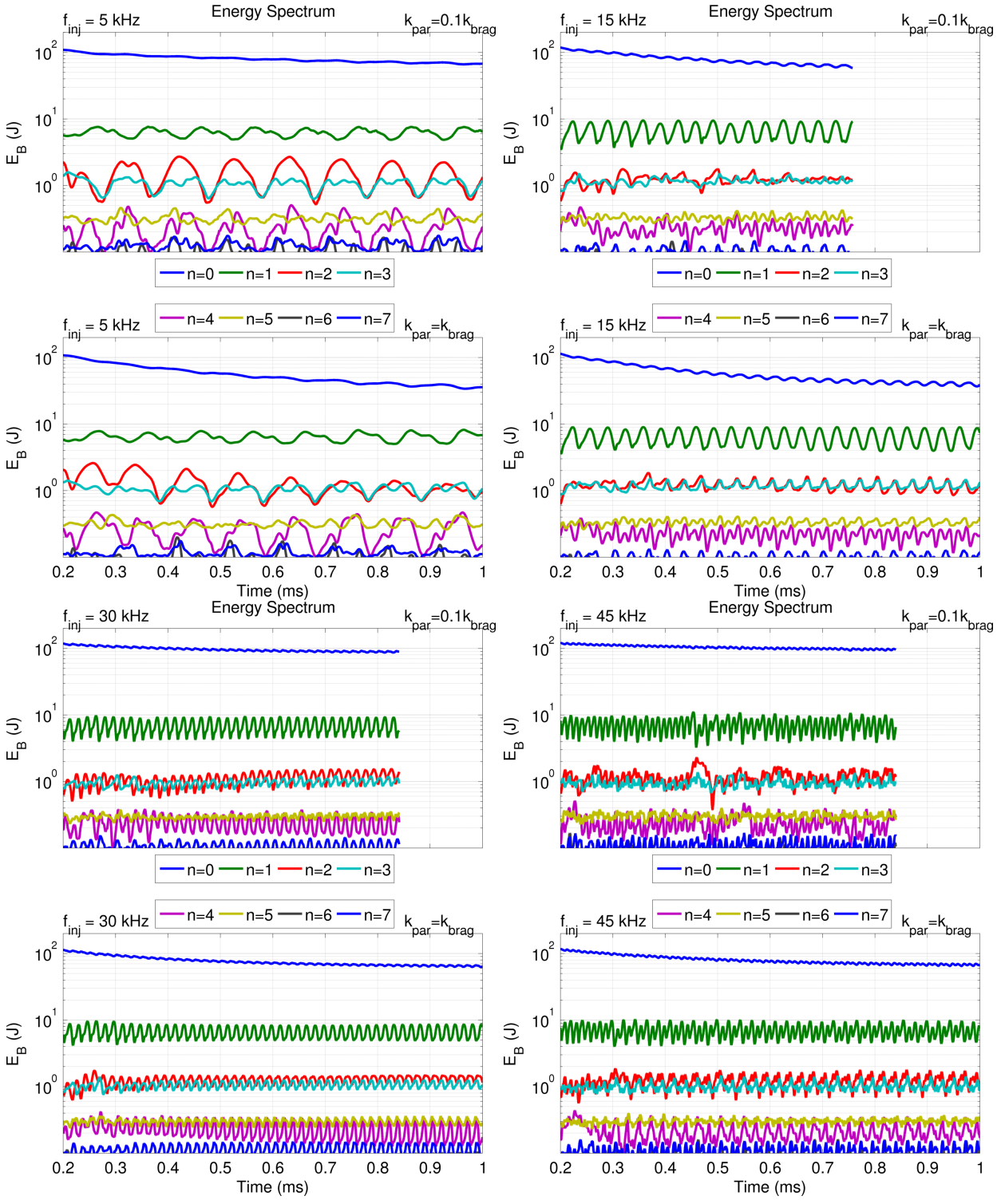

Figure 3.17: Magnetic Energy spectra for the finite-β sustainment simulations.

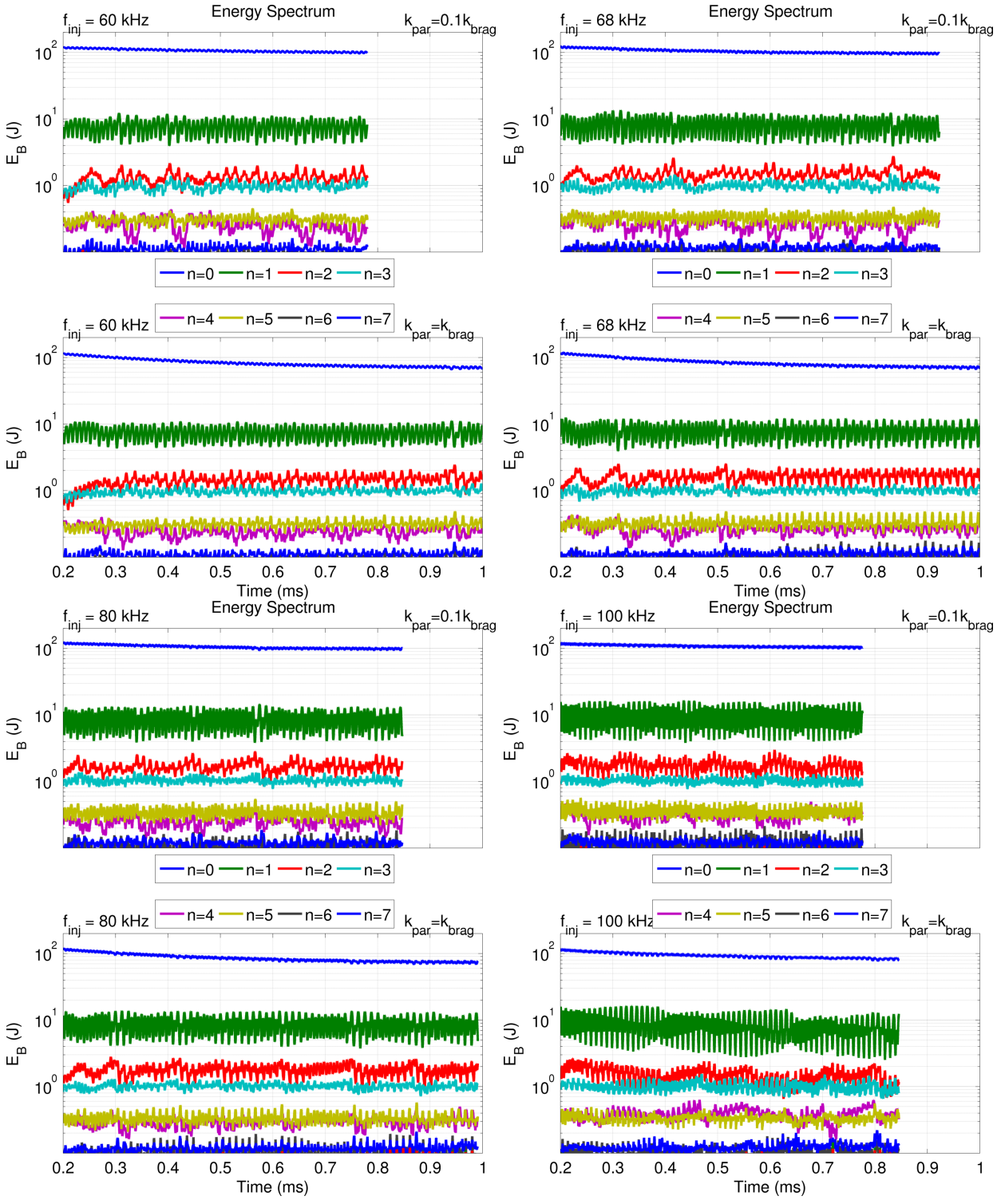

Figure 3.18: Magnetic Energy spectra for the finite-β sustainment simulations.

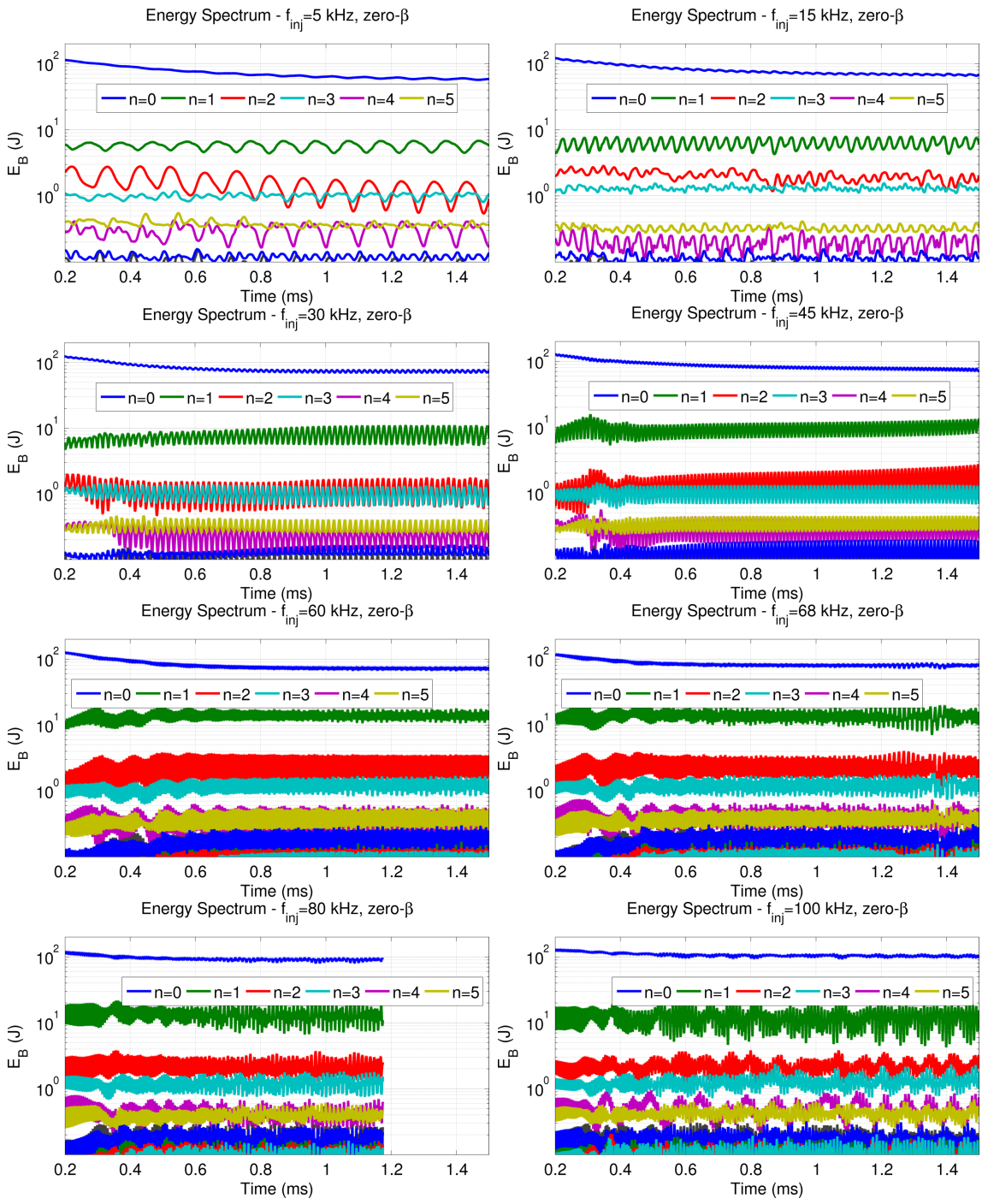

Figure 3.19: Energy spectra for the zero-β simulations.

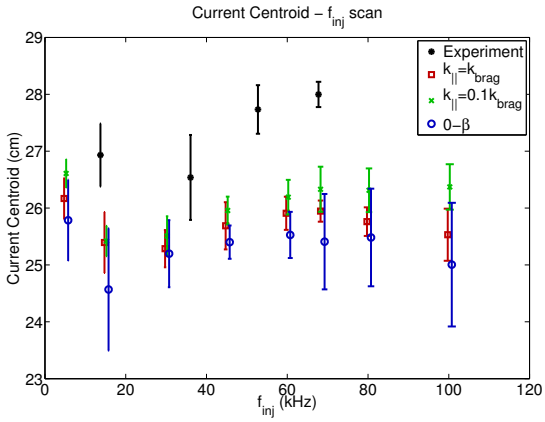

Figure 3.20: The current centroid from Eq. 3.1 for the different simulations performed and the experiment. Points are the average centroid of all four arrays in a period of either 200 μs or 3 injector cycles, whichever is longer. The error bars represent the range of values seen at the four toroidal locations this is measured. The x-axis position of each point is adjusted by up to 1 kHz to distinguish the different lines.

The current centroid mentioned when discussing the experimental result can be calculated for the surface probe signals obtained from the simulation. Time evolution of the centroid for the single-temperature formation cases are seen in Fig. 3.13. Equivalently, the two split-temperature models are shown in Fig. 3.14. The qualitative feature of the increased outward shift as f_{inj} increases is only seen with the split-temperature model. Increased toroidal symmetry is seen by the single-temperature model, but not by the isothermal electron model nor the zero-β model, and the full two-temperature model did not advance far enough to make a determination on this.

The sustainment simulations see similar behavior, shown in Fig. 3.20 alongside the experimental measurement. Unlike the formation simulations, the finite-β simulation is outwardly shifted with respect to the zero-β simulations, but is not shifted out the same amount the experiment observed.

The internal profile of the plasma magnetic field is measured with an internal magnetic

probe, located at $\phi = 225°$ and extending from the outside wall to about $R = 33$ cm. Temporally averaged magnetic profiles of the different cases are seen in Fig. 3.21 for the sustainment cases and the experiment. We see that all models see an outward shift of the magnetic axis as f_{inj} increases, though the experiment sees a more pronounced shift.

Additionally, a usfeul quantity for the measurement of the stability of the plasma is the q profile, which is defined as the ratio of the number of toroidal windings to number of poloidal windings of the magnetic field. Spheromak equilibria can be shown to be stable to $n = 1$ kink instabilities by satisfying $q < 1$ everywhere and stable to $n = 2$ kink instabilities by satisfying $q_{axis} > 1/2$, where the axis is the O-point of the poloidal magnetic field.

Calculating q_{axis} from the internal probe measurements experimentally is done in two different ways, though both methods share assumptions and values of $\vec{B}(r)$ used in the calculation. A primary assumption made when using the probe for equilibrium fitting is that $\left\langle \vec{B} \right\rangle_{f_{inj}} = \vec{B}_0$, in other words that temporally averaging the fields at f_{inj} is equivalent to a toroidally (and vertically) symmetric equilibrium. It is further assumed that these measurements of $\vec{B}$ lie on closed poloidal flux surfaces. This assumption is required for obtaining a value of q since by definition the safety factor only describes an axisymmetric plasma with closed flux surfaces.

For calculating q_{axis} directly, we take the limit of the minor radius (r) going to zero of q. Writing the definition of q as the ratio of toroidal rotations to poloidal rotations of the magnetic field, we can obtain:

$$q_{axis} = \lim_{r \to 0} \frac{R B_{tor}}{r B_{pol}}$$

We can fit a quadratic function to B_{pol} using the innermost three probes to evaluate the value of q_{axis}, with the results shown in Fig. 3.22.

While experimental results only have one diagnostic that can measure the internal q profile of the experiment, NIMROD results have the flexibility of double-checking assumptions that are made when using the internal probe by incorporating additional measurements. Two additional calculations of q_{axis} are done using the synthetic probes, a measurement of the profile from the actual $n = 0$ component of $\vec{B}$ and measurements from internal

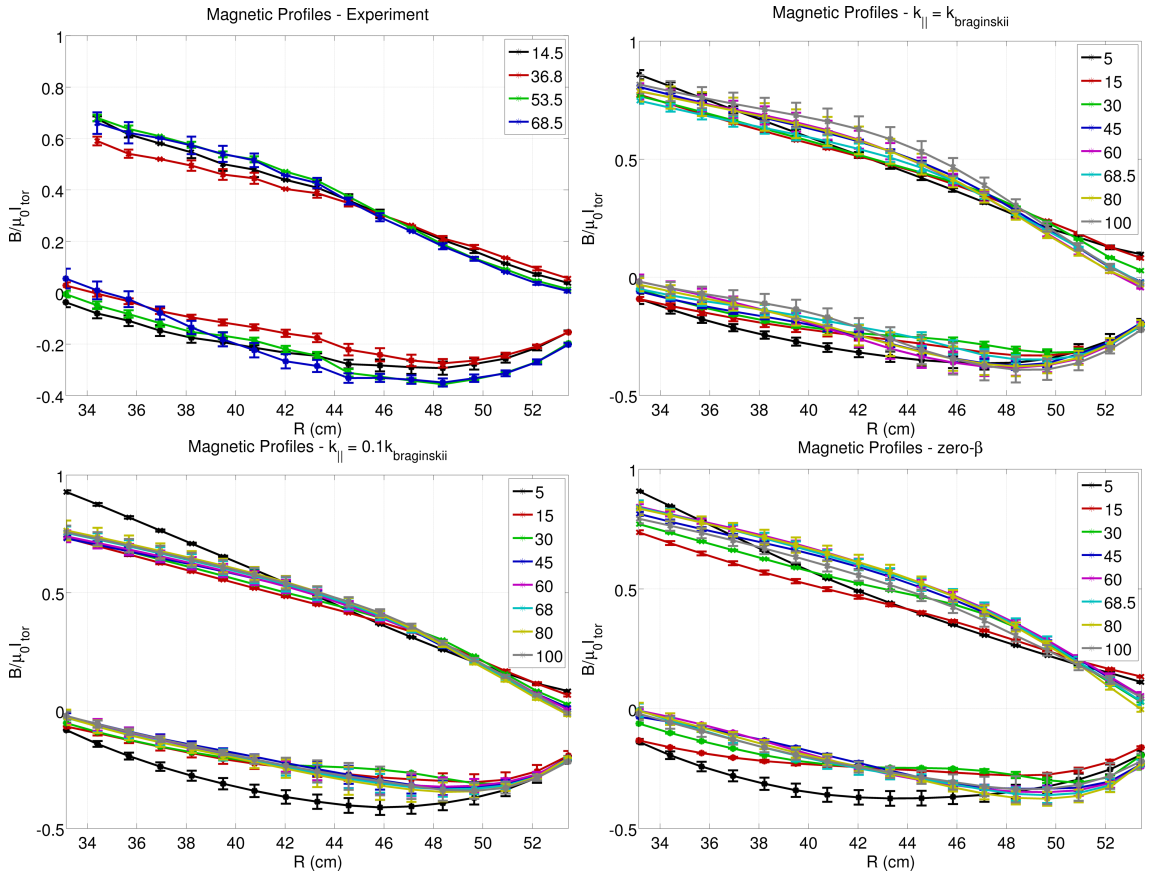

Figure 3.21: The magnetic profile, scaled by the toroidal current, at each injector frequency operated at in both the simulations and the experiment. Both the toroidal B_ϕ (positive) and poloidal B_z (negative) are plotted. The profile is created by averaging the value over several injector cycles. The error bars represent the standard deviation over the injector cycles, after subtracting the component that oscillates at f_{inj}. The experimental toroidal probe at $R = 33$ cm is missing.

probes located at different toroidal angles, seen in Fig. 3.23. We see that while in all cases $q_{\text{axis,NIMROD}} > q_{\text{axis,Exp}}$, the measurement becomes cloudy as to whether this method of calculating q_{axis} is useful. In particular, lacking closed magnetic flux surfaces adds vagueness to the definition of q.

3.3.4 Pressure Profile

The plasma pressure in the simulations is evolved through density and temperature. In the formation simulations, the large diffusivity used to replenish density in the core of the chamber leads to a flat density profile, so all pressure gradients are realized through temperature gradients. The time evolution and midplane spatial profile of the temperature profile in single-temperature formation simulations is seen in Fig. 3.24. The spatial profile of the final state reached in sustainment simulations is seen in Fig. 3.25 for the reduced thermal conduction case. We see that both cases evolve to reach similar temperature profiles, and as a result feature different pressure profiles.

Temperature profiles for the split-temperature model are shown in Fig. 3.26. We see, as expected, the ions are significantly hotter than the electrons. Additionally, the electron temperature profile is flatter than the ion profile.

The time evolution of the temperature is useful to observe, even in the final steady state equilibrium. Temperature oscillations are seen at the injector frequency, shown in Fig. 3.27 and 3.28, which correspond to the motion of the plasma as the injectors oscillate. These images were created from the $k_{\|} = k_{Braginskii}$ sustainment simulation.

Additionally, the density evolution is dominated by oscillations at the injector frequency. Fig. 3.29 and 3.30 show the density evolution during the 16 sustainment simulations with density evolution, as seen by the experimental interferometry chord. To see the toroidal dependence of these oscillations, a second chord was located 180 degrees toroidally from the original chord. Typically, these oscillations are 180 degrees apart in temporally as well, indicating $n = 1$ motion.

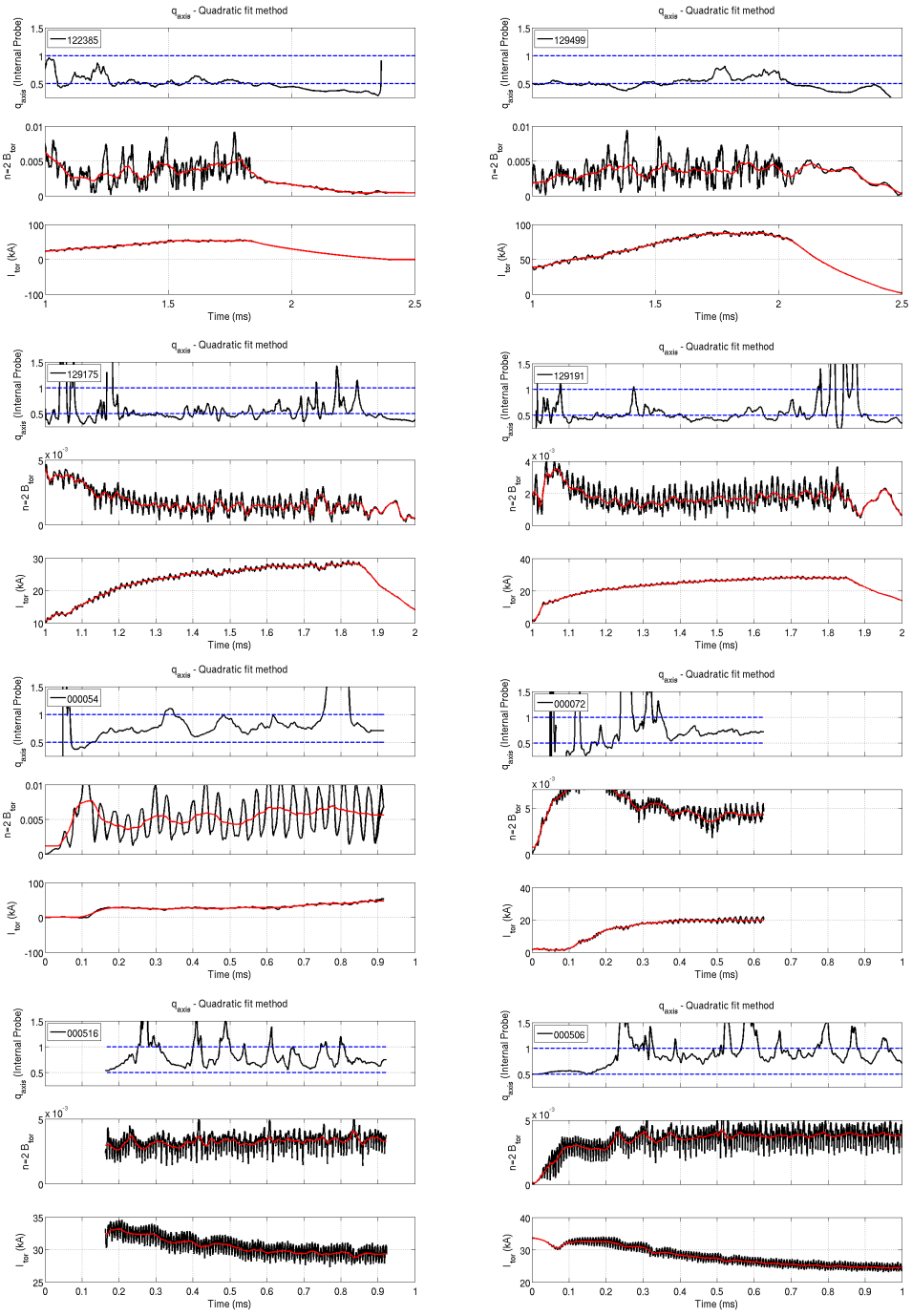

Figure 3.22: q_{axis} measurement made by using a quadratic fit to estimate the slope of the poloidal field as it approaches the magnetic axis. The top row is two typical $f_{inj} = 14.5$ kHz discharges, second row is two typical $f_{inj} = 68.5$ kHz discharges, third row is a low and high frequency formation simulations and the bottom row is the (left) $k_{||} = k_{Brag}$ and (right) $k_{||} = 0.1k_{Brag}$ of the $f_{inj} = 68.5$ kHz sustainment simulations.

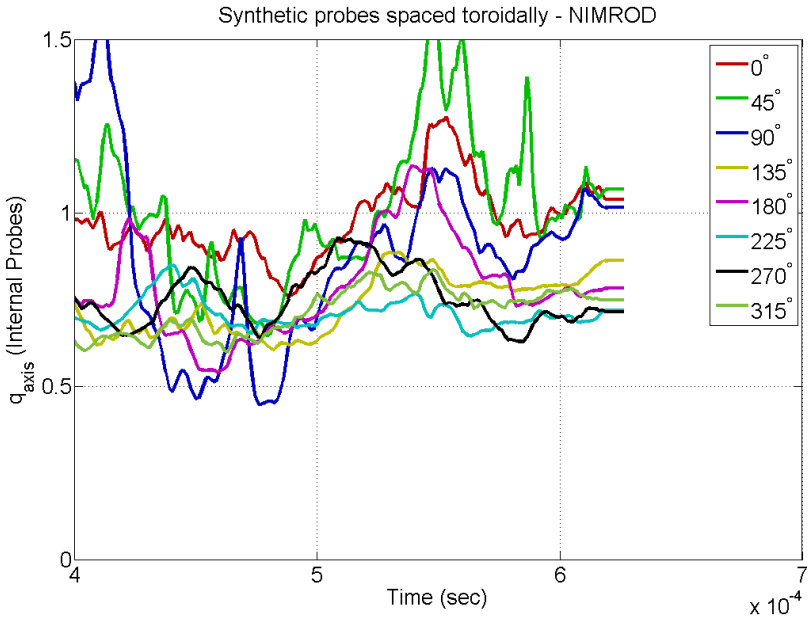

Figure 3.23: The quadratic fit method applied to calculate q_{axis} in a NIMROD simulation, where each line is using an internal probe located at a different toroidal angle. The experimental measurement is at $\phi = 225°$.

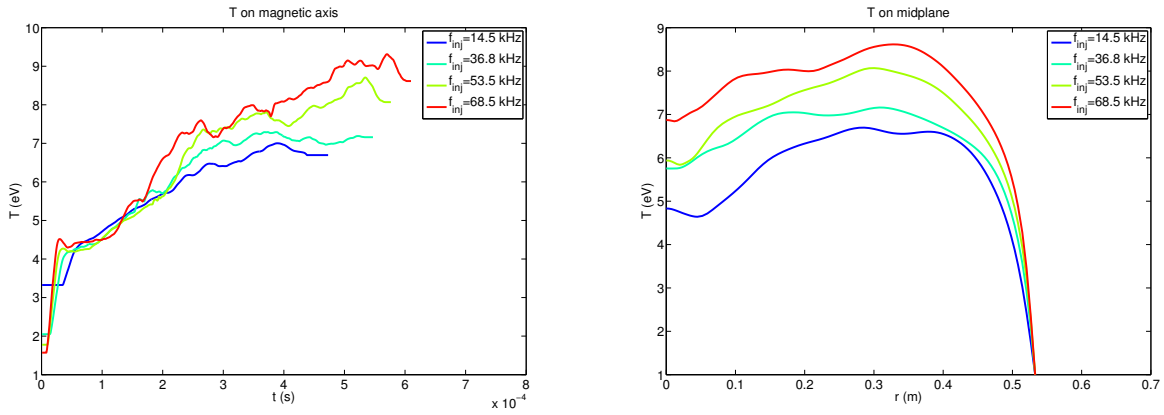

Figure 3.24: Plotted are (left) the values of T on magnetic axis and (right) the midplane T profile during the sustainment phase of the formation set of simulations. As can be seen T increases with f_{inj} which corresponds to increased β and current gain.

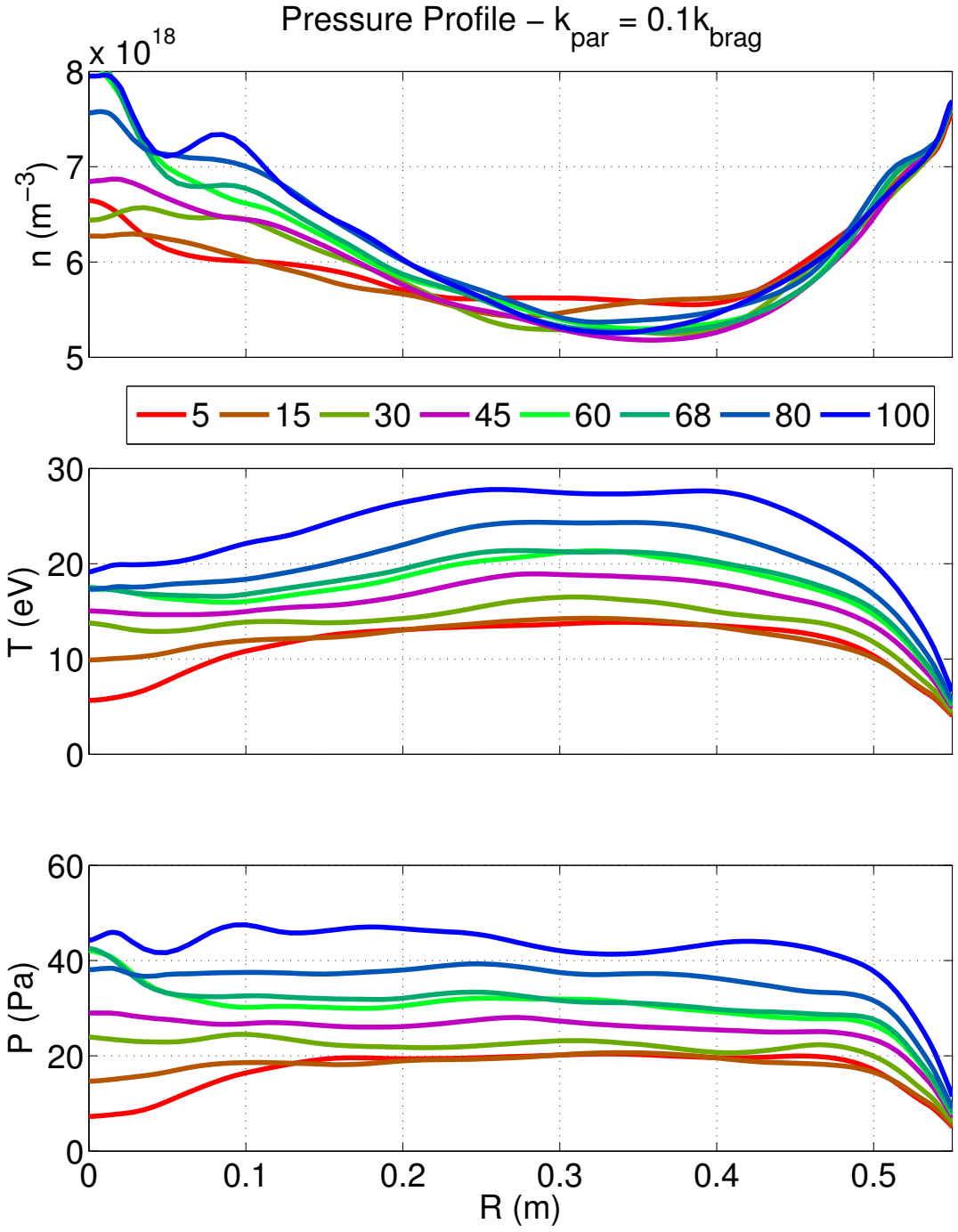

Figure 3.25: Toroidally and temporally averaged density, temperature, and pressure profiles along the midplane.

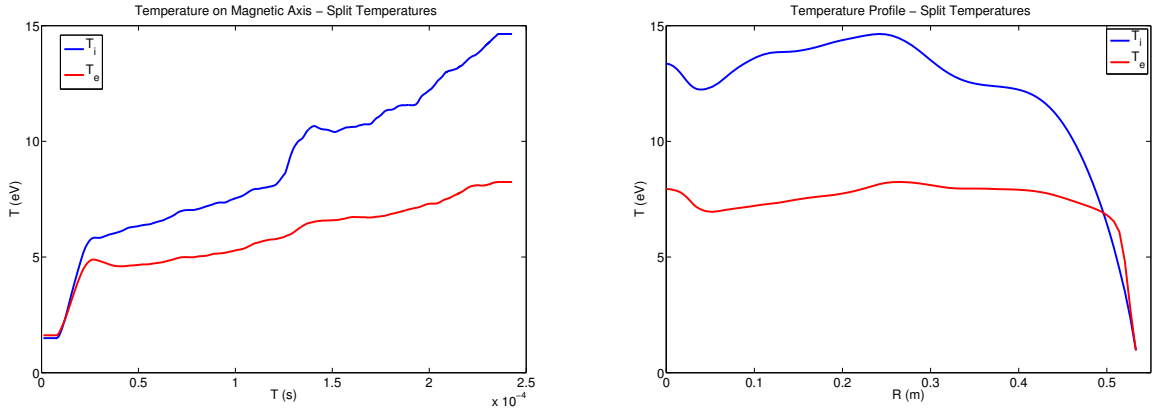

Figure 3.26: Time and spatial evolution of T_i and T_e. We see that $T_i \approx 2T_e$ which is expected. The large growth in T_i is during the relaxation event and thought to be reconnection heating.

3.3.5 Flow Velocities

The ion flow velocities of the plasma serve as a useful tool to validate our modeling of $\vec{V}$. Using the Ion Doppler Spectroscopy (IDS) diagnostic [18], the experiment was able to measure the motion of the spheromak, which moved back and forth in the confinement region at f_{inj}. Hossack [18] found the flow oscillations at f_{inj} demonstrated coherent motion of the plasma inside a region that was consistent with a equilibrium in motion in the region. Unfortunately, the flow oscillation measurements were unable to be taken at $f_{inj} > 36$ kHz, as the experimental diagnostic was unable to collect enough light at higher frequencies. We are able to compare with the IDS diagnostic through chord-averaging our $\vec{V}$ field along the line of sight of the chord, where we assume the intensity of each point along our chord goes as n^2.

All comparisons with experimental results use shot 129499, the primary shot studied in Hossack's dissertation. Beginning from chord-averaged velocity measurements, seen in Fig. 3.31, we can calculate the plasma displacement as a function of time as $x = \int V \mathrm{d}t$. Next, this displacement is decomposed into a Fourier series in time, with the component at $f = f_{inj}$ being the main point of interest. Finally, finding the complex angle of the Fourier

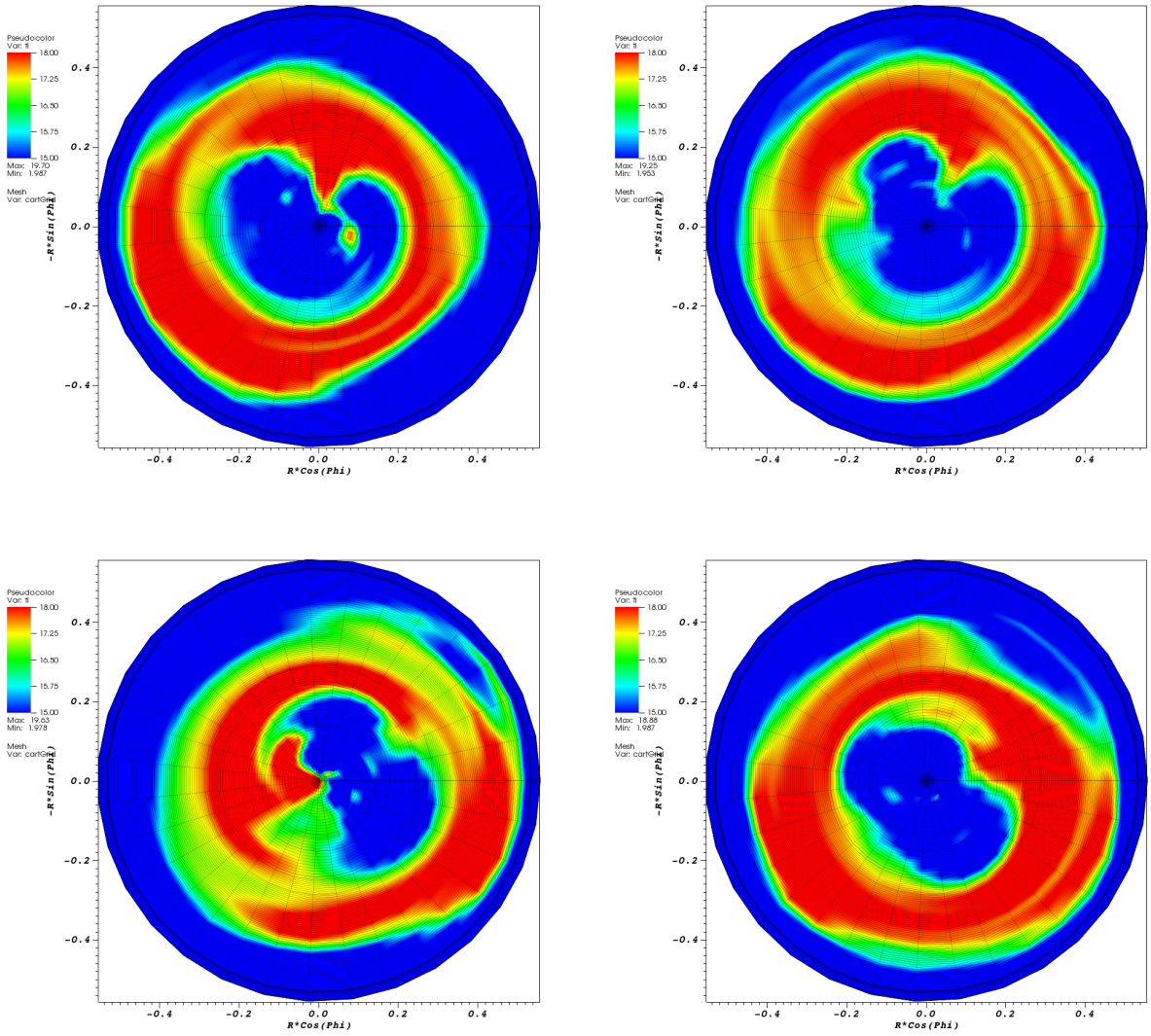

Figure 3.27: Pseudocolor plots of T on the midplane taken at 4 different snapshots during an injector cycle, going from left to right, top to bottom. It can be seen that the warm torus mapped out by the temperature has a geometric center that moves back and forth through the volume. In the top left, the spheromak begins located on the left side of the image, but a half-cycle layer (the bottom left image) it has moved to the right side of the image.

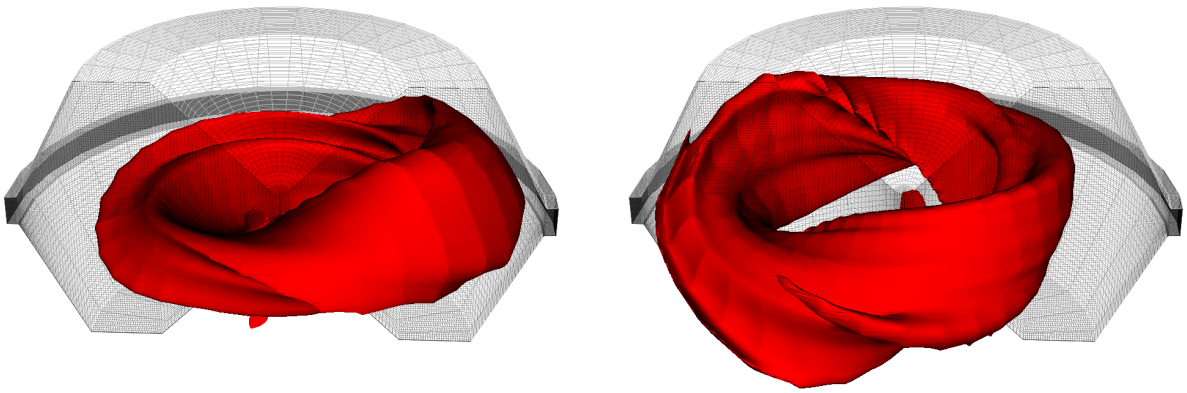

Figure 3.28: Full 3-D views of the $T = 17.5$ eV contour from Fig. 3.27. On the right one can see small filaments of hot temperature which look to follow the injector current path.

component at f_{inj} provides us with the temporal phase of motion along the given chord. The results of these for 4 different simulations and an experimental discharge are seen in Fig. 3.32. Comparing these phases we see that the edge and core of the plasma both exist as regions with constant phase, with a 180° phase shift between them. The NIMROD results, interestingly do not always see the phase shift at the location of the presumed separatrix as the experiment does at low frequency, instead seeing coherent motion through the entire volume. The high-frequency NIMROD results, however, do see the phase transition.

We notice that the phase of the oscillations is strongly dependent on the pressure model used, with the three different models seeing large differences. Additionally, in Fig. 3.31, we see that the zero-β model has strong flow oscillations near the edge of the plasma, while the finite-β simulations do not. These are indicative that properly modeling the pressure is key to correctly modeling the flow evolution, and in turn correctly evaluating the entire system.

Finally, in Hossack's work, a set of simulations performed early on in this work were compared and found not to have agreement with the experimental measurement of coherent

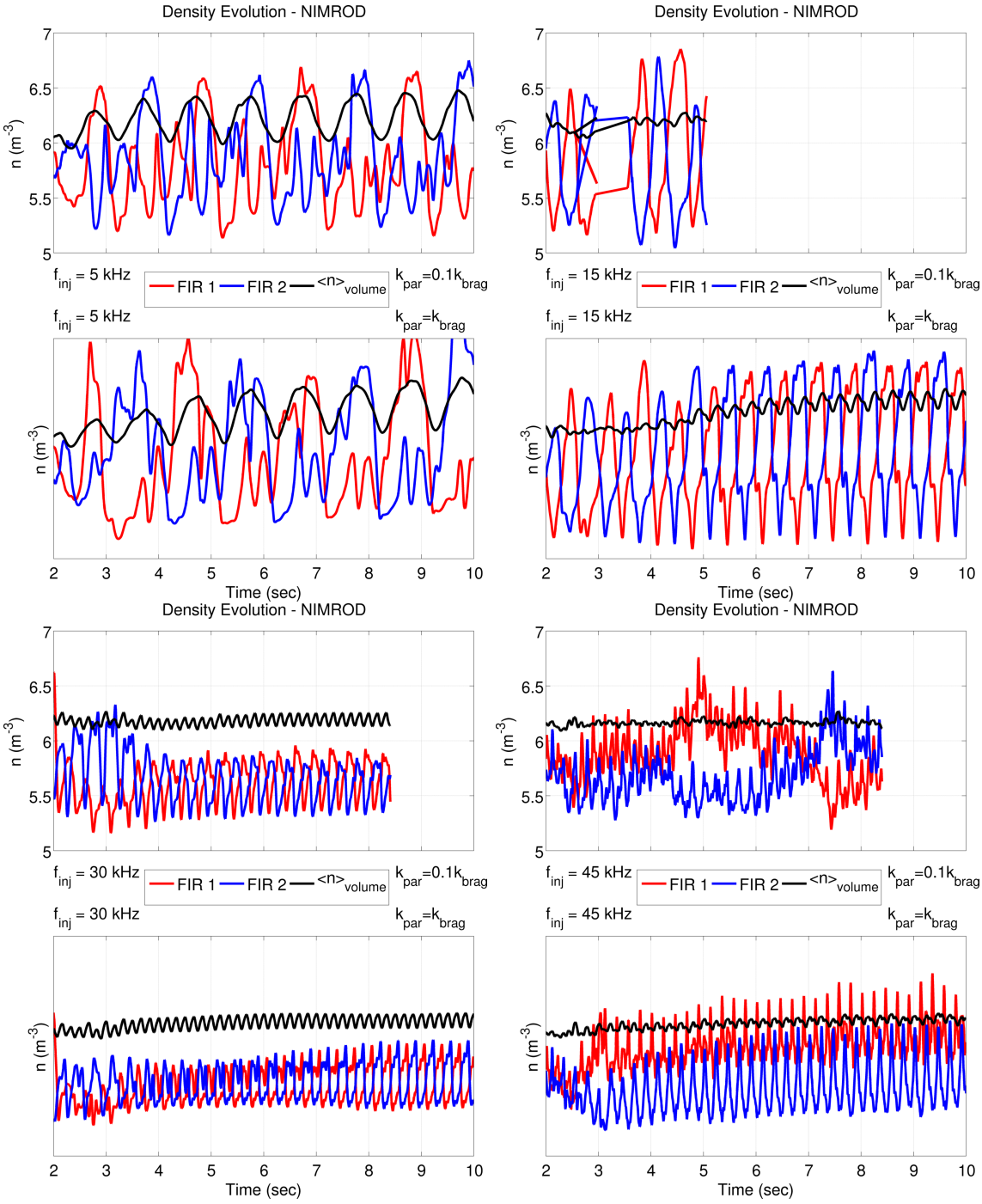

Figure 3.29: Density evolution for the lower f_{inj} simulations. The first FIR signal is a line-averaged density on an equivalent chord as the experimental measurement while the second signal is located toroidally 180° away to show $n = 1$ activity. The volume-averaged density is larger than the mean interferometer measurement in all cases.

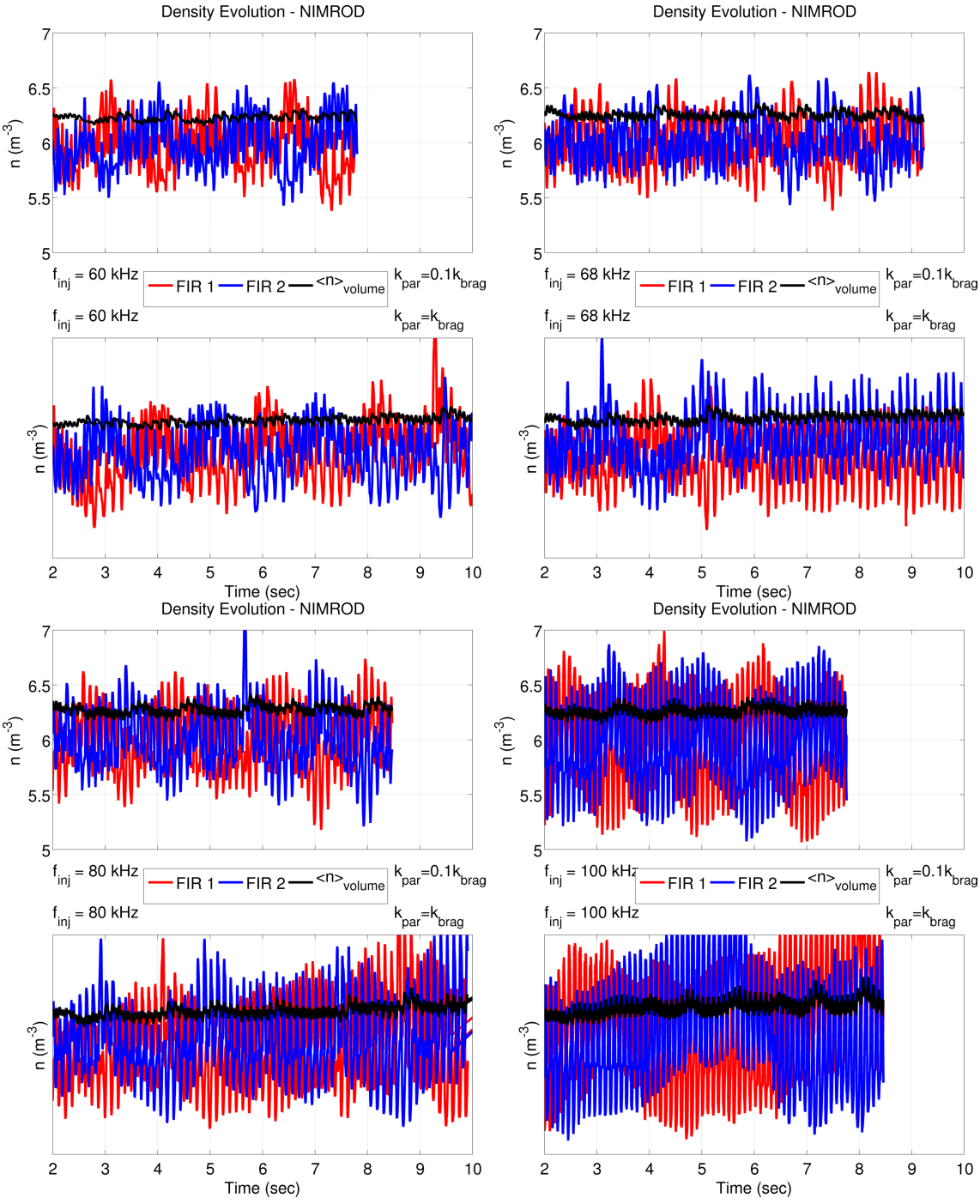

Figure 3.30: Density evolution for the high f_{inj} simulations. The first FIR signal is a line-averaged density on an equivalent chord as the experimental measurement while the second signal is located toroidally 180° away to show $n = 1$ activity. The volume-averaged density is larger than the mean interferometer measurement in all cases.

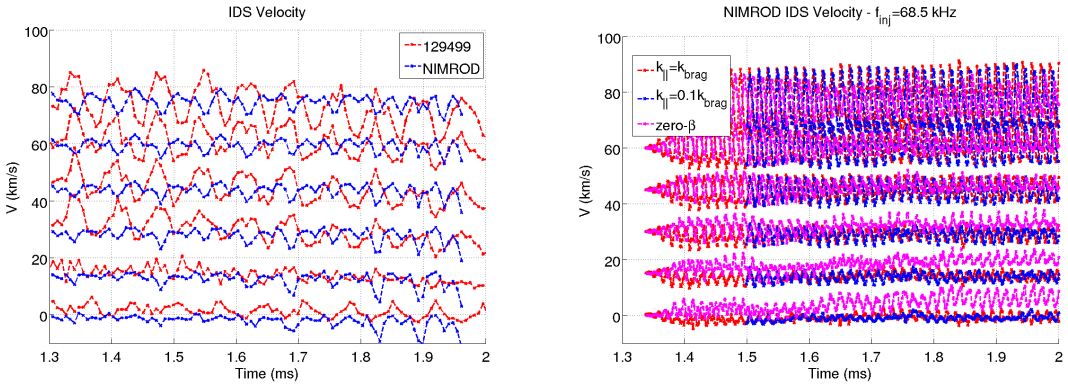

Figure 3.31: Flow velocity at different impact parameters. From bottom to top, the impact parameters are 9.3, 14.9, 20.4, 25.6, 30.5, and 35.1 cm. On the left is the experimental and NIMROD measurement from a typical $\sim$ 70 kA discharge and on the right are the three $f_{inj} = 68.5$ kHz simulations with gain above 3.

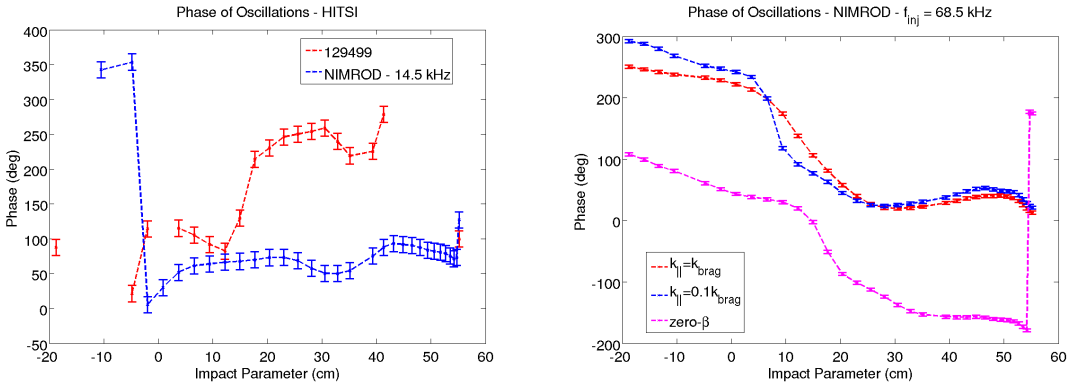

Figure 3.32: Temporal phase of displacement at different impact parameters. On the left is the experimental and NIMROD measurement from a typical $\sim$ 70 kA discharge and on the right are the three $f_{inj} = 68.5$ kHz simulations with gain above 3.

motion. These simulations were found later to have an error in their usage of thermal conduction coefficients, and as such have not been included in this work.

3.4 Biorthogonal Decomposition Comparison

Using the metrics as described in Chapter 2, we can use the Biorthogonal Decomposition (BD) metrics to compare the validity of the simulations at capturing experimental results. Taking 5 simulations at $f_{inj} = 68.5$ kHz, one with zero-β, one using the isothermal electron model, and three using single temperatures with modifications to thermal conduction and particle diffusivity, we look at the BD metric compared over a set of 10 injector cycles during the steady-state sustainment period of the discharge. Table 3.2 shows the results of these comparisons, where we see that while the zero-β model is effective at controlling the energy in the volume through having direct control over the resistivity, the finite-β models tend to be better at capturing the magnetic profile of the system. It is pleasing to note that the most physically realistic model, with the least artificial particle diffusivity and using Braginskii thermal conduction coefficients, is the closest to getting agreement with the experimental results. Because the single-T model is successful at matching the toroidal symmetry and the isothermal electron model is successful at matching the outward shift of the magnetic axis, our expectation is that successfully completed two-temperature models would see the best agreement.

We can additionally look at the role of pressure gradients in the individual correlations which make up the total Y metric. Fig. 3.33 shows us that there is little difference between zero-β and finite-β simulations at $f_{inj} = 14.5$ kHz. At $f_{inj} = 68.5$ kHz, however, the zero-β model swaps the structures of the 2^{nd} and 3^{rd} modes, while the finite-β model correctly captures their order in amplitude space. Since these modes are distinct, with geometric asymmetries of the probe location causing the splitting, swapped agreement between these is indicative of inaccuracies in the zero-β model.

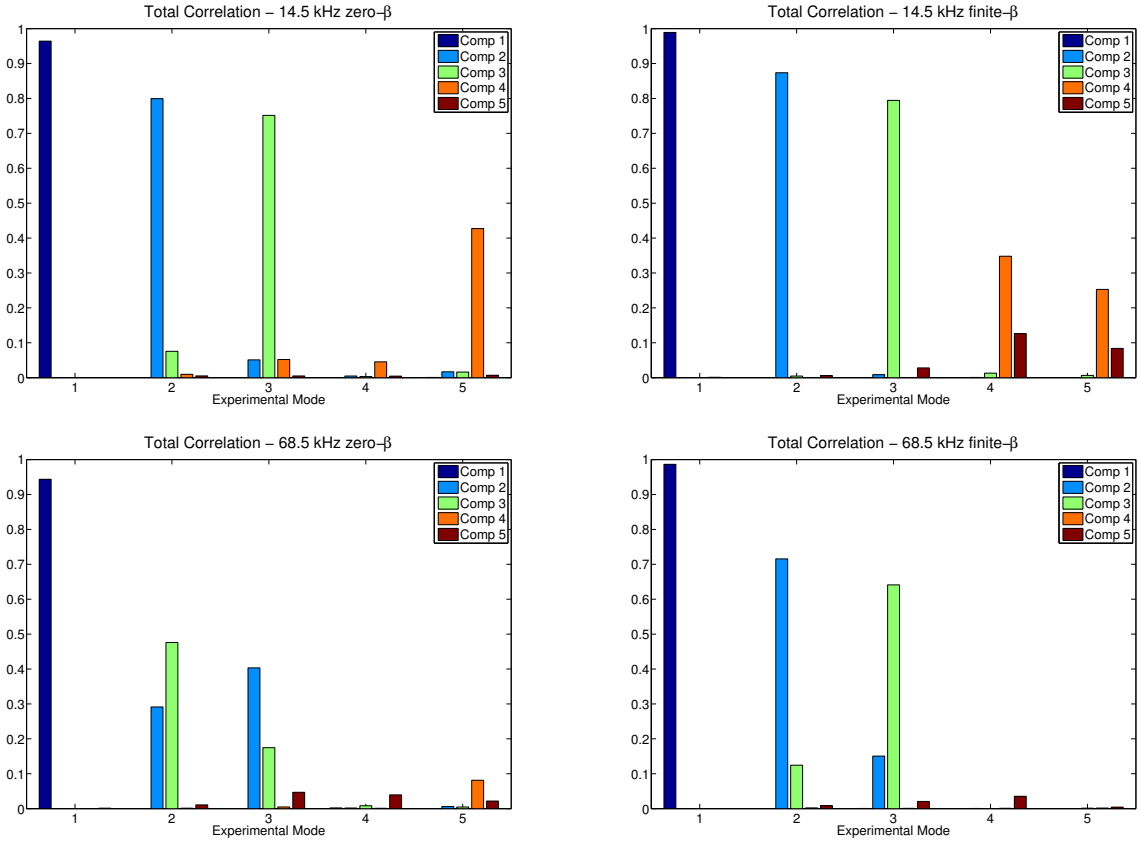

(a) Zero-β (b) Finite-β

Figure 3.33: At low f_{inj} the BD metrics show similar agreement with both the zero and finite-β models, at high f_{inj} the agreement between modes 2 and 3 is improved significantly with the finite-β model.

BD Comparison, $f_{inj} = 68.5$ kHz

Model	$\langle B^2 \rangle$ (10^{-4})	Y_{topo}	Y_{chrono}	Y_{mean}
Exp. Shot 129175	2.27	0.915	0.91	0.913
Zero-β	2.23	0.882	0.850	0.866
Isothermal $T_e = 13$ eV, $D = 1000$ m^{-2}/s	1.5	0.907	0.847	0.877
Single-T, $D = 1000$ m^{-2}/s, $k_{\|\|} = k_{braginskii}$	0.83	0.91	0.848	0.869
Single-T, $D = 250$ m^{-2}/s, $k_{\|\|} = k_{braginskii}$	2.05	0.907	0.883	0.895
Single-T, $D = 250$ m^{-2}/s, $k_{\|\|} = 0.1k_{braginskii}$	2.65	0.874	0.854	0.864

Table 3.2: The $\langle B^2 \rangle$ metric from Eq. 2.15 applied to a set of simulations. The experimental values of Y are typical values from a set of four similar discharges: 129173, 129177, 129191, and 129195.

3.5 Current Driving Terms

As was seen in Fig. 3.15, the plasma β increases with f_{inj}. Looking at the n and T profiles that make up this pressure, seen in Fig. 3.25, we notice that gradients go in opposite directions, creating a largely flat pressure profile. The temperature profile is a result of the majority of thermal losses happening near the edge of the plasma and a similar amount of heating ($\sim \eta J^2$) occurring throughout the entire volume, so the plasma is hotter farther away from the wall.

Of important note, we see that in almost every case the temperature is warmer in almost the entire volume than the assumed temperature for the zero-β cases ($T_e = 12$ eV), and hence are operating at a lower resistivity. Since the zero-β simulations see the current gain increase at $I_{tor}/I_{inj} \sim T^{0.9}$ [33], the expectation would be that these simulations, particularly the high f_{inj} with more than a factor of 2 increase in temperature, should see much higher gain than the zero-β cases. Surprisingly, this scaling with temperature appears to not be the case in

the zero-β simulations, as seen in Fig. 3.12, indicating that some portion of the finite-β model, most likely pressure gradients, is inhibiting the current drive of the spheromak.

Looking at our generalized Ohm's law in Eq. 2.4 we note that there are two places for pressure gradients to interact with the electric current, the dynamo ($\vec{E}_{dyn} = -\vec{V} \times \vec{B}$) and diamagnetic ($\vec{E}_{dia} = -\frac{1}{ne}\nabla P_e$) terms. To quantify the differences between zero and finite β simulations, we can calculate the axisymmetric current-driving power from the different components of Ohm's law:

$$P_0 = \int \vec{E} \cdot \vec{J}_0 \mathrm{d}^3x = \int \left(\underbrace{\eta \vec{J} \cdot \vec{J}_0}_{P_{Res}} - \underbrace{(\vec{V} \times \vec{B} \cdot J_0)}_{P_{Dyn}} + \underbrace{\frac{1}{ne}(\vec{J} \times \vec{B}) \cdot \vec{J}_0}_{P_{Hall}} + \underbrace{\frac{1}{ne}\nabla P_e \cdot \vec{J}_0}_{P_{Dia}} \right) \mathrm{d}^3x \quad (3.2)$$

The current driving-portion of $\vec{E}$ is expected to be generated through the two dynamo terms, with the resistive term balancing the drive. The diamagnetic term is expected to be small, with pressure gradients primarily perpendicular to $\vec{B}$ and $\vec{J}$ forming due to the anisotropic thermal conduction. Figure 3.34 shows the time traces of these terms during a typical simulation, where we note the diamagnetic term is indeed small.

Figure 3.35 shows the comparisons of the dynamo terms for the three different types of simulations. Two main observations become immediately apparent, with differences seen based on both f_{inj} and the pressure model used. While at low frequencies both terms combine to each drive current, we see that at the higher frequencies the two terms get significantly larger, but one changes sign so that the sum is a similar amount of total current driving power. The big difference between zero-β and finite-β models becomes clear, where the zero-β simulations see current drive through $\vec{V} \times \vec{B}$ and the finite-β simulations seeing the drive through the Hall term. This is a very surprising result and tells us that there are clear differences in the way that the injector fields interact with the spheromak based on the pressure model used.

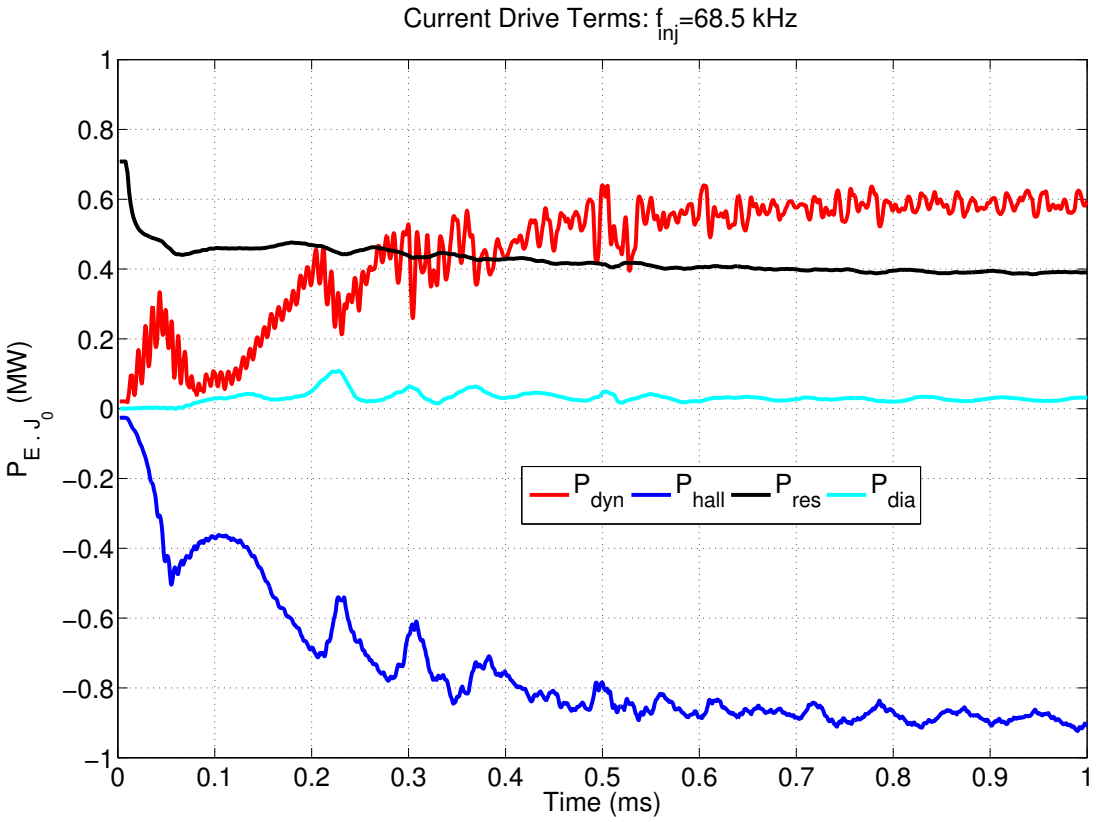

Figure 3.34: The four terms in Eq. 3.2 for $f_{inj} = 68.5$ kHz. As the spheromak decays and approaches steady-state behavior where the sum of all terms is zero, with positive terms dissipating current and negative terms driving current. In this case, the Hall term is driving the toroidal current while the MHD dynamo term is actually anti-driving current. The diamagnetic term is small, as most pressure gradients are perpendicular to $\vec{J}$.

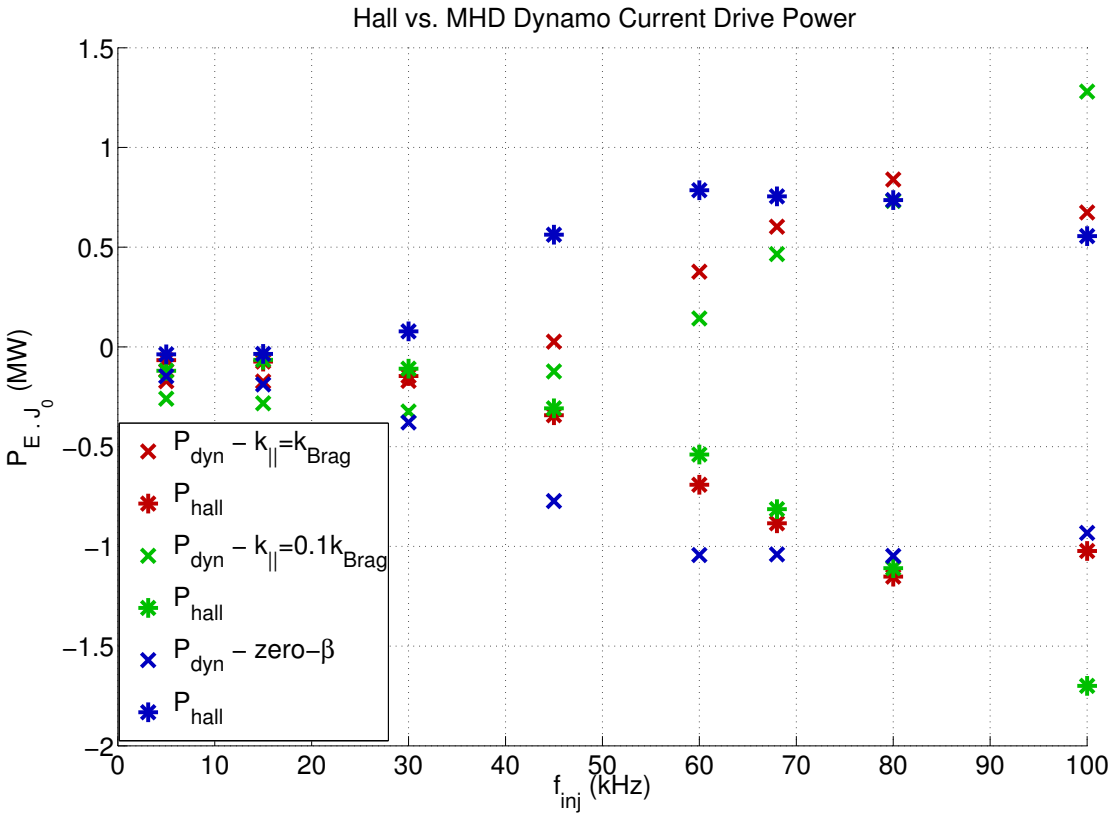

Figure 3.35: The volume integrated current drive powers for the two dynamo terms in Eq. 3.2. Each color represents a different pressure model of injector frequency scan and each symbol is either the $\vec{V} \times \vec{B}$ (P_{dyn}) or $\vec{J} \times \vec{B}$ (P_{hall}) related term. Note negative values are driving current, while positive values are anti-driving current. The two terms become larger but cancel out at high frequencies, but the signs of the terms flip with the introduction of pressure gradients.

3.6 Injector Impedance

The injector plasma impedance ($Z_{inj} = V_{inj}/I_{inj}$) accounts for the most significant observed quantity with a dependence on f_{inj}, making it a useful quantity for validation of the model. The IDCD model [23, 24] serves as a good model to describe the experimental behavior for comparisons. Noting equation 6 in [23]:

$$I_{inj}^2 = 8\pi a^3 ne \left[\frac{I_{tor}}{\tau_{L/R}} + \dot{I}_{tor} \right]. \tag{3.3}$$

We can use a power balance model to express the energy balance inside the spheromak as:

$$\epsilon V_{inj} I_{inj} = 2 \left[\frac{L_{sph} I_{tor}^2}{\tau_{L/R}} + \frac{1}{2} \frac{\mathrm{d}}{\mathrm{d}t} \left(L_{sph} I_{tor}^2 + L_{inj} I_{inj}^2 \right) \right] \tag{3.4}$$

where the left-hand side is the injected power and the right-hand side is the resistive and inductive losses. Using $L = \frac{\mu_0 R}{2}$ as the inductance of a plasma and $I_{inj} \propto sin(\omega_{inj} t)$, we can rearrange this as:

$$V_{inj} I_{inj} = \frac{\mu_0 R_0}{\epsilon} I_{tor} \left[\frac{I_{tor}}{\tau_{L/R}} + \dot{I}_{tor} \right] + \frac{\mu_0 R_{inj}}{\epsilon} \omega_{inj} I_{inj}^2. \tag{3.5}$$

Dividing both sides by equation 3.3, we obtain:

$$Z_{inj} = \frac{V_{inj}}{I_{inj}} = \frac{\mu_0}{\epsilon} \left[\frac{R_0}{8\pi a^3 e} \frac{I_{tor}}{n} + R_{inj} \omega_{inj} \right]. \tag{3.6}$$

The quantity $\epsilon = \frac{\lambda_{sph}}{\lambda_{inj}} = \frac{R_{inj}}{R_0}$ is the efficiency of the helicity injection. We can then simplify to an expression of the injector impedance:

$$Z_{inj} = \mu_0 R_0 \left[\frac{1}{8\pi a^3 e} \frac{\lambda_{inj}}{\lambda_{sph}} \frac{I_{tor}}{n} + \omega_{inj} \right]. \tag{3.7}$$

We notice that there are two terms of interest, with linear dependence in both I_{tor}/n and ω_{inj}. The I_{tor}/n term can be thought of as a damping force that the edge perturbation currents, which are driven directly by the injector, experience as they drive current in the

spheromak. The ω_{inj} term can be thought of as the injector forming a complete magnetic equilibrium and injecting the entire object into the confinement region twice per injector cycle. This model is found to agree fairly well with experimental results [23, 24] and forms the basis of our comparing the accuracy of the energy transfer mechanism between the non-axisymmetric perturbation and the spheromak in the simulations.

Due to the fact that the injectors are treated as boundary conditions in the simulation, with the magnitude of $\vec{E}_{\|}$ on the surface being scaled to match a specific I_{inj}, we use a power balance model to extract the injector impedance. Using our Ohm's law to calculate the time-derivative of the magnetic energy:

$$\frac{\mathrm{d}W_B}{\mathrm{d}t} = P_{inj} - \int \vec{E} \cdot \vec{J} \mathrm{d}V. \tag{3.8}$$

Because we know $W_B = \int \frac{1}{2\mu_0} B^2 \mathrm{d}V$, $\vec{J} = \frac{1}{\mu_0} \nabla \times B$, and $\vec{E}$ from Ohm's law directly, we are able to calculate the injector power from the output of the simulations. Similarly, since we also know I_{inj} we are able to extract both

$$V_{inj} = \frac{P_{inj}}{I_{inj}}, \text{and}$$

$$Z_{inj} = \frac{P_{inj}}{I_{inj}^2}$$

The reason we use this method instead of directly calculating $\int \frac{1}{\mu_0} \vec{B} \times \vec{E} \cdot \mathrm{d}\vec{s}$ on the surface concerns the high-resistivity edge layer present in the simulation. A much larger potential is applied in order to drive the injector current ($V_{edge} \sim 10$ kV) through that layer than is needed to drive the current throughout the rest of the volume ($V_{inj} \sim 500$ V). This power balance model allows us to isolate just the injector power that makes it inside the 'plasma-portion' of the volume.

Computing these from the simulations we immediately see that both of these linear dependencies are captured by the model, though with varying degrees of agreement. Taking Eq. 3.7 and adding fitting coefficients to account for geometric details that are neglected in

the derivation, we can fit the impedance measured to:

$$Z_{inj} = \mu_0 R_0 C_1 \left[\frac{1}{8\pi a^3 e} \frac{\lambda_{inj}}{\lambda_{sph}} \frac{I_{tor}}{n} + C_2 \omega_{inj} \right] \tag{3.9}$$

where both C_1 and C_2 should be of order 1. Experimental results from reference [24] give $C_1 = 0.8$ and $C_2 = 1.1$. Fits to the simulation data, from all 24 sustainment simulations performed, give $C_1 = -0.06$ and $C_2 = -3$, indicating that while seeing the proper trend for the ω_{inj} dependence, the j/n dependence is not accurately resolved. Figure 3.36 shows the Z_{inj} obtained from the simulations. The cause of this disagreement is most likely from incorrect modeling of the plasma density due to the artificial diffusivity.

Similar to the injector power increasing linearly with f_{inj}, the kinetic energy similarly increases. Figure 3.37 shows the amount of kinetic energy seen in each simulation. At all frequencies, this kinetic energy is largely focused in the $n = 1$ component of the flow velocity and corresponds to the motion the injector perturbations impose on the plasma. This is consistent with the IDCD picture of HIT-SI, which includes a central stable equilibrium (the spheromak) being pushed at f_{inj}. If the displacement distance is the same, then an increase in f_{inj} will increase the velocity with which this equilibrium moves throughout the volume.

3.7 High f_{inj} instabilities

As seen in the bulk evolution of the sustainment simulations, all simulations see primarily oscillations at f_{inj}. In the high-f_{inj} cases, oscillations at a much lower frequency, typically 5–10 kHz, are also observed. Similar oscillations are seen on high-f_{inj} experimental discharges, as we saw in Fig. 3.4. We will discuss three possible explanations for this activity.

As our magnetic signal of this activity shows up primarily in $n = 2$ modal activity, the first possibility involves $n = 2$ kink instabilities. Equilibrium reconstructions of shot 129175 showed that just prior to the activity, the q profile drops below 1/2 which is the typical threshold for stability to an $n = 2$ kink mode. This was the conclusion reached in the Victor paper [15], though improved sampling in the NIMROD simulation lends doubt to what the q profile actually is. As we saw earlier, q_{axis} could be somewhere between 0.7 and 1.2 in

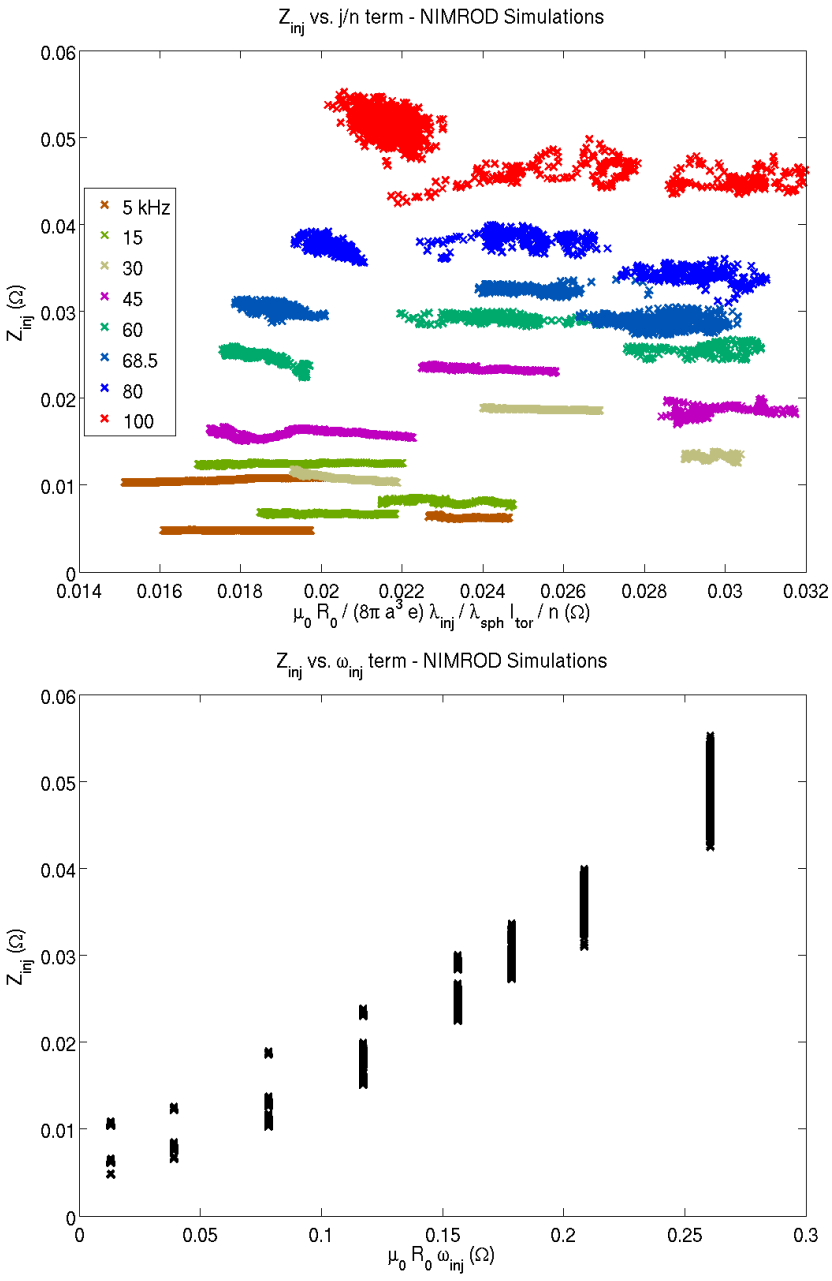

Figure 3.36: The injector impedance vs. both I_{tor}/n and ω_{inj} from simulation results. A linear dependence is expected on both plots, and we see the frequency dependence is close.

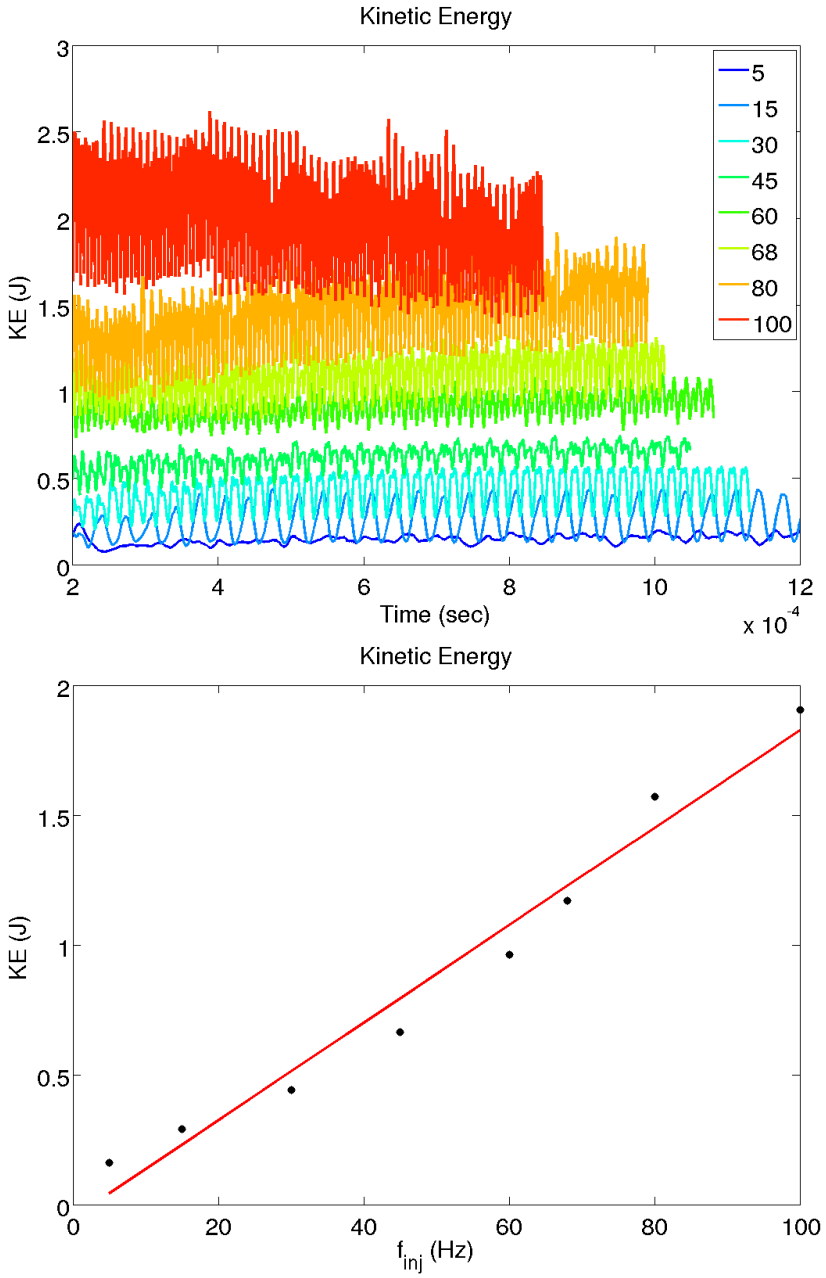

Figure 3.37: Upper: time traces of the kinetic energy of the plasma during the sustainment period, which can be seen to oscillate at f_{inj} with a mean value. Lower: the mean kinetic energy at each f_{inj}.

a NIMROD simulation, adding to the uncertainty of what the experimental measurement meant. To identify whether the $n = 2$ activity seen on the surface magnetic probes is associated with the equilibrium or some external instability, an analysis performed in [15] subtracted the injector dominated modes from the probe measurement and reconstructed the mode structure. It was found that at low f_{inj}, most of the $n = 2$ activity is associated with the equilibrium fields and $n = 1$ activity is associated with the injector fields. We find the same is true on the simulation results, as seen in Fig. 3.38 and 3.39.

Our second explanation involves the $n = 2$ activity that was seen during formation of the equilibrium. As we saw when looking at the relaxation dynamics, the minimum energy state of the plasma during the injector-dominated portion of the discharge is dependent on the injector frequency. A possibility is that a state similar to this is being driven for a short while, before undergoing another relaxation event to add energy to the spheromak state. This can be thought of as injector flux tubes being injected into the volume at the injector frequency, but only relaxing into the spheromak at a slower rate.

The final possibility is pressure-driven activity. As we saw from comparisons to experimental results, pressure gradients are important for capturing the dynamics at high f_{inj}. This, coinciding with oscillations in both density and $\langle\beta\rangle_{vol}$ at this lower frequency being seen experimentally, indicate the plasma pressure is involved in this activity. More discussion of this possibility is given in the following section, as we describe possiblities for the increase in $\langle\beta\rangle_{vol}$.

3.8 Explanation for increased β

Three possibilities have been considered for the increased β observed at higher injector frequencies, which we see are related to one another. These are dynamic stabilization of pressure-driven instabilities, increased heating power from injector impedance, and reduced thermal losses from magnetic field lines more rapidly oscillating. The second two will be treated together, as they involve the total power balance of the system.

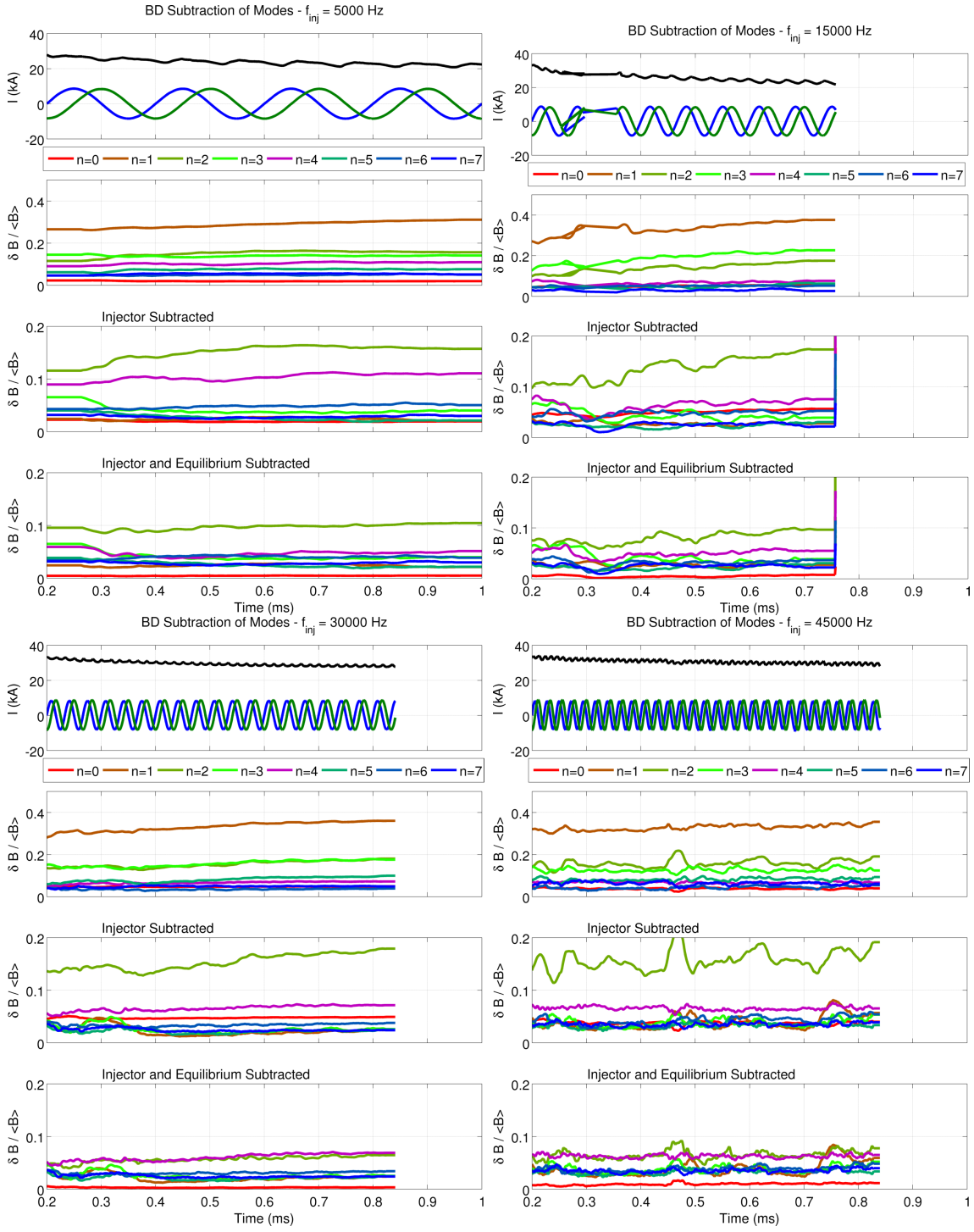

Figure 3.38: In each segment shown are: a) I_{tor} and I_{inj}, b) The modal activity from the midplane surface probes, c) The mode activity subtracting the injector BD modes, and d) the mode activity subtracting the injector and equilibrium modes.

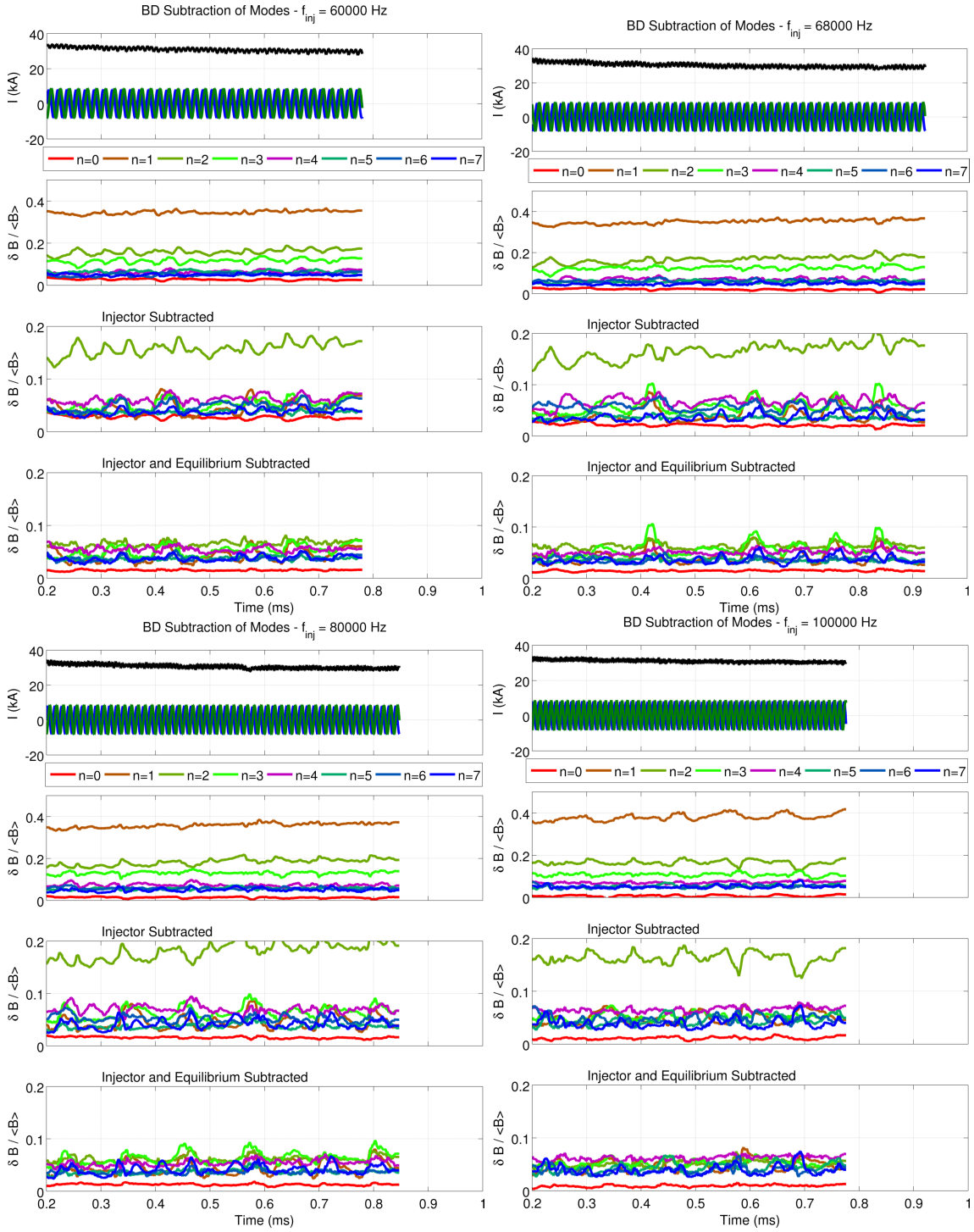

Figure 3.39: In each segment shown are: a) I_{tor} and I_{inj}, b) The modal activity from the midplane surface probes, c) The mode activity subtracting the injector BD modes, and d) the mode activity subtracting the injector and equilibrium modes.

3.8.1 Dynamic stabilization

Typically plasma pressure in spheromaks is observed to increase from Ohmic heating until β becomes greater than some stability limit, then a pressure-driven instability occurs which releases the contained pressure. An experimental example of such an event occurring is seen in decaying spheromaks created by the CTX experiment [43]. A possibility to explain the increased values of β that are seen in sustained HIT-SI discharges is dynamic stabilization. The applied perturbation from the injectors is sufficiently large that oscillating the perturbation faster than the growth rate of the instability may lead to stabilizing effects by preventing the conditions under which the instability is able to saturate. If this sort of stabilization was occurring, we would expect the β limit of a HIT-SI equilibrium to be set by the relationship between growth rates of these pressure-driven instabilities and the injector frequency.

Gautier [41] calculated the growth rate of these sorts of instabilities in an oblate geometry, similar to the HIT-SI bowtie shape, and found that a linear relationship $\gamma \propto \langle\beta\rangle_{vol}$. Interestingly, the value of β for the 'low-f_{inj}' cases, seen in simulations to be $\beta = 8\%$ and experimentally $\beta = 6\%$, aligns closely with the onset of these instabilities, with $\beta \sim 8\%$. Using a poloidal Alfvèn time of $\tau_A = 2\ \mu$s, we can evaluate the growth rates specific to the HIT-SI parameters. Comparing Fig. 3.40 with Fig. 3.15, we note the value of $\langle\beta\rangle_{vol}$ seen in low-f_{inj} simulations is near the value that the pressure instability begins to appear, with minor differences being from differences in the modeled equilibria. Once crossing the threshold frequency where stabilization begins to occur, possibly the sound transit time of the system, we then see the β observed increase linearly, much in the same way the growth rate does.

These growth rates are expected to be insensitive to the thermal conductivity of the plasma, leading to the expectation that if the β limit realized should be insensitive to the thermal conduction model used, as the excess pressure will be expelled from the system through convective and advective forces. This is in agreement with the β's observed in the two pressure models seen in Fig. 3.15, where the β's are similar between the two cases of

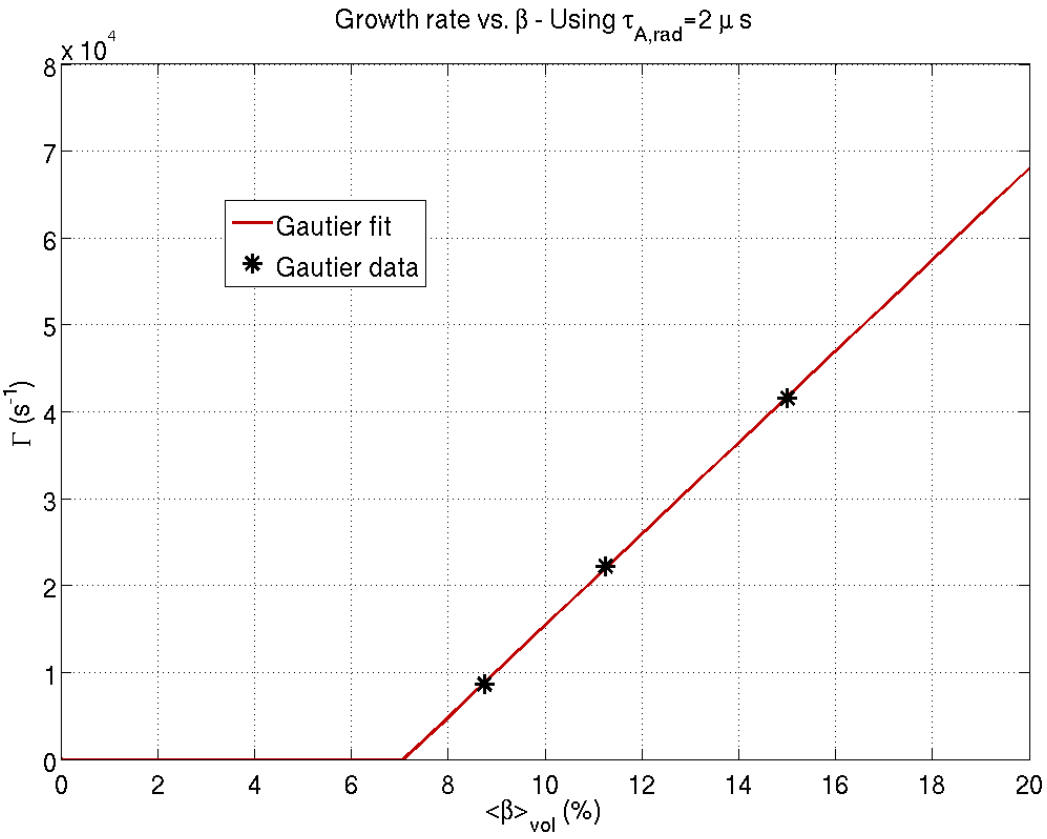

Figure 3.40: Growth rate of pressure driven instabilities vs. β for an oblate spheromak. Values are taken from [41].

parallel thermal conduction.

3.8.2 Power balance

As we saw previously, the injector impedance scales linearly with the injector frequency. This has the unfortunate consequence of changing multiple parameters when we vary only the frequency. Because these simulations opted to keep the injector current and flux fixed, the power injected increased linearly with f_{inj}. We noted earlier that this increases the current gain, but the question arises of how the thermal energy balance is affected. While the heating power is increased, both from larger viscous and Ohmic heating, the thermal losses would additionally be expected to change.

We can classify the power balance terms as three types: Ohmic and viscous heating terms (ηJ^2, $\nabla\vec{V} : \Pi$), thermal conduction to the injectors and wall ($\vec{q}$), and convective forces ($V \cdot \nabla T$). Looking at these individual terms in Fig. 3.41, we immediately notice that the viscous heating increases linearly with ω_{inj}, as expected from the change in kinetic energy. The displacement of the spheromak oscillating at f_{inj} remains a static distance, so increased frequency leads to higher velocities, which in turn lead to higher viscous forces acting on the plasma. This increased viscous heating is consistent with the observation from Hossack [18], where the ion temperature, which viscous heating preferentially targets, was significantly hotter in the high-f_{inj} discharges taken experimentally. The Ohmic heating increases at the higher frequencies in these simulations, as would be expected from driving larger currents and the injector power being generally larger.

Additionally, we notice that in the $k_{parallel} = k_{Braginskii}$ case, the thermal conduction losses nearly balance the heating power. This is in contrast to the $k_{parallel} = 0.1k_{braginskii}$ case where the heating power is significantly larger than the thermal conduction losses. The terms neglected from Fig. 3.41 are the convective and advective terms acting on the temperature, which in the lower parallel conduction case appears to be more important. One explanation for this is that pressure-driven instabilities discussed before are holding the plasma at the β limit, through the dynamic stabilization mentioned above.

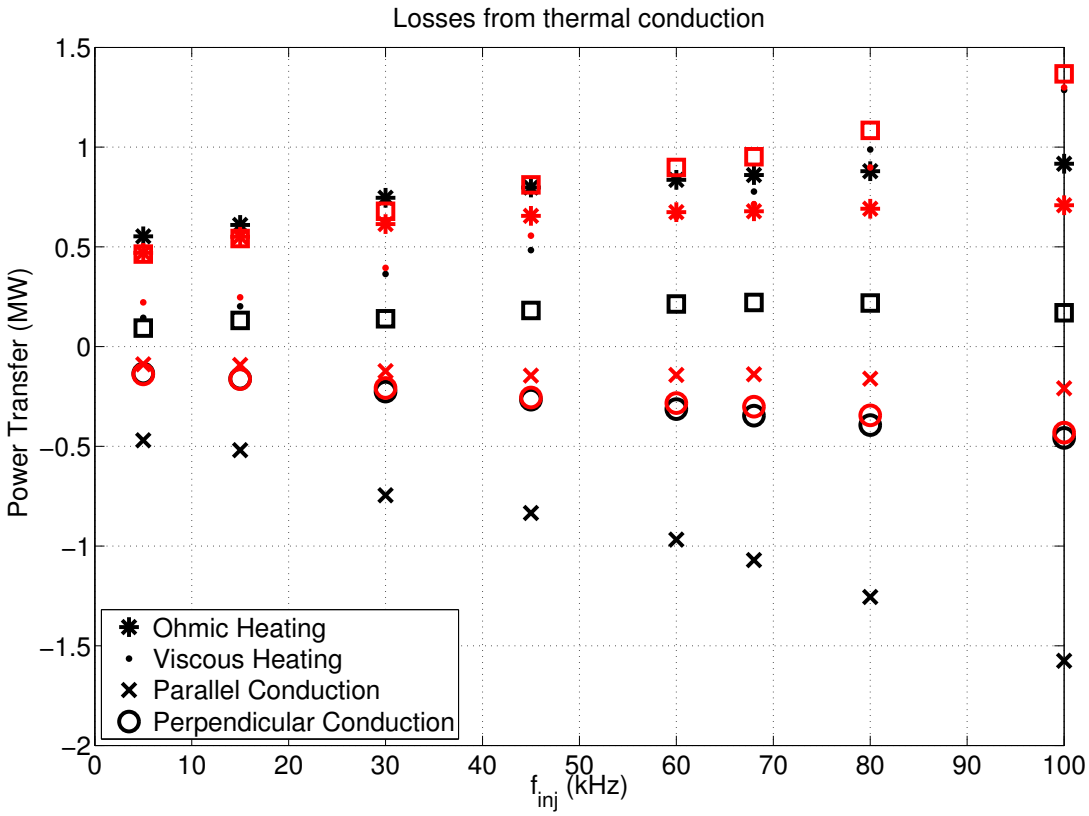

Figure 3.41: Heating power and thermal conduction losses in the plasma for the (black) $k_{\|} = k_{Braginskii}$ case and the (red) $k_{parallel} = 0.1k_{Braginskii}$ cases. The differences of the sum from zero are indicative of the thermal losses in the system through advective forces.

3.9 Limitations of models used

While the different finite-β models used are able to improve qualitative agreement with results seen experimentally, quantitative agreement has still not been achieved. The next step is to determine which physical processes, or terms in the equations, are likely to play an important role in capturing agreement. Unfortunately, the additions to the models that will be discussed in this section are currently too computationally difficult to implement successfully. We can divide these two types of improvements to the model into two groups, reduced artificial diffusivities and enhanced physics.

3.9.1 Reduced artificial diffusivities

There are three sources of artificial diffusivity in the model used: particle diffusivity, enhanced cross-field viscosity, and increased electron inertia. These diffusivities apply to the evolution of n, $\vec{V}$, and $\vec{B}$, respectively. We can quantify the influence of each term by comparing the magnitude of the unphysical behavior with the magnitude of the other terms in the advance.

For the particle evolution, Eq. 2.1, the comparison is simple. In our post-processing routines, we can calculate $D\nabla^2 n/(D\nabla^2 n + \nabla \cdot n\vec{V})$ to see what percentage of $\frac{\partial n}{\partial t}$ comes from the diffusivity. Unfortunately, even in our lowest-diffusivity runs ($D = 250$ m^2/s), the diffusion term is about a factor of four larger than the physical advection terms when we look at the average contribution. This is due to large local gradients that are created from the large perturbations caused by the injector fields. While the diffusion ends up being smaller than the advective terms in these regions of rapid change, simply damping the observed oscillations at f_{inj},

In the momentum evolution, Eq. 2.2, we artificially enhance the cross-field viscosity for numerical stability. Scans in particle viscosity performed thus far have focused on either the increase in isotropic viscosity or parallel viscosity. As seen in the HIT-SI3 studies, the parallel viscosity can either enhance or diminish the magnetic energy in the spheromak, depending on the style of perturbations applied.

As a stabilization tool for the Hall term in Ohm's law, Eq. 2.4, we artificially increase the electron mass in the electron inertia term. To determine whether this artificial electric field is inappropriately adding energy to the system, we can look at the different terms of $\int \vec{E} \cdot \vec{J} \mathrm{d}V$. As was shown in Akcay [33] and Hansen's [34] work, at low injector frequency a mass ratio $m_i/m_e = 36$ is sufficient to keep the magnitude of this term down, but at higher frequencies reduction of the electron mass is needed. We have found that mass ratios as large as $m_i/m_e = 200$ can be sufficient to stabilize the numerics, so scaling the electron mass according to the injector frequency being operated should be sufficient for modeling HIT-SI.

3.9.2 Enhanced physics

In the derivation of the two-fluid MHD model, a variety of terms are dropped due to being assumed smaller than the remaining terms. Most of these terms involve the evolution of the electron fluid, which the standard derivation of ideal-MHD assumes are massless. While we have shown earlier that both initial modeling and experimental evidence indicate that $T_i \sim 2T_e$ in HIT-SI, indicating that a two-temperature model is more appropriate, here we will look at two terms in the Ohm's law, electron viscosity and the full electron inertia.

The electron viscosity term expressed as an electric field is $\vec{E}_{visc} = \frac{-1}{ne} \nabla \cdot \left(\rho \nu_e \nabla (\frac{\vec{J}}{ne} + \vec{V}_i) \right)$. Commonly in numerical studies of reconnection physics, this term is used for numerical stability reasons and referred to as hyper-resistivity, though generally the dependence on n is removed and is cast simply as $\vec{E}_{hyp} = -\eta_H \nabla^2 \vec{J}$. We can approximate the magnitude of this term by calculating a realistic $\eta_H = \frac{m_e}{ne^2} \nu_e$ and comparing $\vec{E}_{hyp}$ to the other components of Ohm's law. If we assume that $\vec{J}$ is parallel to $\vec{B}$ ($\nabla \times \vec{J} = \lambda \vec{J}$) and quasineutrality ($\nabla \cdot \vec{J} = 0$), then we can use $\nabla^2 \vec{J} = -\lambda^2 \vec{J}$ to approximate the magnitude of this hyper-resistivity. We can evaluate the viscosity coefficient ν_e from Braginskii [36] using $\nu_e = 0.73 k T_e \tau_e / m_e$. Using $n_e = 10^{19}$ m^{-3}, $T_e = 10$ eV, and $B = 50$ mT, we obtain typical values of $\eta_{H,\parallel} = 5 \times 10^{-7} \frac{\mathrm{V}}{\mathrm{m}} \frac{\mathrm{m}^4}{\mathrm{A}}$. and $\eta_{H,\perp} = 5 \times 10^{-13} \frac{\mathrm{V}}{\mathrm{m}} \frac{\mathrm{m}^4}{\mathrm{A}}$. The perpendicular component is negligible when compared with the resistivity ($\frac{\eta_{H,\perp} \lambda^2}{\eta} = 4 \times 10^{-6}$), however the parallel component could be significant, with $\frac{\eta_{H,\parallel} \lambda^2}{\eta} = 4$. Unfortunately, it would be expected that

additional dissipation parallel to $\vec{J}$ would reduce the efficiency of the current drive, which is already under-valued in the simulations that have been performed. However, we also note that a full treatment of electron viscosity in the model would additionally include viscous heating, with a comparable magnitude of heating $\frac{\rho_e \nu_e \lambda^2 / n^2 e^2}{\eta} \sim 1$ as the Ohmic heating. The largely anisotropic nature of the viscosity, coupled with the fact that λ might not be appropriate for approximating the gradient scale length of $\vec{J}$ parallel to $\vec{B}$ in a case like HIT-SI, make it a topic that warrants future study.

While a partial electron inertia is used for numerical stability of the Hall term, the full version includes the convective component. This is cast as

$$\vec{E}_{electron\_inertia} = \frac{m_e}{ne^2}\left(\frac{\partial \vec{J}}{\partial t} + \nabla \cdot \left(\vec{J}\vec{V} + \vec{V}\vec{J}\right)\right).$$

We can estimate the ratio of the convective component to the temporal component of $\frac{\mathrm{d}\vec{V}_e}{\mathrm{d}t}$ to identify the importance of this term. Assuming that $\nabla \cdot \vec{J}\vec{V} \sim \lambda V J$ and that the dominant component of $\frac{\partial \vec{J}}{\partial t} \sim \omega_{inj}\vec{J}$, we can write the ratio of temporal component / convective component as $\frac{\omega_{inj}}{\lambda V}$. Assuming a typical velocity of $V = 10$ km/s, this ratio becomes 1 at $f_{inj} = 15.9$ kHz, and increases linearly with f_{inj}. Since the enhanced version of the temporal component has been shown to have little impact on the final solution, it would be expected that a physically realistic version of the electron convective term would also have little impact on the final solution.

3.10 Conclusions of f_{inj} studies

These studies have shown us that while we are seeing improvements on the ability to model HIT-SI, there is still more work to be done. The formation phase of a discharge is well modeled, with NIMROD accurately capturing the $n = 2$ intermediate state that forms in high-f_{inj} discharges. The sustainment phase of a discharge shows improvement, though several experimental measurements are not fully captured. The outward shift of the magnetic axis has a component that is related to finite-β effects, but the full shift seen experimentally is not captured. Additionally, the temperature that simulations require in order to capture

Experimental Observation	zero-β	Single T	Isothermal T_e	Split-T
Increased n=2 activity during relaxation	Yes	Yes	Yes	Yes
Increased gain	Yes	Yes	Yes	Yes
β increase	No	Yes	Yes	Yes
Increased toroidal symmetry	No	Yes	No	?
Outward shift of magnetic axis	No	No	Yes	Yes (?)
Low-frequency activity during sustainment	Yes	Yes	Yes	?
$Z_{inj} \sim f_{inj}$	Yes	Yes	Yes	?

Table 3.3: Listed are a set of experimental observations seen when the injector frequency f_{inj} is increased. Four different pressure models have been used to attempt to simulate these results, and their success is told through a yes or no statement. The two-temperature model (split-T) was unable to fully simulate the sustainment phase, so a statement cannot yet be made.

the current gains seen experimentally is much larger than that measured. Two improvements to the model would be the reduction of particle diffusivity and the full inclusion of electron temperature evolution.

Since we have performed simulations using several different pressure models, we can categorize the experimental observations seen and which models successfully see that effect. Table 3.3 summarizes these results, where we see that the full two-temperature model is the most likely to be successful in fully capturing a high-frequency discharge.

Chapter 4

VALIDATION OF SIMULATIONS OF HIT-SI3

The results and analysis presented in this chapter have also been published in a paper by the journal Physics of Plasmas [44]

HIT-SI3 is the presently operated device in the HIT lab. It shares the flux conserver shape and diagnostic set of HIT-SI, but differs primarily in the injector geometry. This chapter will begin with a description of the HIT-SI3 device before moving into the results of simulations that capture specific experimental discharges.

4.1 The HIT-SI3 Device

The injector geometry of HIT-SI3 is seen in Fig. 4.1. There are two primary differences with the injector geometry as compared with HIT-SI. The first is that all injectors have been moved to one side of the machine, in this case the top of the device. Second is that because there are now three injectors, the relative temporal phasing for constant helicity injection has changed. Three relative temporal phasings of the injectors have been studied to date, indicated in table 4.1.

ϕ_A	ϕ_B	ϕ_C	Constant $\dot{K}$
0°	120°	240°	Yes
0°	60°	120°	Yes
0°	0°	0°	No

Table 4.1: The relative injector phasing of the injector drive for the different phasings examined. Ψ_{inj} and V_{inj} are driven as sine waves of the form $f_{A,B,C}(t) = f_0 sin(\omega_{inj} t + \phi_{A,B,C})$.

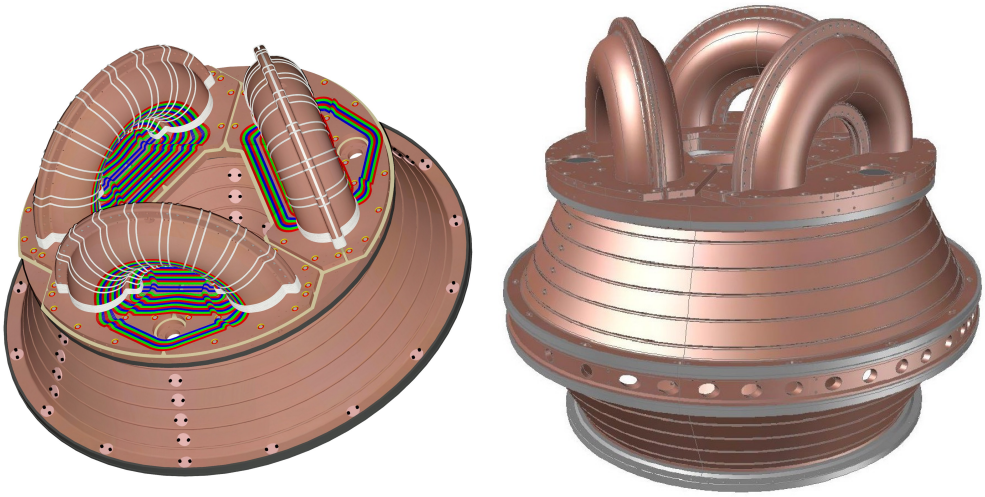

Figure 4.1: The HIT-SI3 injector geometry is installed on the same bow-tie shaped flux conserver volume that HIT-SI occupied. White coils drive injector flux while the colored coils drive the injector current. The spatial location of these injectors is the primary difference between HIT-SI and HIT-SI3.

As would be expected, operation of the injectors at these different phasings provide drastically different 3-D structures to the imposed perturbation in the confinement region. So far experimental efforts have focused on the study of these structures [45]. Additionally, by placing all injectors on one side of the device we can answer the question if a rotating perturbation imposes a rotation on the spheromak equilibrium.

4.2 Simulation Parameters

Simulations have been performed using an equivalent model to those used for HIT-SI, on the geometry seen in Fig. 4.2. As shown, the injectors are implemented in a similar way with an $\vec{E}_{tan}$ and $\vec{B}_{\perp}$ boundary condition determined from projecting injector equilibria onto the domain. We are able to reproduce an experimental discharge by driving the injectors with waveforms measured during a shot. This is accomplished by driving the injector current and

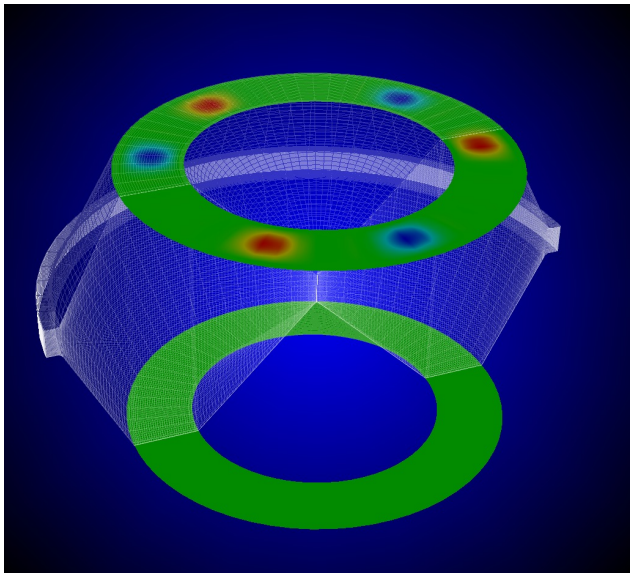

Figure 4.2: NIMROD mesh used for HIT-SI3 simulations. Because of the importance of correctly capturing the more complex toroidal mode spectrum of the injector drive, the diagnostic gap is added to the simulation domain. This gap is the location of the only toroidal mode probes on the experiment.

flux in the form of:

$$[\psi_{inj}, I_{inj}] = [\psi_0, I_0] f(t) cos(\omega_{inj} t + \delta\phi(t))$$

where f and $\delta\phi$ are piecewise linear functions, with one point per injector period. Figure 4.3 compares this drive to the actual measured experimental waveform.

A total of 9 simulations were performed, with 3 simulations performed at each injector phasing referenced in Tab. 4.1. These 3 simulations can be further divided based on the pressure and viscosity models used. Two of the simulations used the zero-β eMHD model previously used by Akcay [33] and Hansen [34, 35] to model HIT-SI. The zero-β model assumes that n, T, and p are all uniform in space and constant in time. These simulations were divided between the viscous model used, with one using an isotropic viscosity and the other using an anisotropic viscosity. Additionally, a simulation that allowed pressure

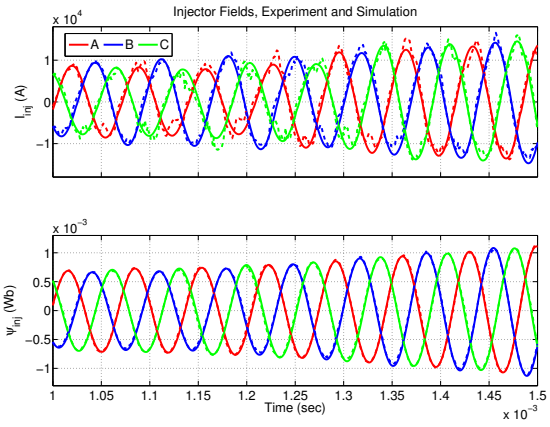

Figure 4.3: Comparison of the injector current (top) and flux (bottom) from the experiment (dashed lines) and simulation (solid). The deviations from sinusoidal shape in the injector currents is significant while the deviations in flux is small.

gradients to form was performed with the anisotropic viscosity model. The parameters for these simulations is shown in Tab. 4.2.

Similar to simulations of HIT-SI, several deviations from the desired needed to be made for numerical convenience. The electron mass, which appears only in the electron inertia term in the generalized Ohm's law, is enhanced to increase the numerical stability of the Hall term. An enhancement factor of 100 is used in this particular set of simulations.

Diffusion coefficients in the simulation are determined from several sources. An enhanced electron mass of $m_e = 9.1 \times 10^{-29}$ kg is used in the electron inertia term of Ohm's law for stability of the Hall term. The particle diffusivity $D = 1000$ m^2/s is used purely for numerical stability, as these simulations were performed before the technique of refueling via boundary conditions on $\vec{V}_\perp$ were realized for diffusion reduction. The resistivity $\eta = \eta_0 T^{-3/2}$, with $\eta_0 = 461$ $\mu\Omega$m, is determined from Spitzer assuming a constant $\log(\Lambda)$. In order to match the current gain more closely with the experiment, the zero-β models use $\eta = 10$ $\mu\Omega$m, corresponding with $T = 12.8$ eV. The viscosity values used are obtained from Braginskii [36] assuming plasma parameters late in the discharge. In the isotropic

Parameter	Simulation	Experiment
n_e (m^{-3})	2×10^{19}	4–8 $\times 10^{19}$
T_e (eV)	12	13 ± 7
T_{inj} (eV)	15	10–20
η/μ_0 (Spitzer) (m^2/s)	8.8	25–9
Viscosity ($\nu_\parallel$) (m^2/s)	3300	300–5000
Viscosity ($\nu_\perp$) (m^2/s)	300	100–500
f_{inj} (kHz)	14.5	14.5

Table 4.2: The parameters for simulations of HIT-SI3 are shown.

case, $\nu_\parallel = \nu_\perp = 300$ m^2/s, while in the anisotropic and finite-β cases $\nu_\parallel = 11\nu_\perp = 3300$ m^2/s. The thermal conductivity coefficients are determined from Braginskii [36] in the same method used by O'Bryan for similar modeling of the Pegasus experiment [31]. The cross-field heat flux is assumed to be dominated by the ion contribution while the parallel heat flux is dominated by the electron contribution. $k_\parallel$ is computed using the enhanced electron mass mentioned above, which has the result of damping $k_\parallel$ by a factor of $\sqrt{\frac{m_{e,physical}}{m_{e,simulation}}}$, which is $\frac{1}{10}$ in this case. Limited simulations using $m_{e,physical}$ have been performed but were insufficient for two reasons. First, the model becomes very stiff numerically because of the large non-axisymmetric fields present in the device ($\frac{\delta\vec{B}}{\vec{B}} \sim 25\%$), significantly increasing the computational time required. Second, due to chaotic field paths, a larger $k_\parallel$ transports excessive thermal energy to the edges of the chamber which leaves the volume. This leads to a colder ($T < 6$ eV) plasma, exhibiting a resistivity that is too large for a spheromak to form, disagreeing with the experimental results. As was observed by Akcay [38], the resistivity value needed to obtain agreement with experimental results is lower than would be expected from experimental electron temperatures, so these $T < 6$ eV results are consistent with the experiment in the temperature evolution, just not in the magnetic field evolution.

Analogous to the simulations of HIT-SI, a large resistivity is projected onto the outermost cell of the domain to impose the $\vec{J}_\perp = \vec{0}$ boundary condition as a pseudo-boundary condition.

Like HIT-SI, a discharge of HIT-SI3 consists of three main stages, which can be seen in Fig. 4.4. The first stage is the build-up of the non-axisymmetric injector-dominated state. While in HIT-SI this state was primarily $n = 1$ in structure, in HIT-SI3 the injector phasings determine the Fourier spectrum of this state. The second stage occurs once a threshold value in the energy of the injector state is met and a relaxation process begins to form the spheromak. The spheromak forms on a fast time scale relative to the L/R time of the plasma, reaching a current amplification of 1 within a few Alfvèn times. This formation event is a global reconnection event the occurs at the Sweet-Parker timescale, with the Lundquist number in the region being $100 < S < 1000$. Current filaments form connecting the different injectors together and induce these reconnection events, which play a role in the dynamics similar to those seen in CHI on NSTX [46, 47] or LHI on Pegasus [31]. Due to the 3-D and time-dependent nature of the injector fields, a more detailed study of the relaxation event on HIT-SI3 is a topic for future work and not discussed in this thesis. The third stage of the discharge is the slow growth and sustainment of the spheromak, eventually reaching a current amplification of between 2.5 and 3, depending on the parameters. Eventually, the third stage is ended by shutting off the injectors, marking the beginning of the decay stage of the spheromak. Figure 4.4 shows the evolution of these three stages for each injector phasing, where the differences in the applied non-axisymmetric perturbation can be clearly seen. We note that the magnetic energy spectrum in the volume does not match the perturbation spectrum that is applied at the boundary, seen in Figure 4.5, where the higher n modes tend to quickly combine into lower n structures, dominated by $n = 1, 2$, and 3. Figure 4.6 shows more about the sustained equilibrium, where we see that the poloidal flux profile of the axisymmetric component of the magnetic field forms a similar profile in each case, even with large differences in the perturbation spectra. Late in time spheromaks with Lundquist number $S \sim 10^4$ are observed.

The temperature evolution of the simulation expands further on the differences between

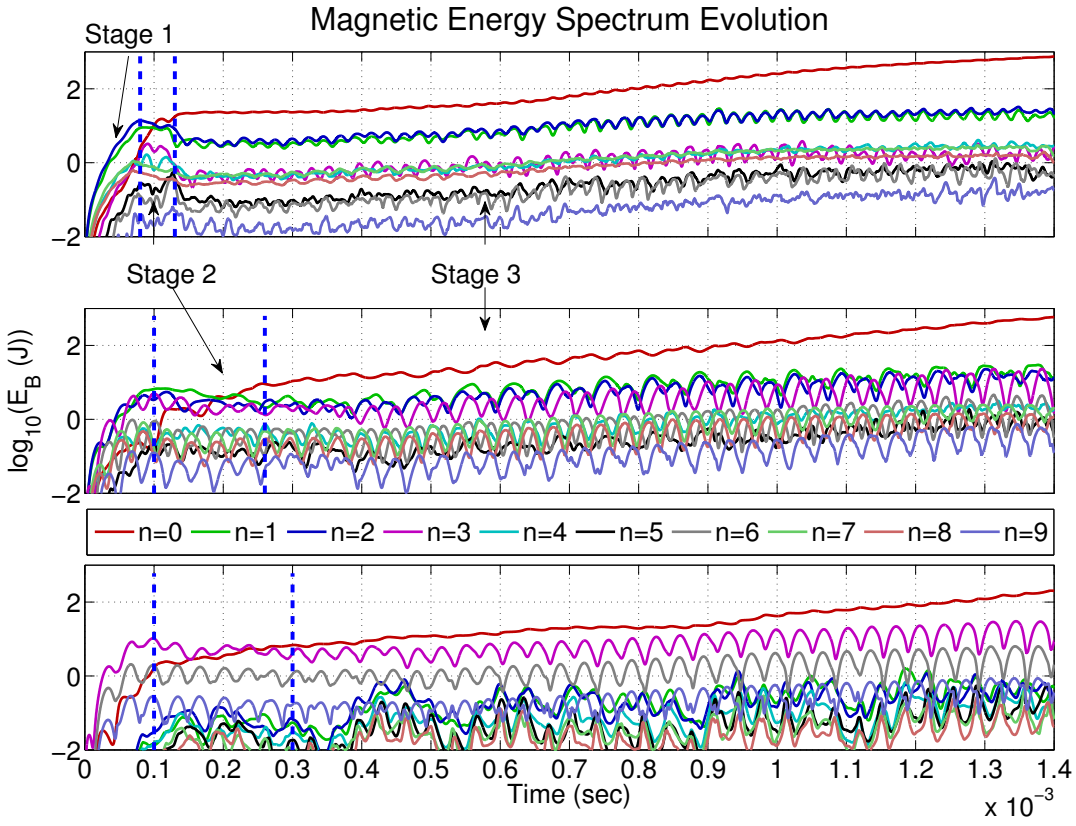

Figure 4.4: Global evolution of the magnetic energy spectrum for the three injector phasings examined. With phasing ϕ_A-ϕ_B-ϕ_C, the plots from top to bottom are 0-120-240, 0-60-120, and 0-0-0. The three stages of a typical discharge are characterized by (1) the buildup of the non-axisymmetric injector fields, (2) the relaxation event which forms the dominant axisymmetric structure of the spheromak and (3) the slow growth and sustainment of the axisymmetric object. The modal structure of the perturbation as well as the time scales involved depend on the injector phasing.

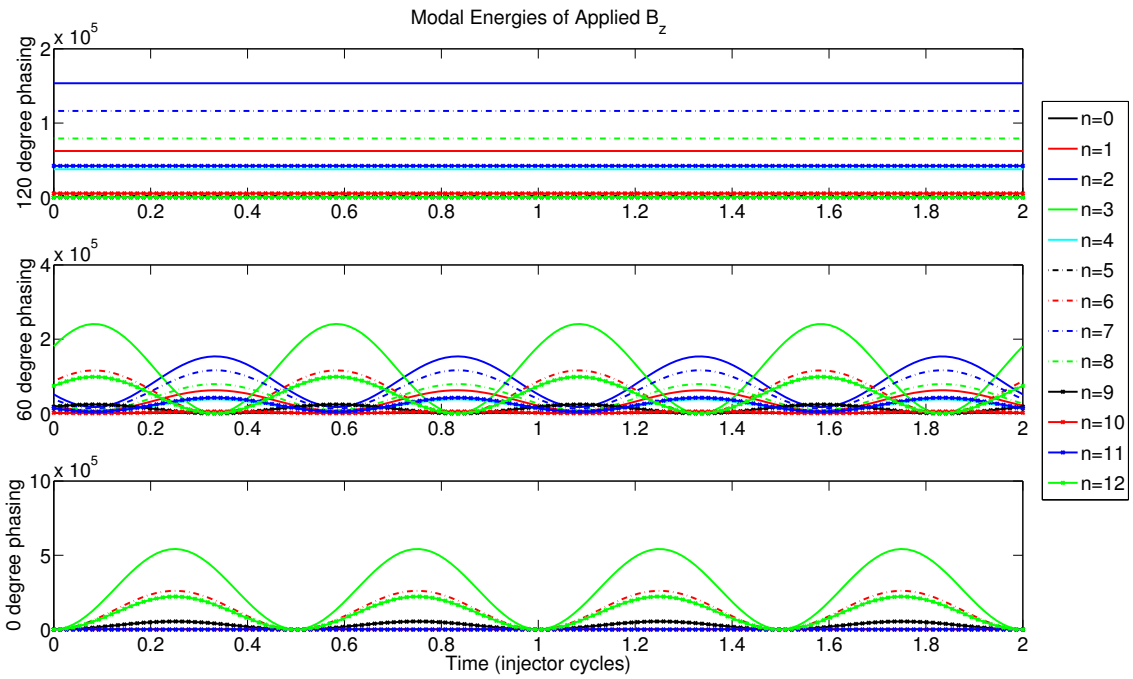

Figure 4.5: The toroidal Fourier decomposition of the magnetic fields at the injector mouths for three different phasings. The 0-60-120 phasing oscillates between the structures seen for 0-120-240 and 0-0-0.

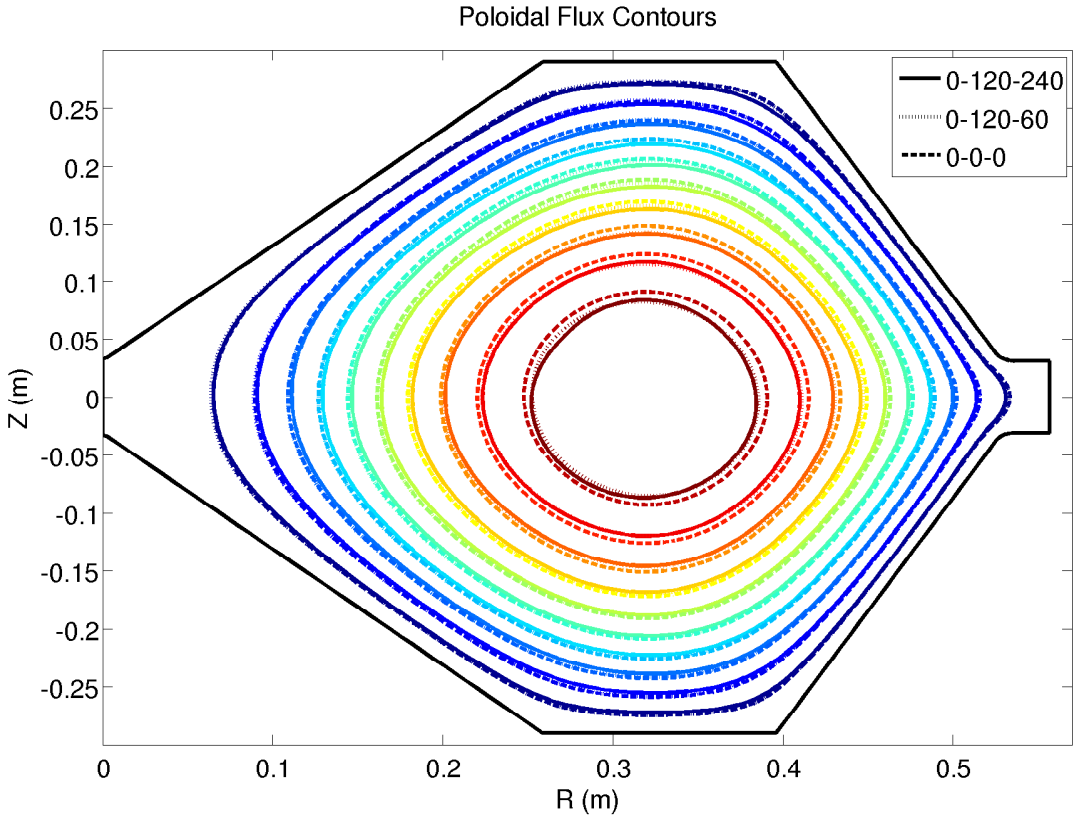

Figure 4.6: Contours of the axisymmetric poloidal flux are shown from a time late in the finite-β simulations, when the spheromak is being sustained.

stage 1 and stage 3 of the discharge. As seen in Figures 4.7, 4.8, and 4.9, the temperature profile during the injector-dominated stage of the simulation is defined by current channels that travel between the various injector mouths. These current filaments are thought to play a significant role in the relaxation dynamics. During the period of the simulation when the hot regions of the plasma connect to the injectors, we note that the hot-regions connect the various injectors together. Figure 4.9 shows this most clearly, where the hot filaments connect each injector mouth to another injector. Due to the boundary condition implementation of the injectors, it is unclear how accurate the paths of these filaments are. During the spheromak sustainment stage, the profile is more axisymmetric, with a hot channel disconnected from the injectors.

4.3 Validation Results

Validation of these simulations is performed by comparing measurements of synthetic diagnostics with experimental measurements, focusing primarily on comparisons of magnetic signals. A total of nine simulations are analyzed, with three simulations performed at each injector phasing of interest. A typical experimental discharge is selected for each injector phasing, then two zero-β simulations with isotropic and anisotropic viscosity models and one finite-β simulation with the anisotropic viscosity model were performed. Additionally, validation is done with velocity measurements from HIT-SI3's Ion Doppler Spectroscopy (IDS) system and density measurements a Far-InfraRed (FIR) interferometer. The diagnostics used for the experimental measurements are discussed in more detail in references [17, 18, 19, 48].

4.4 Magnetic Comparison

There are two sets of probes used for magnetic measurements on HIT-SI3, as seen in Fig. 4.10. The surface probes [17] are used to measure the poloidal and toroidal dependence of B, as well as measure the toroidal plasma current, while the internal probe [19] is used to measure the radial profile.

The first point of comparison for the magnetics is the global evolution of the spheromak.

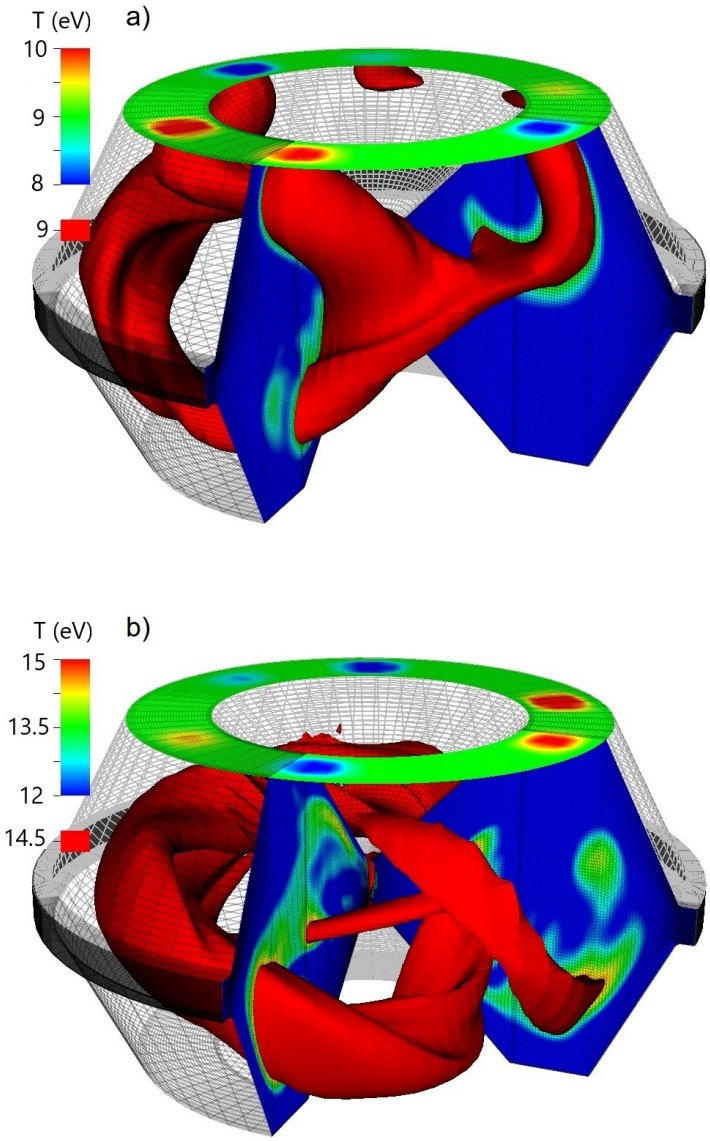

Figure 4.7: Temperature contours at two different times in the simulation at 0-120-240 phasing. a) is early in stage 3 of the evolution, when the hottest regions of the plasma are connected to the injectors. b) image is late during stage 3 of the evolution, when the hottest region of the plasma has disconnected from the injectors.

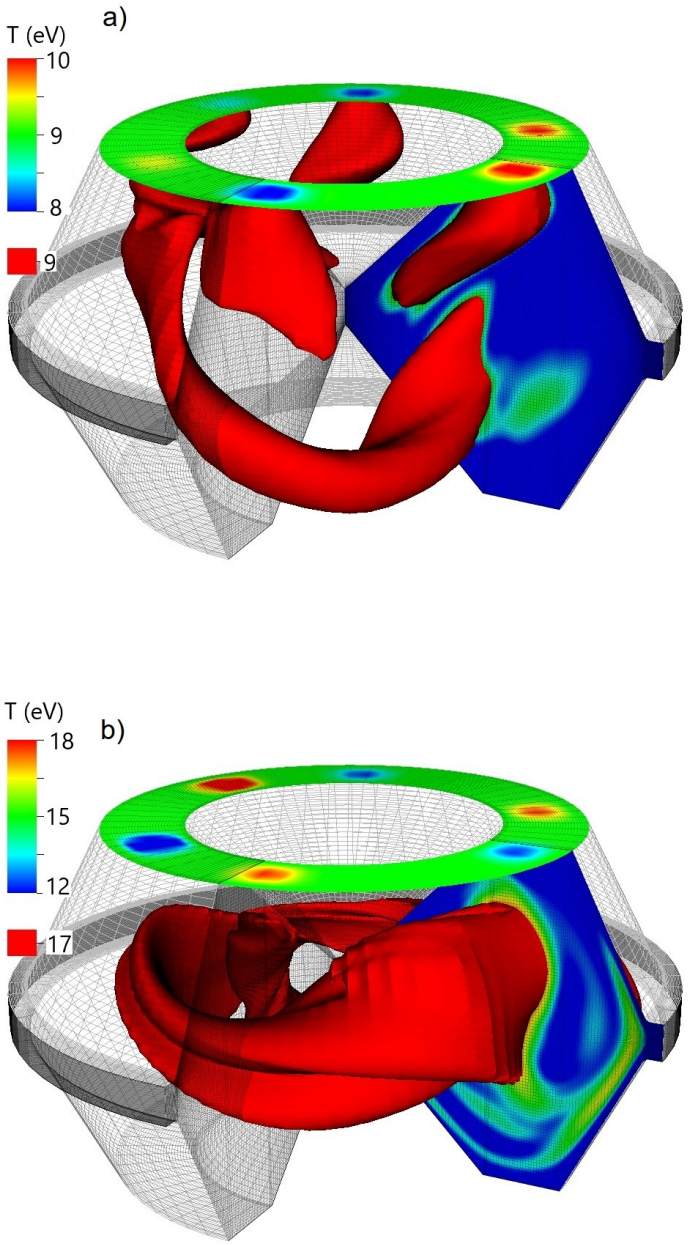

Figure 4.8: Temperature contours at two different times in the simulation at 0-120-60 phasing. a) is early in stage 3 of the evolution, when the hottest regions of the plasma are connected to the injectors. b) is late during stage 3 of the evolution, when the hottest region of the plasma has disconnected from the injectors.

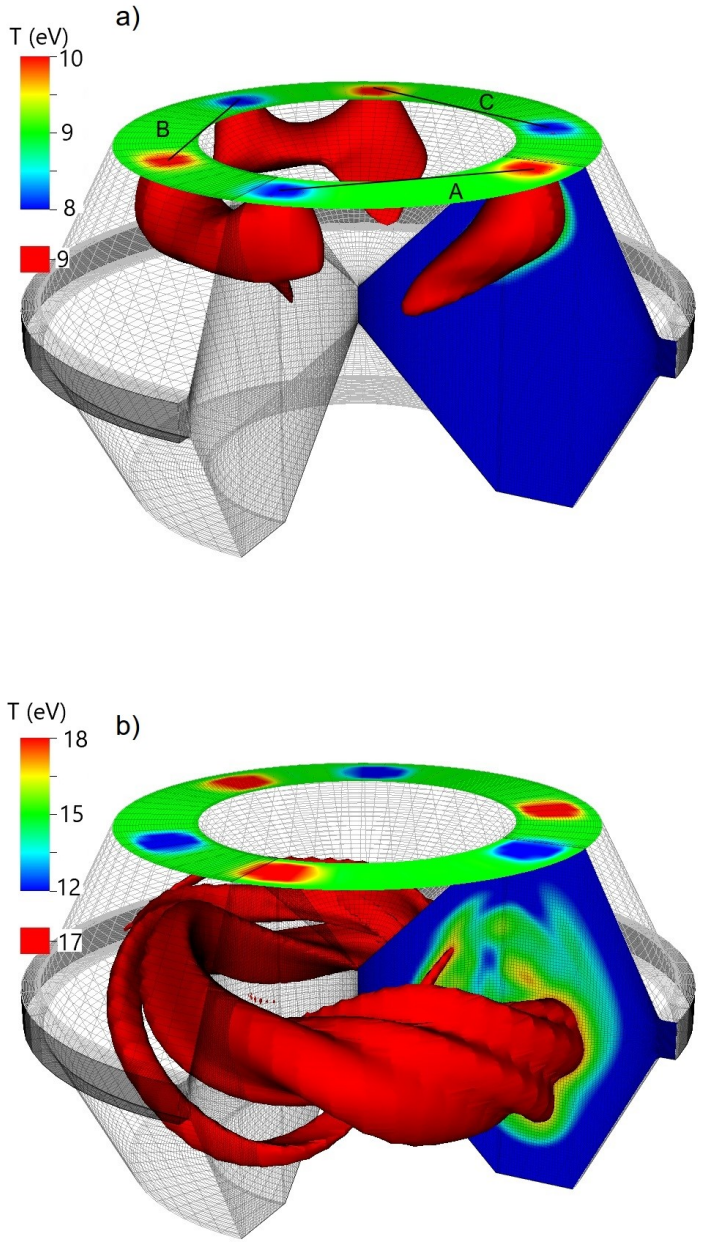

Figure 4.9: Temperature contours at two different times in the simulation at 0-0-0 phasing. a) is early in stage 3 of the evolution, when the hottest regions of the plasma are connected to the injectors. The three injectors are identified, noting that the hot regions are heated by currents which flow through all three injectors. b) is during stage 3 of the evolution, when the hottest region of the plasma has disconnected from the injectors.

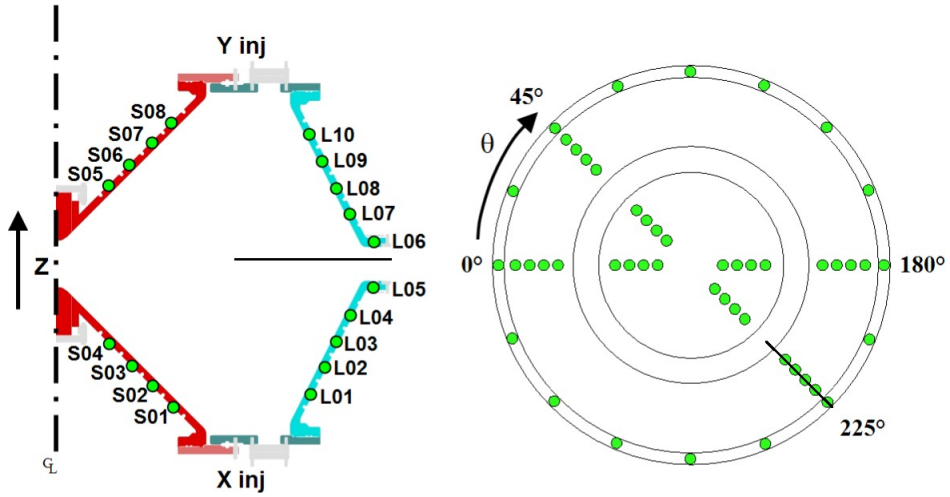

Figure 4.10: Location of the magnetic probes in the HIT-SI3 device. There are four poloidal sets of 16 probes and two toroidal sets of 16 probes located in the outboard midplane. An internal probe is inserted into the device indicated by the black line.

Experimentally this is examined by looking at the toroidal plasma current, measured by creating Ampèrian loops using the four poloidal arrays of surface probes. Shown in Fig. 4.11 is I_{tor} for both the experimental and simulation shots. As can be seen each phasing exhibits different trends with respect to the viscosity model. While the 0-120-240 phasing sees $\sim 10\%$ increase in I_{tor} in the anisotropic viscosity case, the 0-120-60 phasing sees little difference and the 0-0-0 phasing sees a $\sim 10\%$ decrease in I_{tor}. Additionally, for all three injector phasings the finite-β case sees I_{tor} reduced early in time and enhanced later compared with both the experiment and zero-β simulations. This is consistent with $\eta \sim T^{-3/2}$; as the plasma heats up the gain increases.

Another point of interest is the magnetic profile of the plasma for these three injector phasings. The toroidal mode structure of the plasma is obtained by a Fourier decomposition of the 16 midplane toroidal probes, allowing a decomposition of $n = 0$–7. For reducing the effect of the geometric shaping in the area on the analysis, the decomposition of the toroidal magnetic field is used. Direct comparison between simulation and experiment of the toroidal

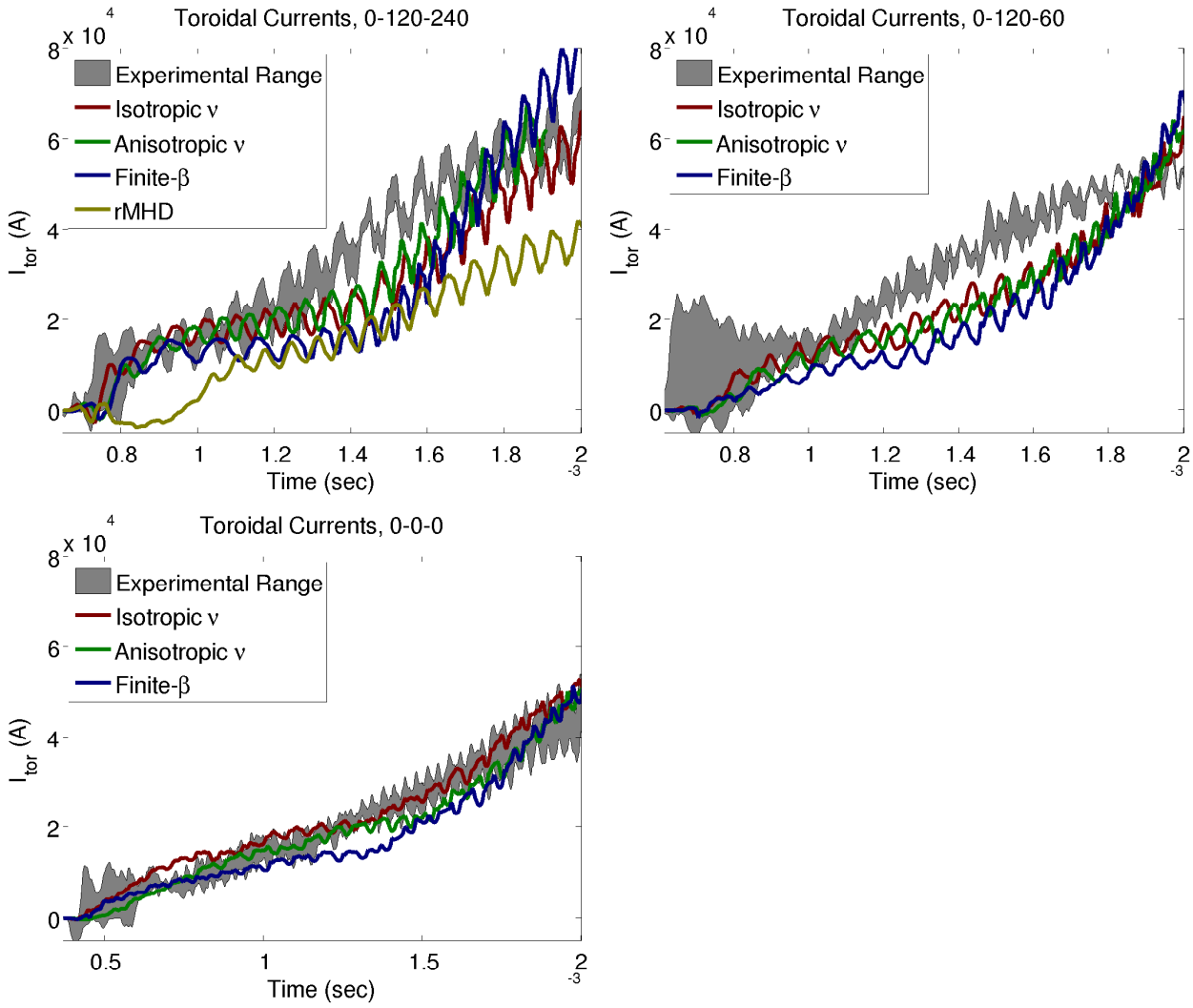

Figure 4.11: Toroidal currents from the simulations (solid lines) and a set of experimental discharges (shaded region) from each injector phasing. In general the simulations tend to undervalue I_{tor} shortly after the relaxation event and overvalue towards the end of the discharge. In the 0-120-240 case a case labeled resistive MHD (rMHD) is the isotropic ν model without the Hall term, which we see experiences both delayed formation and a lower amplitude of I_{tor}.

mode structure of the plasma measured by these probes is seen in figure 4.12. There are fine experimental features of the device near these probe locations which are expected to account for the differences in absolute magnitude seen between the simulation and the experiment. In particular, there are a number of holes in the flux conserver for midplane diagnostic access, as close as 2 cm from the probes, which can lead to flux loss that the simulation does not capture.

It is important to note that unlike HIT-SI simulations, the HIT-SI3 modal spectrum observed by the midplane gap probes is much more sensitive to the simulated geometry, with the two geometries simulated shown in Figure 4.13. When comparing a simulation that does not fully resolve the gap, as seen in Figure 4.14, we see that the diagnostic gap has the effect of substantially damping $n = 2$ activity.

The surface probes can also be used to calculate the current centroid of the spheromak. At each poloidal set of probes the centroid can be calculated of the poloidal field. The formula used to compute this centroid is given by:

$$\langle R \rangle = \frac{\sum_n R_n B_{pol,n}}{\sum_n B_{pol,n}}.$$

This calculation can be performed at each of the four toroidal locations that have a poloidal array of probes. By comparing these four sets of probes we can also obtain a description of the toroidal symmetry of the spheromak object. These comparisons are seen in Fig. 4.15. We can see that the finite-β calculations capture a ~ 1 cm shift in the location of this center that the zero-β calculations do not.

The perturbations in the core of the device and the internal magnetic profile of the spheromak can be directly compared using the internal magnetic probe. The magnetic field signals from these probes can be seen in Fig. 4.16, with agreement seen on the phasing of oscillations at the injector frequency and disagreement seen with the magnitude of the field near the magnetic axis.

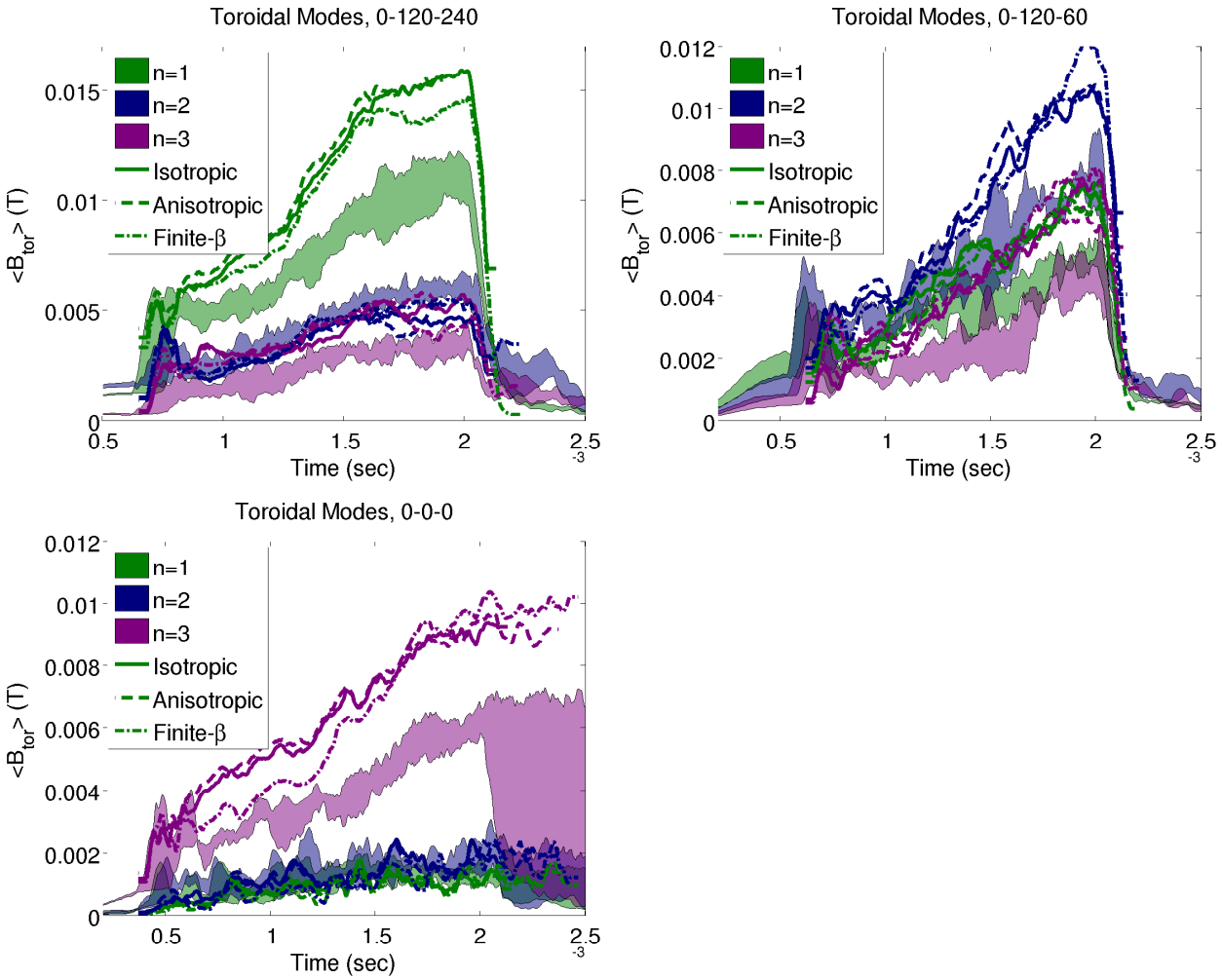

Figure 4.12: The toroidal mode spectrum of the perturbations as measured by the toroidal surface probe array. The signals have been smoothed at f_{inj}, with the filled region representing the spread of a set of similar discharges.

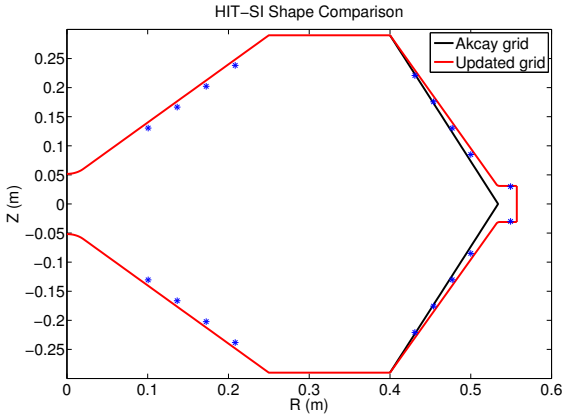

Figure 4.13: The two geometries used for simulations of HIT-SI3. The black geometry is the same one used by Akcay [38] for his simulations of HIT-SI while the red one incorporates the midplane gap for better resolution of the midplane surface probes. The physical probe locations are shown in blue and are sampled at the nearest grid point in the simulation.

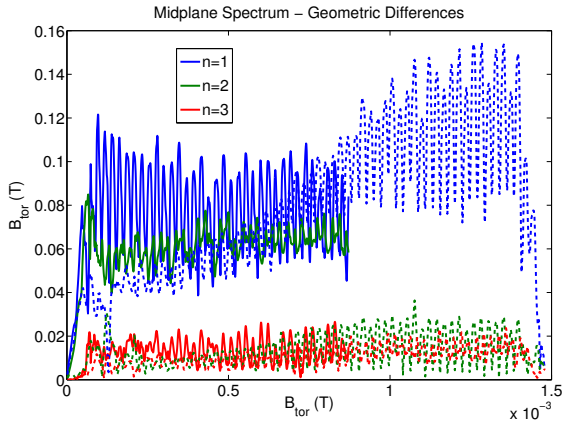

Figure 4.14: The mode spectra of two different simulations at 0-120-240 phasing. The solid lines are a simulation performed with a sharp corner instead of the experimental diagnostic gap, while the dashed lines include the gap. Total $n = 2$ energy is similar in the two cases. The gap appears to significantly suppress the $n = 2$ activity seen on these probes.

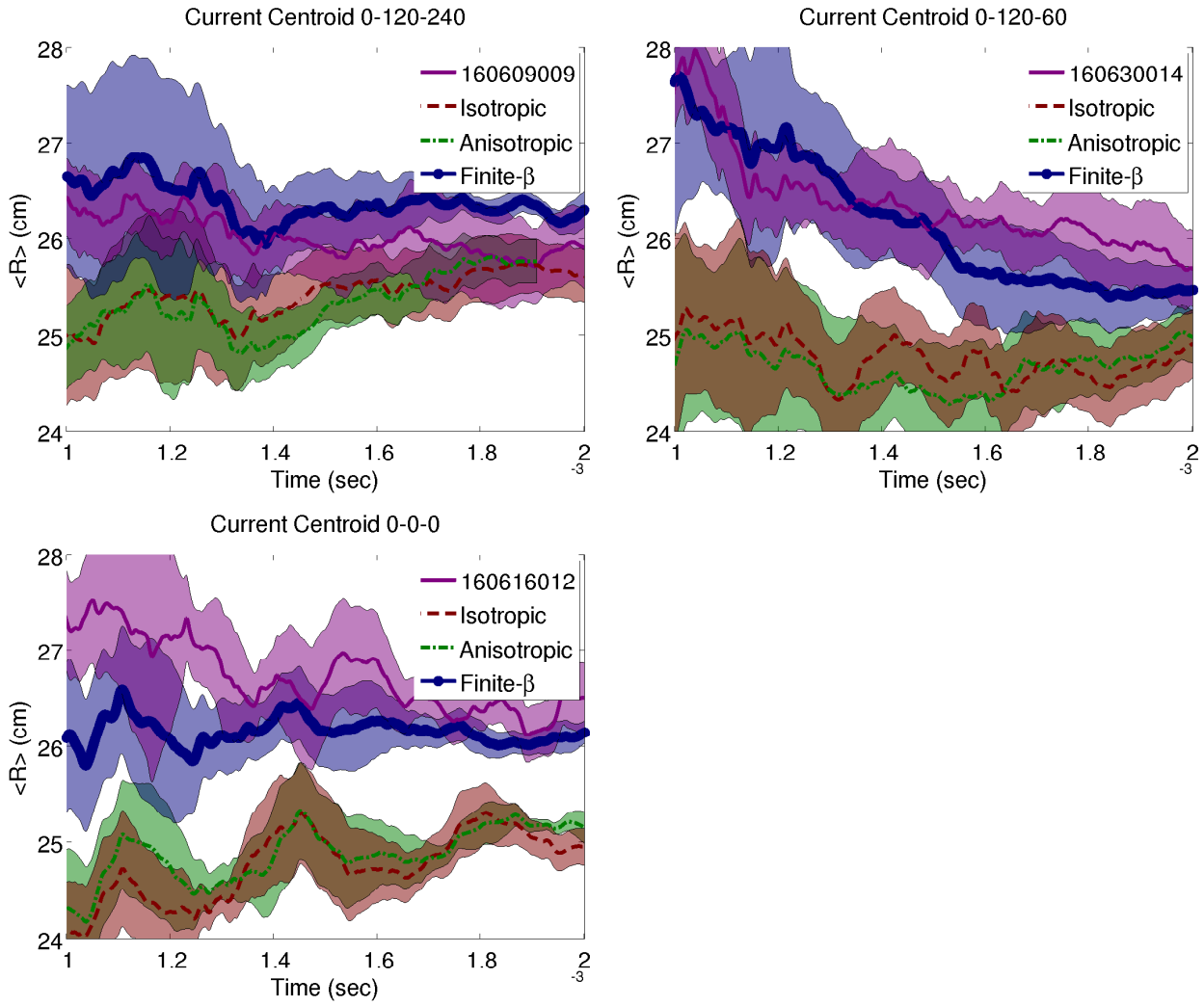

Figure 4.15: The current centroids for all three injector phasings. The measurement is performed at each of the 4 toroidal locations that have a poloidal probe array and the shaded region represents the two extremes from the four measurements with the curve representing the mean. We can see that the finite-β calculations capture a $\sim$ 1 cm shift in the location of this center that the zero-β calculations do not.

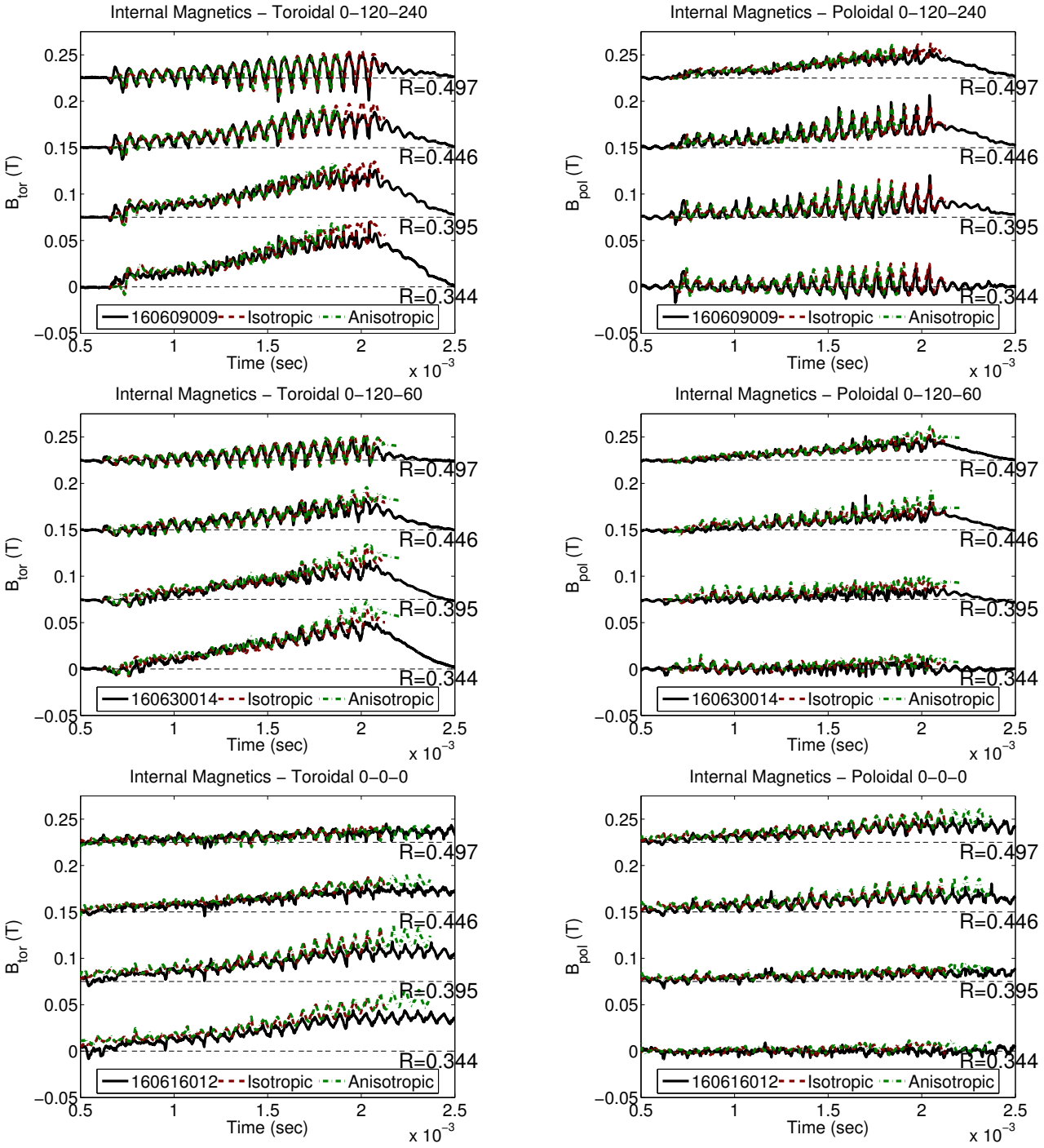

Figure 4.16: Comparison temporal signals of a set of internal magnetic probe signals from the experiment and simulation. The viscosity model has little influence on the measurement, and NIMROD is able to capture the phasing of oscillations seen in the experiment. The main point of disagreement is with the magnitude of the mean toroidal field near the magnetic axis at $R = 34.4$ cm.

Energy $\langle B^2 \rangle \, (10^{-4})$

Phasing	**0-120-240**	**0-120-60**	**0-0-0**
Exp. Range	8.6 ± 0.68	3.47 ± 3	(3.93 ± 0.6)
Isotropic	13.7	5.17	5.83
Anisotropic	15.2	5.99	6.63
Finite-β	10.1	3.65	3.35

Table 4.3: The $\langle B^2 \rangle$ metric from Eq. 2.15 applied to the simulations

Shape Metric Y

Phasing	**0-120-240**	**0-120-60**	**0-0-0**
Exp. Range	0.990 ± 0.001	0.918 ± 0.006	0.978 ± 0.04
Isotropic	0.953	0.916	0.936
Anisotropic	0.954	0.917	0.936
Finite-β	0.951	0.914	0.935

Table 4.4: The Y from Eq. 2.16 applied to the simulations

4.4.1 Bi-orthogonal Decomposition Metrics

Using the same procedure introduced in Chapter 2 and used in Chapter 3, we can compare the results of the surface magnetic probes experimentally with the simulation using BD. Tables 4.3 and 4.4 show the values computed when following the metrics described in Chapter 2. We see that in general the finite-β simulations agree the best with the total energy of the system, though all three cases look similar with the shape metric Y.

4.5 Grad-Shafranov Fit of HIT-SI3 Equilibria

The spheromak magnetic profile seen in Fig. 4.17, with an equilibrium fit to Grad-Shafranov following the method used in reference [15] and described in Chapter 2, is obtained by averaging the signal from the probe at f_{inj}. We can compare this equilibrium reconstruction to the toroidally symmetric component of the magnetic field to test the equilibrium reconstructions ability to model the field. The two profiles agree fairly well with one another, indicating that Grad-Shafranov fitting is a useful tool for extracting the axisymmetric component of the magnetic field.

4.6 Fluid Comparison

In addition to magnetic comparisons, the fluid properties of the plasma can be compared. The IDS system is used to measure the flow velocity ($\vec{V}$) and the ion temperature (T) in a chord-averaged sense. A Far-InfraRed (FIR) interferometry system is used to measure the line averaged electron density ($\langle n \rangle$). These diagnostics are located on the midplane and Fig. 4.18 shows the chord locations relative to the injector mouths.

Previous investigations with the IDS system on the HIT-SI3 [18, 48] device have focused on measurements of the axisymmetric toroidal flow, phase coherence of oscillations at f_{inj}, and the temperature profile. As seen in Fig. 4.18, two sets of IDS chords are positioned looking in opposite directions of the plasma. An absolute toroidal flow can be calculated from the difference in mean velocity at a given impact parameter. Due to limitations on data gathered during experimental operations, comparisons can only be done with the 0-120-240 phasing. The comparison of this toroidal flow from simulations with experimental results is seen in Fig. 4.19. We see little difference in the axisymmetric flow profile observed by the three models, instead the different models change the amplitudes of the non-axisymmetric flows. As discussed later, the flows are dominated by $\mathbf{J} \times \mathbf{B}$ forces related to the injector perturbation.

The temperature profile between the experiment and the simulation can be compared

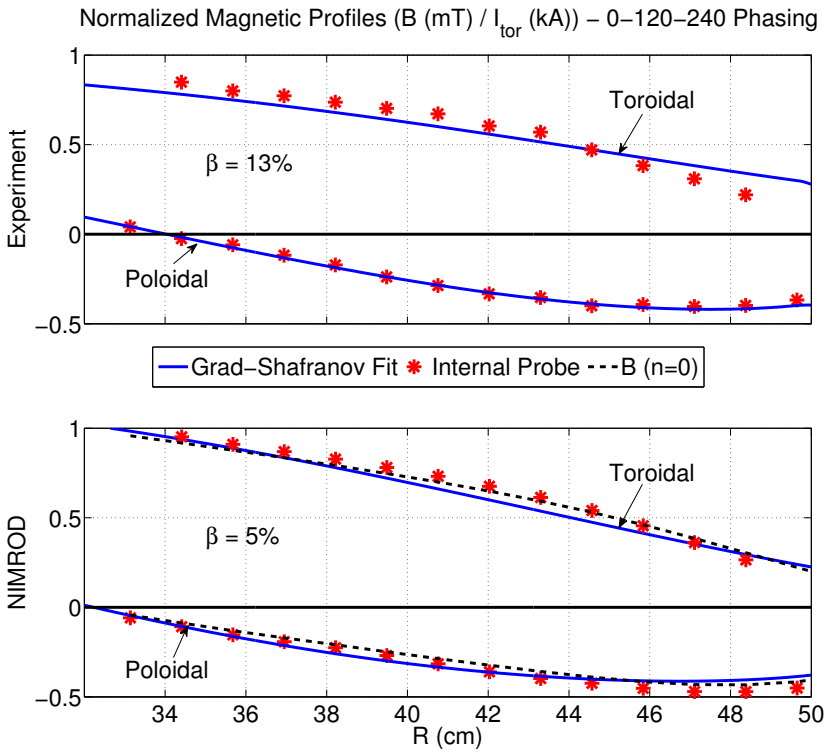

Figure 4.17: The time-averaged magnetic profile measured by the internal probe for the experiment (top) and simulation (bottom), along with the results of a Grad-Shafranov fit which provide the measurement of β. The NIMROD plot additionally shows the profile of the axisymmetric component of the field, to highlight the small 3-D asymmetry in the equilibrium.

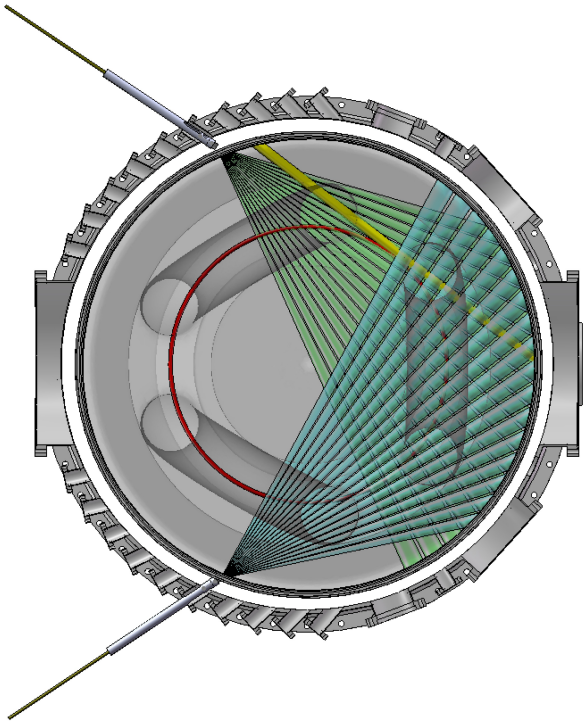

Figure 4.18: The location of optical diagnostic chords on HIT-SI3. The two fans are the viewing chords for Ion Doppler Spectroscopy to measure line averaged $\vec{V}$ and T_i, while the singular chord is the Far-InfraRed interferometer for measuring $\langle n_e \rangle$. The red circle indicates the mean magnetic axis of the device, with the positive toroidal direction being counter-clockwise.

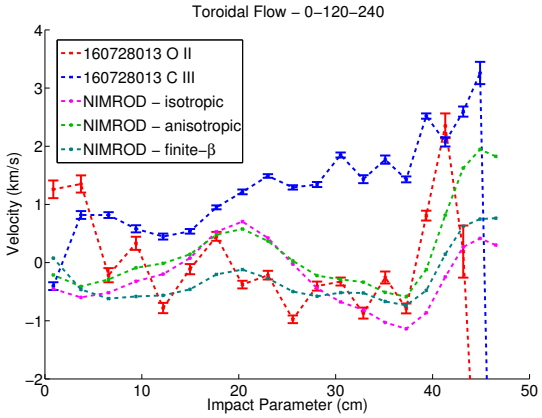

Figure 4.19: The toroidal flow profile measured from the IDS diagnostic compared between simulation and experiment. The toroidal current is in the positive direction.

with results from the IDS system. Shown in Fig. 4.20 is the comparison of the measured and simulated temperatures late in time of the discharge. We see that NIMROD resolves a much flatter and smooth profile than the experimental measurement, potentially related to the spatial variation of the spectral intensities. We can similarly compare the effect of line-averaging by comparing the synthetic IDS signal with the radial temperature profile in NIMROD. Figure 4.21 shows that while NIMROD observes radial dependance on T, the line-averaged profile is flat. Likewise, Fig. 4.22 shows the same is true for toroidal flow velocity. Of note is that while the simulations begin cold with $T = T_{wall}$ everywhere and heat up throughout the discharge, the experiment tends to observe a relatively flat T_{ion} evolution in time. This can be seen in Fig. 4.23. The simulation heats up to the temperature observed by the CIII spectral line throughout the length of the discharge, indicating reasonable modeling of the total thermal energy of the plasma.

The FIR measurements [19] of $\langle n \rangle$ can be extracted from the three finite-β simulations and the results can be seen in Fig. 4.24. Unfortunately, due to the large particle diffusivity used for numerical convenience the oscillations are significantly damped in the simulation. A possible improvement would be the implementation of a boundary condition on $\vec{V}_{\perp}$ to refuel

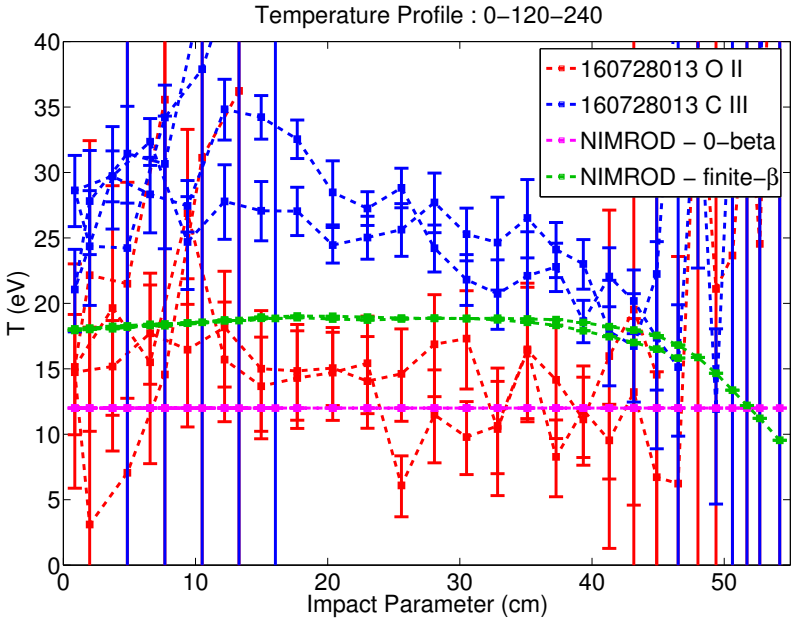

Figure 4.20: The temperature profile measured by IDS compared between experiment and simulation. The simulations see a much flatter T profile than the experiment. The two-values at each impact parameter are a result of two fiber arrays making the measurements at different toroidal locations.

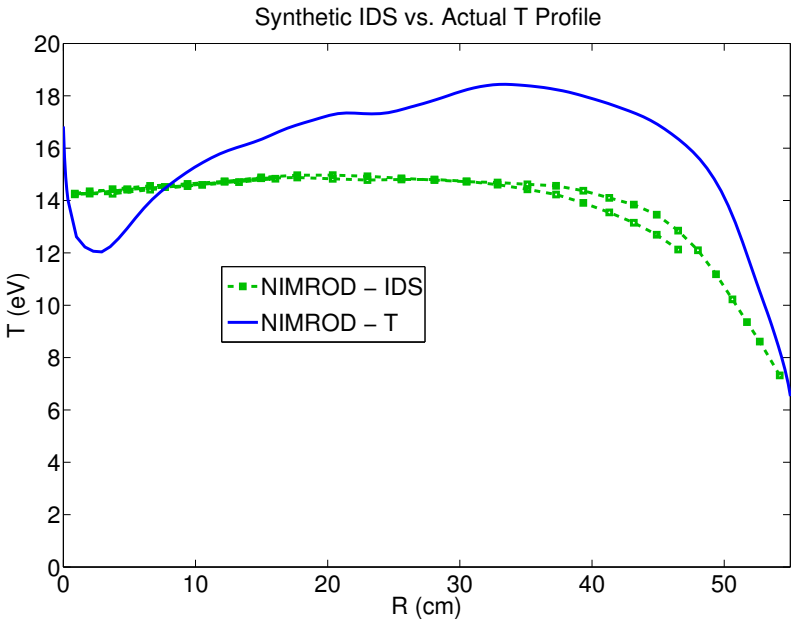

Figure 4.21: The temperature profile measured by the synthetic IDS diagnostic compared with the axisymmetric profile obtained from the simulation directly. The line-averaging nature of the IDS diagnostic smooths out the observed temperature profile.

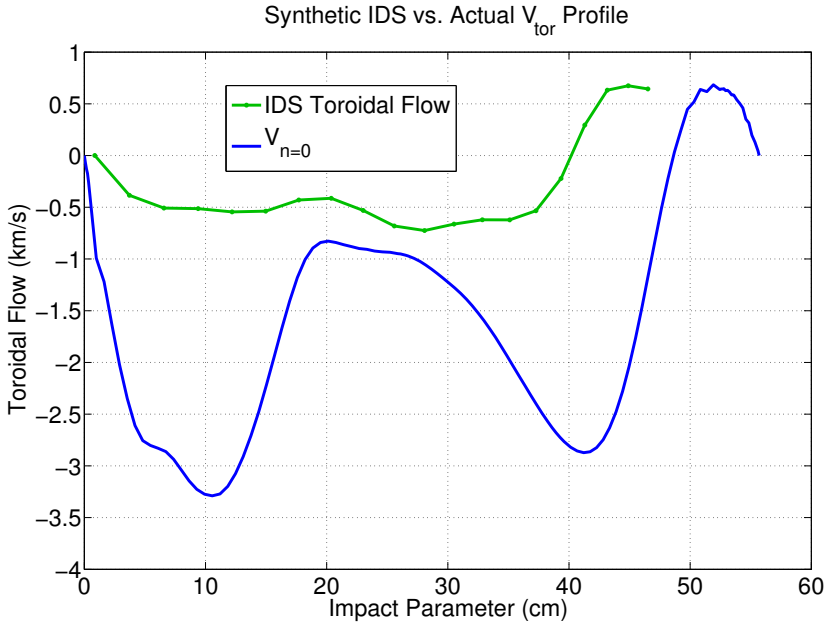

Figure 4.22: Toroidal flow comparison between the synthetic IDS diagnostic and the actual axisymmetric flow velocity. Can see that the line-averaging nature of the IDS diagnostic smooths out gradients in the toroidal flow velocity.

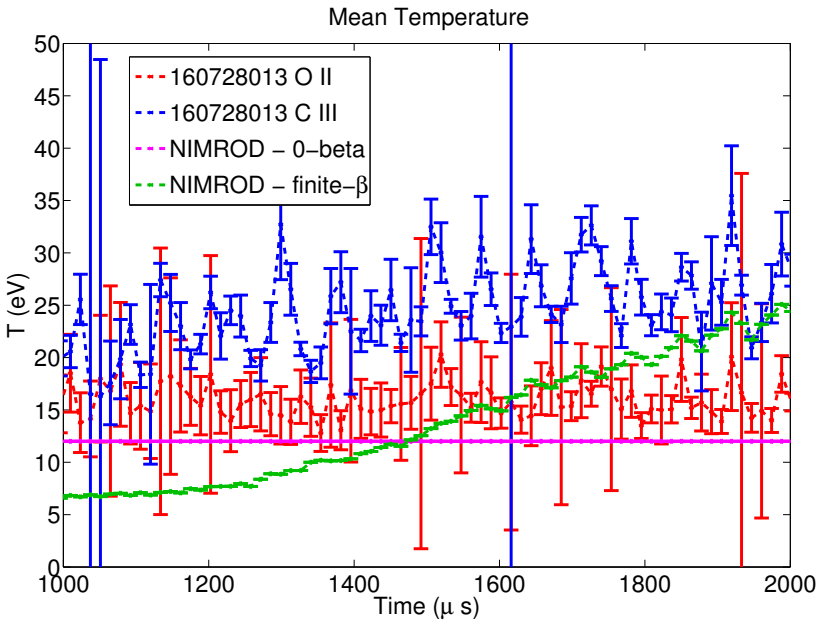

Figure 4.23: Mean temperature of the IDS chords in the experiment and simulations. The simulations heat up gradually throughout the discharge while the experiment remains at a constant temperature throughout.

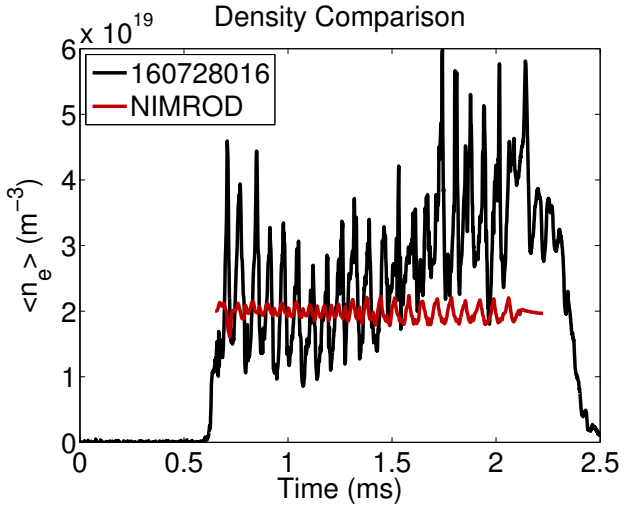

Figure 4.24: Line-averaged density measured by the FIR diagnostic on HIT-SI3 compared with the simulations. Reduction in density oscillations is a result of the high artificial diffusivity.

the particles lost to the wall when diffusivity is decreased.

As can be seen in the current centroid and internal magnetic probe comparisons, the location of the magnetic axis undergoes a shift when pressure gradients are included in the model. This shift improves agreement with the experimental measurements indicating that these pressure gradients have a significant effect on the plasma. We can calculate $\langle\beta\rangle_{vol} = \frac{\int p \mathrm{d}V}{\int \frac{B^2}{2\mu_0} \mathrm{d}V}$ and find that at each injector phase the simulations exhibit $\langle\beta\rangle_{vol} \sim 5-8\%$ towards the end of the discharge, with the value oscillating at f_{inj}. This can be compared with the experimental value obtained from equilibrium fits to the Grad-Shafranov equation in Fig. 4.17, using the same method in reference [15], which tend to give values between $10-15\%$ late in the discharge. Additionally, the value of $\langle\beta\rangle_{vol}$ obtained from taking synthetic experimental measurements from the simulation and fitting to a Grad-Shafranov equilibrium is close to the value obtained from volume integrating the fields directly, giving confidence in the usage of equilibrium fits on these time-averaged fields.

This disagreement of a factor of two in $\langle\beta\rangle_{vol}$ could be caused by a combination of

increased particle diffusivity smoothing the pressure profile and the simplified model of assuming $T_i = T_e$. Experimental evidence suggests that $T_i \sim 2T_e$, though numerical studies thus far have proven too computationally difficult to carry out.

4.7 Discussion of Simulation Results

An interesting feature observed when comparing the toroidal mode activity seen from both the experimental and simulation results is the large difference in spectrum between the total volume energy and the surface probe measurement, indicating underestimation of the amplitude of certain modes. In particular, while the 0-120-240 phasing sees primarily $n = 1$ perturbation activity from the surface probes in both experiment and simulation, there is an equivalent magnitude $n = 2$ shaped perturbation concentrated closer to the core of the device. In addition, the 0-120-60 phasing shows a similar discrepancy concerning the magnitude of $n = 2$ activity relative to other modes, though in this case the $n = 1$ is near the core as opposed to the edge. As would be expected, when the phasing is dominant in only one toroidal fourier mode, as in both HIT-SI ($n = 1$) and 0-0-0 HIT-SI3 ($n = 3$), this effect is not observed and the spectrum of the surface probes matches the spectrum of the volume integrated energy.

Additionally, the comparisons of magnetic profile between the experiment and the simulations show the importance of finite-β effects. An outward shift of the magnetic axis is seen between the zero and finite-β simulations, which are consistent with $\beta \sim 10\%$. An analogous outward shift from rotation would require $\vec{V}_{tor} \sim 100$ km/s which is not observed in either the experiment or the simulation. While these effects lead to a change in the magnetic profile, the evolution of global parameters (such as I_{tor}) changes little, resulting primarily from changes in energy dissipation from the plasma resistivity. This indicates that the mechanism for creation and sustainment of the axisymmetric component of the equilibrium is a zero-β phenomenon.

The additional diagnostic capability provided by the simulation allows us to examine questions that have been raised in previous studies of HIT-SI and make predictions for

future measurements. The magnetic profile of the equilibrium is constructed by taking a running average of the internal magnetic probe at f_{inj}. Because of the large non-axisymmetric nature of the perturbation and the probe only located at one toroidal location, it is unclear whether this time-averaged field is axisymmetric. We are able to produce synthetic internal magnetic probes throughout the device and see the deviations this time-averaging has from axisymmetry. The results are that the radial position of the magnetic axis varies by ± 1 cm, as can be seen in Fig. 4.25. This is consistent with the toroidal deviations seen in the current centroid measurement from the surface probes, and can be verified with an additional internal magnetic probe that has been installed for the next run campaign.

We can additionally judge the accuracy of the experimental method of calculating toroidal current. The experiment calculates I_{tor} through the line integration of $\vec{B}$ along the edge of the device, then averages this calculation at four toroidal locations to determine the value [17]. The decision of four toroidal locations was made back when the device was in the HIT-SI configuration, where it was expected that the dominant mode that needed to be averaged away was the $n = 1$ contribution from the injectors. The expectation with HIT-SI3 is that the addition of $n = 2$ and $n = 3$ components to the injector current shape, we should expect that the surface probe method loses its accuracy. We see in Fig. 4.26 that when we compare the actual toroidal current in a NIMROD simulation with the surface probe calculated toroidal current that they are within 10% of each other for the amplitude. The inability to correctly average $n = 2$ and $n = 3$ components appears to primarily impact the measurement in an increased oscillation of the signal.

While IDS comparisons were only made for 0-120-240 phasing, we can make predictions about the axisymmetric flow profile expected at the other phasings. Figure 4.27 shows the $n = 0$ component of $\vec{V}_{tor}$ during the sustainment phase. In all three phasings the angular velocity $\vec{V}_{tor} \ll \omega_{inj} R \approx 25$ km/s at $R = 0.3$ m, suggesting that there is not plasma rotation at f_{inj}. The 0-120-60 phasing appears to have the most significant variation based on viscosity model, with the anisotropic model having a flat angular velocity profile at $f_{rot} \approx 3.5$ kHz.

As seen in the IDS flow velocity comparison with Fig. 4.19, the magnitude of axisym-

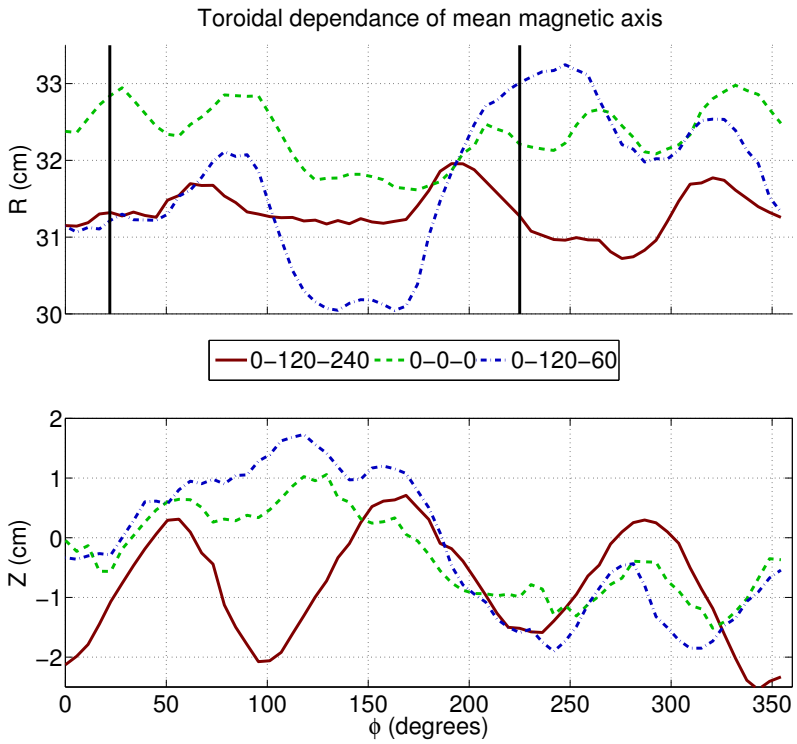

Figure 4.25: The R and Z locations as a function of toroidal angle of the position of the magnetic axis averaged at f_{inj}. As can be seen each phasing sees a different dependence, with 0-120-240 seeing $n = 3$ shaping and 0-120-60 seeing primarily $n = 1$. The black lines show the location of the two internal probes of the device, with the one at $\phi = 225°$ providing the data used in this paper. The vertical asymmetry in the mean value of Z is caused by the injector pressure originating from the top of the device.

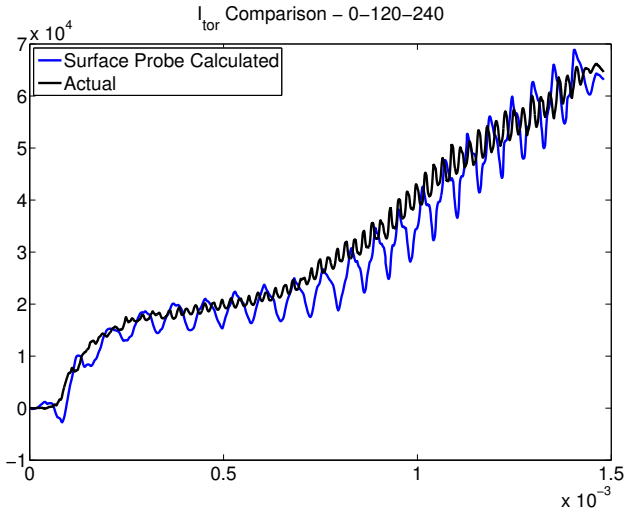

Figure 4.26: The toroidal current from a NIMROD simulation at 0-120-240 phasing calculated in two methods. In black is the actual axisymmetric current flowing toroidally, $I_{tor} = \int \vec{J_0} \cdot \mathrm{d}\vec{a}$. In blue is the piecewise integration performed with the surface magnetic probes $I_{tor} = \sum_n B_n L_n$ where L_n is the effective arc length to approximate $I_{tor} = \int \vec{B} \cdot \mathrm{d}\vec{l}$.

metric flow does not depend strongly on the viscous model used. The axisymmetric flow in the simulation ends up being a minor component of the ion flows, with the majority having a toroidal spectrum similar to the injector magnetic perturbation, as seen in Fig. 4.28. We see that while the anisotropic viscosity model damps away $n \neq 1$ kinetic energy from the system, the finite-β model more closely resembles the isotropic kinetic energy spectrum, despite using the anisotropic viscosity model.

While no present experimental diagnostics exist to measure the temperature at specific locations in the device, we can look at the profile produced for each injector phasing in the simulation. Figure 4.29 shows the temperature evolution and profile late in time, where temperatures of $T > 30$ eV are seen at the magnetic axis. From these, we see that the temperature of the plasma evolves similarly to the toroidal current in the simulations, which is consistent with the heating power being proportional to I_{tor}^2 from resistive heating.

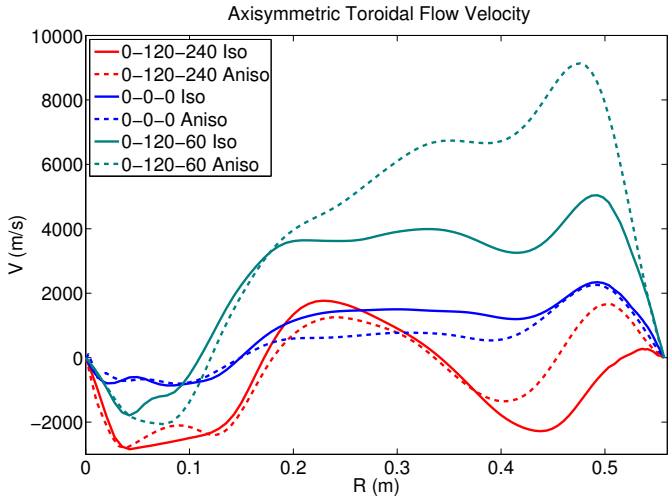

Figure 4.27: The axisymmetric toroidal flow velocity of the different viscosity models are shown. The toroidal current is in the positive direction.

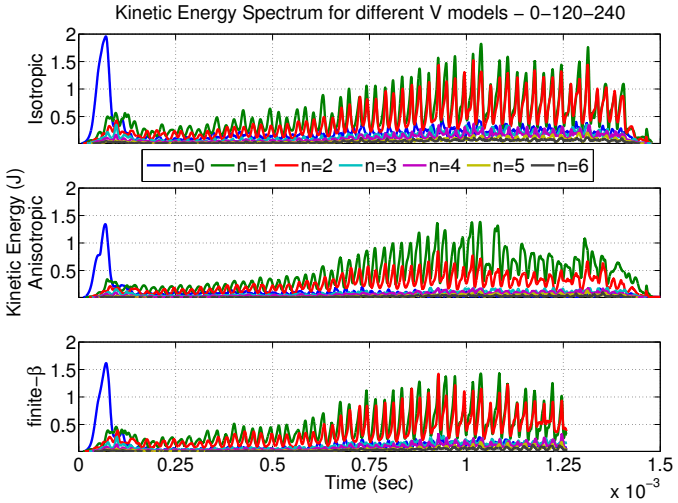

Figure 4.28: The kinetic energy spectrum of the three different momentum equation models used. The top is the zero-β isotropic viscosity model, the middle is the zero-β anisotropic viscosity model, and the bottom is the finite-β with anisotropic viscosity model. We see that though the anisotropic viscosity damps flows with $n \neq 1$, pressure gradients can similarly drive those flows.

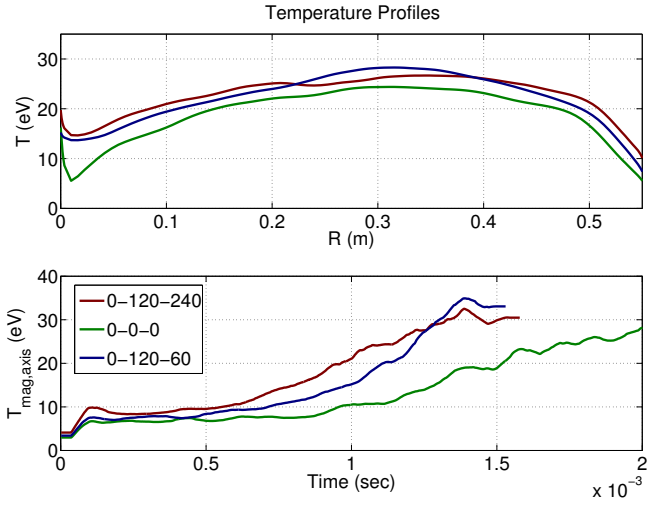

Figure 4.29: Top is the temperature profile during the end of the simulation, averaged over 3 injector cycles. The warm region at $R = 0$ is additional heating from injector currents which cross through the geometric axis. The bottom is the temporal evolution of the temperature at magnetic axis, which we see resembles the growth of I_{tor} in each case.

4.8 Future Work for HIT-SI3 Modeling

During the course of this research, HIT-SI has largely served as the experimental geometry to test changes to the physical models considered while HIT-SI3 has served to further validate those models. As a result, the next steps for simulating HIT-SI3 will be to repeat simulations that have already been performed with improved pressure models, both through reduced diffusivity and enhanced electron physics, as well as modeling parameter spaces not yet explored, such as high-f_{inj} operations.

While significantly more effort has been put into the low-f_{inj} operations of HIT-SI3, some discharges at higher f_{inj} have been taken. Similar to high f_{inj} simulations of HIT-SI, we see the appearance of significant oscillations at frequencies other than f_{inj}, with the primary difference being that these oscillations are much larger on HIT-SI3. A single NIMROD simulation was performed at $f_{inj} = 53.6$ kHz, seen in Figure 4.30, was able to capture these

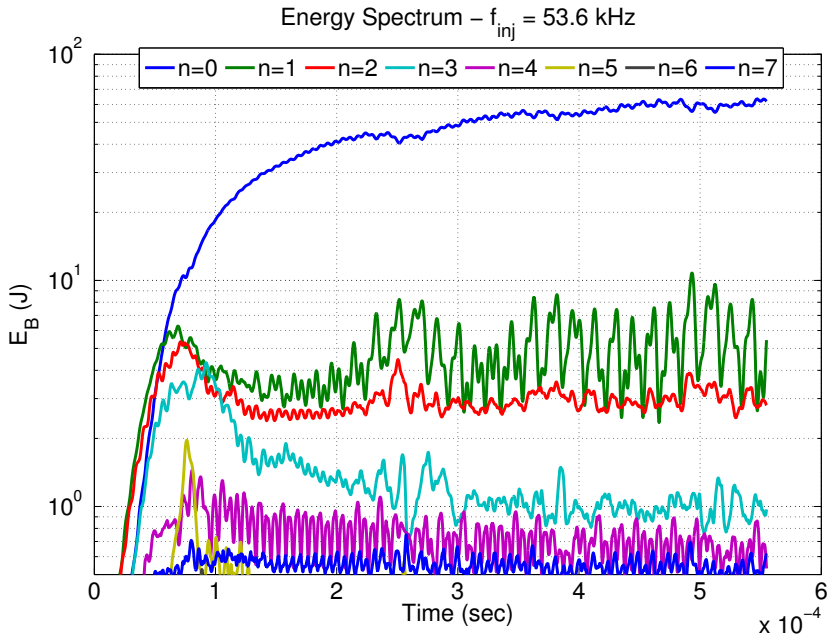

Figure 4.30: The energy spectrum for a simulation at $f_{inj} = 53.6$ kHz. Similar to HIT-SI high f_{inj} discharges, lower frequency oscillations are seen.

low-frequency oscillations. Similar to HIT-SI, the modal spectrum of the plasma changed during the formation, with additional $n = 3$ activity being seein in the 0-120-240 phasing, analogous to the increased $n = 2$ activity seen during startup of HIT-SI.

Additionally, more in-depth parameter scans of the injector phasing can provide more insight on the role of different modal spectra in sustaining the spheromak. Using the applied injector boundary conditions as a guide, and assuming that all of the energy in $n > 3$ will find its way into a lower energy mode during the full dynamics, Figure 4.31 shows the amount of $n = 3$ activity, relative to the total applied perturbation, that can be expected from different injector phasings. If we assume, as was seen at both 0-120-240 and 0-120-60 phasing, that the remaining perturbation energy tends to evenly distribute between $n = 1$ and $n = 2$ activity, we see that all phasings lie on a spectrum, with 0-120-240 and 0-0-0 being the two extremes. Scans to both confirm that the phasings transition as expected and to understand

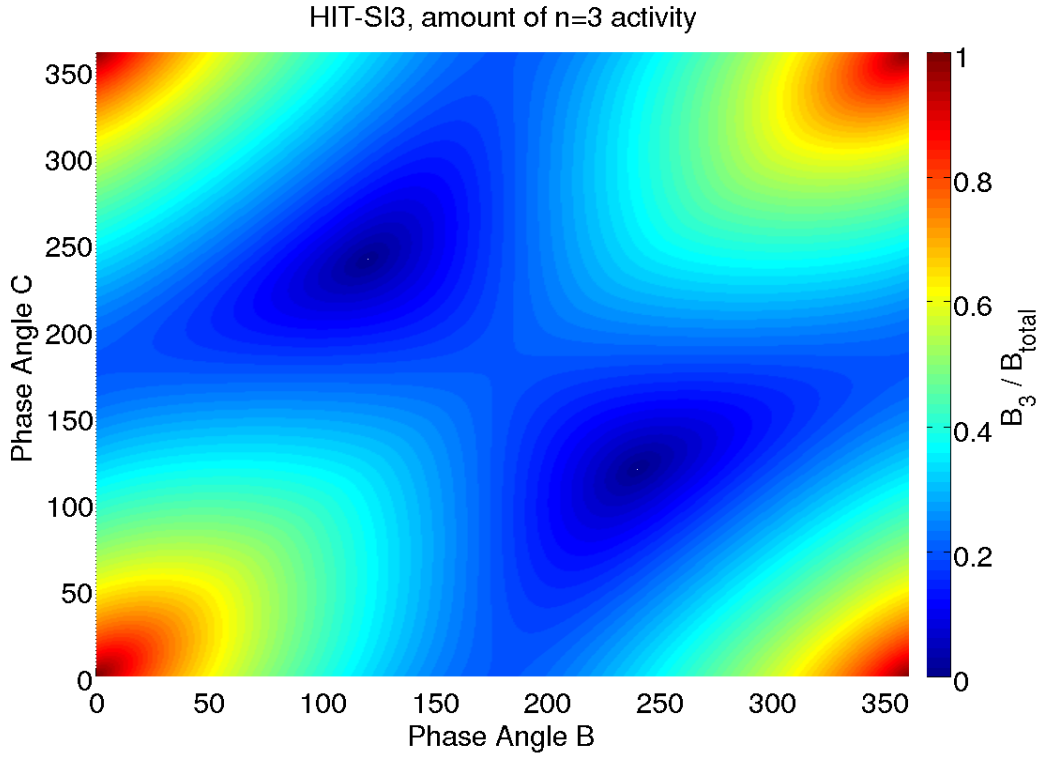

Figure 4.31: The amount of $n = 3$ activity relative to the total applied perturbation expected from the NIMROD boundary conditions. The phasings are represented as 0-$\delta\phi_B$-$\delta\phi_C$, with the A injector held fixed at 0 degrees. Phases of interest are 0-120-240 where the $n = 3$ is minimized, 0-60-120 where $n = 3$ is 1/3 of the content, 0-0-0 where the $n = 3$ is the majority of the energy, and 0-40-80 where $n = 3$ is half of the perturbation.

the interaction with the spheromak can be looked at both experimentally and in simulation.

Chapter 5
EXTRAPOLATION STUDIES OF HIT-SI

The main goal of this work is to produce a predictive model that can guide the design of future devices in the goal of fusion power. A set of studies have been performed looking at future devices similar to HIT-SI.

5.1 'Big HIT'

The first extrapolation study performed was a zero-β simulation on a geometrically larger version of HIT-SI. Each physical dimension was expanded by a factor of 2.5 and the temperature was increased by a factor of ~ 10, with parameters seen in Tab. 5.1. This simulation was begun by Cihan Akcay [38], though the bulk of the analysis was performed following his graduation.

The bulk behavior of the simulation begins similarly to HIT-SI. The simulation began with the growth of the injector-dominated $n = 1$ mode followed by a relaxation event and the formation of the spheromak object. Significant deviations from HIT-SI begin to appear around current gain of 6, as seen in Fig. 5.1. These deviations are the appearance of sawtooth oscillations on the toroidal current and $n = 0$ energy.

To identify what is occuring during this period we can look at the magnetic field structure. Fig. 5.2 5.3 and 5.4 help provide a description of the structure. The sawtooth oscillations are associated with the formation of closed-flux surfaces that are able to persist for up to 20 injector cycles. While these flux surfaces exist, they experience motion at the injector frequency about the midplane magnetic axis, though this motion does not break apart the flux surfaces.

Figure 5.5 gives us a tool to evaluate the 'closed-flux-ness' of the configuration, by count-

Parameter	HIT-SI	Big HIT
R(m)	0.53	1.33
Poloidal Resolution (m_x, m_y)	24x24 pd4	40x40 pd4
Toroidal Resolution (n_{modes})	11	11
Injector Flux (mWb)	1.2	2.5
Injector Current (kA)	20	20
λ_{inj} (m^{-1})	20	10
n_e (m^{-3})	1.5×10^{19}	1.5×10^{19}
T_e (eV)	12	108
η (Spitzer) (m^2/s)	8.8	0.707
Viscosity ($\nu_{\|}$) (m^2/s)	260	260
$\tau_{L/R}$ (ms)	2.4	80
τ_A (μs)	20	20
Current Amplification	3	10

Table 5.1: Parameter differences from HIT-SI and the big HIT simulation.

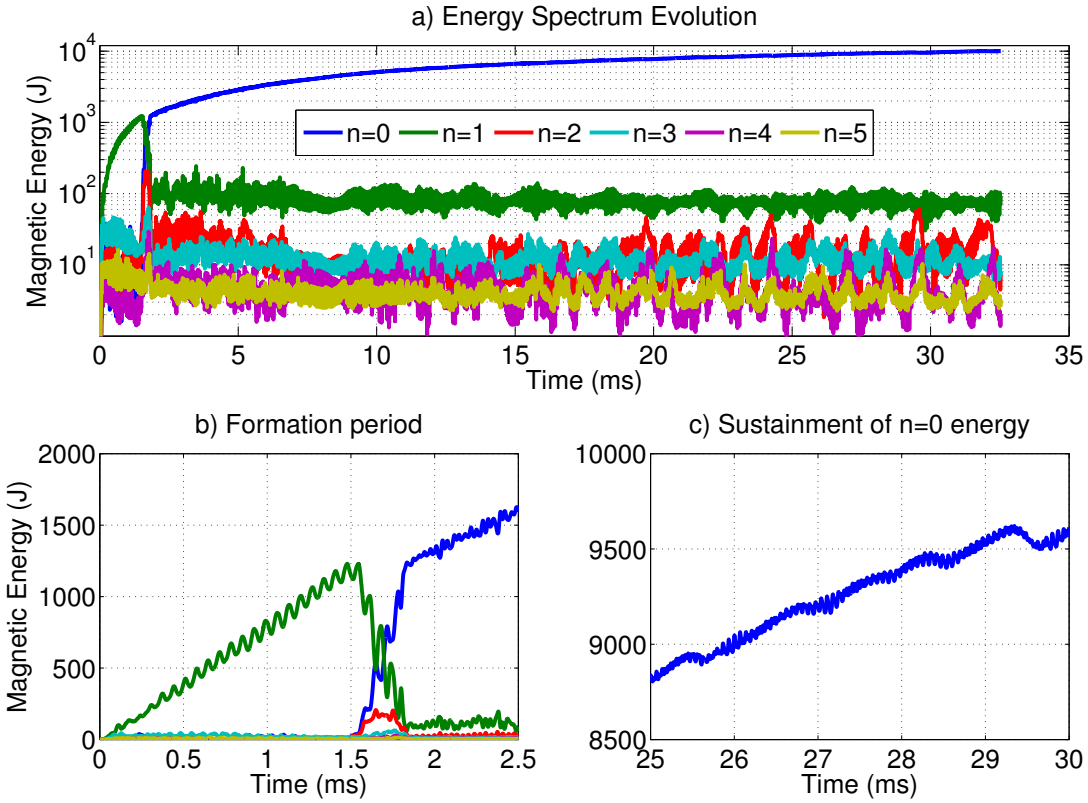

(a) Energy growth

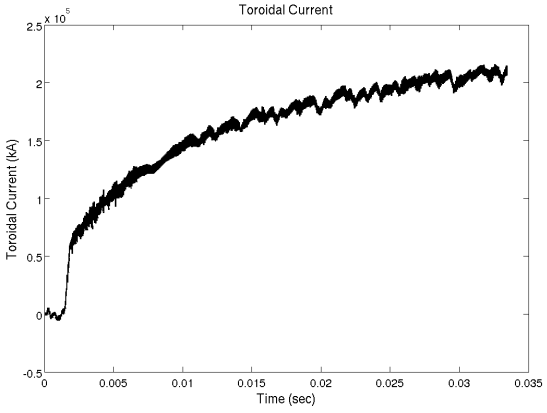

(b) I_{tor}

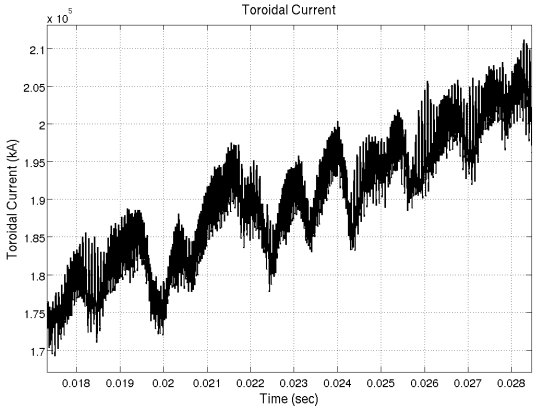

(c) Sawtooth behavior later in time.

Figure 5.1: The bulk energy and toroidal current growth for big HIT, as well as the sawtooth behavior at gain > 6.

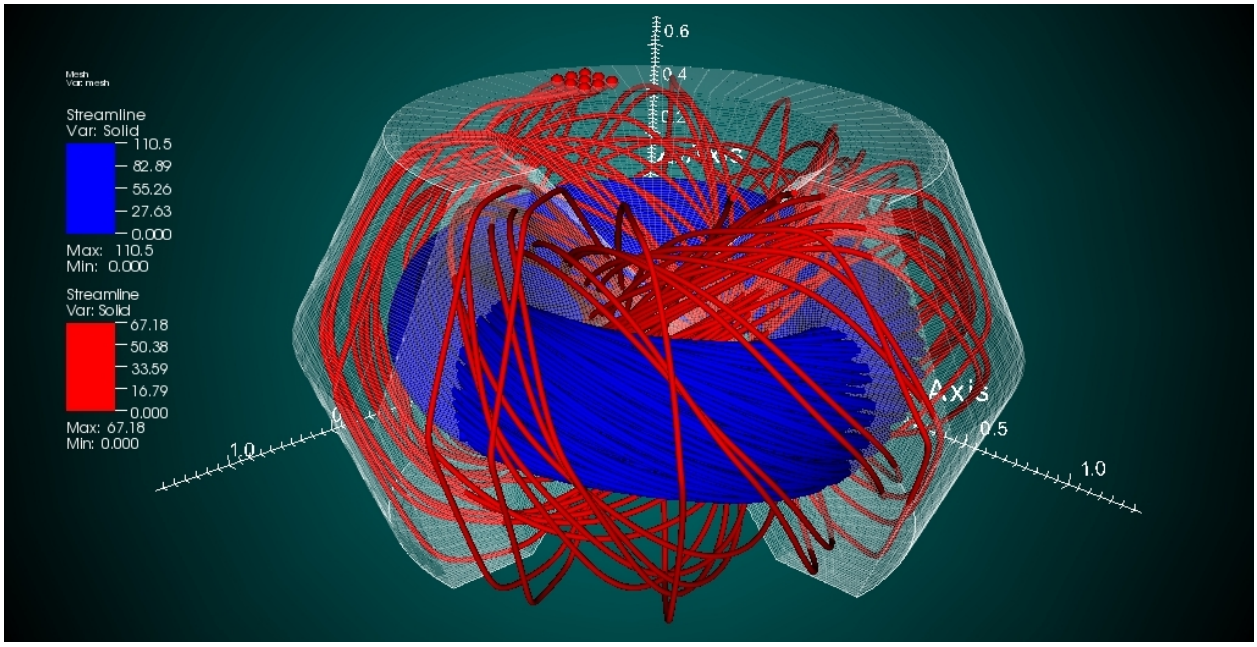

Figure 5.2: Streamlines of $\vec{B}$. The red lines originate at an injector mouth and wrap around the blue lines, which originate near the magnetic axis. This shows the closed flux nature of the magnetic structure.

ing the number of essentially infinitely long field lines when launched from simulation mesh points. We are able to see that during the closed flux period the poloidal flux at the magnetic axis decays at the L/R time of the plasma. This indicates that during this time, no current sustainment is occuring inside the closed flux surfaces. During this decay, the $|q|$ profile slowly becomes more peaked, eventually having $|q|_{max} > 1$ inside the domain. This creates a resonant surface for a $n = 1$, $m = 1$ kink mode, which appears to break apart the flux surfaces. Once the flux surfaces are dissipated a refluxing event occurs resupplying poloidal flux to the magnetic axis. After the refluxing event the closed surfaces form once again and the process repeats.

To visualize an event happening, Fig. 5.7 shows the cycle of this sawtooth behavior. The general evolution of the fields proceeds as follows:

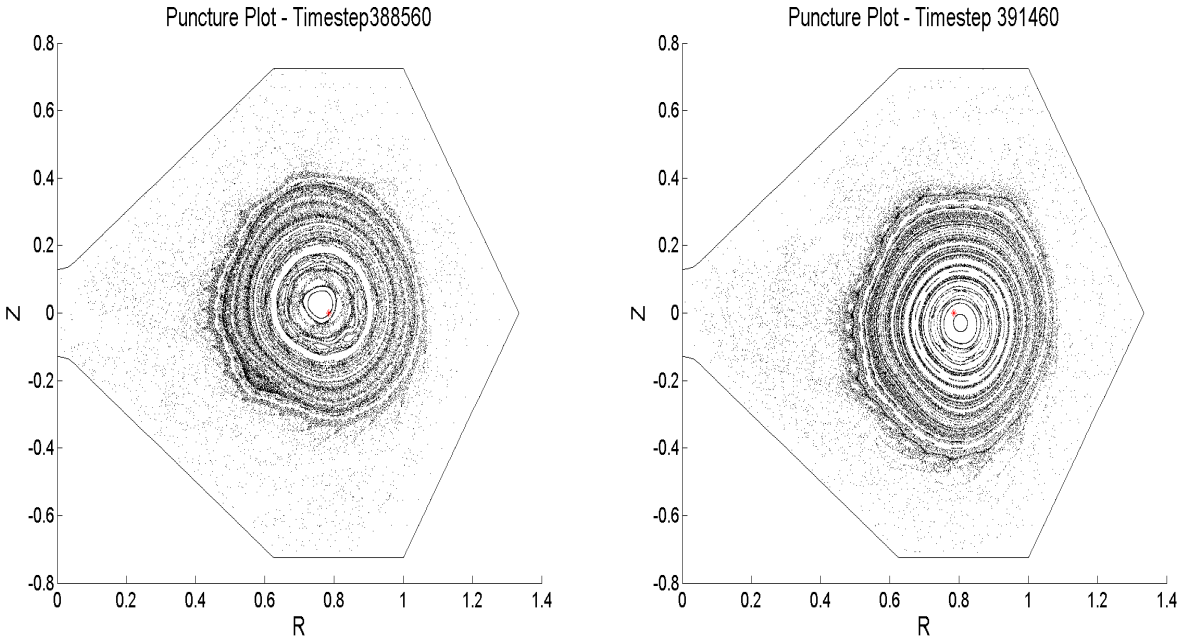

Figure 5.3: Poincarè puncture plots of $\vec{B}$ at two times one injector period apart. The red dot indicates the location of the mean magnetic axis, so we can see the motion of the flux surfaces.

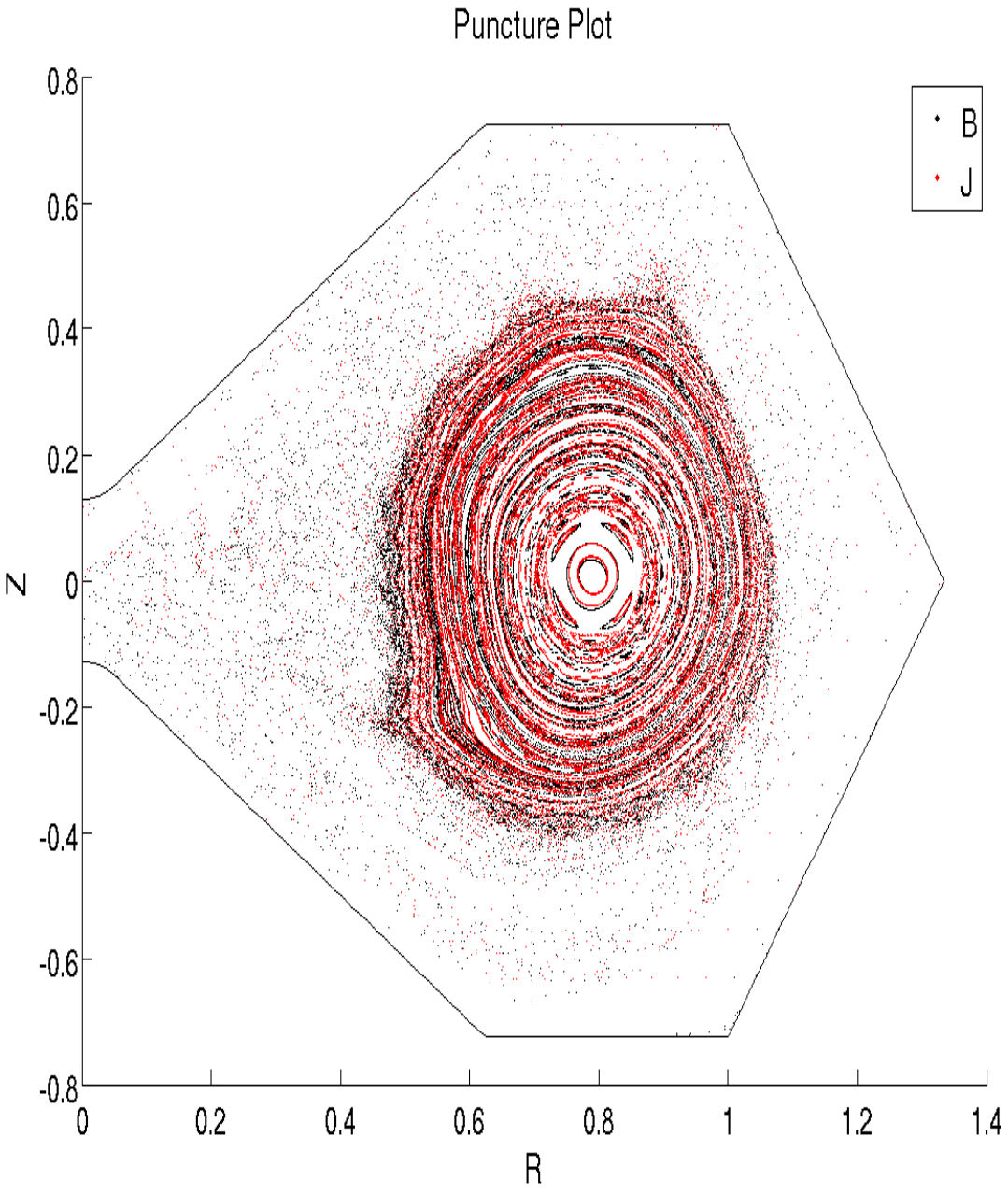

Figure 5.4: Poincarè puncture plots of $\vec{B}$ and $\vec{J}$. We can see that they are mostly aligned, though a small $\vec{J}_\perp$ exists.

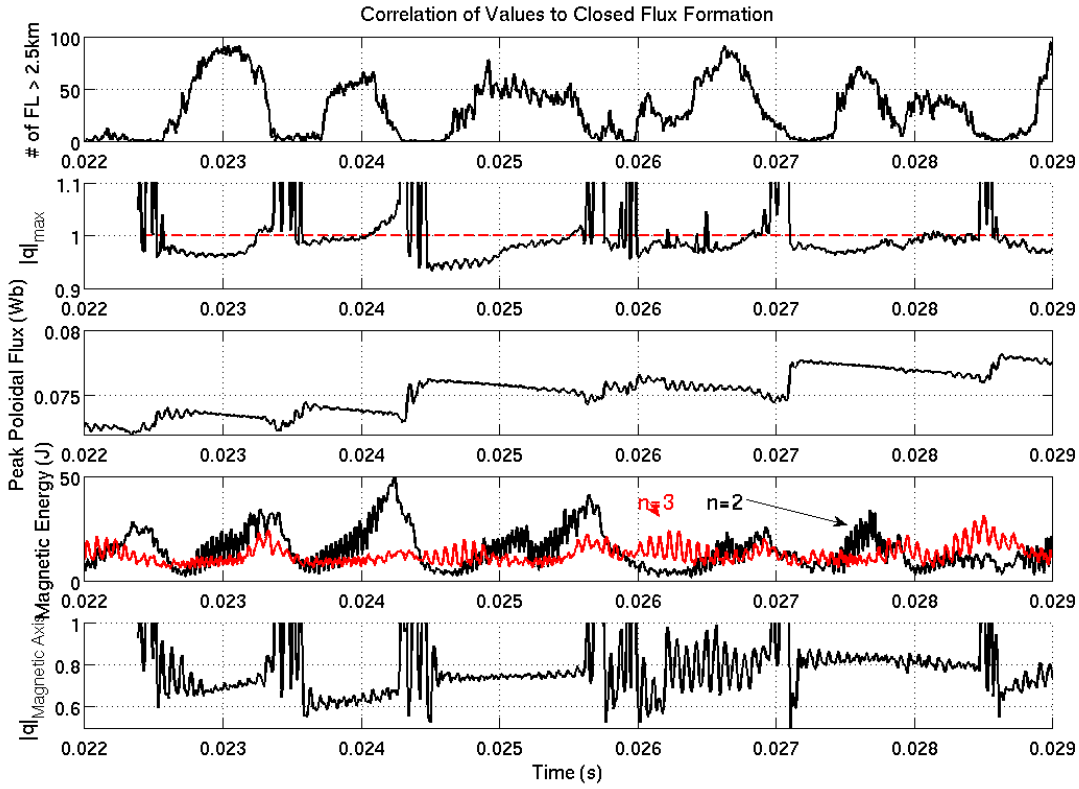

Figure 5.5: Various parameters during the sawtooth phase of the simulation. We can see closed flux surfaces form, last several injector cycles, then vanish when $|q|_{max} > 1$. During this a refluxing event occurs replenishing the poloidal flux near the magnetic axis. This refluxing event sees an increase in $n = 2$ and $n = 3$ activity.

1. Closed flux surfaces form and oscillate at ω_{inj}. This state is stable to both kink modes and injector activity.

2. The current inside the closed flux region decays, which raises q at the last closed flux surface, until the safety factor q becomes greater than 1.

3. A $n = 1$ kink instability occurs, which opens the flux surfaces. The opening of flux surfaces allows a refluxing event to occur, where the core current is replenished.

4. The closed flux surfaces reform.

To help understand the effect the injectors have on the persistance of these closed flux surfaces, we can restart the simulation at various points with modified parameters. The first parameter to be modified was λ_{inj}, which was modified by raising and lowering ψ_{inj}. This found that lower values of λ_{inj} (or higher ψ_{inj}) were able to sustain the closed flux for longer periods of time before the refluxing event occured. This is seen in Fig. 5.8. Of note is that an instability happens almost immediately, opening up the flux surfaces, if the injectors are turned off, indicating that the oscillating perturbation fields have a stabilizing effect on some instabilities the equilibrium encounters.

These simulations give the conclusion of helicty injected via SIHI is unable to trigger the IDCD effect and drive current in the region where magnetic field lines are longer than some critical length. There are several caveats to this conclusion, namely that IDCD relies primarily on electron dynamics while the eMHD equations neglect portions of the electron dynamics in the plasma. A full two-fluid implementation of big-HIT (or a device of similar paramters) would be a good test for the validity of these results, as no experimental measurements at these plasma parameters exist to compare the simulation with.

While being unable to drive plasma current along the long magnetic field lines is problematic from the perspective of a sustained spheromak fusion reactor, this formation of closed flux surfaces which are stable to the helicity injection is a positive result. One application of helicity injection, primarily CHI on NSTX [10] and LHI on Pegasus [31], is the

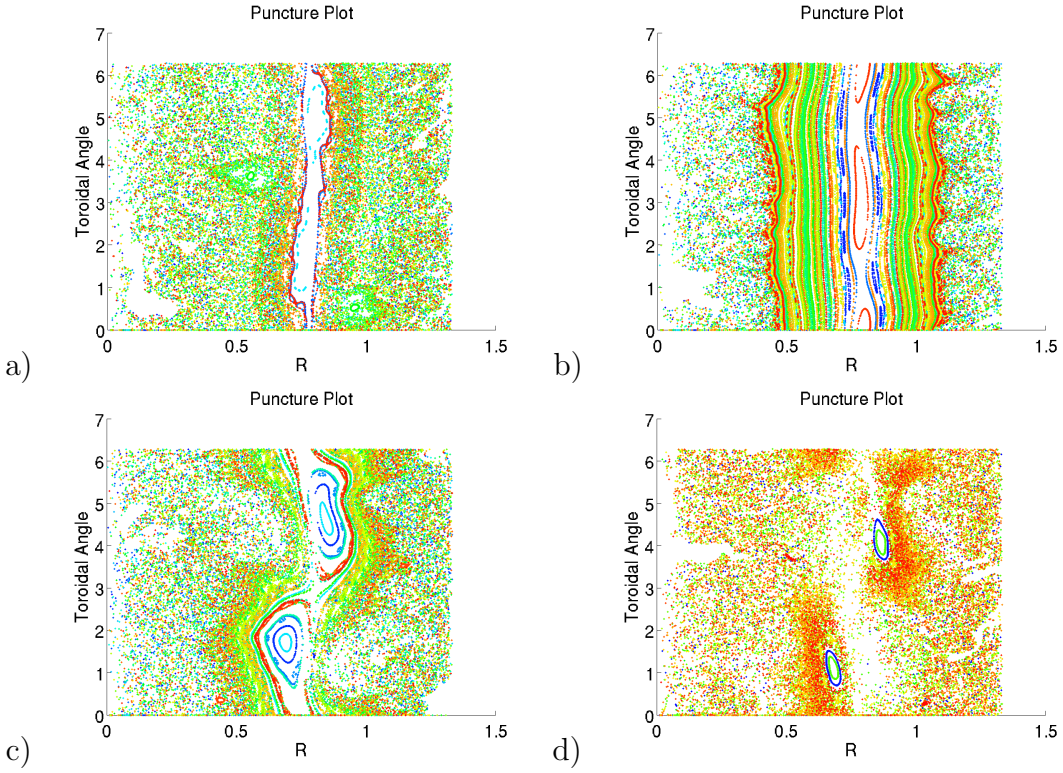

Figure 5.6: Puncture plots of the magnetic field lines at four instances during a closed-flux period. These punctures are taken on the $R-\phi$ plane at the geometric midplane ($Z=0$) to see the toroidal activity. a) Shows the initial formation, where the flux surfaces first form at the magnetic axis. b) Shows the axisymmetric object during the peak of closed field lines. c) Shows the kink instability that forms to break apart the surfaces and d) Shows the opened flux surfaces.

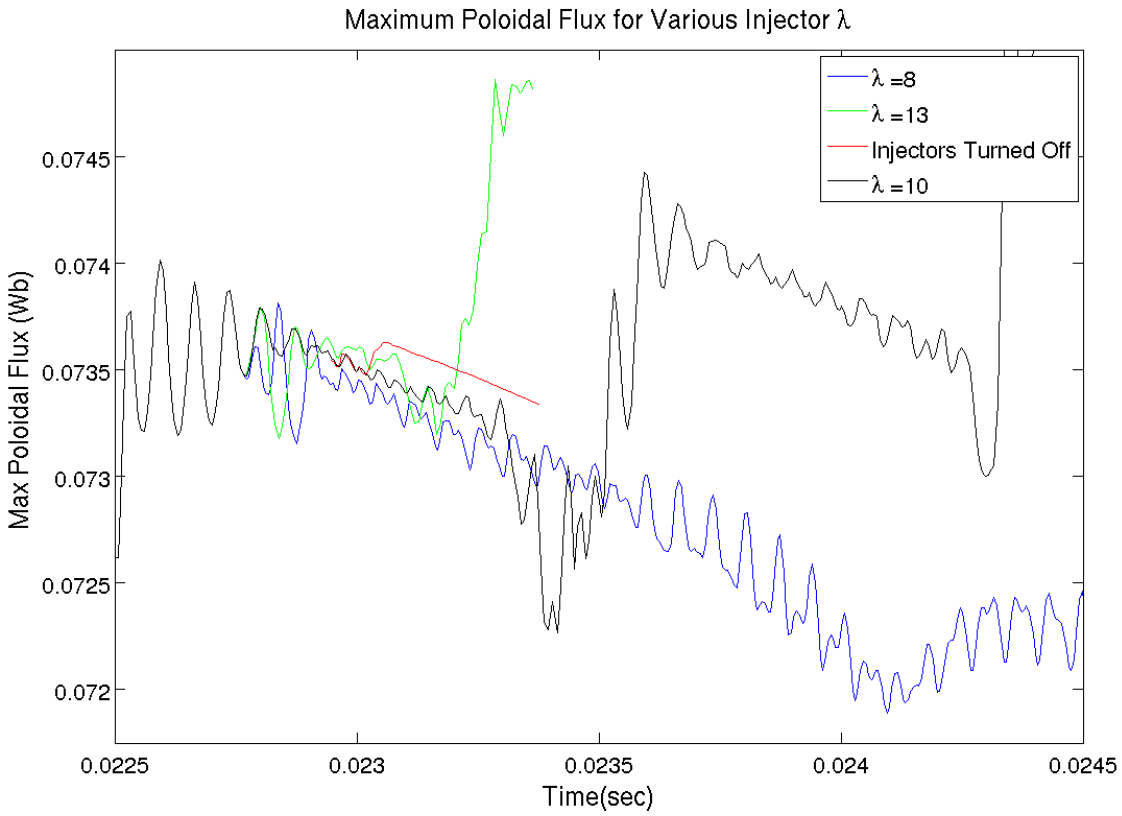

Figure 5.7: Poloidal flux decay during a closed flux period for different values of λ_{inj}. The linear decay is indicative of the closed flux persisting, and we see that at lower λ_{inj} the region lasts longer.

formation of warm plasma equilibria that can transition into other forms of current drive for total non-inductive sustainment. Recent results from tokamak plasmas have shown that 3-D perturbations (known as Resonant Magnetic Perturbations (RMPs)) can be used for stabilization of edge localized modes (ELMs) which are a hindrance from the operation of high performance plasmas. Since big-HIT shows the closed flux equilibrium being stable to a large perturbation ($\frac{\delta b}{B} \sim 10\%$) which would ordinarily be expected to open flux surfaces, it is conceivable that an attractive use of SIHI would be to combine both the formation and RMP equipment on a tokamak into one item. Results from HIT-SI3 (see chapter 4, [44], and [45]) inform us that it is possible to control the toroidal mode spectrum of a SIHI-produced magnetic perturbation.

5.1.1 Finite-β

The initial zero-β simulation of big-HIT allowed us to generate an equilibrium to use as an initial condition of a finite-β simulation. Using the single-temperature finite-β model described in Chapter 2, we are able to restart the simulation with a uniform T profile and allow the evolution to capture the final profile. Beginning with a uniform initial temperature of $T = 10$ eV, we allow the spheromak to decay as it heats up.

During this decay the dynamics show a lot of similarities to the zero-β case but a few key differences are observed, and are shown in Fig. 5.9 and 5.10. The same general structure of sawtooth behavior persists, with periods of closed flux that last about 1-2 ms being interrupted by kink-driven instabilities. However, while the zero-β simulation observed these kink-instabilities occuring at $q \sim 1.02$–1.05, the finite-β simulations typically do not see $q > 1$, which ideal MHD analysis says is the threshold. The signatures of these instabilities still appear to be $n = 1$ kink instabilities, indicating that non-axisymmetric and time-dependant components to the equilibrium can modify the q values where the instability resonates.

The high-gain equilibrium of big-HIT lends itself to numerically well-behaved split-temperature simulations, due to the NIMROD algorithm being optimized around modeling

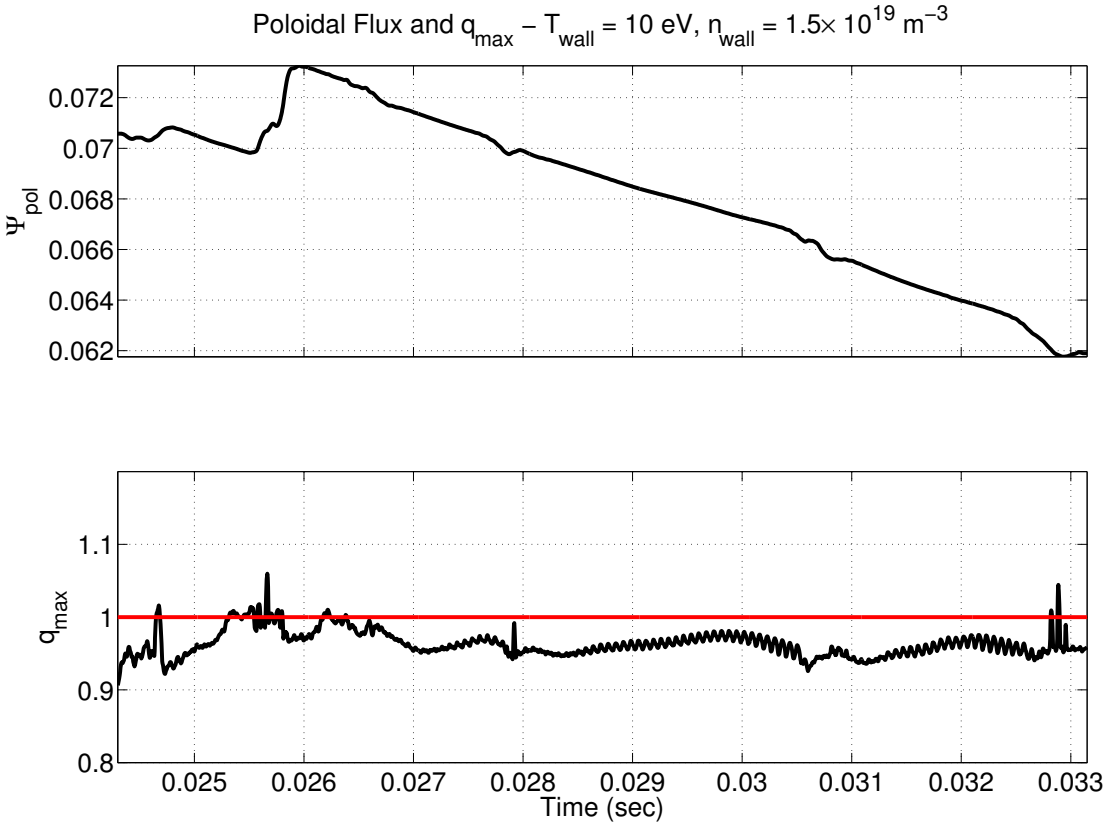

Figure 5.8: Evolution of the poloidal flux and q_{max} during the big-HIT finite-β decay. During the period between kink-events, can see that q_{max} does not go above $q = 1$, which is different than the zero-β case. Kink events are coincident with poloidal flux seeing activity that deviates away from resistive decay.

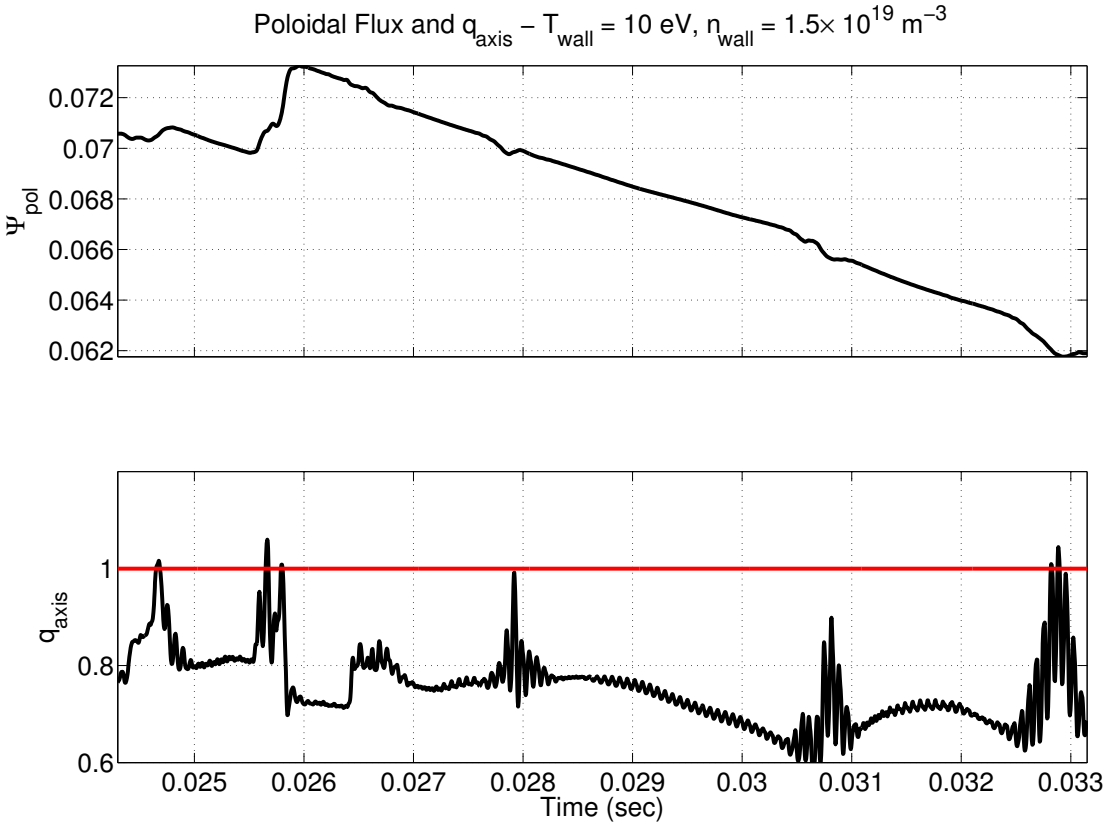

Figure 5.9: Shown is the evolution of the poloidal flux and q_{axis} during the big-HIT finite-β decay. During the period between kink-events, can see that q_{axis} oscillates between 2/3 and 4/5. Kink events are coincident with poloidal flux seeing activity that deviates away from resistive decay.

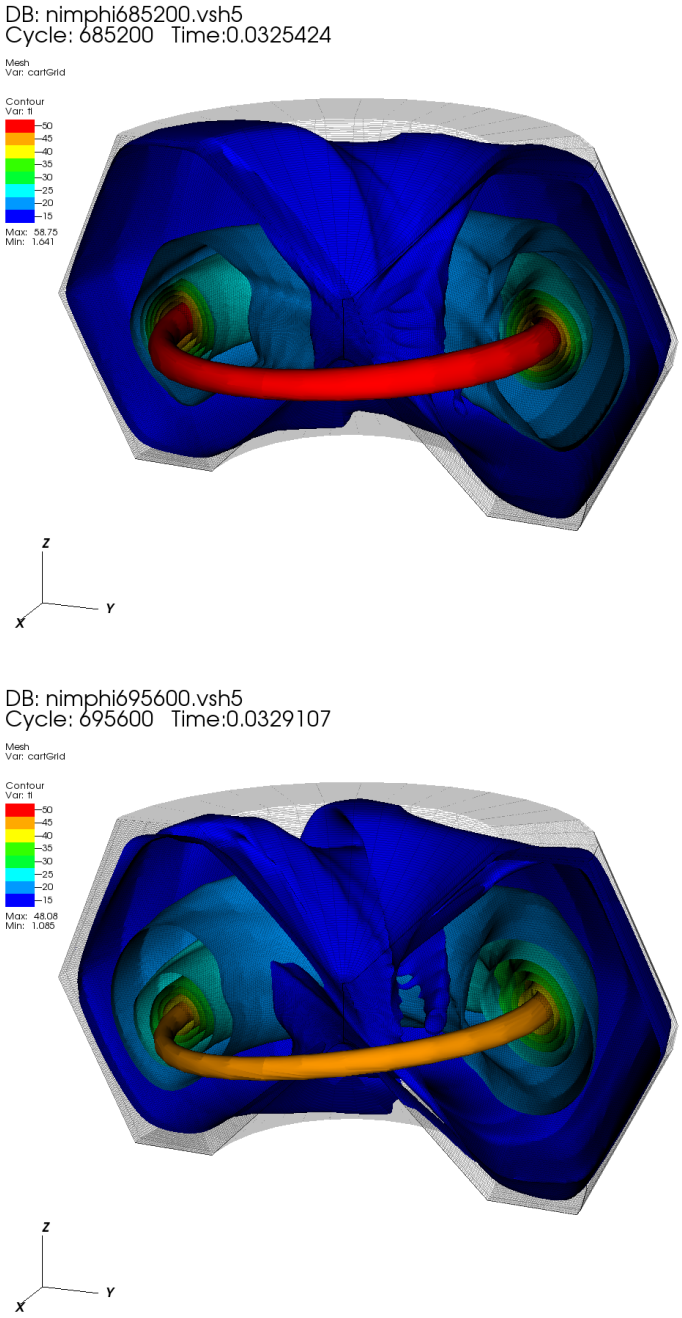

Figure 5.10: Top is the temperature profile that big-HIT obtains during the stable period of closed flux while bottom is during one of the kinking events seen during the decay. We can see in both cases the majority of the volume is cold ($T < 20$ eV), but the closed flux region is much warmer, with temperatures as large as 60 eV. During closed flux, the temperature profile aligns with the poloidal flux surfaces, deviating from a circle the same way the puncture plots do. During the kink events the temperature on magnetic axis reduces significantly.

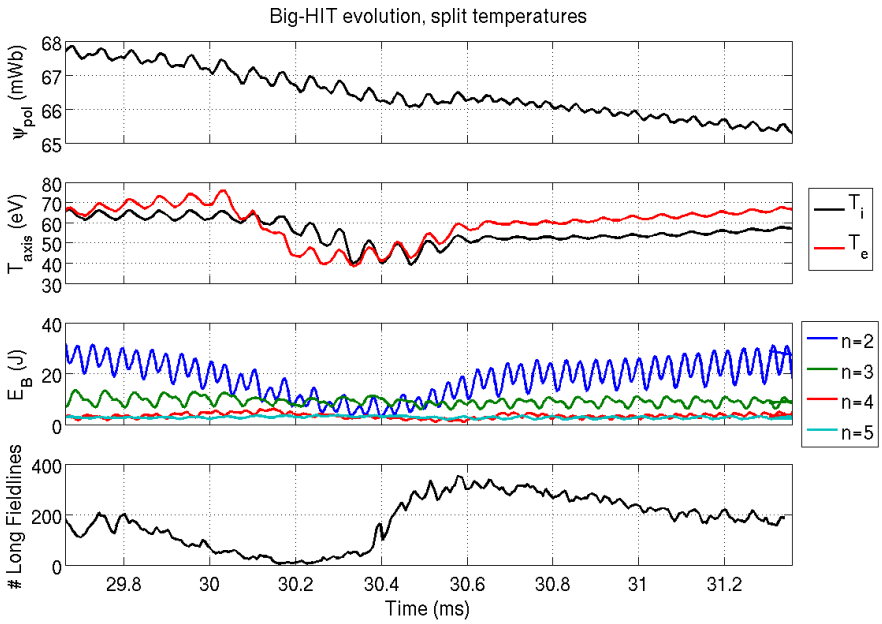

Figure 5.11: From top to bottom are the poloidal flux, temperature on magnetic axis, magnetic energy of $n > 2$ modes, and the 'closed-flux' nature of the fields.

of plasmas with large axisymmetric fields. A restart allowing for a refluxing event to occur was run with the full two-temperature model described in Chapters 2 and 3. In Fig. 5.12, we see that unlike HIT-SI and other sustained spheromaks, the closed flux equilibrium of big-HIT actually features hotter electrons than ions. This suggests a combination of increased energy confinement, expected from the closed field line structures, as well as a reduction in the viscous heating in the system. During the re-fluxing event, we see the electron thermal energy quickly leave the system, as would be expected from the high parallel thermal conduction.

Figure 5.13 gives a good idea of the poloidal structure of the equilibrium. We see that both λ and T_e appear to be flux surface quantities, with their shapes largely following the shape of the closed flux structures observed. Interestingly, as noted in the zero-β case, the λ profile decreases from the wall to the beginning of the closed flux region, but inside the

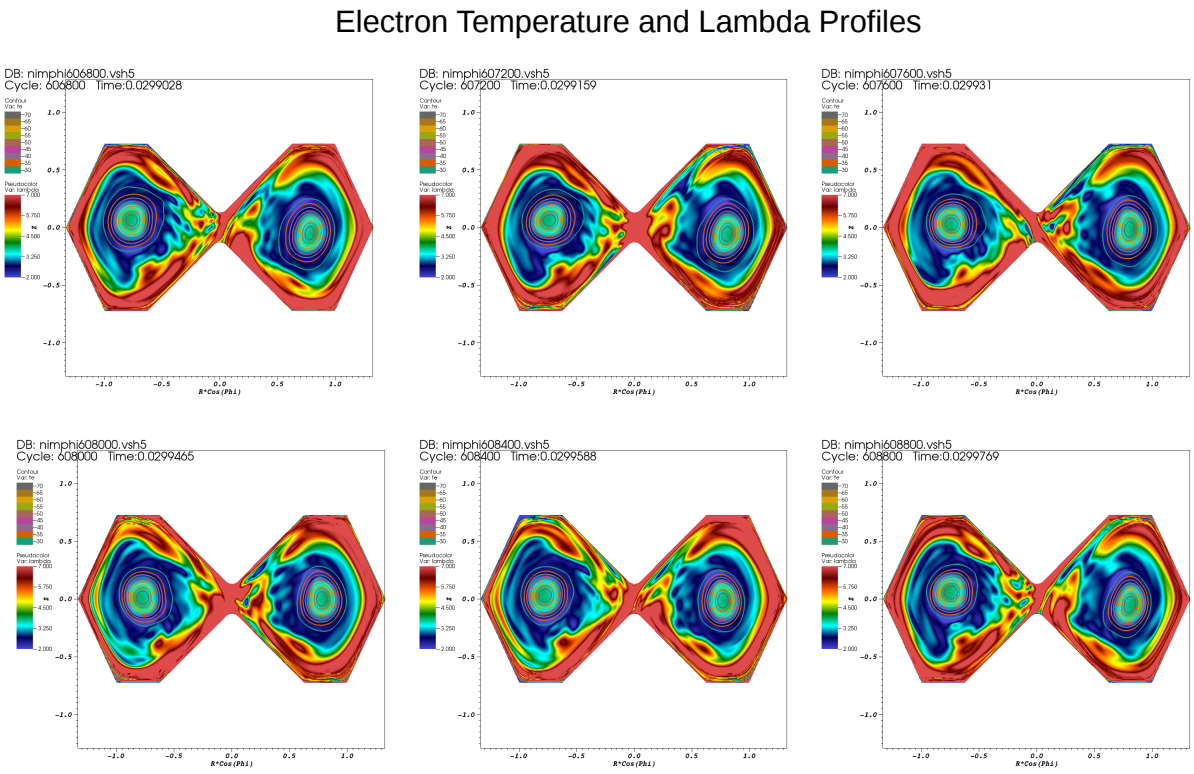

Figure 5.12: Contours of the electron temperature and pseudocolor of λ at 6 different time points during an injector period. The T_e contours are similar in shape to the closed flux structures that exist at this point in the simulation.

closed flux λ becomes peaked.

5.1.2 $n = 2$ Drive

The high gain equilibrium generated through this big-HIT calculation allows us to ask additional questions regarding the current drive mechanism. While the standard HIT-SI injector set imposes a toroidal $n = 1$ perturbation onto the volume to drive the toroidal plasma current, the poloidal spectrum of the current drive is unclear. We can restart the calculation with the high-gain equilibrium, but having adjusted the boundary conditions to drive a $n = 2$ shaped injector perturbation. The $n = 2$ perturbation is achieved by projecting

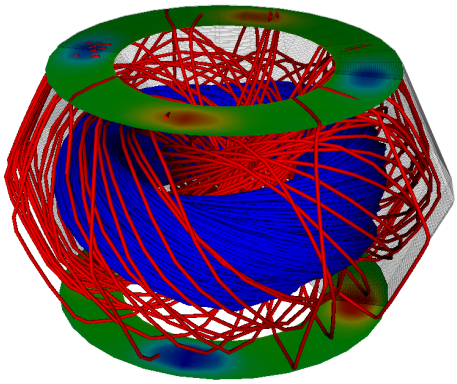

Figure 5.13: Field line traces from a period of closed-flux while the injectors are driven in an $n = 2$ orientation. The pseudocolor plots on the top and bottom of the geometry show the injector orientation, with the colors representing $\vec{B}_\perp$

the equivalent of both injectors onto both the top and bottom, so that each surface has four injector mouths that can be phased in an $n = 2$ way. Figure 5.14 shows both the boundary conditions and the field line traces during a period of closed flux.

The main result of the $n = 2$ drive simulation is that the bulk evolution is independent of the modal structure of the 3-D perturbation, only the details of the dynamics change. We see in Fig. 5.15 that the same general sawtooth behavior exists, with periods of resistive decay broken apart by refluxing events. Similar to the $n = 1$ drive, each refluxing event experiences different modal activity on the energy spectrum. In particular, we notice that the $n = 1$ activity is not the dominant or initial activity in all of the events, further bolstering our earlier claim that the instabilities have a 3-D nature, similar to the shape of the equilibrium.

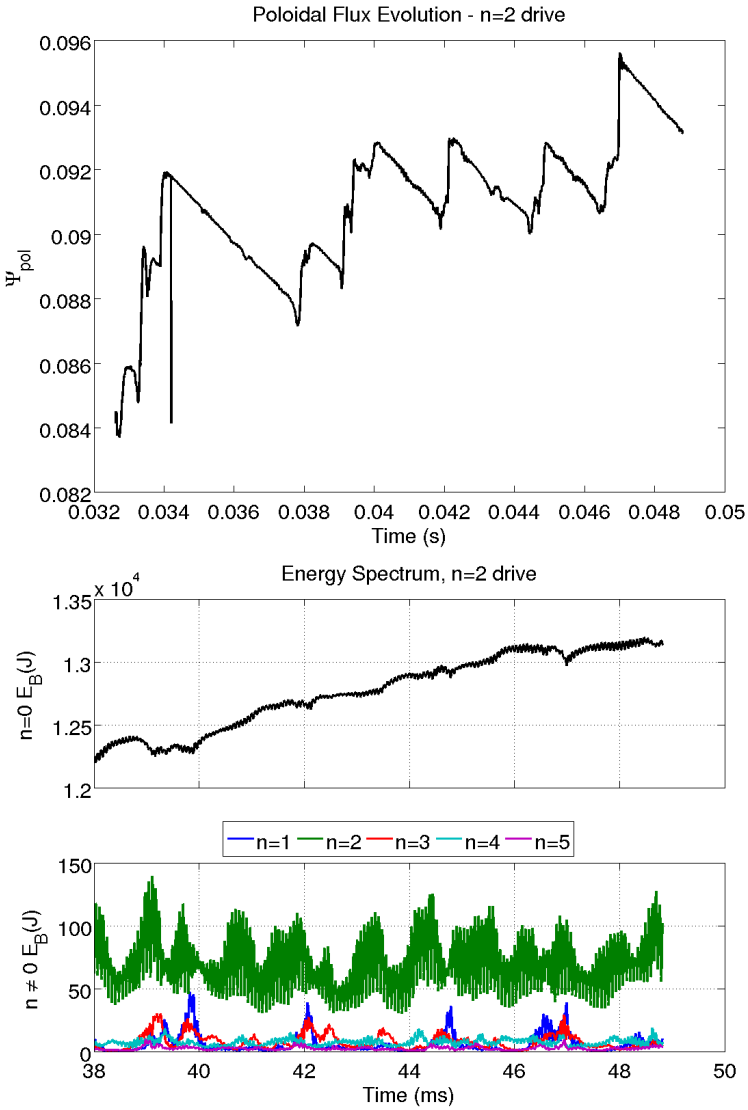

Figure 5.14: Top is the poloidal flux evolution with the $n = 2$ drive. Periods of decay at the L/R time are broken up by refluxing events. Bottom plot shows the energy evolution during these periods, where we see that each refluxing event has different modes get excited. Some (such as $t = 40$ ms) look like $n = 1$ dominated kink events while others ($t = 44$ ms) appear to transition from $n = 4$ dominated to $n = 1$ dominated.

5.1.3 Conclusions of Big-HIT

These simulations provided some insight into how we can expect high-gain equilibria to behave. First, they show that closed flux structures, often an important quality for confinement, are compatible with a large injector perturbation. Instead of forming a typical axisymmetric equilibrium, instead a dynamic state forms that sees oscillations at the injector frequency. The stability of these states to the injector perturbation can be seen from the closed flux structures persisting for as many as 20 injector periods. Additionally, these equilibria show a wide variety of non-axisymmetric structure, with the variety of high-m and n island structures seen throughout.

5.2 The HIT-TD Device

Initial simulations in an attempt to guide the design of a future device have been started. The two parameters of interest are the shape of the flux conserver and the injector toroidal mode spectrum.

5.2.1 Injector Manifolds

Future device designs implement a more customizable injector geometry which is referred to as a manifold. The manifold consists of a complete torus separate from the confinement region, with a series of injector ducts connecting the two torii together. These manifolds can be located on the top and bottom, similar to HIT-SI, or on the outboard midplane, with examples of these seen in Fig. 5.16. The attractiveness of this configuration is that it allows flexibility in the imposed perturbation spectrum. While the semi-toroidal injectors of HIT-SI and HIT-SI3 require that each injector opening into the volume has an equally opposite partner, the manifold allows the application of a wider variety of mode structures by relaxing that condition. The condition that the manifolds must satisfy is that the total current into the volume must be zero. An example of a mixed $n = 1$ and $n = 2$ configuration is seen in Fig. 5.17.

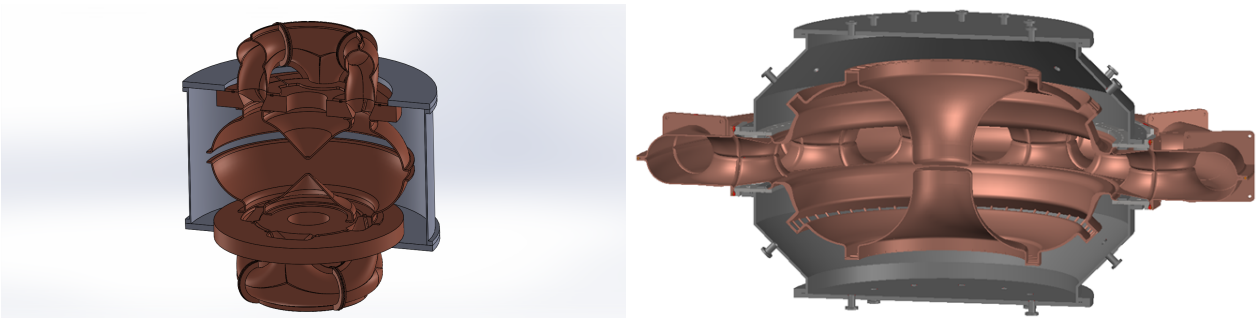

Figure 5.15: Two different injector manifold configurations. On the left is two manifolds located on the top and bottom of the confinement volume, while on the right a single manifold is located on the outboard midplane.

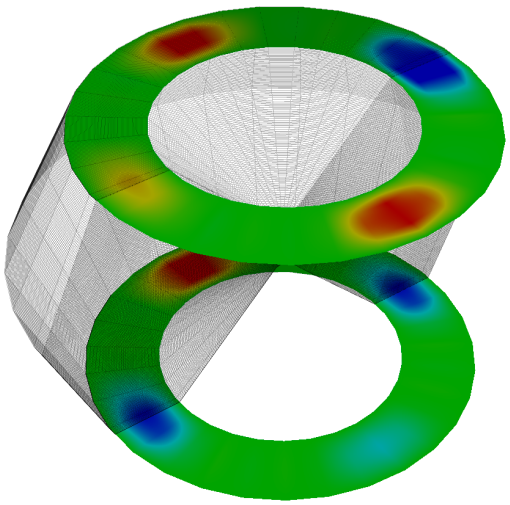

Figure 5.16: $\vec{B}_{\perp}$ with a top/bottom manifold design with the injector manifold configured for 50% n=1 drive and 50% n=2 drive. The total current through the surface is zero, though the magnitude of each mouth differs.

Number of injector mouths	λ_{inj} (m^{-1})	I_{tor}/I_{inj}
HIT-SI	19.61	2.44
4	13.47	1.99
4	18.68	2.21
4	19.39	2.43
4	21.82	2.34
4	24.95	2.45
4	27.99	2.56
8	20.18	1.91
8	26.10	1.99

Table 5.2: The current gain achieved for different values of λ_{inj} and different manifold configurations. The HIT-SI simulation serves as a baseline value using the plasma parameters (η, ν, n) used in the other simulations.

A starting place for understanding the influence of these injector manifolds is to operate a midplane manifold on the HIT-SI flux conserving shape, but operated with a $n = 1$ imposed perturbation. This case is used to confirm that the injectors located on the outboard midplane still correctly form a spheromak and sustain it. Two manifold configurations were used, one with 4 injector mouths and one with 8 injector mouths. The parameter scanned in each case was λ_{inj}, to see if the relationship between current gain and λ_{inj} varies at all. Figures 5.19 and 5.20 show the evolution of these cases, with Table 5.2 highlighting the current gains that were achieved in each case. We note that while the 4-mouth setup is able to closely match the gains achieved in comparable HIT-SI simulations at the same λ_{inj}, the 8-mouth configuration does not.

Injector impedance can describe the difference between the 8-injector and 4-injector configurations. The current was kept the same between the two cases, but with a shorter path

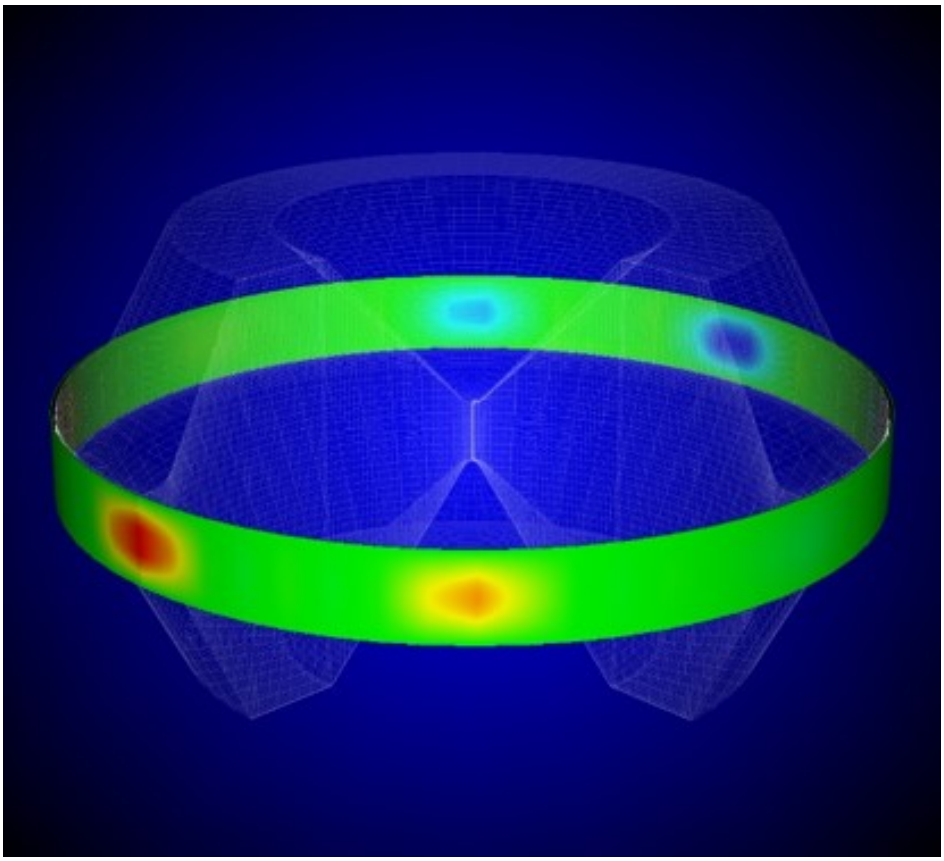

Figure 5.17: $\vec{B}_{\perp}$ with a midplane injector manifold on the HIT-SI3 experimental geometry.

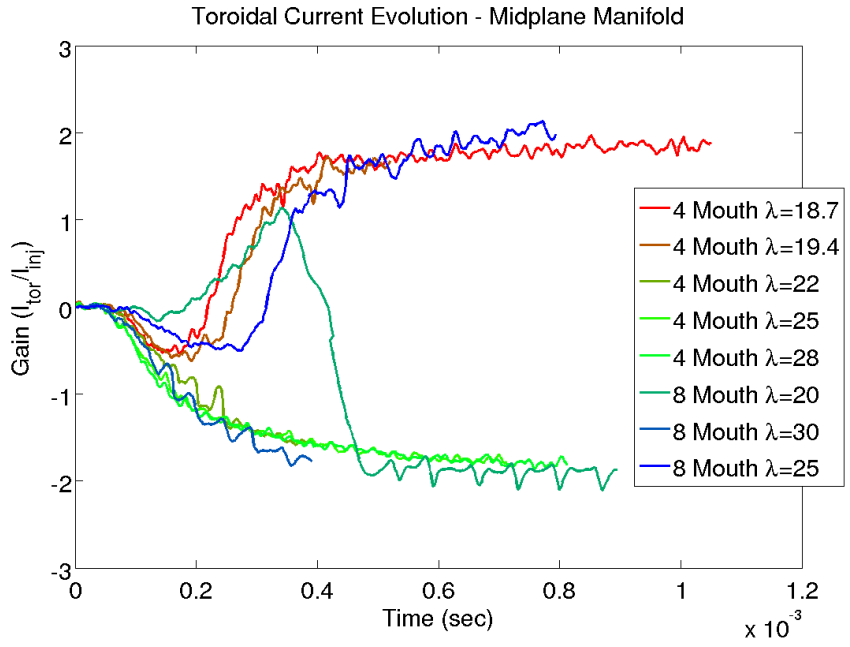

Figure 5.18: Toroidal current for the midplane manifold simulations performed.

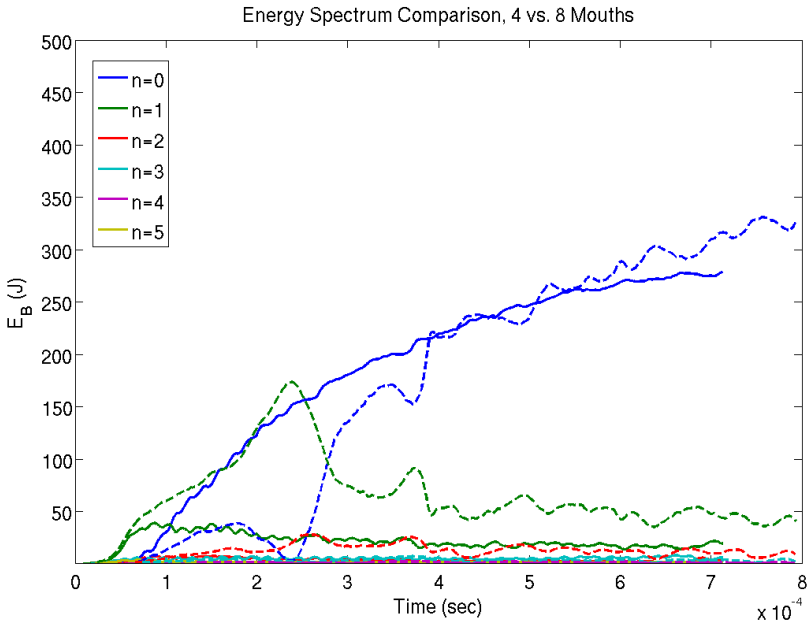

Figure 5.19: Energy spectrum observed when operating with four and eight injector mouths. Dashed lines indicate the simulation with 8 injector mouths.

to travel between the injector mouths we expect a lower impedance and thus a lower voltage between the injector mouths. Noting the helicity injection rate is $\dot{K}_{inj} = 2V_{inj}\psi_{inj}$, the 8-injector case is then injecting less helicity into the volume, and thus with equivalent resistive dissipation in the volume reaches a lower-helicity final state.

Additionally, these midplane simulations allow us a very clean picture to highlight the result that the injector fieldlines align with the equilibrium fieldlines in their path through the volume. Figure 5.21 shows this, where the $n = 1$ perturbation seen in the volume is consistent with the path that the injector currents would take to align with the spheromak currents.

To conclude, we find that a set of injectors located on the midplane of the geometry are successful at forming and sustaining HIT-SI-like spheromaks. This is a promising confirmation of what was expected, that helicity conservation allows flexibility on the location and geometry of the helicity injection system. Looking forward, the role of complex structures of poloidal and toroidal dependence on the injector geometry can be explored experimentally with a set of injector manifolds.

5.2.2 Flux-conserver Shape

One limitation of the bow-tie shape that HIT-SI and HIT-SI3 employ is the β limit of equilibria. While HIT-SI has a Mercier β limit of $\sim 3\%$, shapes closer to a circular design are able to achieve $\beta \sim 10\%$. Figure 5.16 shows two different variations of the circular shapes. As fusion power scales with $\beta^2 B^4$, optimizations to the flux conserver shape are important for the eventual goal of power generation. Since imposed dynamo current drive is reliant on the 3-D structure of magnetic perturbations on the edge of the plasma, which in turn rely on the shape of the flux conserving geometry, there is a question of the current-drive efficiency between different geometries. Because the zero-β NIMROD model is able to obtain the correct current gain, with an assumed η in the experimentally measured range, we can use it to perform testing of the feasibility of these high-β shapes.

We performed initial simulations that compared several shapes with the HIT-SI injector

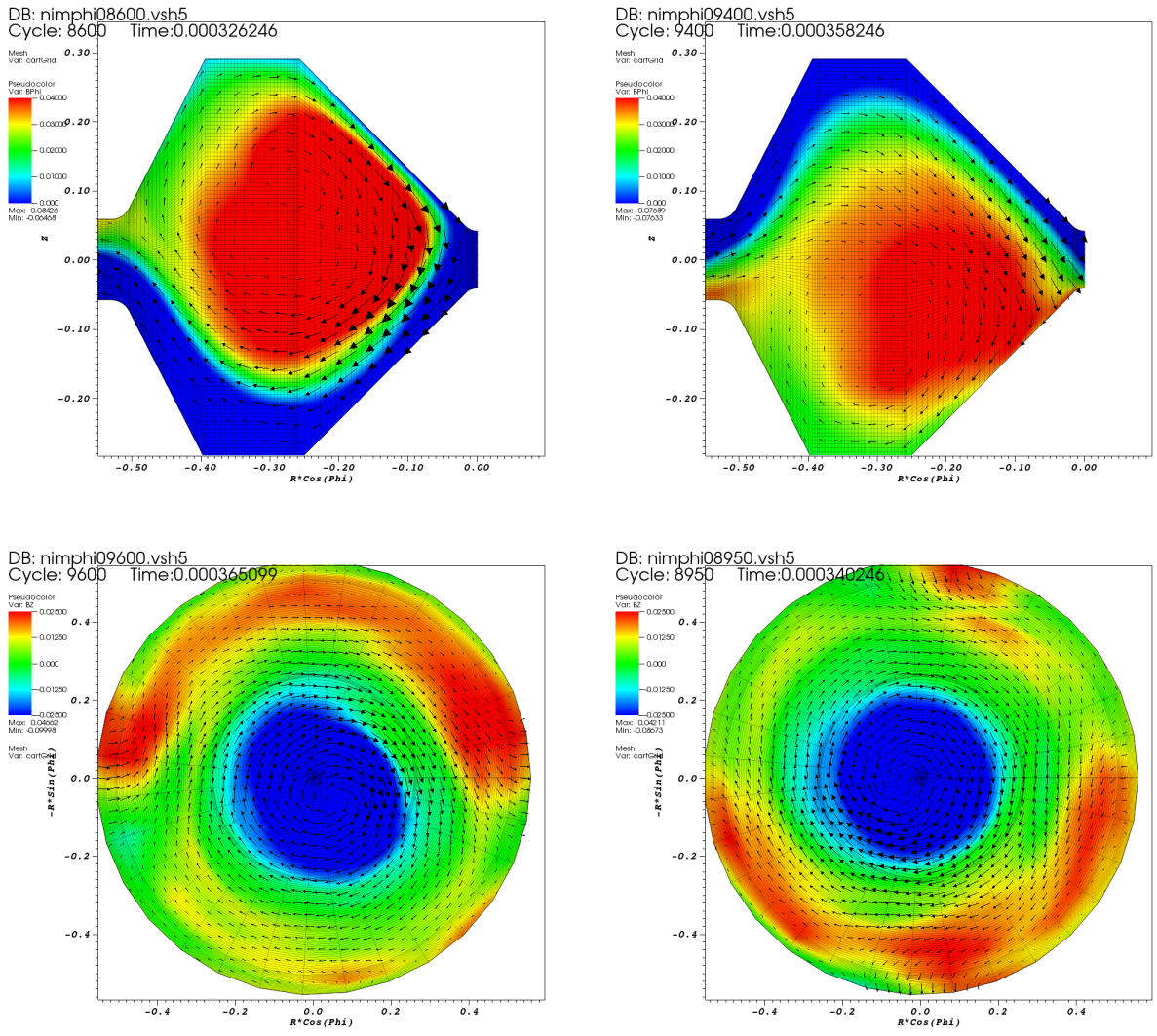

Figure 5.20: $\vec{B}$ from a midplane (top) and poloidal (bottom) view at two different times in an injector cycle. Arrows correspond to component in the plane, while pseudocolor corresponds to the perpendicular component. We can see that the injector fields, which originate from the outboard midplane gap, align with the equilibrium fields.

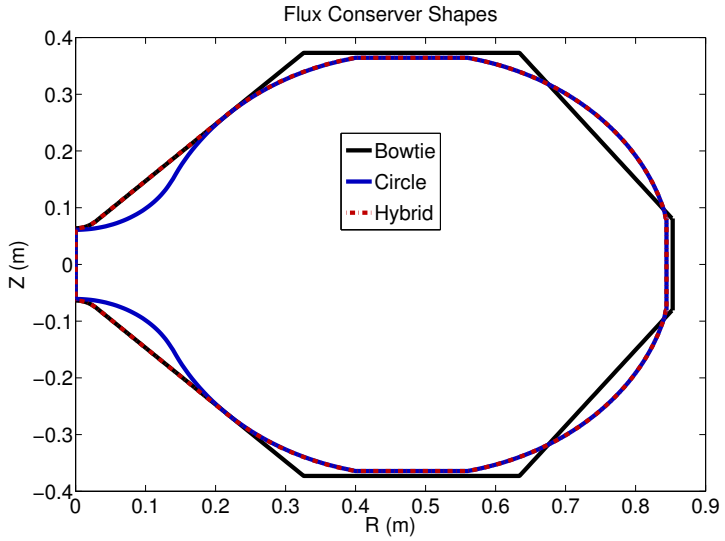

Figure 5.21: The three shapes of flux conserver that were tested in NIMROD. Each case features three flat surfaces to allow for top, bottom, and midplane injector manifold structures. The bowtie shape is the most analogous shape to HIT-SI, while the circular shape was designed around optimizing β. The hybrid shape undergoes a smooth transition between the two shapes.

configuration, while keeping the dominant size parameters ($R_0 = 85$ cm, $L = 75$ cm) constant, at a 40% increase in size over HIT-SI. A resistivity assuming a temperature of $T_e = 50$ eV is used, to allow the spheromak to reach high current amplification. The first of these shapes is the bowtie configuration, which is used as a baseline for performance of the current drive. As we saw with the big-HIT simulations, the current amplification scaling with η is not sensitive to geometry size, so a bowtie simulation should work fine. The other two shapes are based on the two flux conservers shown in Fig. 5.16, and all three can be seen in Fig. 5.22.

Evolution of the three cases during initial formation can be seen in Fig. 5.23. The bowtie geometry behaves as would be expected at this size and resistivity, initially forming a $n = 1$ state then relaxing into a spheromak object that then grows at $\tau_{L/R}$. This is in contrast with the two cases of circular-shaped outboard side to the flux conserver, where we see that

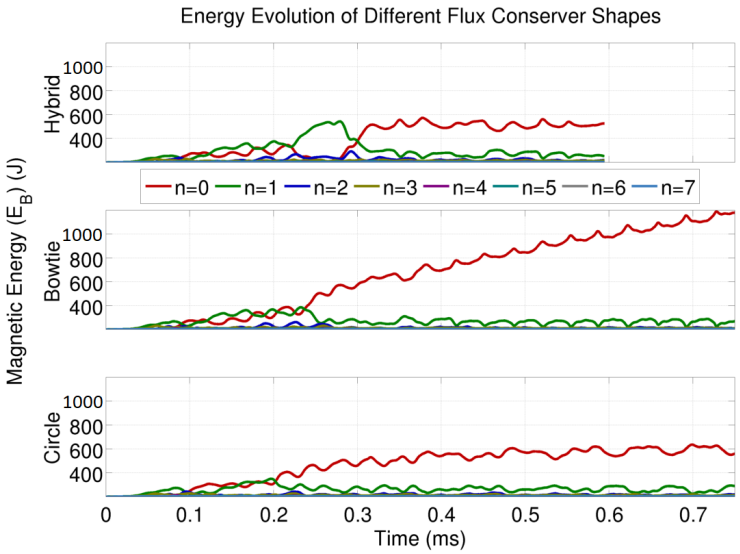

Figure 5.22: Energy spectrum evolution for the three flux-conserver shapes examined.

the energy reaches a balance at both a timescale much shorter than $\tau_{L/R}$ and a lower energy level than the bowtie case. Looking at the individual current-drive terms from Eq. 3.2 in Figure 5.24, we see that while the bowtie case resembles a standard HIT-SI simulation, in this case the transition region from low to high f_{inj}, both the circle and hybrid shapes see the dynamo terms drive equal amounts of current both directions. Figure 5.25 gives us more detail as to the differences, seeing that in the hybrid case less current is driven by the MHD dynamo and in the hall case more anti-current is driven.

These simulations lead to an interesting and unexpected conclusion. While previous thoughts regarding helicity conservation and HIT-SI have found that the evolution is only sensitive to the injector flux, voltage, and current, these simulations find that the shape of the flux conserver can play a role. The complex poloidal shape of the bowtie, compared with the circular shapes, appears to resonant a richer spectrum of poloidal modes which can contribute towards the current drive mechanism.

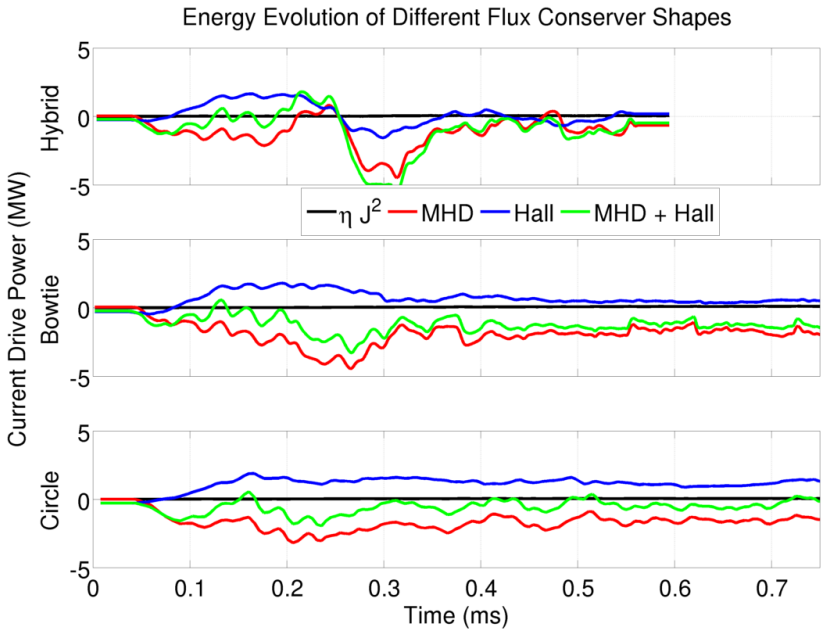

Figure 5.23: $\int \vec{E} \cdot \vec{J}_0 \mathrm{dV}$ for different terms in Ohm's law during the formation of the spheromak in HIT-TD simulations. In all three cases the toroidal current is not significant enough so $\eta J^2 \ll \vec{V} \times \vec{B} \cdot \vec{J}$.

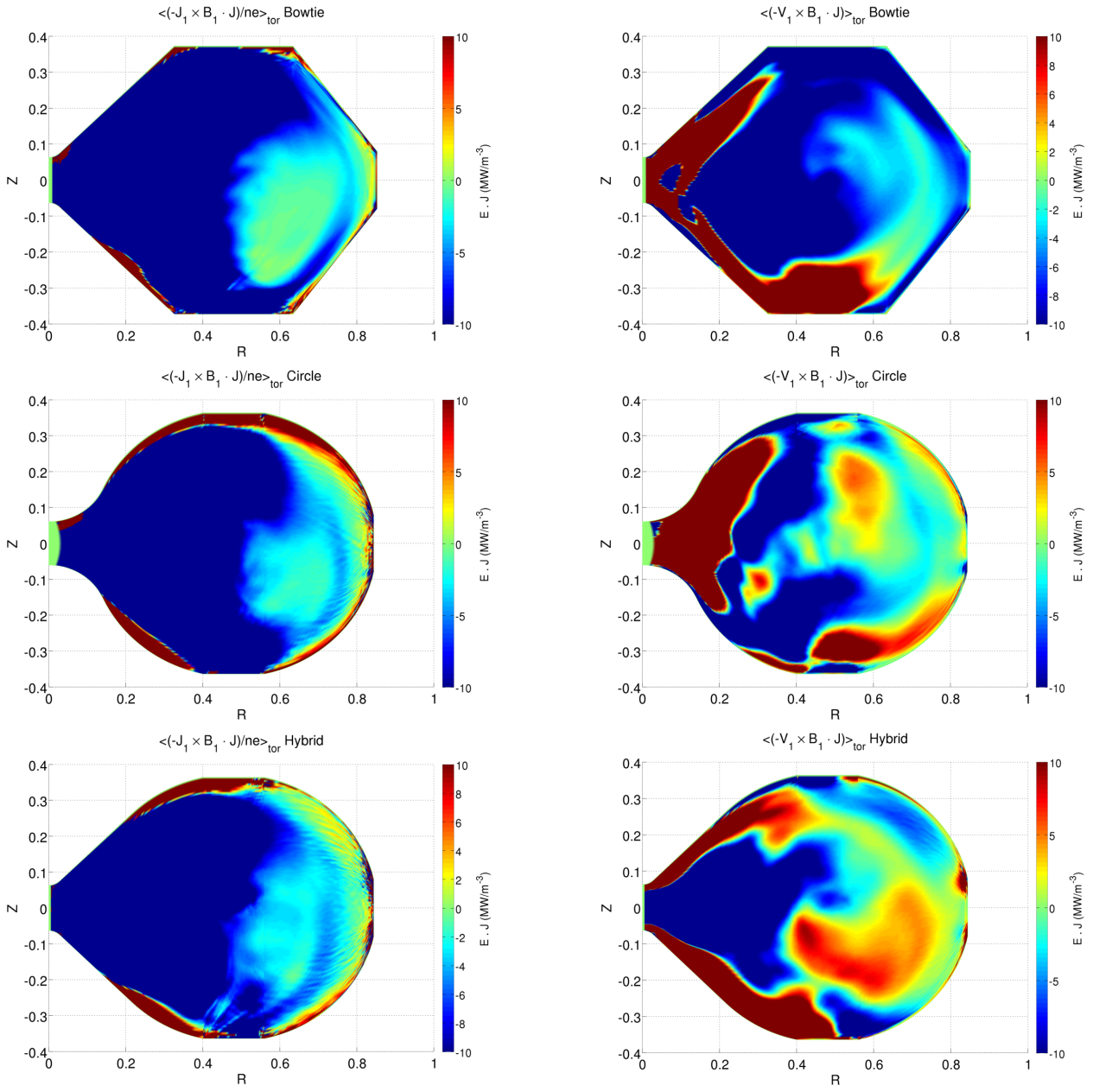

Figure 5.24: Pseudocolor plots of the toroidally- and temporally-averaged dynamo current drive power densities for the $n = 1$ fields. Negative values indicate driving current parallel to the spheromak, while positive values indicate anti-driven current. The expectation is that anti-current drive near the edge is indicative of the injectors losing energy/helicity, while drive in the core is sustaining the spheromak. We can see that while all 3 flux-conserver shapes have similar spatial profile of the Hall term, the MHD dynamo sees anti-current drive near the magnetic axis in the two circular cases that the bowtie shape does not see.

5.3 HIT-SI3 with Toroidal Field Coils

The HIT-SI and HIT-SI3 devices were constructed with the capability for toroidal-field coils to be added, in the event of wanting to study this helicity injection scheme on the formation of a tokamak equilibrium. A small scale study was performed to get an initial scaling expectation. If the experiment was to be modified for TF-Coil operation, a $R \sim 2.5$ cm copper rod would be inserted down the geometric axis of the flux-conserver to allow an external current to be driven inside the copper shell, the 2-D shape of this flux-conserver is seen in Fig. 5.26. A set of 4 simulations that scanned the magnitude of this toroidal field were run using the $0-\beta$ model discussed in chapter 2 with the HIT-SI3 injector boundary condition operating at $I_{inj} = 24$ kA and $\lambda_{inj} = 20$ m^{-1} and the $0-120-240$ injector phasing. It was run at similar parameters (η, ν) as previous $0-\beta$ studies of HIT-SI and HIT-SI3, with the primary difference being the addition of a $B_{tor} = B_0/R$ field, analagous to one that would be supplied by an external coil. Table 5.3 shows the values used in these simulations.

In order to make the simulation geometry more consistent with this external coil, the simply-connected nature of the flux conserver was removed, with a conducting medium closing the gap at $R = 0$. This changes the minimum energy state of the volume, making the Taylor MECH state no longer axisymmetric, and instead having an $n = 1$ shape. Applying the axisymmetric B_{tor} allows the drive of an axisymmetric state, though there is a threshold B_0 that if less than the $n = 1$ state still dominates the dynamics.

To see the bulk evolution of the simulations, Fig. 5.27 shows the toroidal current evolution and Figure 5.28 shows the energy evolution. Similar to standard HIT-SI3 discharges, these simulations begin from a vacuum field and are allowed to relax into their final equilibrium. As would be expected from an external field being applied, the relaxation of the equilibrium occurs almost instantaneously, with the toroidal current quickly rising. In the two 'weak' toroidal-field cases ($I_{TF} \sim I_{inj}$), the $n = 1$ minimum energy state of the flux conserver ends up growing and becoming a significant part of the final equilibrium. This is in contrast to the 'strong' toroidal-field cases ($I_{TF} > I_{inj}$), where the final energy spectrum is similar to a

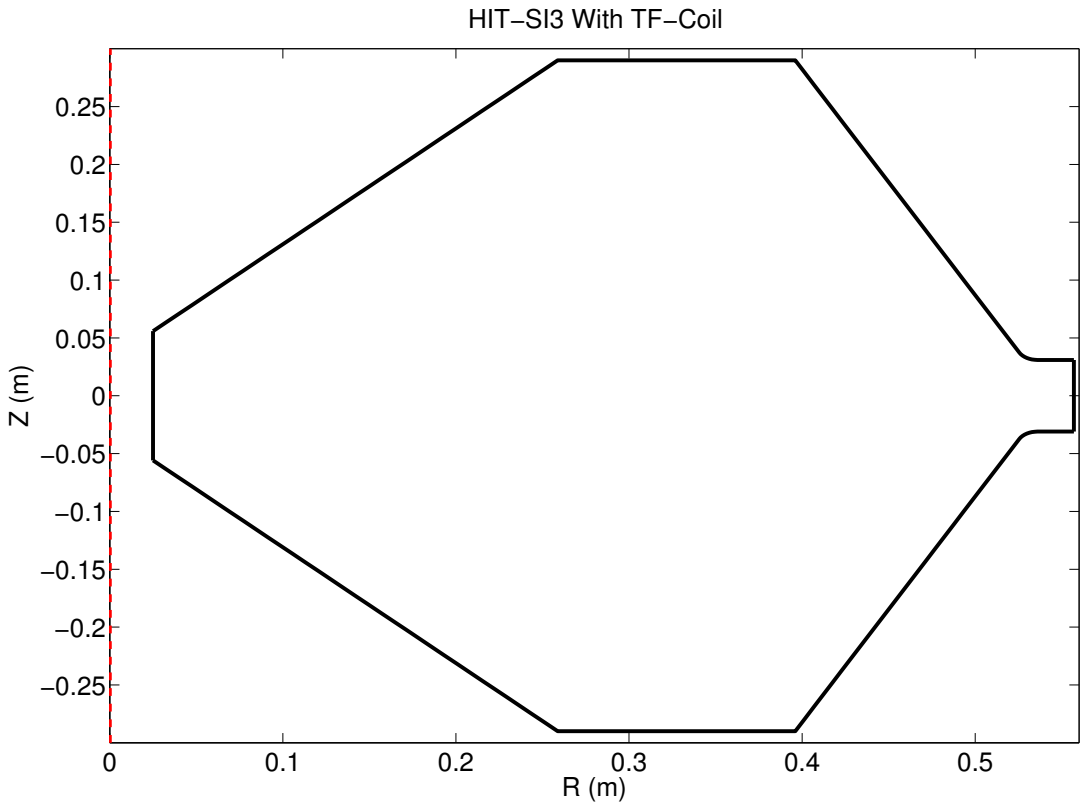

Figure 5.25: The HIT-SI3 bow-tie flux conserver with an $R = 2.5$ cm short down the geometric axis.

Simulation Number	B_0 (mT)	$I_{TF}(kA)$
1	3	15
2	6	30
3	12	60
4	24	120

Table 5.3: The different toroidal magnetic fields used in the simulations of toroidal-field effects. The I_{TF} refers to the amount of current that would need to flow through the center of the device to generate the desired field.

standard HIT-SI3 discharge, which in this case is a mixture of $n = 1$ and $n = 2$. As would be expected, increasing Φ_{tor} similarly increases the magnitude of I_{tor} in the final equilibrium that forms.

One interesting result of these simulations is the significant difference in the magnetic profile between the $I_{TF} = 60$ and 120 kA cases. Figure 5.29 shows the first of these exhibits $q < 1$ everywhere, more indicative of a spheromak profile, while the second case exhibits $q > 1$ everywhere, more indicative of a tokamak profile. In both of these cases a IDCD-like λ profile is seen, with high edge-λ and low core-λ. Since the current gain increases with the magnitude of the toroidal field, this indicates it may be feasible to do experimental tests of spontaneous closed-flux formation in plasmas sustained with IDCD at gains comparable to big-HIT on the presently built HIT-SI3 device with a relatively minor upgrade to enable the toroidal field coils.

A modification to the HIT-SI3 device to experimentally explore this setup is currently being designed, though the realized device will likely have key differences than the version simulated. First, the experimental design will likely not have a complete poloidal conducting loop, instead having a insulating gap at the geometric axis between the two small cones. Second, since the soak-through time of the copper flux conserving walls is not significantly larger than the shot duration, modified boundary conditions to correctly simulate the toroidal field soaking into the walls would likely be necessary. O'Bryan [31] demonstrated the implementation of a similar constraint on simulations performed of the Pegasus experiment at University of Wisconsin.

To conclude, some initial predictions regarding the addition of an externally applied toroidal field were made using simulations. We found that both spheromak-like and tokamak-like states can be formed, based on the magnitude of externally applied field. This provides a useful tool to apply experimentally, as it would be the cheapest method to study plasmas with a higher current amplification, with gains close to where closed flux was observed in simulation appearing possible.

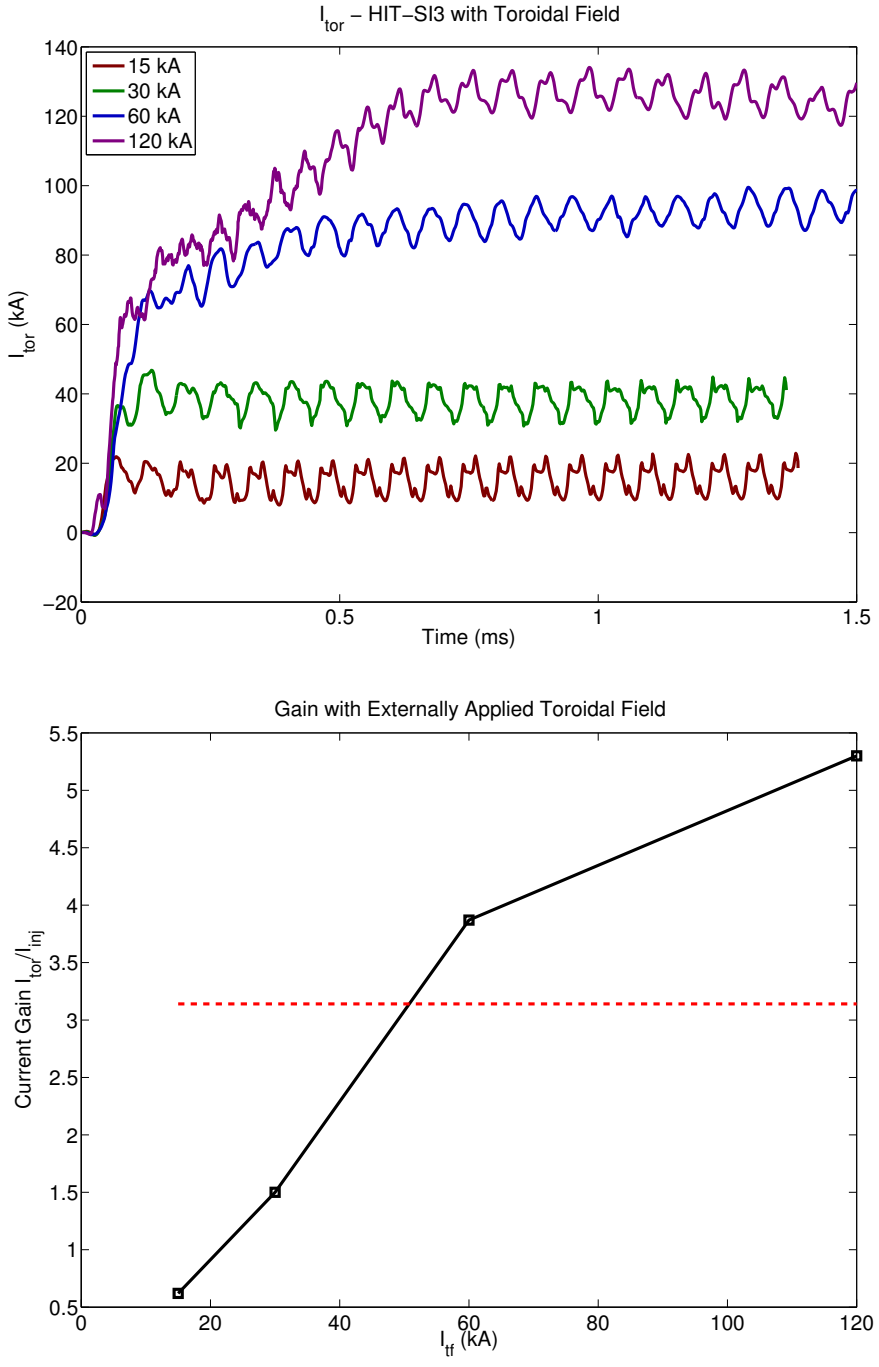

Figure 5.26: Top is I_{tor} from each simulation as the magnitude of the externally applied toroidal field is increased. Each case had $I_{inj} = 24$ kA. Bottom is the current gain, where we see that $gain > 1$ occurs near $I_{TF} = I_{inj}$. The red dashed line is the current gain that an equivalent standard HIT-SI3 simulation without TF-coils would achieve.

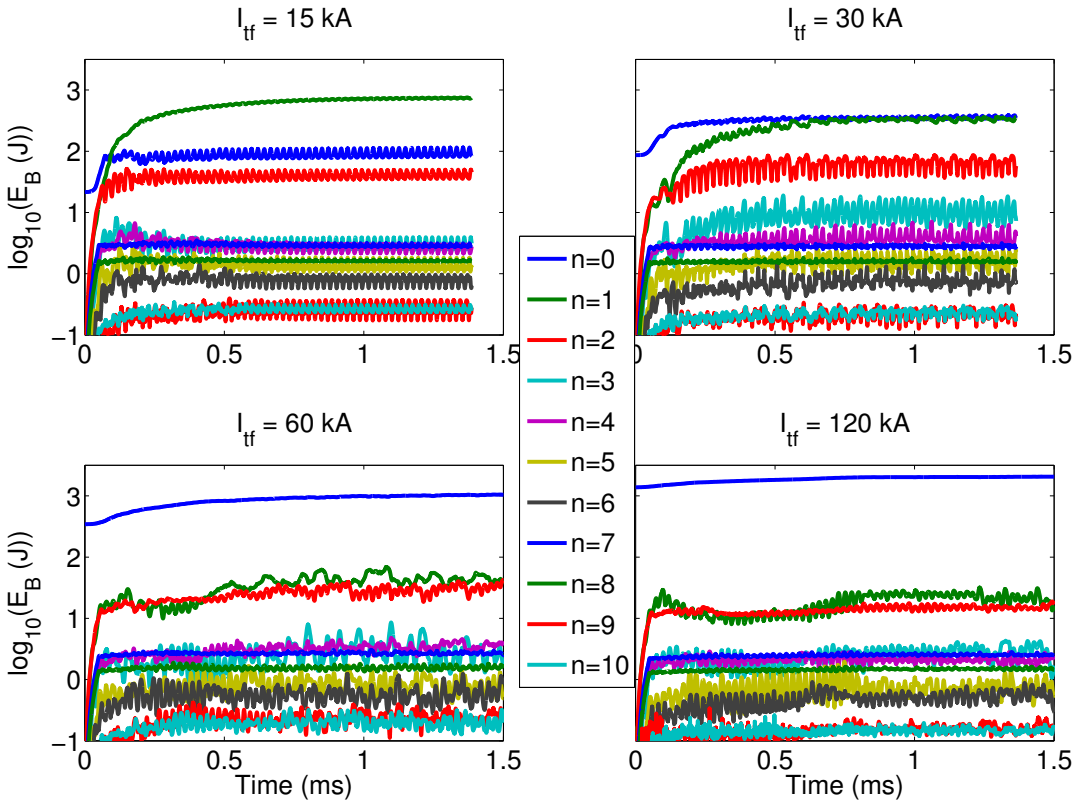

Figure 5.27: The evolution of the magnetic energy spectrum from each simulation as the magnitude of the externally applied toroidal field is increased. Each case had $I_{inj} = 24$ kA. In the first case, the $n = 1$ minimum energy state that forms when no external field is applied dominated the solution while in the second case the energy levels of each mode were equivalent. In the two cases that reached gain > 3, MHD activity is seen later in time during the sustainment phase.

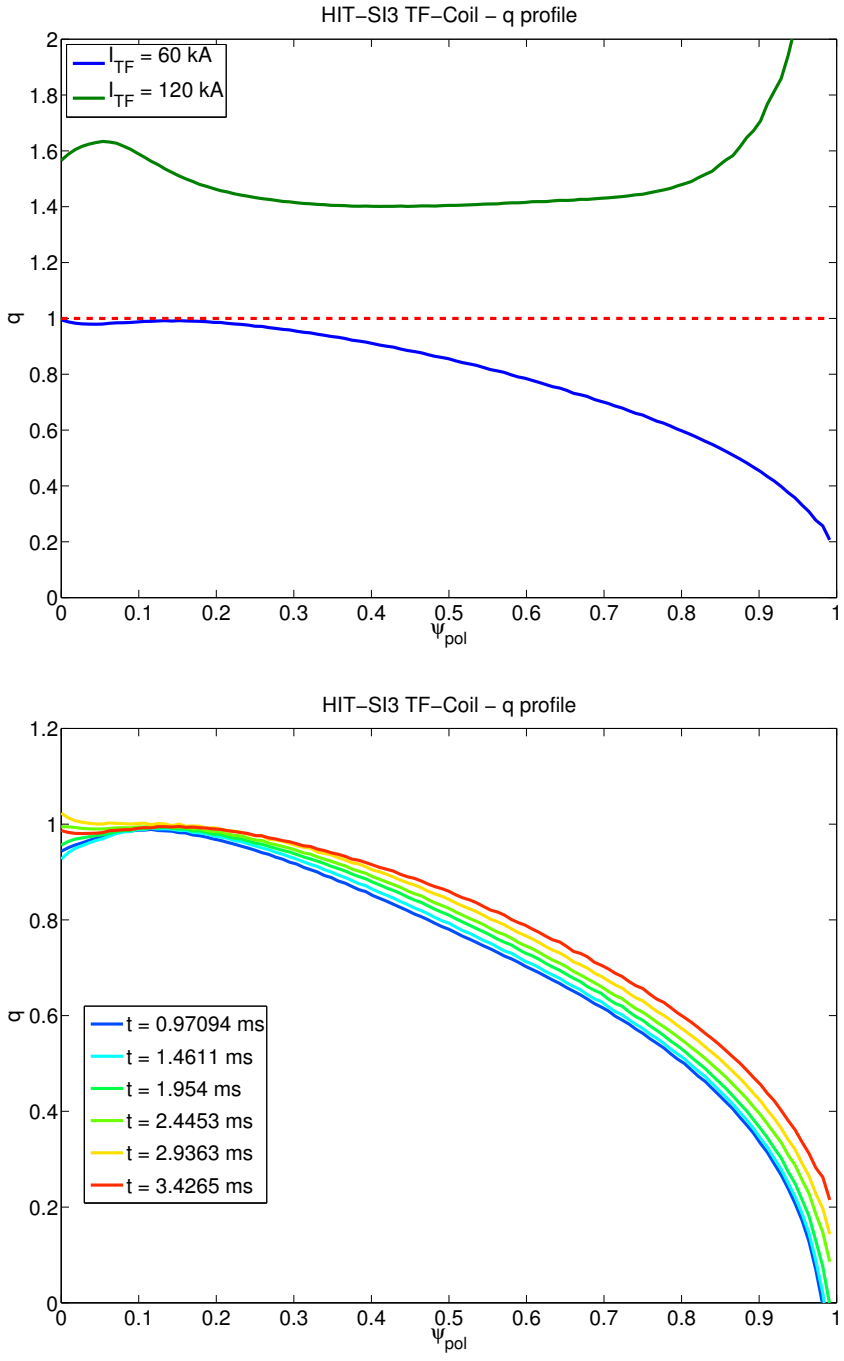

Figure 5.28: Top: final q profile obtained in the two high-gain simulations. The magnetic axis is at $\psi_{pol} = 0$ and the edge of the plasma is $\psi_{pol} = 1$.The high-TF case resembles a tokamak equilibrium while the moderate-TF case resembles a spheromak. Lower: evolution of this profile in the 'spheromak-like' case, where we can see initially a field-reversal near the edge exists as it relaxes into the equilibrium.

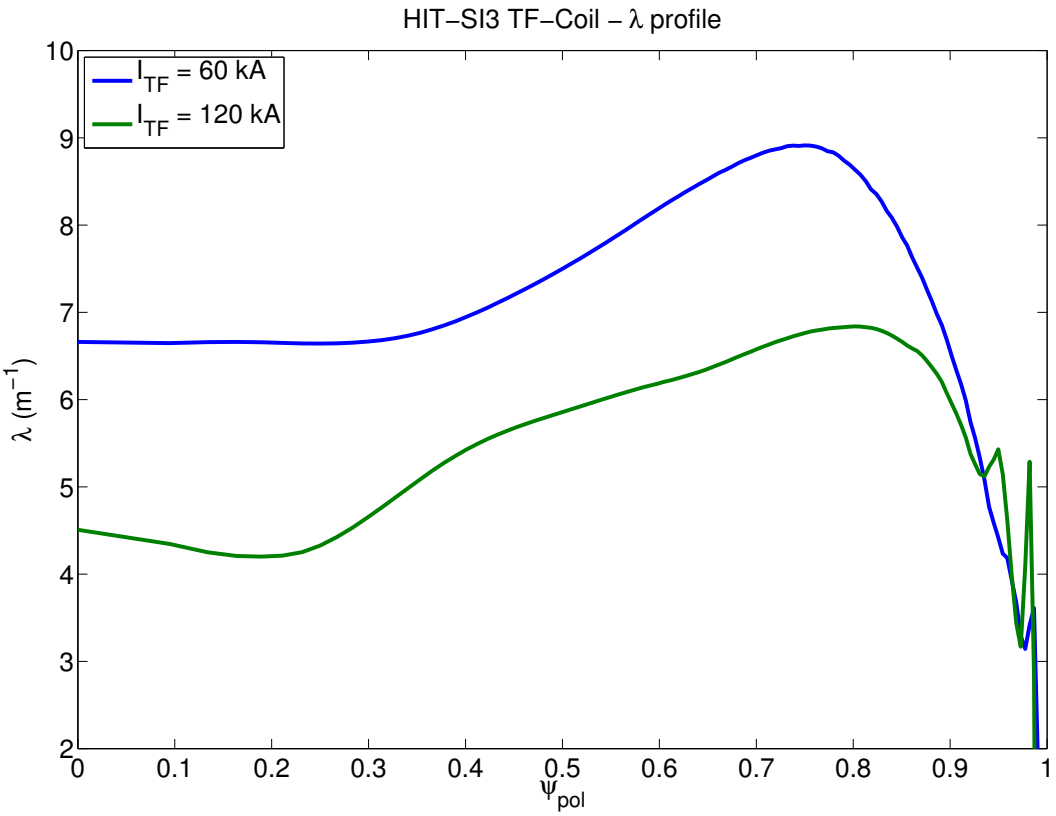

Figure 5.29: The λ profile for the two high-gain cases with externally-applied toroidal field. Both have similar profiles, with a larger λ on the edge and a lower value near the magnetic axis. The 'spheromak-like' case has a flat λ profile near the core, while the 'tokamak-like' case has an increasing field.

Chapter 6

CONCLUSION AND FUTURE WORK

6.1 Conclusion

The primary conclusion of this work is the demonstration that the NIMROD extended MHD code can successfully model the bulk dynamics of both the HIT-SI and HIT-SI3 devices, in every parameter space that has been experimentally explored. This is a significant advance over previous work, which was limited to the low-frequency zero-β space of HIT-SI.

While the HIT-SI simulations have trouble with exact quantitative matches of experimental results, they succeeded at capturing the same trends that were observed as f_{inj} was varied. In particular, these trends are increases in β, Z_{inj}, and current gain with f_{inj} increasing. The direct matching of results remains difficult, likely due to a combination of geometric differences between simulation and experiment, artificial diffusion required to stabilize the numerics, and higher order physics that is neglected. In general, we see that the more 'two-fluid' the model becomes, the more accurate the model appears to be, indicating that electron dynamics are an important factor.

The primary result of the HIT-SI3 simulations is the understanding that 1) HIT-SI3 is able to form an axisymmetric spheromak with seemingly any non-axisymmetric helicity injection mode structure and 2) NIMROD is able to capture the general evolution of the formation and sustainment of HIT-SI3 plasmas. These sustained spheromaks show hints of energy confinement, with T_{max} existing at the magnetic axis during the high gain portion of the simulation. Additionally, while there are changes to the flow profile between isotropic and anisotropic viscosity models, they tend to have little influence on the bulk evolution of the plasma.

Finally, we show that not only are these simulations are tractable to the design points

of the next evolution of these devices, but promising results might be expected in such devices. For example, in the larger, high-gain scenarios we see that the HIT-SI configuration is able to form closed-flux surfaces that persist for many ($\sim 10 - 20$) injector cycles. These closed flux surfaces allow Ohmic heating of the plasma to significantly larger ($T \sim 60$ eV) temperatures than HIT-SI is capable of, though it is unclear if this is achievable in steady-state operation. Additionally, we show that the NIMROD implementation of SIHI-driven plasmas is capable of driving any given injector configuration, and in every case tried so the helicity balance holds true and a spheromak forms. Finally, we lay the initial predictions for a future modification to the HIT-SI3 device, and show that this method of helicity injection is similarly able to form equilibrium that have an externally applied toroidal field.

6.2 Suggestions for Future Work

By opening up the door to modeling of such a large parameter space, a significant amount of study is now possible with NIMROD on the HIT-SI and HIT-SI3 devices. These generally include more in-depth parameter scans, additions to the model, and comparisons with new diagnostics as they come online.

The two most significant points to improve the model include the numerical diffusivity and the split-temperature models. Even with the reduced diffusivity used for the HIT-SI frequency scan, the density oscillations are still a factor of 5 lower than the experimentally observed values, indicating that the diffusivity is still over-damping the system. Possible solutions to this could involve hyperdiffusivity, enhanced resistivity, an increase in the mesh resolution, or more physically realistic density boundary conditions. Separating the electron and ion temperatures is likely important, as they are experimentally observed to be related roughly by $T_i = 2T_e$. The T_e equation is quite stiff, primarily due to the $\vec{V}_e \cdot \nabla T_e$ term, so a question comes up in determining how to deal with it. The first is if that advection term is unimportant, perhaps removing it from the model would allow a still-accurate solution, and if it is important then a small limited-parameter scan could be performed.

There are four new diagnostics in the process of coming online on HIT-SI3. The first is

called the Diametric Internal Probe (DIP) which is an internal probe that stretches across the entire diameter of the device. DIP measurements will allow the measure of how axisymmetric the equilibrium magnetic fields are. The second diagnostic is an insertable Langmuir triple probe. This probe, previously used on HIT-SI, provides local measurements of n_e and T_e, which are beneficial in both finding gradients in n and T and comparisons with simulation results. The third diagnostic is a Thomson scattering diagnostic for measurements of T_e. This provides local measurements of T_e in a non-perturbative method, providing both comparisons to simulation and checks on the model with regard to T_e. The fourth diagnostic is a spectroscopy-based tomography system. The purpose of this diagnostic is that by using a large number (~ 1000) of optical chords, can measure the spatial profile of n inside the plasma with good time resolution, to track the motion of the plasma.

Simulations performed with the PSI-Tet code have recently begun making progress to similarly capture high-frequency HIT-SI and HIT-SI3 discharges, providing an excellent space to confirm the boundary conditions used are valid. The PSI-Tet code uses a tetrahedral finite-element mesh to capture more complex geometries and is able to solve the same extended MHD model as NIMROD, though with the injector plasma fully modeled as well. Work currently being performed by Tom Benedet to reproduce the simulations presented in Chapter 4 for HIT-SI3 will provide verification of the NIMROD simulations presented.

Additionally, one major component of the plasma that the model neglects is the role of neutral particles. A series of measurements taken on HIT-SI3 of the neutral content [49], as well as a study currently being performed by Derek Sutherland will show the effect this has on the edge temperature of the domain. Current work is being done by Sina Taheri and Uri Shumlak to implement a neutral fluid model in NIMROD, which HIT-SI3 may serve as a source of validation of the model already having the neutral properties measured. The neutral fluid model was developed by Eric Meier and Uri Shumlak [50] It is possible that the neutral model will provide a more realistic approach to reducing particle diffusivity by encouraging more realistic plasma density profiles with low n at the wall and high n at the core.

A potential model that can explain the results observed in this work is the existence of helicity barriers formed by electron shear flows. It may be that driving current inside the closed flux regions requires a magnetic resonance to the given surface. Developing a helicity injection scheme that can generate a rich spectrum of perturbations may be necessary to successfully sustain an equilibrium.

The economic attractiveness of a IDCD-based fusion power plant has encouraged the design of a larger, higher performance device using the same form of helicity injection. While NIMROD simulations take more time to perform than an experimental discharge, the setup time to build a new device is significantly longer than the simulation time. Because of this, the design process is aided by simulations performed, as well as mapping out initial parameter spaces to explore once the experiment comes online. To aid in this process, the current implementation of the boundary conditions and mesh generation related to HIT-SI modeling have been written in a more general way, to allow scans of different flux-conserver shapes and injector geometries.

BIBLIOGRAPHY

[1] The ITER organization. Iter - the way to new energy. `http:www.iter.org`, 2016. Accessed: 2016-03-07.

[2] T.R. Jarboe. Review of spheromak research. *Plasma Phys. Control. Fusion*, 36:945–990, 1994.

[3] Dave Hill. A dynamo of a plasma. `https://str.llnl.gov/str/September05/Hill.html`, 2005. Accessed: 2015-05-26.

[4] J.B. Taylor. Relaxation and magnetic reconnection in plasmas. *Rev. Modern Phys.*, 58:741–763, 1986.

[5] T. R. Jarboe, I. Henins, A. R. Sherwood, Cris W. Barnes, and H. W. Hoida. Slow formation and sustainment of spheromaks by a coaxial magnetized plasma source. *Phys. Rev. Lett.*, 51:39–42, Jul 1983.

[6] J.B. Taylor. Relaxation of toroidal plasma and generation of reverse magnetic fields. *Phys. Rev. Letters*, 33(19):1139–1141, 1974.

[7] B. Hudson, R. D. Wood, H. S. McLean, E. B. Hooper, D. N. Hill, J. Jayakumar, J. Moller, D. Montez, C. A. Romero-Talams, T. A. Casper, J. A. Johnson III, L. L. LoDestro, E. Mezonlin, and L. D. Pearlstein. Energy confinement and magnetic field generation in the SSPX spheromak. *Physics of Plasmas*, 15(5):056112, 2008.

[8] C.R. Sovinec, B.I. Cohen, G.A. Cone, E.B. Hooper, and H.S. McLean. Numerical investigation of transients in the SSPX spheromak. *Physical Review Letters*, 94:035003, 2005.

[9] R. Raman, T.R. Jarboe, W.T. Hamp, A.J. Redd, B.A. Nelson, R.G. O'Neill, P.E. Sieck, and R.J. Smith. Transient coaxial helicity injection for solenoid-free plasma startup in HIT-II. *Phys. Plasmas*, 14:022504, 2007.

[10] R. Raman, D. Mueller, T.R. Jarboe, B.A. Nelson, B.G. Bell, S. Gerhardt, B. Leblanc, J. Menard, M. Ono, L. Roquemore, and V. Soukhanovski. Experimental demonstration of tokamak inductive flux saving by transient coaxial helicity injection National Spherical Torus Experiment. *Phys. Plasmas*, 18:092504, 2011.

[11] D.J. Battaglia, M.W. Bongard, R.J. Fonck, and A.J. Redd. Tokamak startup using outboard current injection on the Pegasus Toroidal Experiment. *Nuclear fusion*, 51:073029, 2011.

[12] M.K. Bevir and J.W. Gray. Relaxation, flux consumption and quasi steady state pinches. *Proceedings of Reversed Field Pinch Theory Workshop*, 1980.

[13] K.J. McCollam, J.K. Anderson, A.P. Blair, D. Craig, D.J. Den Hartog, F. Ebrahimi, R. O'Connel, J.A. Reusch, J.S. Sarff, H.D. Stephens, D.R. Stone, D.L. Brower, B.H. Deng, and W.X. Ding. Equilibrium evolution in oscillating-field current-drive experiments. *Phys. Plasmas*, 17:082506, 2010.

[14] T.R. Jarboe, W.T. Hamp, G.J. Marklin, B.A. Nelson, R.G. O'Neill, A.J. Redd, P.E. Sieck, R.J. Smith, and J.S. Wrobel. Spheromak formation by steady inductive helicity injection. *Phys. Plasmas*, 12:056109, 2005.

[15] B.S. Victor, T.R. Jarboe, C.J. Hansen, C. Akcay, K.D. Morgan, A.C. Hossack, and B.A. Nelson. Sustained spheromaks with ideal n=1 kink stability and pressure confinement. *Phys. Plasmas*, 21:082504, 2014.

[16] Chris Hansen. *MHD Modeling in Complex 3D Geometries: Towards Predictive Simulation of SIHI Current Drive*. PhD thesis, University of Washington, 2014.

[17] Jonathon Wrobel. *A Study of Plasma Dynamics in HIT-SI using Surface Magnetic Field Measurements*. PhD thesis, University of Washington, 2011.

[18] Aaron Hossack. *A Study of Plasma Dynamics in HIT-SI using Ion Doppler Spectroscopy*. PhD thesis, University of Washington, 2015.

[19] Brian Victor. *Effects of Density Control on the Internal Plasma Dynamics and Current Drive in HIT-SI*. PhD thesis, University of Washington, 2012.

[20] Will Hamp. Alignment and Calibration of the Multi-point Thomson Scattering Diagnostic for the Helicity Injected Torus. Master's thesis, University of Washington, 2003.

[21] Kiyong Lee. *Development of a Thomson Scattering System and its use in a Rotating Magnetic Field Drive Field-Reversed Configuration Plasma*. PhD thesis, University of Washington, 2011.

[22] Jeffrey P. Freidberg. *Ideal MHD*. Cambridge, 2014.

[23] T.R. Jarboe, B.S. Victor, B.A. Nelson, C.J. Hansen, C. Akcay, D.A. Ennis, N.K. Hicks, A.C. Hossack, G.J. Marklin, and R.J. Smith. Imposed dynamo current drive. *Nuclear Fusion*, 52:083017, 2012.

[24] T.R. Jarboe, C.J. Hansen, A.C. Hossack, G.J. Marklin, K.D. Morgan, B.A. Nelson, D.A. Sutherland, and B.S. Victor. A proof of principle of imposed dynamo current drive: Demonstration of sufficient confinement. *Fus. Science and Tech.*, 66(3):369–384, 2014.

[25] T. Jarboe, B.A. Nelson, and D. Sutherland. A mechanism for the dynamo terms to sustain closed-flux current, including helicity balance, by driving current which crosses the magnetic field. *Physics of Plasmas*, 22:072503, 2015.

[26] A.C. Hossack, D.A. Sutherland, and T.R. Jarboe. Derivation of dynamo current drive in a closed-current volume and stable current sustainment in the HIT-SI experiment. *Phys. of Plasmas*, 24:020702, 2017.

[27] C.R. Sovinec, A.H. Glasser, T.A. Gianakon, D.C. Barnes, R.A. Nebel, S.E. Kruger, S.J. Plimpton, A. Tarditi, M.S. Chu, and the NIMROD Team. Nonlinear magnetohydrodynamics with high-order finite elements. *J. Comp. Phys.*, 195:355, 2004.

[28] R.A. Bayliss, C.R. Sovinec, and A.J. Redd. Zero-beta modeling of coaxial helicity injection in the HIT-II spherical torus. *Phys. Plasmas*, 18:094502, 2011.

[29] F. Ebrahimi, E.B. Hooper, C.R. Sovinec, and R. Raman. Magnetic reconnection process in transient coaxial helicity injection. *Phys. Plasmas*, 20:090702, 2013.

[30] E.B. Hooper, C.R. Sovinec, R. Raman, F. Ebrahimi, and J.E. Menard. Resistive MHD simulations of helicity injected startup plasmas in NSTX. *Phys. Plasmas*, 20:092510, 2013.

[31] J.B. O'Bryan and C.R. Sovinec. Simulated flux-rope evolution during non-inductive startup in pegasus. *Plasma Phys. and Control. Fusion*, 56:064005, 2014.

[32] V.A. Izzo and T.R. Jarboe. Three-dimensional magnetohydrodynamic simulations of the Helicity Injected Torus with Steady Inductive drive. *Phys. Plasmas*, 12:056109, 2005.

[33] C. Akcay, C.C. Kim, B.S. Victor, and T.R. Jarboe. Validation of single-fluid and two-fluid magnetohydrodynamic models of the Helicity Injected Torus spheromak experiment with the NIMROD code. *Phys. Plasmas*, 20:082512, 2013.

[34] C. Hansen, G. Marklin, B. Victor, C. Akcay, and T. Jarboe. Simulation of injector dynamics during steady inductive helicity injection current drive in the HIT-SI experiment. *Physics of Plasmas*, 22:042505, 2015.

[35] C. Hansen, B. Victor, K. Morgan, T. Jarboe, A. Hossack, G. Marklin, B.A. Nelson, and D. Sutherland. Numerical studies and metric development for validation of magnetohydrodynamics models on the HIT-SI experiment. *Physics of Plasmas*, 22:056105, 2015.

[36] S.I. Braginskii. Transport processes in a plasma. *Reviews of Plasma Physics*, 1:205, 1965.

[37] Jeong-Young Ji and Eric D. Held. Closure and transport theory for high-collisionality electron-ion plasma. *Physics of Plasmas*, 20:042114, 2011.

[38] Cihan Akcay. *Extended Magnetohydrodynamics Simulations of the Helicity Injected Torus (HIT-SI) Spheromak Experiment with the NIMROD Code.* PhD thesis, University of Washington, 2013.

[39] T.D. de Wit, A.L. Pecquet, J.C. Vallet, and R. Lime. The biorthogonal decomposition as a tool for investigation fluctuations in plasmas. *Phys. Plasmas*, 1:3288, 1994.

[40] B.S. Victor, T.R. Jarboe, C.J. Hansen, C. Akcay, and K.D. Morgan. Development of validation metrics using biorthogonal decomposition for the comparison of magnetic field measurements. *Plasma Phys. and Control. Fusion*, 57:040510, 2015.

[41] P. Gautier, R. Gruber, and F. Troyon. Numerical study of the ideal-MHD stability limits in oblate spheromaks. *Nuclear Fusion*, 21:1399, 1981.

[42] D.A. Ennis, B.S. Victor, J.S. Wrobel, C. Akcay, T.R. Jarboe, G.J. Marklin, B.A. Nelson, and R.J. Smith. New understandings and achievements from independent-injector drive experiments on HIT-SI. *Nuc. Fusion*, 50:072001, 2010.

[43] F.J. Wysocki, J.C. Fernandez, I. Henins, T.R. Jarboe, and G.J. Marklin. Evidence for a pressure-driven instability in the CTX spheromak. *Phys. Rev. Letters*, 61(21):2457–2460, 1988.

[44] K.D. Morgan, T.R. Jarboe, A.C. Hossack, R.N. Chandra, and C.J. Everson. Validation of extended magnetohydrodynamic simulations of the HIT-SI3 experiment using the NIMROD code. *Phys. of Plasmas*, 24:122510, 2017.

[45] A.C. Hossack, T.R. Jarboe, R.N. Chandra, K.D. Mogran, D.A. Sutherland, J.M. Penna, C.J. Everson, and B.A. Nelson. Plasma response to sustainment with imposed-dynamo current drive in hit-si and hit-si3. *Nuc. Fusion*, 57:076026, 2017.

[46] F. Ebrahimi. Dynamo-driven plasmoid formation from a current-sheet instability. *Phys. of Plasmas*, 23:120705, 2016.

[47] F. Ebrahimi. Nonlinear reconnecting edge localized modes in current-carrying plasmas. *Phys. of Plasmas*, 24:056119, 2017.

[48] A.C. Hossack, R.N. Chandra, C.J. Everson, and T.R. Jarboe. Improvements to the ion Doppler spectrometer diagnostic on the HIT-SI experiments. *Review of Scientific Instruments*, 89:035107, 2018.

[49] D. Elliot, D. Sutherland, U. Siddiqui, E. Scime, C. Everson, K. Morgan, A. Hossack, B. Nelson, and T. Jarboe. Two-photon LIF on the HIT-SI3 experiment: Absolute density and temperature measurements of deuterium neutrals. *Review of Scientific Instruments*, 87:11E506, 2016.

[50] E.T. Meier and U. Shumlak. A general nonlinear fluid model for reacting plasma-neutral mixtures. *Phys. of Plasmas*, 19:072508, 2012.

Appendices

Appendix 1

RUNNING NIMROD SIMULATIONS OF HIT-SI

A.1 Compiling NIMROD

Major changes of the implementation of HIT-SI-related geometry and boundary conditions in the NIMROD code have been made since Akcay's thesis [38], justifying this section.

All simulations presented in this thesis are run using the *nimdevel* version of the NIMROD code, which is available from the instructions located at `https://nimrodteam.org/code_access.html`. Specifically, the simulations are run using the subversion branch named *psicenter_exp*. The general procedure for compiling nimdevel consists of:

1. Check out nimall repository (location obtained when granted access to code).

2. Run the ./mknimall.sh script with appropriate settings to compile nimdevel and all the associated libraries. In particular the bilder machine file used should match the machine and compiler being used. The -q flag is required to properly compile the HIT-SI boundary conditions.

3. Using the configure scripts that mknimall created for nimdevels parsurf and sersurf builds as a basis, create configure scripts for the psicenter_exp branch.

4. After succesfully configuring the psicenter_exp branch builds (both serial and parallel), a *make install* command will build and then install the executables in the specified directory.

After succesfully building the psicenter_exp branch of nimdevel, you will now be ready to set up a simulation. The generation of the initial dump file is accomplished using Akcay's

boolean sum interpolation algorithm implemented in nimset. This requires the using of both a *nimrod.in* file and several *input?edge.txt* files. An example *nimrod.in* file (one used for HIT-SI3 simulations) is shown below and annotated to give guidance.

```
 &grid_input
      gridshape='hit_edge'  ! Flag to use Akcay's boolean sum interpolation algorithm
      periodicity='none'
      eqfile="input1edge.txt"  ! Grid input file format
      xmin=0.    ! These need to match
      xmax=0.557 ! the extrema defined
      ymin=-.290 ! in the grid input files
      ymax=0.290 ! ------
      geom='tor'
      mx=30 ! Number of cells in R direction
      my=30 ! Number of cells in Z direction
      nxbl=6
      nybl=6
      lphi=6 ! (2^lphi+1)/3 fourier modes
      lin_nmodes=1
      lin_nmax=1
      nlayers=22
      poly_degree=4 !polynomial degree of finite elements
 /
 &init_input
      transfer_eq=.true.  ! No fixed equilibrium.
/
&equil_input
```

```
      ds_function='quad'  ! Required for edge-resistivity to function
      beta=0.2 ! 0 turns off T and n evolution
      ds_use='elecd'
      ndens=2.0e19
 /
&const_input
      me_input=9.1093898e-29 ! Enhanced electron mass
/
&physics_input
      coil_type='hit3' ! Sets injector type, described in appendix 2
      advect='V only'
      elecd=25 ! Resistivity, eta/mu0
      elecd_min=0.1
      elecd_max=2e6
      separate_pe=.false.
      iso_visc=300. ! Viscosity
      par_visc=3300
      ohms='2fl'
      eta_model='eta full' ! 'fixed' for zero-beta model
      eta_ref_t=6
      nonlinear=.true.
      continuity='full' ! 'none' for zero-beta model
      nd_diff=1000
      ndensity_bc='dirichlet'
      magnetic_bc='no enforce homo'
/
&closure_input
      p_model='aniso_tdep' ! 'adiabat' for zero-beta model
```

```
      k_perp=1
      k_pll=1
      k_perpi=1
      k_perpe=1
      k_plle=1
      k_plli=1
      bhat="full"
      closure_dump=.false.
      ohm_heat=.true.
      visc_heat=.true.
      qpi_model="braginskii"
      tdep_coul_log=.true.
      closure_model='stpstpstpstp'
      tdep_tequil=.true.
      tequil_rate=1
/
&numerical_input
      dtm=4.E-8
      v_cfl=2
      nl_cfl_lim=1e4
      fv_vdgv=0.51
      fp_vdgp=0.51
      fb_vxb=0.51
      feta=1.
      fvsc=1.
      fthc=1.
      split_visc=.false.
      mhd_si_iso=0
```

```
      mhdadv_alg='centered'
      split_divb=.true.
      divbd=1e4
      kdivb_2_limit=1e6
      ave_change_limit=5e-3
      ngr=3
      met_spl='iso'
      tmax=2.0e-3
      si_fac_mhd = 1.5
      si_fac_nl = 1.5
      si_fac_j0 = 1.5
      si_fac_pres = 1.5
      cpu_tmax=21560
      nstep=5000000
 /
&solver_input
      solver='slu_dsta'
      tol=1.e-10
      extrap_order=2
      nsym_bpre_band=0
      nsym_tpre_band=0
      nsym_pre_rpass=2
      maxit=400
      maxit_nl=25
      tol_nl=1.e-4
/
&output_input
      nhist=5
```

```
      ihist=  1
      jhist=  4
      hist_binary=t
      ndump=50
      dump_over = 0
      dump_file = 'dump.95474'
/
&hitsi_input
      inj_R1=0.2674 ! Physical location of injectors
      inj_R2=0.3826
      edge_fac=37440 ! Ratio of edge to plasma resistivity.
      new_SI_eq=.false.
      inj_B_norm1=0.1124 ! Sets magnitude of B_norm
      inj_Volt1=1322.46 ! Sets magnitude of E_tan
      inj_B_norm2=0.1124
      inj_Volt2=1322.46
      inj_B_norm3=0.1124
      inj_Volt3=1322.46
      lambda_inj=30
      inj_T_norm1=8.00 ! Sets magnitude of T_inj
      inj_T_norm2=8.00
      omega1=91106.186954104
      t0_SIHI=0
      t_ramp=5e-5
      n_flat=100
      n0bias=0.0
      ethick=0.001
      ramp_file=.true.
```

```
      wform_fname='160609009.ramp' ! Waveform file for injectors
      init_phase=-1.5707963267948966
      n_inj_step=22
      xphase_curr=0
      xphase_flux=0
      yphase_curr=1.5707963267948966
      yphase_flux=1.5707963267948966
      tdep_phase=.true.
      grid_input_num=7 ! Number of grid input files to use
/
&particle_input
      pdbg=.false.
/
```

In a directory with the *nimrod.in* and grid input files, the nimset executable can be run. Nimset will create the individual blocks specified by each grid input file and stitch them together. Following this the initial condition needs to be created in the dump file using nimeq. A sample *nimeq.in* file is shown below:

```
&nimeq_input
     f_model="quad_closed"
     dfdpsi=10.28
     f_open=0.0
     f1_closed=1.4e-6 ! Sets magnitude of initial B
     f2_closed=0.0
     pressure0=1.6e-5 ! Sets magnitude of initial T, as well as T_wall
     p_open=0.0
```

```
    eq_iters=200
    gsh_tol=1.e-7
    gscenter=0.9
    linmaxit=600
    nimeq_tx=.true.
    write_iters=.true.
/
```

After running nimeq, a file named *dump_gs.00000* will be created, which can serve as the initial dump file for the simulation. The NIMROD program can then be run, which will produce a variety of binary files of output results. The post-processing of these results is discussed in detail in Appendix 2.

A.2 Modifications to the NIMROD Code for HIT-SI Simulations

A small number of changes to the *nimdevel* version of NIMROD were made to allow the HIT-SI and HIT-SI3 simulations to be performed. These changes are separated into two groups, boundary conditions and modifications to the temperature advance. The modified version of the code is stored inside the *psicenter_exp* branch of the *nimdevel* subversion repository.

A.2.1 Details of Injector Boundary Conditions

A sizeable amount of work has been put into the implementation of *almost* fully generalized SIHI boundary conditions into the NIMROD code. These routines are all contained inside the source file *nimdevel/nimrod/sihi.f* of the *psicenter_exp* branch. Additionally, legacy versions of these routines used for the simulations presented in chapters 2-5 are included in this file, and form largely the same format as will be described below, just less generalized.

Before diving into the main routines, it will help to discuss the analytic form of boundary conditions being applied, which can be divided into two general forms. The first form

concerns the boundary conditions that are applied directly, such as $B_\perp$, $V_\perp$, T, and while not used in any simulation presented in this work, routines to apply n in a similar method were also written. In all cases these boundary conditions are known in an analytic form

$$f(R,\phi,t) = f_0(t)\left[\sum_{m=0}^{4} a_m R^m\right]\left[\sum_{n=0}^{N} c_n e^{in\phi} + c_n^* e^{-in\phi}\right]$$

that is assumed to be separable in the R and ϕ spatial components. $f_0(t)$ is in the form of $f_0(t) = l(t)sin(\omega_{inj}t+\delta\phi(t))$, where $l(t)$ and $\delta\phi(t)$ are both piecewise linear functions. The R component is the tangent direction of the geometric surface where the boundary conditions are applied, so for injectors that are located on the outboard midplane of the geometry this is the Z direction in our conventional cylindrical coordinates. These boundary conditions are directly applied at the end of the timestep. The second form is a surface-integrand term, such as the Electric field used for the injectors, given by

$$E_\parallel = -\nabla V + E_{faraday}$$

where $V(R,\phi)$ is of the form of $f(R,\phi)$, with the gradient being

$$\nabla V = f_0\left[\sum_{n=0}^{N} c_n e^{in\phi} + c_n^* e^{-in\phi}\right]\left[\sum_{m=1}^{4} m a_m R^{m-1}\right]\hat{r} + f_0\frac{1}{R}\left[\sum_{n=0}^{N} inc_n e^{in\phi} - inc_n^* e^{-in\phi}\right]\left[\sum_{m=0}^{4} a_m R^m\right]\hat{\phi}.$$

$E_{faraday}$ is the component of $E_\parallel$ that forms from Faraday's law and time-dependent flux injection. The details of the signs differ slightly depending on the surface that this is calculated for, with the example derivation given for injectors located on the bottom of the device. In this case, the flux is injected in the $\hat{z}$ direction, so Faradays law reduces to:

$$\frac{1}{R}\frac{\partial RE_\phi}{\partial R} - \frac{1}{R}\frac{\partial E_R}{\partial \phi} = -\frac{\partial B_z}{\partial t}$$

The temporal derivative is easy to evaluate analytically, with the important detail being the derivative of $f_0(t)$:

$$\frac{\partial f_0}{\partial t} = \frac{\partial l}{\partial t}sin(\omega_{inj}t + \delta\phi(t)) + l(t)(\omega_{inj} + \frac{\partial \delta\phi}{\partial t})cos(\omega_{inj}t + \delta\phi(t))$$

The left hand side of Faraday's law allows for multiple solutions, and so following the reason given in [38] the choice of $E_\phi = 0$ is made. Of the choices available, this is the most similar to the insulating gaps on the experiment. Knowing that E_R will eventually be cast in an finite Fourier series, we can then relate the coefficients of E_R to the coefficients of B_Z as:

$$E_{R,n} = \frac{\partial f_0}{\partial t}\frac{R}{in}B_{Z,n}(R)$$

where we have used $\frac{\partial E_{R,n}}{\partial \phi} = inE_{R,n}$. In cases where the geometric radius is not equivalent to the spatial variable used in $f(R,\phi)$ (such as injector on the outboard midplane), care must be taken in doing the derivation. We also note that in the case $B_z(n=0) \neq 0$, this form does not work and a component of E_ϕ is required to balance the equations.

With the analytic forms of the different types of boundary conditions we can now discuss the implementation in the code. The file *psicenter.f* contains the switchyard routines for these different boundary conditions, as some machinery is shared with FRC calculations performed by Richard Milroy. At the end of each advance routine a subroutine (such as *psi_inj*) is called which then calls the appropriate routine from *sihi.f* (such as *inj_flux_gen*)

A boundary condition call in *sihi.f* will typically involve 3 subroutines from the module. First is the main routine which will eventually apply the boundary conditions, with the second and third handling the details of $f_0(t)$ and the spatial coefficients (a_m and c_n). In the generalized routines the module will read the input files (creation of these input files is described in Appendix 2) of the coefficients at the beginning of the simulation and store them inside the module, whereas the experiment-specific routines will call a separate subroutine that contains the coefficients each timestep. The temporal subroutine calculates both $f_0(t)$ and $\frac{\partial f_0}{\partial t}$ and as such is useful in general for both $B_\perp$ and $E_\parallel$ calculations.

The boundary condition routine for T has an additional option that in specific cases can help with stiff numerical difficulties related to chaotic magnetic fields in the high-resistivity region. Temperature gradients can be eliminated in this region by enforcing that the entire thin layer be at the temperature of the wall in each time step. In most cases this increases the iteration count, but in some cases it has been found to be useful.

A.2.2 The temperature advance

The modifications that were made to the temperature advance in NIMROD are support for the high-resistivity edge-layer and minor changes to improve the symmetric preconditioning operator. When the resistivity is calculated, logic was added to the *ave_eta_check* and *find_eta_t* subroutines to directly set the resistivity inside the edge layer, effectively holding it fixed throughout the simulation. A rough calculation of the unphysical ohmic heating present in the high-resistivity edge-layer from the driven injector currents gives a value on the order of 10 MW, which is equivalent to the expected injector power that the rest of the system should see. A simple fix was created that simply reduces the ohmic heating in this volume by the factor that the resistivity is enhanced by.

The preconditioning operator in the temperature advance (*t_aniso_op*) attempts to apply the symmetric component of the anisotropic thermal conduction to reduce iterations required during the full solve. The form of the parallel component ($(k_\parallel - k_\perp)\hat{b}\hat{b}$) used in the standard version of *nimdevel* is:

$$(k_\parallel - k_\perp)_{n=0}\frac{(\vec{B}\vec{B})_{n=0}}{B_0^2}$$

Where we see that the normalization of $\hat{b}\hat{b}$ is incorrect during times when $\vec{B}_1$ is the dominant component of the field (where $\vec{B}\vec{B}_{n=0} = 2\vec{B}_1\vec{B}_{-1}$). Most simulations presented in this thesis use only this correction, with the form:

$$(k_\parallel - k_\perp)_{n=0}\frac{(\vec{B}\vec{B})_{n=0}}{(B^2)_{n=0}}$$

Recently, a minor improvement has been seen by including cross terms between $\hat{b}\hat{b}$ and the thermal conduction coefficients. By computing the full 3-D operator then taking the symmetric component, reduction of iterations $\sim 10\%$ can be seen during dynamic 3-D periods of simulations. Figure A.1 shows an example of a simulation that demonstrates this improvement, though the exact gains in computational time have not been quantified and likely depend on other factors.

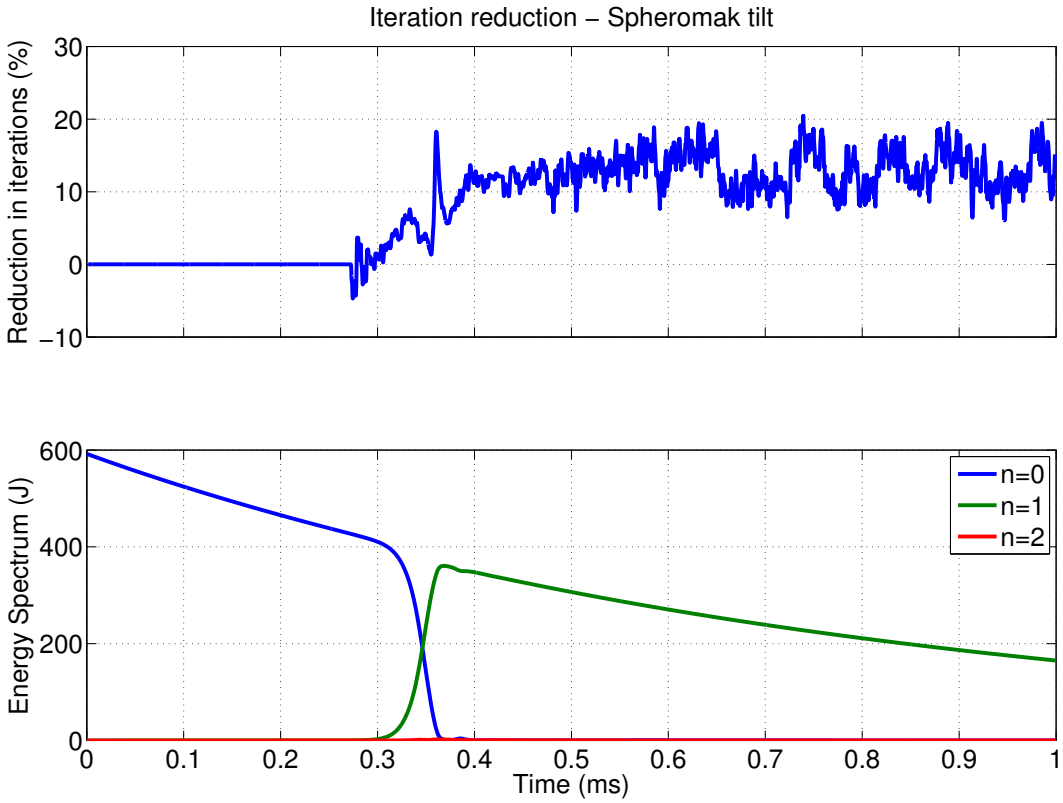

Figure A.1: The iteration reduction from including the full symmetric parallel thermal conduction operator in *t_aniso_op*. The simulation is a tilting spheromak, we see that during the $n = 0$ decay the iterations are not reduced, but once the $n = 1$ tilt mode becomes dominant the iterations are reduced by $\sim 10\%$. HIT-SI simulations see similar improvements, though the exact improvement has not been quantified.

A.3 Isothermal electron model

In chapter 3 it is mentioned that a model using fixed electron temperatures was used. This model is not a natively supported model in the NIMROD code, so changes were made to implement it. The flag *isothermal_tele* was added as an option in *nimrod.in*, and when set to true the following changes in the simulation are made:

- The *adv_t_aniso* subroutine is not called for the electron fluid, leaving the values of the array at the initial conditions.

- The CFL number calculations no longer use the electron flow CFL number, as typical two-temperature simulations would.

Additionally, a similar reduced model is intended to be explored in the future, where only the toroidally symmetric electron temperature is evolved. This may allow simulations of HIT-SI to be tractable, as the complex 3-D dynamics are thought to be the largest source of numerical difficulties in the simulation.

Appendix 2

NIMROD-HITSI MATLAB LIBRARY

A github repository has been created which contains both pre and post processing matlab routines for the NIMROD HIT-SI simulations. This appendix consists of descriptions / usage of these routines.

B.1 Grid-Generation

Grid generation is performed using the Boolean-Sum interpolation algorithm implemented in the dump file generation program *nimset* by Akcay [38]. In addition to a standard *nimrod.in* input file, additional files of the form *input?edge.txt*, with ? being sequential integers beginning with 1, are required. Each of these input files defines a logically rectangular section of the geometry, and the total mesh is generated by stitching these together. While the nimset routines work reasonably well, the generation of the input files for different meshes can be troublesome. In order to streamline the process, a set of Matlab routines were generated to speed up the process.

B.2 Injector Generation

The routines for calculating the injector boundary condition coefficients have been completely rewritten in a more generalized sense. As a reminder, the boundary conditions for $B_\perp$ and $E_\parallel$ are:

$$B_\perp = B_0 f(t) \left[\sum_{m=0}^{4} a_m R^m\right] \left[\sum_{n=0} N c_n e^{in\phi} + c_n^* e^{-in\phi}\right]$$

$$V = V_0 f(t) \left[\sum_{m=0}^{4} a_m R^m\right] \left[\sum_{n=0} N c_n e^{in\phi} + c_n^* e^{-in\phi}\right]$$

$$E_{\|} = -\nabla V + E_{faraday}$$

To generate the a_m and c_n coefficients, we begin by generating a 2-D mesh (in R and ϕ) with the shape of the injector mouth. The variable of interest for implementing $B_{\perp}$ is the B_z component, which is the 'axial' injector field. A zero-β plasma equilibrium is assumed to satisfy the momentum equation in MHD, with $\rho\frac{\mathrm{d}}{\mathrm{d}t}\vec{V} = \nabla p = \vec{J} \times \vec{B} = 0$. This requirement that $\vec{J} \parallel \vec{B}$ allows to write an eigenvalue problem for the equilbrium in terms of $\vec{B}$:

$$\nabla \times \vec{B} = \lambda \vec{B}$$

For an injector mouth from a manifold, it is assumed that the straight portion of the manifold is sufficiently long that the length can assumed to be infinite, to simplify the geometric concerns. It is convenient numerically to cast our applied boundary condition in a shape that allows for separable equations, so for an injector on the top or bottom of the device a pie-slice shape is chosen, as seen in figure B.1.

To solve this equation in the polar coordinates of the mesh, we separate into different vector components, noting that the assumed infinite length sets $\frac{\partial}{\partial z} = 0$:

$$\frac{1}{R}\frac{\partial B_z}{\partial \phi} = \lambda B_r$$

$$R\frac{\partial B_z}{\partial R} = -R\lambda B_{\phi}$$

$$\frac{1}{R}\left(\frac{\partial R B_{\phi}}{\partial R} - \frac{\partial B_R}{\partial \phi}\right) = \lambda B_z$$

Taking derivatives of the top two equations (with respect to ϕ and R, respectively) gives:

$$\frac{1}{\lambda R}\frac{\partial^2 B_z}{\partial \phi^2} = \frac{\partial B_r}{\partial \phi}$$

$$\frac{1}{\lambda}\frac{\partial^2 B_z}{\partial R^2} = -\frac{\partial B_{\phi}}{\partial R}$$

Which we can then use to write an expression purely in terms of B_z:

$$-\frac{1}{R}\frac{\partial}{\partial R}\left(R\frac{\partial B_z}{\partial R}\right) - \frac{1}{R^2}\frac{\partial^2 B_z}{\partial \phi^2} = -\nabla^2 B_z = \lambda^2 B_z$$

We then portion B_z into a separable form, that is $B_z = f(R)g(\phi)$, and separate the equations, obtaining:

$$\frac{\partial^2 g}{\partial \phi^2} = 0$$

and

$$\frac{\partial}{\partial R}\left(R\frac{\partial f}{\partial R}\right) = \frac{1}{R}\frac{\partial f}{\partial R} + \frac{\partial^2 f}{\partial R^2} = -\lambda^2 f(R)$$

To numerically solve the equations, a successive over-relaxation method is used, with the amplitude of the solved functions is normalized such that $max(B_z) = 1$ and the boundary conditions of $B_z = 0$ on the edge of the geometry. After obtaining our solution to B_z, we then fit the solution to an analytic form in order to apply the correct value at any arbitrary spatial location in the simulation domain, with examples seen in figure B.2. The radial dependence of the field is fit to a 4th order polynomial, while the toroidal dependence is fit to a Fourier series with the same resolution as intended to be used in the simulation.

As we saw in chapter 2 (Figure 2.3), this form of the injector boundary condition is likely not physically accurate when compared with the actual experimental setup. The dynamics of the plasma physics inside of the injectors are not captured in this simplistic force-free equilibrium treatment, however current results indicate that the deviation from reality is relatively minor. Detailed PSI-Tet studies of HIT-SI dynamics are currently underway, and will be compared with NIMROD results in the future.

B.3 Post-processing

Post-processing a simulation is a time-consuming process, that is made easier by a set of automated functions to do common tasks. These can be divded into several categories: general signal processing, synthetic diagnostics, reading *nimrod* and *nimplot* output files, and plotting. At the top level a set of master scripts mediate the post-processing of a simulation.

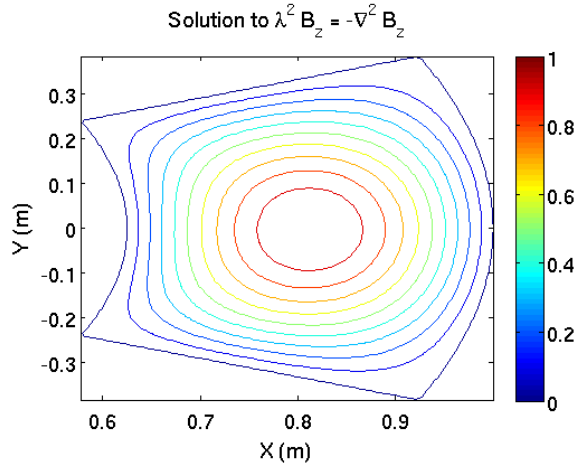

Figure B.1: Solution to the equilibrium equation $\lambda^2 B_z = -\nabla^2 B_z$ for an injector mouth of a manifold configuration.

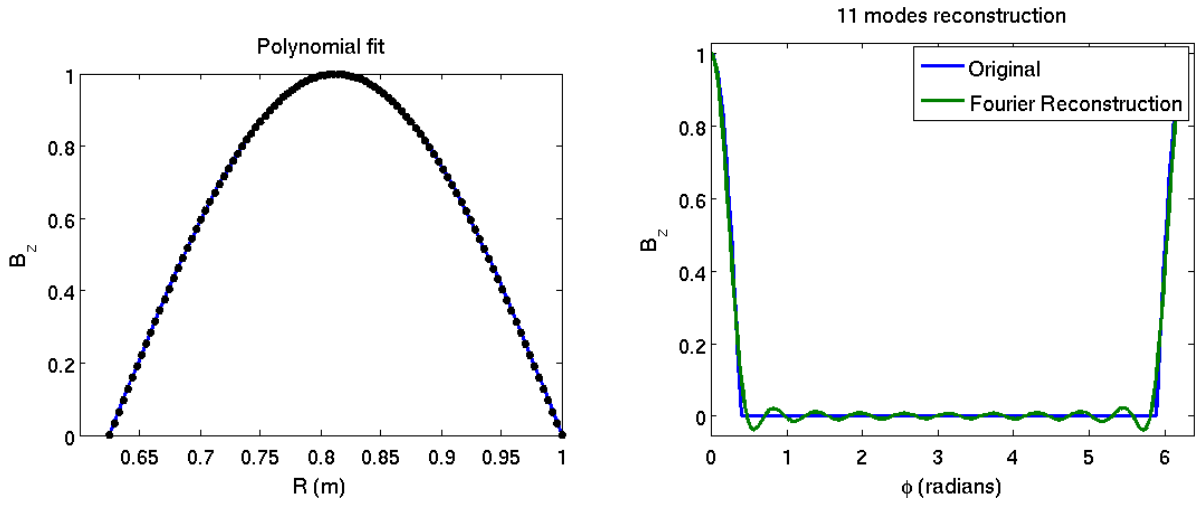

Figure B.2: The injector equilibrium solutions of figure B.1 reconstructed with the analytic form. The radial function is fitted to a 4th order polynomial, while the angular function is decomposed into a finite-fourier series with $N = 11$.

B.3.1 Master Scripts

In the root of the *nimrod-hitsi* library lives a set of scripts that serve as the initial processing of simulation output. Due to differences in both what processing is desired and specific simulation specifics, separate scripts are made for each injector type. These scripts all follow the same general routine:

1. Examine the folder to determine what is there (number of dump files, binary files, etc.)

2. Read the *energy.bin* and *discharge.bin* output files by NIMROD and the final dump file.

3. Produce a series of 'sanity-check' plots, showing $\vec{B}$, $\vec{V}$, n, and T fields, $\nabla \cdot \vec{B}$ error, I_{tor}, energy-spectrum, and numerical grid.

4. Set-up synthetic diagnostics that are to be used.

5. Loop over all dump files, this is the main loop of the post-processing. This will sample the synthetic diagnostics being used at each timestep.

6. Perform final organizing of synthetic diagnostics, such as calculating ψ_{inj}, averaging at f_{inj}, integrating chord-averaged measurements, etc.

7. Save the output results in a *post_process_output.mat* file for further use.

B.3.2 Synthetic Diagnostics

Due to the large number of dynamic processes involved in HIT-SI, an effort is made to reproduce a variety of experimental diagnostics to confirm NIMROD is seeing the same events seen experimentally. What follows is a description of the numerical method used for each type of diagnostic.

Injector Currents and Fluxes: The injector flux is computed directly by computing $\psi_{inj} = \int \vec{B} \cdot \mathrm{d}\vec{a}$ on the surface of the simulation domain in the region of the injector. The injector current is computed via Ampere's law, finding $I_{inj} = \int \vec{B} \cdot \mathrm{d}\vec{l}$ on the path surrounding the injector mouth. The $R-Z$ components of these integrals are performed using trapezoidal integration, while the ϕ component of the integral is evaluated directly in the Fourier space.

Chord-Averaged Optical Diagnostics: The two experimental diagnostics of interest are the Far-InfraRed (FIR) interferometer and the Ion Doppler Spectroscopy (IDS) system. Figure 4.18 shows the location of these in the HIT-SI device. The FIR system measures the line averaged electron density ($< n_e >= \int n_e \mathrm{d}l/L$) through measurement of the index of refraction of the plasma. The IDS system measures the ion velocity and temperature through measurements of the width and redshift of specific ion spectral lines. An important parameter in the IDS measurement is the spatial distribution of the spectral intensity from the plasma. At present, a simple $I \sim n^2$ model is used, with an example being the comparisons done in the HIT-SI3 chapter. Future work is ongoing to incorporate the open Atomic Data and Analysis Structure (ADAS) into more detailed models of line intensities as functions of n and T.

Both of these diagnostics are implemented in MATLAB by sampling the relevant values (n, T, $\mathbf{V}$) and then performing the relevant integrals. Work has been done by Aaron Hossack [18] to more closely replicate the experimental procedure of synthetic IDS data, by constructing a synthetic CCD image from simulation data that can be then fed through the standard analysis package. The MATLAB functions that attempt to replicate the diagnostics in this package instead just calculate the temperatures obtained by weighting the line integration by the density profile.

Spatially Localized Probes: There exist an array of probes on the HIT-SI and HIT-SI3 devices for taking localized in space measurements. The majority of these are magnetic probes, though a retractable Langmuir probe and Thomson scattering exist for measurements of n_e and T_e. These are implemented in the post-processor via prescribing the logical location of the nearest gridpoint in the setup, then sampling the values of the fields at dump file that

is processed.

B.3.3 Description of Subroutines

What follows is a list of all of the *.m* post-processing files that were written and what their purpose is.

```
==> areaInt.m <==
function N = areaInt(rz,A,option)
%% Area Integrates 2d A over plane described rectangularly by rz
%% Option=0 does area integral, option=1 does volume integral of a n=0 object.

==> av_dens.m <==
%% av_dens.m
%% Runs following main loop of post-processing script,
%% does line averaging of FIR chords.

==> bd_FullField.m <==
function [U,S,V] = bd_FullField(A,t)
%% Generates the bd of a full field from a NIMROD simulation
%% See bd_FullRecon

==> bd_FullRecon.m <==
function A = bd_FullRecon(U,S,V,B,it)
%%Reconstructs total BD field from simulation data
%%See bd_FullField for generating U,S,V

==> bd_inj_sub.m <==
function int_sub = bd_inj_sub(int,tin,C)
```

```
%% Does injector subtraction from the Victor 2014 and Hossack 2017 papers
%% Uses surface probe in the sp_imp_den[sn].mat format

==> bdSP_allProbes_eval.m <==
function int = bdSP_allProbes_eval(U,S,V,tin)
%% Evaluates the BD modes back onto the probes
%% Does all surface probes.

==> bdSP_allProbes.m <==
function [U, S, V, b_mat, Xp, Yp, Xt, Yt] = bdSP_allProbes(int,tin,C,exp)
%% This generates the Biorthogonal Decomposition Stuff from the internal probe signals
%% Using the way they are formatted in a mat file given by BSV

==> bdSP.m <==
function [U, S, V, b_mat, Xp, Xt] = bdSP(int,tin)
%% This generates the Biorthogonal Decomposition Stuff from the internal probe signals
%% Uses fields in the sp_imp_den[sn].mat format

==> bdSP_wgap_eval.m <==
function int = bdSP_wgap_eval(U,S,V,tin)
% Evaluates the BD modes back onto the probes

==> bdSP_wgap.m <==
function [U, S, V, b_mat, Xp, Yp, Xt, Yt] = bdSP_wgap(int,tin,C,exp)

%% This generates the Biorthogonal Decomposition Stuff from the internal probe signals

==> boxcar_aver.m <==
```

```
function A = boxcar_aver(B,Npt)
%% Does a boxcar average, assuming periodicity, go Npt in each direction

==> BSV_BD_int.m <==
function [mB2, Y, Akp, VCor, UCor, Dk, Aval] = BSV_BD_int(fnExp,fnSim,ts,ph,sihi,Ncycle)
%% Function which evalutes a BD metrics described in BSV's paper:
%% "Development of validation metrics using biorthogonal decomposition for the compariso

==> BSV_BD.m <==
function [mB2, Y, Akp, VCor, UCor] = BSV_BD(fnExp,fnSim,ts,ph,sihi)
%% Function which evalutes a BD metrics described in BSV's paper:
% "Development of validation metrics using biorthogonal decomposition for

==> calc_alfven_velocity.m <==
function vA = calc_alfven_velocity(B,n)
%% Given B,n calculates an Alfven Velocity

==> Calc_Amperian_TrapBCmirrored.m <==
function [I_amp, t_amp, tag, ProbeProfile, AmperProfile, ZerosProfile] = Calc_Amperian_T
%% Port of routine by JSW for computing toroidal current from HIT-SI Surface Probes

==> calcCrossHel.m <==
function K_c = calcCrossHel(V,B,N,rz)
%% Calculates cross-helicity given V,B,N on a mesh given by rz

==> calc_EdJ.m <==
function [edj1,edj2] = calc_EdJ(ve,be,ja,nd,mode)
%% Caculates n=0 component of E dot J from fields of the given mode number
```

```
%% This is E0 = -V_1 X B_-1 - V_-1 X B_1 + 1/(ne) ( J_1 X B_-1 + J_-1 X B_1)

==> Calc_FIR_nd.m <==
function ndE = Calc_FIR_nd(rz,N,phi,fir_dat,fang)
%% Calculates n at the points described by an FIR chord.
%% These are later averaged with av_dens.m

==> calcGradV.m <==
function grdv = calcGradV(V,dVdphi,rz)
%% Calculates grad V

==> calc_heat_flux_loss.m <==
function [prp_loss,pll_loss] = calc_heat_flux_loss(nimIn,R,Z,N,T,B)
%% Calculates the amount of thermal energy leaving the volume.
%% Assumes NIMROD's implementation of Braginskii thermal conduction

==> calc_heat_flux.m <==
function [q_prp,q_pll] = calc_heat_flux(nimIn,N,T,B)
%% Calculates Braginskii heat flux coefficients

==> calc_IDS_2D.m <==
function vdl = calc_IDS_2D(rz,V,N,phi,in,npt)
%% Calculates v for a given IDS_Coord.
%% This is a 2-d version assuming we are on the plane z=0.

==> calc_IDS_2D_N.m <==
function vdl = calc_IDS_2D_N(rz,N,phi,in,npt)
%% Calculates n for a given IDS_Coord.
```

```
%T% his is a 2-d version assuming we are on the plane z=0.

==> calc_IDS_2D_T.m <==
function vdl = calc_IDS_2D_T(rz,T,N,phi,in,npt)
%% Calculates T for a given IDS_Coord.
%% This is a 2-d version assuming we are on the plane z=0.

==> Calc_IDS_vel.m <==
function vdl = Calc_IDS_vel(rz,V,phi,IDS_Dat,dir)
%% Calculates v in the direction of the chord being measured.
%% Full 3-D Version, t~2.5 minutes per chord.

==> calc_inj_flux_gen.m <==
function [Iinj,psi_inj] = calc_inj_flux_gen(Bdata,rz,inj)
%% Injector current and flux calculation - gen_sihi case
%%

==> calc_inj_flux_hitpc.m <==
function [Iinj,psi_inj]=calc_inj_flux_hitpc(Bdata,RZgl,ang,nimIn)
%% Injector Current and Flux Calculation - hit_pc case

==> calc_ja.m <==
function ja = calc_ja(be,rz)
%% Calculates (1/mu0) curlB in the NIMROD Fourier space
%%

==> calc_Jphys.m <==
function [J,r,z] = calc_Jphys(B,dBdphi,rz)
```

```
%% Calculates (1/mu0) curlB in the R-Z-Phi spatial representation

==> calcKinHel.m <==
function K_v = calcKinHel(V,N,dVdphi,rz)
%% Calculates the Kinetic Helicity in a NIMROD grid
%%

==> calcMagHel.m <==
function K_b = calcMagHel(A,B,N,rz)
%% Calculates magnetic helicity in the NIMROD grid.
%% Does not work well on HIT-SI simulations.

==> calcSP.m <==
function B = calcSP(loc,be,phSP)
%% Given probe_locations, finds B
%% To be run in main post-processing script.

==> calculate_Binjphi.m <==
function [phi,Binjphi,rad,Binjrp] = calculate_Binjphi(Bdata,r)
%% Finds the center of an injector mouth

==> calculate_inj_flux_HIT3.m <==
function [psi,I] = calculate_inj_flux_HIT3(Bdata,r,inj,fang)
%% Calculates Injector Current and Flux, hit-si3
%%

==> calculate_inj_flux.m <==
function [psi_inj,Iinj]=calculate_inj_flux(Bdata,RZgl,inj,nimIn)
```

```
%% Calculates Injector Current and Flux - hitsi

==> calculate_inj_flux_side.m <==
function [psi_inj,Iinj]=calculate_inj_flux_side(Bdata,RZgl,inj)
%% Calculates injector current and flux - hit_side

==> colorSpectrum.m <==
function ColorCodes = colorSpectrum(N)
%% colorSpectrum Creates a spectrum of colors from red to green to blue.
%%   Copywrite 2013 Kirk T. Smith

==> combineBlockja.m <==
function qb = combineBlockja(rb,cb)
%% Given a ja variable inside of a set of rblocks, combine rblocks.
%% ja will typically have come from countour.bin

==> combineBlockjpar.m <==
function qb = combineBlockjpar(rb,cb)
%% Given parallel_current.bin from nimplot put into an rblock,
%% combine rblock values.

==> compute_flux_HIT3.m <==
function [flux]=compute_flux(V,r,dphi)
%% Computes flux, used in injector flux calculation

==> compute_flux.m <==
function [flux]=compute_flux(V,r,dphi)
%% Computes flux, used in injector flux calculation.
```

```
%%

==> construct_injector_waveform.m <==
function [I1,I2,p1,p2] = construct_injector_waveform(time,sihi,tshift)
%% Old format of injector current/flux waveforms.  Constructs the timebase from input fi

==> convertIDS.m <==
function IDS_Coord=convertIDS(ids)
%% Converts the r,z,phi cylindrical coordinates to x,y,z machine coordinates
%%

==> create_bd_mesh.m <==
function [Ap,At] = create_bd_mesh(U,X,Y,Xt,Yt,mode)
%% Create the [x,y] mesh for the BD surface probes

==> create_interpolant2D.m <==
function A_int = create_interpolant2D(B,x,y)
%% Creates the 2-D Interpolant for synthetic IDS diagnostic
%%

==> create_interpolant.m <==
function A_int = create_interpolant(B,x,y,z)
%% Creates interpolant for synthetic IDS
%% Full 3-D Version, often not needed and slow.

==> createLine.m <==
function [out,dir]=createLine(in,n)
%% Creates line for sample points for synthetic IDS
```

```
%%

==> cyl2cart.m <==
function [A,x,y,z] = cyl2cart(rz,theta,B)
%% Takes B input in cylindrical coordinates and converts to cartesian
%% coordinates

==> cyl2cart_unstructured.m <==
function [A,x,y,z] = cyl2cart_unstructured(rz,theta,B)
%% Takes B input in cylindrical coordinates and converts to cartesian
%% coordinates

==> evalIMP.m <==
function [br,bz,bt,b0] = evalIMP(B,imp_R,imp_Z,imp_ph,rz,phi,be)
%% Evalutes the internal magnetic probe at the specified locations

==> fft_shape.m <==
function [out,fc] = fft_shape(R,Z,R0,Z0,nmodes)
%% Finds the poloidal fft of a NIMROD grid

==> findClosest2D.m <==
function j = findClosest2D(x,y,z)
%% Find the index of y and z that is closest to the values of x

==> findClosest.m <==
function j = findClosest(x,y)
%% finds the index of y that is closest to the value of x
%%
```

```
==> findOpoints.m <==
function [R_pol,R_tor] = findOpoints(rz,phi,B)
%% Calculates the null point of the toroidal and poloidal magnetic fields

==> findQMax.m <==
function [Qmax,lambdaMean] = findQMax(dumps,flname,psicutoff)
%% Legacy code, designed for reading bigHIT flsurf.bin files

==> find_surf_probies.m <==
function [locations,SP_phi_ind]=find_surf_probies(RZgl,phi,pd)
%% Locate grid points of surface probes
%% Originally by Cihan Akcay

==> findTmax.m <==
function [r,z,p,Tmax] = findTmax(T,rz,phi,magAx)
%% Finds the location of maximum value of function T on rz plane and phi

==> gen_NIMspn.m <==
function surf = gen_NIMspn(surf)
%% Appends the probe names to the NIMROD surface probe data

==> getBIMP.m <==
function BIMP = getBIMP(be,rind,zind,phi)
%% Gets the internal magnetic probe signal for given be.  Takes be straight out of NIMRO
%% And iFFT's at the location.

==> getEnergy.m <==
```

```
function [et,emn,ets] = getEnergy(fname,m)
%% Reads an energy.bin file produced by NIMROD.
%% m is number of fourier modes

==> getInjCurr.m <==
function [psi,I] = getInjCurr(B,rz,inj,nimIn)
%%% Calculates the injector current
% Currently unfinished, but should finish to clean up injector calculation

==> getItor.m <==
function [ttor,itor] = getItor(fname)
%% Reads discharge.bin and gets I_tor
%%

==> getKinEnergy.m <==
function [et,emn,ets] = getKinEnergy(fname,m)
%% Reads energy.bin and outputs kinetic energy
%% There are m fourier modes.

==> getMidSurf.m <==
function out = getMidSurf(rz,pd)
%% Finds location of the midplane surface probes on NIMROD mesh

==> getPunct.m <==
function q = getPunct(fname)
%% Reads a nimfl.bin file

==> getPunctMP.m <==
```

```
function R = getPunctMP(fname)
%% Reads a nimfl.bin file produced on the midplane

==> get_SP_modes.m <==
function nimsave = get_SP_modes(nimsave)
%% Calculates the surface probe modes in the same way as JSW's code

==> getSProbe.m <==
function out = getSProbe(rz,pd)
%% Spits out the logical RZ locations of the surface probes in the
%% experiment.

==> getThomson.m <==
function Tmeas = getThomson(thom,rz,T,phi)
%% Given Thomson measurement locations, returns T_e

==> getTonAxis.m <==
function [T,T1] = getTonAxis(rz,be,ti)
%% Evaluates T on the magnetic axis, currently using midplane zero crossing of Bz.

==> gridPropertes.m <==
function [grmax,gzmax,gtmax] = gridProperties(R,Z,phi)
%% Computes properties of NIMROD mesh

==> gridProperties.m <==
function [gr,gz,gt] = gridProperties(R,Z,phi)
%% Computes properties of NIMROD mesh
```

```
==> HIT3_inj_flux.m <==
function [pa,Ia,pb,Ib,pc,Ic] = HIT3_inj_flux(Bdata,r,expFlag)
%% Calculates injector flux and current, hit-si

==> IDS_impacts.m <==
function impact = IDS_impacts(IDS_Coord)
%% Calculates the impact parameters of IDS_Coords

==> IDS_Rigid_Anal.m <==
function IDS_Disp = IDS_Rigid_Anal(nimsave)
%% This does the filtering of the IDS signal as in Aaron's thesis.

==> IMP_Fluct_Plot.m <==
function [polfig,torfig] = IMP_Fluct_Plot(nimsave,imp,pind,tshift)
%% This creates a comparison of the Internal Magnetic Probe from NIMROD and
%% Experiment to create a beautiful  plot showing fluctuations in time.

==> injector_waveform_HIT3.m <==
function [I1,I2,I3,p1,p2,p3] = injector_waveform_HIT3(time,sihi,tshift,nimIn)
%% Reconstructs input injector waveform from [sn].ramp

==> injector_waveform.m <==
function [I1,I2,p1,p2] = injector_waveform(time,sihi,tshift,nimIn)
%% Reconstructs input waveform from [sn].ramp


==> load_synthetic_diag.m <==
%% load_synthetic_diag.m
```

```
%% Legacy Cihan Akcay code that saves synthetic diagnostics to a matlab struct

==> machine_coord.m <==
function [A,theta] = machine_coord(phi,B,fang)
%%  Converts NIMROD R-Z-Phi to more-standard R-Phi-Z

==> make_log_rect.m <==
function [x,y,z,A] = make_log_rect(xr,yr,zr,Ar)
%% makes logically cylindrical mesh into logically rectangular

==> make_polsp.m <==
function surf = make_polsp(surf)
%% Creates a surface probe poloidal signal from surf.B(1:2,:,:,:)

==> make_torsp.m <==
function surf = make_torsp(surf)
%% Takes toroidal component of surface probe data.
%% Negative sign is to convert to standard right-handed cylindrical

==> math_Curl.m <==
function [J,r,z] = math_Curl(B,dBdphi,rz)
%% Takes the curl of a vector field via finite differences

==> max_polfl.m <==
%% max_polfl.m
%% This script reads a batch of polflux.*.bin and then calculates their max values
%% Legacy, use polfl_post.m now
```

```
==> nim2expSP.m <==
function int = nim2expSP(nimsave,tshift,doIMP)
%% Converts nimsave.surf into our magical int.sp format
%% This is the format used by sp_imp_den[sn].mat files

==> nimCurl.m <==
function A = nimCurl(B,C)
%% Evalutes A = B X C in cylindrical coordinates (post fft from nimrod).
%% This is a right-handed operation - that is it keeps nimrod's left handed

==> nimDiverg.m <==
function divB = nimDiverg(B,rz)
%% Computes divergance, good for debugging divb errors

==> nimflRead.m <==
function d=nimflRead(fn)
%% Reads a nimfl.out file

==> nimsaveCreate_bu.m <==
%% Saves stuff into output file for nim_hit_post:

==> nimsaveCreate.m <==
%% nimsavecreate.m
%% Saves synthetic diagnostics and other fields into nimsave struct

==> NIM_sp_conv.m <==
% NIM_sp_conv.m
%% Reformats the NIMROD Surface Probe data into the Experimental Naming
```

```
%% System

==> phys_fields_fluct.m <==
function [a,c,dBdphi]=phys_fields_fluct(b)
%% produces real space representation of the fundamental NIMROD fields.
%% Does this for non-axisymmetric fields only.

==> phys_fields.m <==
function [a,c,dBdphi]=phys_fields(b)
%% produces real space representation of the fundamental NIMROD fields.

==> phys_fields_mode.m <==
function [a,c,dBdphi]=phys_fields_mode(b,mode)
%% produces real space representation of the fundamental NIMROD fields.
%% For the given fourier mode

==> plotIntProbe.m <==
function fig = plotIntProbe(int,leg)
%% Takes int object and plots the internal probe

==> plotPss.m <==
function plotPss(fname)
%% Creates a plot of a nimfl.bin file

==> pol_mode_analysis.m <==
function [Bpm,Btm,r,psi,theta] = pol_mode_analysis(be,polfl,Rp,Zp)
%% Analyzes poloidal mode spectrum of magnetic field.
```

```
==> readBin.m <==
function q = readBin(fname)
%% read a nimrod produced binary file

==> readEn.m <==
function q = readEn(fname)
%% Reads energy.bin

==> read_fieldline_length.m <==
%% read_fieldline_length.m
%% read in field line length data per launch point from NIMROD's poincare
%% plotter, nimfl and bin the field lines or make contour plots. - Legacy

==> read_flines.m <==
function [tpss,pss] = read_flines()
%% Reads the fieldlines*.dat files inside flines directory of current working directory
%% Current version used.

==> readFL.m <==
function [tfl,flp,fls] = readFL(fname)
%% Reads and parses a flsurf.bin file
%% This contains q and lambda

==> readInjInput.m <==
function out = readInjInput(fname,nmodes)
%% Reads a mmnn.txt file for the injector input for coil_type='gen_sihi'

==> read_inputs.m <==
```

```
%% read_inputs.m
%% Legacy from Cihan Akcays post-processor

==> read_nim_namelist.m <==
%% read_nim_namelist.m
%% Script to read a nimrod.in file and parse out the variables

==> read_nimplot_ja.m <==
function [rb] = read_nimplot_ja(fname,rb,pd)
%% Reads a contour.XXXXXX.bin file produced by make_nimplot.py
%% and extracts the current density ja from it

==> read_nimplot_jpar.m <==
function [rb] = read_nimplot_jpar(fname,rb,pd)
%% Reads a parallel_current.XXXXXX.bin file produced by make_nimplot.py
%% and extracts the current density ja from it

==> readPolfl.m <==
function [R,Z,polfl] = readPolfl(fname)
%% Reads polflux.bin from nimrod and spits out the poloidal flux values
%% and logically rectangular grid of the geometry

==> readQ.m <==
%% readQ.m
%% Legacy script, read bigHIT flsurf.bin files and make plots of q.

==> readQmax.m <==
%% readQmax.m
```

```
%% Legacy file, read flsurf.bin files for big HIT

==> red2blue.m <==
function c = red2blue()
%% Generates a color spectrum from red to blue

==> removeDead.m <==
function A = removeDead(q)
%% Remove 'bad' data points in the discharge.bin / energy.bin files
%% If multiple simulations used same binary file (restarts, etc) this will output the la

==> sihi_smooth.m <==
function x = sihi_smooth(y,time,inj_freq)
%% take a boxcar average over an injector cycle

==> sliding_FFT.m <==
function [A,w,T] = sliding_FFT(t,f,N)
%% Performs fft on windows of length N

==> surf_centroid.m <==
function [cR,cZ] = surf_centroid(surf)
%% Calculates the current centroid for surface probe data

==> time_der.m <==
function dEdt = time_der(t,e)
%% Calculates a derivative of a given field

==> volumeIntegrate.m <==
```

```
function N = volumeIntegrate(rz,B)
%% Area Integrates 3D B over volume described rectangularly by rz and toroidally by phi

==> write_puncture.m <==
%% write_puncture.m
%% Used to create a image file that is from a puncture plot.
%% Used in making puncture movies.
```